REFERENCE ONLY

UNIVERSITY OF LONDON THESIS

Degree PhD Year 2006 Name of Author WANG, C.

NUMERICAL SIMULATIONS OF INTERACTIONS BETWEEN NONLINEAR WAVES AND SINGLE- AND MULTI-STRUCTURES

by

Chizhong Wang

A dissertation submitted for the degree of Doctor of Philosophy

Department of Mechanical Engineering

University College London

2006

ProQuest LLC
789 East Eisenhower Parkway
P.O. Box 1346
Ann Arbor, MI 48106-1346

ABSTRACT

Computational methods are developed to simulate interactions of nonlinear waves with single- and multi-structures through the finite element method based on second order and fully nonlinear theories. The three dimensional (3D) mesh with prism elements is generated through an extension of a two dimensional (2D) unstructured mesh. The potential and velocity in the fluid field are obtained by solving finite element matrix equations at each time step using the conjugate gradient method with SSOR preconditioner. The combined Sommerfeld-Orlanski radiation condition and the damping zone method is used to minimize wave reflection. The regridding and smoothing techniques are employed to improve the stability of the solution and the accuracy of the result.

The method is first used to simulate interactions of waves and an array of cylinders in the time domain based on the second order theory. It is shown that the interference between the cylinders has magnificent influence on the phase and amplitude of the waves and forces.

The fully nonlinear problem is tackled first by considering the two dimensional problem, which allows the developed method to be properly tested and validated. Simulation is made for a body in a tank and a wedge-shaped body in oscillation. Comparison is made with results obtained from other methods.

In the next application, the 3D interactions between single- and multi-cylinders with or without flare and waves generated by a wave maker in a rectangular tank are investigated based on the fully nonlinear theory. The effect of the flare on waves and hydrodynamic forces is analysed, and the mutual interference of multiple cylinders is also studied.

The method is also employed to solve the 3D fully nonlinear radiation problems by single- and multi-cylinders undergoing oscillation in the open sea. The result is compared with those obtained from the linear and second order theories.

It is concluded that the developed numerical approaches based on the finite element method can be used to effectively simulate interactions of waves and single- and multi-cylinders with or without flare, which can provide some valuable information to design of offshore structures.

ACKNOWLEDGEMENTS

This study was supported by EPSRC (GR/R26719/01), which entitles "Interactions between steep waves and structures". The support is gratefully acknowledged.

I would like to express my sincere gratitude to my supervisor Prof. G.X. Wu for his valuable suggestions, guidance and constant encouragement and support through my time at UCL.

I would also like to thank Dr. K.R. Drake and Mr James Page who read part of the manuscript and gave helpful suggestions on making improvement of the writing in English. In addition, thanks are given to Dr. Z.Z. Hu who gave me much help and encouragement to finish this study.

Finally I also thank my family who has always been a fountain of support and encouragement.

CONTENTS

LIST OF FIGURES

LIST OF TABLES

LIST OF SYMBOLS

a	radius of section of cylinder
c	phase velocity of wave
d	draught of cylinder
g	acceleration due to gravity
h	water depth
k_0	wavenumber in finite depth
$\vec{n}$:	outward unit normal vector of mean boundary
n_x, n_y, n_z:	components of $\vec{n}$
p	water pressure
$\vec{r}$	position vector
t	time
Δt	time interval
$\vec{u}$	velocity of fluid
u,v,w	velocity component of $\vec{u}$
x, y, z	coordinates in a translating system with an body
x_0, y_0, z_0	spatial coordinates in the inertial (space-fixed) system
$\bar{x}, \bar{y}, \bar{z}$	spatial coordinates in a system fixed on a body
x_f, y_f	coordinates of centre of floatation in *oxyz* system when the body is at rest
$\vec{x}_g$	mass centre of a body
x_g, y_g, z_g	components of $\vec{x}_g$
A	amplitude of motion of a wave maker or a floating body
B	breadth of tank
A_i	acceleration components of a body in motions
A_w	mean waterplane area
$B_{i,3}$	cubic B-spline functions
$\vec{F}$	force
$\vec{F}^{(1)}$	first order oscillatory force
$\vec{F}^{(2)}$	second order oscillatory force
$\bar{\vec{F}}^{(2)}$	second order mean force

$[J]$	Jacobian matrix
$\|J\|$	determinant of $[J]$
$[K]$	global coefficient matrix
K_{IJ}	elements in $[K]$
L	length of tank
L_{cy}	distance between two neighbouring cylinders
L_{dm}	length of damping zone
L_{wc}	distance between wave maker and cylinder at initial time step
$\vec{M}$	moment
$\vec{M}^{(1)}$	first order oscillatory moment
$\vec{M}^{(2)}$	second order oscillatory moment
$\bar{\vec{M}}^{(2)}$	second order oscillatory moment
$\vec{N}$	outward unit normal vector of instantaneous boundary
N_x, N_y, N_z	components of $\vec{N}$
$N_i^{(e)}$	shape function
N_I	global shape function
S_b	instantaneous body surface
$S_b^{(0)}$	mean body surface
S_c	artificial boundary
S_f	instantaneous free surface
$S_f^{(0)}$	mean body surface
S_n	surface on which the normal velocity is given
S_p	surface on which the potential is given
S_w	wave maker surface
S_{wall}	wall of tank
S_{bed}	bottom of fluid domain
T	wave period
$\vec{U}$	constant speed of body advancing in horizontal direction
$\vec{V}$	translational velocity of a body

$\vec{V}_0$ translational velocity of a wave maker

$\vec{X}$ translational motions of a body

X, Y, Z components of $\vec{X}$

α constant

β constant

β_i constant

θ angle

ε perturbation parameter

ξ, η, ζ local coordinate system in an element

η wave elevation

$\eta^{(1)}$ first order wave elevation

$\eta^{(2)}$ second order wave elevation

ϕ velocity potential

$\phi^{(1)}$ first order velocity potential

$\phi^{(2)}$ second order velocity potential

ν constant kinematic viscosity or damping coefficient

λ linear wave length

μ the relaxation coefficient in SSOR preconditioner

χ_i auxiliary functions for calculating hydrodynamic forces

ρ water density or distance between a body and a point in the fluid domain

τ nondimensional time

$\Delta\tau$ nondimensional time interval

ω wave frequency

$\forall$ fluid domain or volume

∇ gradient operator

∇^2 Laplace equation operator

$\frac{\partial}{\partial t}$ partial time derivative in fixed coordinate system

$\frac{D}{Dt}$ substantial derivative and is defined as $\frac{D}{Dt} = \frac{\partial}{\partial t} + \nabla\phi \cdot \nabla$

$\vec{\Omega}$ angular velocity

$\vec{\Theta}$	rotational motion of a body
$\Theta_x, \Theta_y, \Theta_z$	components of $\vec{\Theta}$
$\vec{\Xi}$	displacement vector of a body
Ξ_x, Ξ_y, Ξ_z	components of $\vec{\Xi}$

1. INTRODUCTION

1.1 Background

One of the most important tasks in ocean engineering is to describe and predict water waves. Wave runups, hydrodynamic forces acting on ocean structures and the resulting motions have been intensively studied for many years. However, it is still not easy to obtain accurate results for many practical situations. Further research is required in the fields of mathematical modelling and numerical procedure.

When studying interactions between waves and ocean structures, the fluid is usually assumed to be incompressible and inviscid, and the flow irrotational. The fluid motion can be described by a velocity potential ϕ which satisfies the Laplace equation within the fluid domain and boundary conditions on the free surface, body surface and a surface at the far field. Although the governing equation is linear, the boundary conditions are fully nonlinear, which is the main source of difficulty. There are several issues: (i) a complicated condition has to be satisfied on the free surface which is not known a priori, (ii) numerical tracking of the free surface is prone to instability, (iii) an appropriate boundary condition to simulate the open sea condition is required at the far field to avoid numerical reflection, (iv) the body motion and the fluid flow is fully coupled.

Perturbation theories have traditionally been used to solve the problem. Based on the assumption that the wave amplitude is small relative to the wavelength and the body dimension, the conditions on the free surface and body surface are satisfied on their mean positions through the Taylor expansion. There are two commonly used methods: the frequency domain method and the time domain method. The former is based on the assumption that the fluid motion has reached a periodic state. The advantage of this method is that for each frequency the equation has to be solved only once for each order of the perturbation expansion as the time factor has been taken out. By contrast, the time-domain method needs to solve the problem at each time step, which can usually be repeated for thousands of time steps.

Studies of interactions between nonlinear water waves and structures are very important both in design and theoretical studies. The linear model has been popular since it provides many useful results. In particular, it can capture resonant phenomenon well. The second or higher order model can further provide some interesting features of nonlinearity such as drift forces and ringing oscillations. But these analyses are based on the assumption of small amplitude waves. The motivation of the current study arises primarily because of the need to obtain more accurate prediction of runups, forces and motions in extreme conditions where the perturbation theory becomes invalid.

1.2 Theories of wave-structure interactions

The studies of the interactions between waves and structures have received a considerable amount of interest over the past years and many theories and numerical methods have been developed. This chapter will give a review of the previous work in this and the next sections.

There are a variety of theories for the nonlinear wave model that have been developed such as linear theory, second order theory and fully nonlinear theory. The solutions of these theories give insight into the propagation of waves and can provide answers to problems when their assumption is valid. In the linear theory, conditions on both the free surface and body surface are satisfied on their mean positions and all the nonlinear terms are ignored. The second order theory imposes the boundary conditions on the same position, but all the product terms in the perturbation expansion are retained. Strongly nonlinear problems may be described by the fully nonlinear theory with all the terms included. More information can be found from Lamb (1945), Whitham (1974), Sarpkaya & Isaacson (1981), Mei (1983) and Dingemans (1997).

1.2.1 Linear frequency-domain theory

In this theory, it is assumed that interactions between waves and structures have lasted for a long time, the initial transient effect has disappeared, and the flow and the motion of the structure have reached a periodic state. If the wave is sinusoidal, the corresponding motion of the structure is also sinusoidal but with a phase difference.

Since the 1940s, researchers have tried to seek a theory to predict floating body motions. Haskind (1946a, b) decomposed the disturbed potential into a diffracted potential and a radiated potential. He used the Green's theorem to construct an integral equation for the potential and obtained some results for a thin ship. Nearly at the same time, Havelock (1942) and Ursell (1949) solved the boundary value problem for motions of a ship and floating cylinders, respectively.

A realistic 3D simulation of ship motions was not easy and new methods were required to efficiently predict ship motions. There was a breakthrough in the 1950s. The approach was the strip theory/slender body theory, which is stemmed from Korvin-Kroukovsky (1955) and then further developed by Korvin-Kroukovsk & Jacobs (1957) to investigate the pitching and heaving motions of a ship. The strip theory assumes that ships are slender and may be longitudinally divided into many intervals and that the 3D fluid flow around the hull is simplified as a 2D flow around each transverse section. The hydrodynamic loading on the ship was obtained by integrating the 2D results along the ship length from which the ship response could be determined. Several strip theories such as rational strip theory (Ogilvie & Tuck, 1969), new strip theory (Tasai & Takagi, 1969), STF theory (Salvesen, Tuck & Faltinsen, 1970) have been developed. The STF method has the most successful application in estimating motions and loads of conventional ships in waves. In 1980, a new theory called unified theory was developed by Newman & Sclavounos (1980) and got remarkable success in practical applications of predicting ship motions. This theory divided the fluid domain into an interior domain near the ship and an exterior domain away from the ship. The strip theory was used in the interior domain and 3D source distribution along a line was used in the exterior domain. Some other slender theories such as those on high speed vessels (Chapman, 1975 & Faltinsen, 1993) were also developed. Kashiwagi (1995) presented a theory which combined the two theories by Newman & Sclavounos (1980) and Chapman (1975) together. This theory was suitable for medium speed. It was reported that it may provide good results of hydrodynamic coefficients in surge motions. It should be mentioned here that the strip theory has been extended to nonlinear problems such as Yamamoto *et al.* (1978, 1979), Jensen & Pedersen (1979), Meyerhoff & Schlachter (1980), Wu & Moan (1996), Xia *et al.* (1998) and Fonseca & Guedes Soares (1998), and a recent development was made by Gu, Shen & Moan (2003).

Strip theory is efficient and provides good global results such as body motions but it does not give accurate local results especially near the stern and bow. With the

development of computational speed and memory, three-dimensional (3D) numerical simulations were developed. A successful way to solve 3D zero-speed problems is to use a Green's function in the frequency-domain. This has become a standard design tool for large volume offshore structures (Faltinsen, 1990). Faltinsen & Michelsen (1974) and Garrison (1978) employed the source distribution method to study motions of structures and loads on structures at zero speed. Linton (1991) employed the multipole method to study radiation and diffraction problems on a submerged sphere in finite depth, and a recent work on Green's functions was made by Chakrabarti (2001)

For the problem of ship motions at forward speed, the 3D study began with Chang's pioneering work (1977), this was followed by Inglis & Price (1982), Guevel & Bougis (1982), Wu & Eatock Taylor (1987) and Iwashita & Ohkusu (1989). The 3D frequency-domain analysis of ship motions at forward speed employs Green's functions in complicated mathematical forms. The Green's function has singular and highly oscillatory properties which can lead to difficulties in computation which was captured in a recent study by Chen & Wu (2001). Chang (1977) directly calculated double integrals in the Green's function and the calculation requires a small step in the numerical integration due to the oscillatory behaviour of the Green's function and so is very time-consuming. Inglis & Price (1982) replaced the double integral terms belonging to the principal value formulation by single integrals in the expression of the exponential integral. Wu & Eatock Taylor (1987) introduced the complex exponential integral to reduce the double integral.

The low speed assumption was proposed since the problem of ship motions at forward speed is complex. Based on this assumption, the Green's function of zero speed was used and a modified term was added to consider the effect of the speed such as in that by Wu & Eatock Taylor (1990a). Besides the Green's function method, Dawson (1977) suggested distributing Rankine sources near the free surface and body surface to solve the problem of forward speed. This approach was then used by Nakos & Sclavounos (1990), and extended to nonlinear problems by Jensen *et al.* (1989) and Raven (1992).

1.2.2 Linear time-domain theory

The frequency-domain method is applicable to periodic problems. For the general transient problem, the time-domain method may be used. Many publications have been based on this theory. Maskell & Ursell (1970) considered a transient oscillation of a floating body. Lee & Leonard (1987) studied a free oscillation of a floating body induced by a wave maker. Beck & Magee (1990), Bingham, Korsmeyer & Newman (1994) and Bratland, Korsmeyer & Newman (1997) studied wave-body interactions and obtained the added mass and the damping coefficient.

Like the linear frequency-domain theory, the Green's function method is usually used to study body motions in the time domain. The early study using the Green's function in ship motions are credited to Finkekstein (1957) and Cummins (1962). Finkekstein (1957) derived the Green's functions of infinite and finite water depth in both two and three dimensions, and Cummins (1962) decomposed the velocity potential into the instantaneous and memory parts. Ogilvie (1964) and Kotik & Lurye (1964) extended Finkekstein and Cummis's work to the cases of ship motions at forward speed. Wehausen (1967) derived an integral equation and the Haskind relation for ship motions at zero forward speed. However, it was not until 1976 that Van Oortmerssen (1976) successfully implemented it using a computer. Subsequently, with the development of computer facilities, many researchers began to use the Green's function method to investigate body motions. Yeung (1982) and Newman (1985a) studied the free oscillations of floating bodies in two dimensions and symmetric floating bodies in three dimensions, respectively. Beck & Liapis (1987) calculated the added mass and damping coefficients of floating bodies at zero speed. The calculation of the time-domain Green's function method may be significantly faster than the frequency-domain Green function method when the forward speed is considered (Beck, 1994).

With the increase in computational power, it is possible to use the Rankine source method to calculate wave-body interactions in the time domain. The Rankine source is easier to calculate than the Green function, but it requires a distribution of Rankine sources on the free surface and/or other boundaries. Isaacson & Cheung (1993) studied the effect of current on the radiation and diffraction of regular waves around a two-dimensional body in the time domain and Cheung *et al.* (1996) extended it to the 3D case. Some other work may be found such as that by Prins & Hermans (1994) who calculated wave-current interactions in two dimensions and that by Kim, D.J. & Kim, M.H. (1997) who calculated interactions of wave-current and large body in three dimensions.

1.2.3 Second or higher order frequency-domain theory

The linear theory gives satisfactory results for ship motions of small amplitude or in small amplitude waves. But it ignores all the important nonlinear features such as mean drift forces, slowly-varying forces or sum frequency forces. This leads to the development of the second order theory. The second order theory retains all the product terms in the Bernoulli equation and in the Taylor expansion. Typical publications include those by Eatock Taylor & Hung (1987), Abul-Azm & Williams (1988), Kim & Yue (1989), Wu & Eatock Taylor (1990b) and Newman (1990).

There are two main approaches to calculate the second order force. One is based on the conservation of momentum and the other is the direct pressure integration. The former uses the far field potential to calculate forces and so is called the far field method. This method was mainly developed by Maruo (1960) and extended by others such as Newman (1967), Lee & Newman (1991), Lin & Reed (1976) and Gerritsma & Beukelman (1972). The second method (Pinkster & Van Oortmerssen, 1977) is to directly integrate pressure on the surface of the body to obtain second order forces. It employs the near field potential, and so it is called the near field method. This method has been used by other researchers such as Faltinsen & Loken (1978). The far field method can be used to calculate the mean force in the horizontal direction. However, complete second order forces including the mean force and the oscillatory forces may need the near field method.

Many other publications have also focused on the calculation of second order forces. For example, Ogilvie (1963) obtained the mean vertical force on a submerged cylinder through the integral of pressure on the mean wetted cylinder surface. Wu (1991a) calculated second order forces on horizontal cylinders. McIver (1994) employed the near field method to study second order diffraction problems in two dimensions. For problems involving bodies at forward speed, focus was on added resistance in waves such as in those by Wu (1991b, 1993) about submerged bodies in finite depth and Varyani (1993) about calculation of added resistance on submersibles.

The numerical calculation of the second order potential, which satisfies an inhomogeneous free surface condition, is not an easy thing. However, it was shown by Molin (1979) and Lighthill (1979) independently that it was not necessary to calculate

the second order potential if only the second order forces were required and not the potential. A fictitious radiation potential at double the frequency of the incident wave was introduced and the second order forces were expressed in terms of an integral on the mean free surface. This method was extended by Eatock Taylor *et al.* (1989) to obtain the pressure on the body surface, Wu & Eatock Taylor (1989) to study 2D diffractions by horizontal cylinders and Wu (1991a) to calculate second order wave reflection and transmission at infinity in two-dimensions. Other extensions can be found by those such as Molin & Marion (1986), Eatock Taylor & Hung (1987) and Abul-Azm & Williams (1988). The direct numerical computation of the second order potential needs more effort, and 2D & 3D studies of diffraction problems have been undertaken by Vada (1987) and Kim & Yue (1989). Chau (1989) or Chau & Eatock Taylor (1992) employed the eigenfunction expansion method directly to obtain the second order potential.

In some cases, the second order theory is sufficient for capturing nonlinear features. But higher order forces will be important in many other problems. For example, tension leg platforms (TLPs) and gravity-base structured (GBS) are usually acted on by wave forces with a frequency that is three times the wave frequency and resonant oscillations will occur. This phenomenon is known as 'ringing' and 'springing'. Draugen monotowers in waves will be acted on by third order loads (Faltinsen, 1999). Generally, a study of third order forces requires a high accuracy for results at lower order. There is some works on third order loads such as those by Malensa & Molin (1995) and Faltinsen, Newman & Vinje (1995). Vantorre (1986) presented a third order theory to study radiation problems about floating and submerged bodies experiencing heaving motions, but its mathematical formulation is very complicated.

1.2.4 Second order time-domain theory

An alterative to the frequency-domain second order theory is the time-domain second order theory. This theory was used by Isaacson & Cheung (1990, 1991, 1992). Just like the frequency-domain second order theory, it is possible to apply Taylor expansions to transform the free surface boundary and body surface conditions from their exact locations to their corresponding mean positions. At the same time, an initial condition is given and two linear systems are solved to obtain the first- and second- order potentials

and the hydrodynamic forces in the time domain. Isaacson & Cheung made investigations into the diffraction problems of a submerged body (1990) and floating bodies in two and three dimensions (1992, 1993). Meanwhile, a 2D radiation problem by a floating semi-circular cylinder was studied by Isaacson & Ng (1993) and a 3D radiation problem by Isaacson, Ng & Cheung (1993). Ng & Isaacson (1993) employed this theory to study the motion of a freely-floating cylinder and interactions between waves and a moored floating cylinder. Kim, Kring & Sclavounos (1997) also employed this theory to study 3D wave-body interactions. The interactions between a cylinder and second order waves together with a current were considered by Buchmanna, Skourup & Cheung (1998).

1.2.5 Fully nonlinear theory

The linear and second order theories are based on the small amplitude wave assumption. The linear theory is efficient for some problems such as prediction of ship motions in small waves, and its numerical implementation is simple. But it cannot capture some nonlinear features such as mean forces. These phenomena can be uncovered by using the second order theory. The numerical implementation for the second order theory requires much more work than the linear theory but still has the advantage of a fixed computational domain. For small and mild wave problems, the second order theory gives satisfactory results. However, the second order theory is invalid for large amplitude waves. These kinds of problems require the fully nonlinear model. This model usually employs the boundary element method (BEM) or the finite element method (FEM) in space and the finite difference method (FDM) in time. Longuet-Higgins *et al.* (1976) developed a numerical approach called mixed Euler and Lagrange (MEL) for steep waves. It used the Eulerian method to obtain the solution in the fluid field, and then used the Lagrangian method to track the position of the free surface and velocity potential on the free surface. Faltinsen (1977) used this method to study transient nonlinear free surface motion outside and inside moving bodies. Vinje & Brevig (1981a) studied a two-dimensional radiation problem using complex variable functions. Cointe (1989) & Hwang *et al.* (1988) applied the boundary element method to solve the same problem as Vinje & Brevig (1981a). The MEL method was also used to study the water entry of two-dimensional wedge-shaped bodies (Zhao & Faltinsen,

1993). Scullen & Tuck (1995) calculated the nonlinear resistance increase on a submerged cylinder at forward speed. Other work includes that by Kashiwagi (1996) and Berkvens (1998) on simulating free heaving motion of a sphere and Tanizawa (1996) on the motions of a floating body. Some recent applications were made by Maiti & Sen (2001) on wave diffraction by single and twin hulls and by Koo & Kim (2004) on a freely floating body. Taking a different approach from MEL, Sen (1993) used the Eulerian free surface condition to study the heaving and rolling motions of floating bodies in two dimensions.

In three-dimensional cases, Isaacson (1982) calculated interactions between nonlinear solitary waves and a vertical cylinder in the time domain. Lin *et al.* (1984), Dommermuth & Yue (1987) studied diffraction and radiation problems about circular cylinders based on the MEL boundary element method. Ferrant (1997) simulated strongly nonlinear wave generation and wave-body interactions. Celebi and Beck (1997) used a Rankine source method called desingularised BEM to solve fully nonlinear transient waves. Celebi, Kim & Beck (1998) employed the desingularised BEM simulated 3D numerical wave tank. A recent work is on interactions of linear and nonlinear irregular wave and cylinders by Boo (2002).

All the above mentioned work employed the boundary element method. Some researchers used the finite difference method to study the wave-body interactions such as Wang & Spaulding (1988) who solved the 2D problem. Arai *et al.* (1993) used the FDM to simulate a 3D numerical tank.

In the last decade, simulations of fully nonlinear waves based on the finite element method have been developed. This method was used to simulate nonlinear transient waves problems such as those by Wu & Eatock Taylor (1994, 1995), Greaves, Borthwick, Wu & Eatock Taylor (1997) and Westhuis (2001) in two-dimensions and Wu *et al.* (1998), Ma, Wu & Eatock Taylor (2001a, b), Hu, Wu & Ma (2002) and Wu & Hu (2004) in three-dimensions.

1.3 Numerical methods in studying wave-structure interactions

Generally, there are four main numerical methods used in the fluid problem: the finite difference method (FDM), the finite volume method (FVM), the boundary element

method (BEM) and the finite element method (FEM). Sometimes mixed methods such as coupled FEM and BEM are used. There are a number of reviews on ideal free surface flow problems such as linear flows by Mei (1978), both linear and nonlinear flows by Yeung (1982), nonlinear problems by Schwartz & Fenton (1982) with an emphasis on theoretical methods, and numerical methods by Tsai & Yue (1996).

1.3.1 Finite difference method (FDM)

The finite difference method is an efficient numerical tool in solving fluid problems, and it has been the mainstream numerical method for a considerable time. The fundamental idea of the method is to discretise the fluid domain with an orthogonal structured mesh and replace the continuous derivative in the governing equation and boundary conditions with discretised versions and then solve the difference equation. Actually, it is simple to solve directly time-dependant problems with a regular boundary on which the boundary conditions are easy to handle. For problems of complex domain, a body-fitting system is usually employed to convert the equations of the problem in the physical domain to that in a regular computation one. This method is widely used in viscous flows and wave-making problems such as simulations of nonlinear ship waves by Miyata *et al.* (1985, 1987). It is also employed to handle problems of interactions between waves and structures, For example, Telste (1985) simulated a large amplitude heave motion of a two-dimensional cylinder in a free surface, and Yeung & Wu (1989) calculated the motions of a floating body in a closed domain. Some other work about using the FDM in the problem of flow with a free surface, such as Emmons (1972), Orsag & Israeli (1974) and MacCormack & Lomax (1979), can also be found.

1.3.2 *Finite volume method (FVM)*

The finite volume method is a numerical method for solving partial differential equations of conservation law system; it has been extensively used fluid mechanics, heat and mass transfer and petroleum engineering. One advantage of the finite volume method over the finite difference method is that it can use not only the structured mesh but also the unstructured one, and so it may be used on any domain with arbitrary geometries. A feature of this method is the local conservation of the numerical fluxes

for each control volume, which also ensure the global conservation for the entire domain, and this makes the finite volume method quite attractive when modelling problems for which the flux is of importance, such as in fluid mechanics, semi-conductor device simulation, heat and mass transfer. In fluid mechanics, the FVM method is mainly used to simulate viscous flow problems. Some works on simulations of viscous fluid based on the FVM may be found such as those by Greaves (1995), Hu *et al.* (2002) and Wu & Hu (2006).

1.3.3 Boundary element method (BEM)

Although the FDM is an important numerical method in computational fluid mechanics, in the field of wave-body interactions, the BEM has been widely used for solving linear and nonlinear problems. A noticeable feature of the BEM in linear wave-body interaction problems is that the use of Green's functions ensures that the governing equation and boundary conditions except those on the body surface are automatically satisfied. As a result, it is only necessary to distribute sources on the body surface, and so it has much smaller number of unknowns. An early work in this area was that by Kim (1965), who obtained hydrodynamic coefficients for heaving and swaying motions of a 2D circular cylinder and a sphere both submerged and on free surface. It was then followed by other researchers such as Frank (1967), Yeung (1973), Hearn (1977), Noblesse (1982) and Newman (1984, 1985b). A common feature of these pieces of work is the use of special functions to express Green's functions so the singular integral could be avoided and the corresponding computations become more efficient. For higher order and fully nonlinear problems, no Green's function which satisfies the free surface boundary condition and radiation condition has been found. In these cases, the Rankine source method is usually used. This method is simple in form but it requires discretisation on all the boundaries including the free surface and so it has much more unknowns.

The simplest discretisation scheme in the BEM is to use the constant panel method (CPM) (Hess & Smith, 1964), which assumes that the collocation point is the element centroid and physical variables on an element is constant. It needs a huge number of elements to achieve accurate numerical results. For simulations of nonlinear wave-body

interactions, higher order boundary element method (HOBEM) or linear element method are usually be used. In contrast to the CPM, the higher order element method assumes that the collocation points are the vertices and physical variables such as the potential on an element continuously vary. One advantage of the higher order element method is that it can provide more accurate results using less numerical computation compared with the CPM. Liu, Kim & Lu (1990) gave a comparison between the HOBEM and the CPM and show the efficiency of the former, Choi *et al.* (2000) further verified the efficiency of the HOBEM. The most common higher order element is the 8- or 9-node bi-quadratic isoparametric element such as Choi *et al.* (2000), Xu & Yue (1992) and Boo (2002). Recently, Grilli *et al.* (2001) utilised the 16-node cubic quadrilateral element to study three-dimensional overturning waves and the corresponding numerical method has been developed. Another advantage of the HOBEM for second order wave-body interactions is that spatial first- and second-order derivatives can be obtained through shape functions, which is difficult when using the CPM. Extensive work can be found on second order wave-body interactions based on the HOBEM such as that by Teng & Eatock Taylor (1994), Choi *et al.* (2000) in the frequency domain and Kim, Kring & Sclavounos (1997) in the time domain. It should be mentioned that discontinuous elements are sometimes used in numerical simulations such as those by D. J. Kim & M.H. Kim (1997) and Boo (2002). The discontinuous elements are usually distributed along the intersection of two boundaries that Dirichlet conditions are imposed. The objective of using these elements is to remove the singularity in the coefficient matrix, where two rows in the matrix are identical.

In the last two decades, the fully nonlinear simulations have become popular, and the BEM has gained a wide range of application in this area such as the computation of 3D water waves by Xu & Yue (1992), wave-body interactions by Ferrant (1997) and nonlinear irregular wave simulations by Boo (2002).

As well known, a main feature of the BEM is that singularities exist when source points and field points coincide. The singularities may cause serious computational difficulties and so require special numerical schemes. For 2D problems, exact analytic integrals can be found (Lage & Costa, 1987). For 3D problems, there is also much work on the calculation of the singular integral such as that by Lachat & Watson (1976), Rizzo & Shippy (1977), Cristescu & Loubignac (1978), Srivastava & Contractor (1992) and Liu *et al.* (1995). Some

recent development can also be found such as those by Karami & Derakhshan (1999) and Smith (2000).

Sometimes special elements for example B-spline elements have been used by a few researchers such as simulations in 2D by Maiti & Sen (2001) and Lee & Kerwin (2003) and in 3D by Lee, Maniar, Newman & Zhu (1997) and Kim & Shin (2003). The B-spline element can offer a more continuous representation of potential or velocity and geometry description, and can improve the numerical efficiency. Numerical procedures however, are more complicated.

1.3.4 Finite element method (FEM)

The finite element method was developed in the late 1950s for structural analysis. The fundamental idea of this method is to discretise the continuous fluid domain into separate elements and then use interpolation functions within the elements. At first it was less frequently used in fluid mechanics than the finite difference method, but now it has become a powerful and more popular alternative in water wave problems. Shen (1977) gave a detail review on its applications in fluid-flow problems, and Mei (1978) also mentioned its application in linear wave-wave radiation and diffraction problems.

During the early days of the development of the FEM in fluid mechanics, finite element equations were derived from the variational principle. Luke (1967) derived a formulation for the problem of free surface but did not implement it on computers. This variational principle was then extended by Whitham (1967, 1970) to check the dispersion characteristics of nonlinear waves. Bai (1975b) also employed a variational method to handle two-dimensional linear scattering problems. Other work such as Chan & Larock (1973), Larock & Taylor (1976), O'Carroll (1976), Betts (1979), Aitchison (1980) and Betts & Assaat (1980) also used the variational principle to solve linear and nonlinear fluid problems of a free surface without a body. However, variational principles may not always be found due to the complexity of fluid problems. Actually, the most popular approach is the so called Galerkin weighted residual method and it has been widely used in linear fluid problems such as Bai (1977, 1978, 1979) and Lenoir & Jami (1978).

As the FEM was further developed in fluid mechanics, the hybrid element method was used. They were mainly employed to solve the problem of the infinite domain.

These hybrid methods suggest that the fluid domain is divided into two parts: the interior which is close to the body and the exterior which is away from the body. The interior domain is discretised with finite elements, but the analytical presentations or the infinite element method, which satisfies the radiation condition, is used (Zienkiewicz *et al.*, 1978) in the exterior domain. These methods can effectively decrease nodes and correspondingly require less storage and CPU time. These methods were generally used to handle linear problems. Both the variational principle and the Galerkin formulation can be used in the hybrid method. Bai & Yeung (1974) and Chen & Mei (1974) employed variational methods to solve problems of a free surface in an infinite domain, and then Bai (1975b) applied this method to the diffraction of oblique waves by an infinite cylinder. The Galerkin formulation was used by Yim (1975) to solve a problem of linear ship waves. Bai (1975a, 1977, 1978) also used it to study flow with free surface in both 2D and 3D problems, and then Bai (1979) derived an equation about blockage effects correction with a free surface. The method used by Bai (1978) was also extended to nonlinear steady wave problems by Bai & Han (1994). Other work about applications of hybrid methods in problems of free surface can be found such as Wellford & Ganada (1980), Oomen(1981), Jami (1981), Mei & Chen (1976), Yue and co-workers (1978, 1979) and Euvrard *et al.* (1981). Recently, a method coupled by the FEM and the BEM was developed by Wu & Eatock Taylor (2003) to solve fully nonlinear wave-body interactions. The difference is that the interior domain is discretised with boundary elements and the exterior with finite elements.

The work above-mentioned is mainly about linear problems. The finite element method was also developed to handle weak nonlinear water waves. Clark *et al.* (1991) used a second order model in the frequency domain to simulate Stokes wave diffraction problems on waves acting on offshore structures.

Fully nonlinear simulations of free surface problems based on the finite element method have also achieved a lot. Nakayama & Washizu (1980) used the finite element method to analyse the sloshing of liquid in a container subjected to forced pitching oscillation. Lynch & Werner (1987, 1991) simulated the actions of linear and nonlinear waves on harbours due to winds and tides. Allievi & Calisal (1993) employed a semi-Lagrangian finite element method to solve nonlinear flow with a free surface and used slender body theory to calculate the nonlinear water waves of Wigley ships advancing in static water. In the last decades, Wu & Eatock Taylor completed several pieces of work on the simulation of nonlinear water waves based on the finite element method.

They used the FEM to calculate 2D nonlinear transient waves (1994) and studied a nonlinear wave radiation problem in two dimensions (1995); Greaves *et al.* (1997) simulated fully nonlinear steep waves, and Wu, Ma & Eatock Taylor (1998) gave a fairly broad account of both 2D and 3D sloshing problems based on the finite element method. Recently, Ma, Wu & Eatock Taylor (2001a, b) developed a numerical scheme based on the finite element method to study fully nonlinear interactions between vertical cylinders and steep waves. More recently, Hu, Wu & Ma (2002) extended this method to the case that a cylinder is in forced motion, and then Wu & Hu (2004) considered a floating structure in large amplitude motion based on a hybrid mesh with an unstructured mesh near the cylinder and a structured mesh away from the cylinder. All these pieces of work are for cylindrical structures with no variation of the cross section in the vertical direction. Wang & Wu (2004) extended this method to circular cylinders with flare. All this work employed elements with linear shape functions.

To improve the accuracy and efficiency, some techniques such as high order elements and adaptive methods may be used. The same accurate results with fewer high order elements than that with linear elements may be obtained. Wang & Khoo (2005) employed the quadrilateral element with quadratic shape functions to simulate 2D sloshing problems in forced random oscillations. However, there are some difficulties when using higher order elements. A big challenge is the mesh generation, which will probably be much more difficult than that with linear elements, especially for 3D complex domains. The adaptive technique may lead the simulation to be more efficient and the result to be more accurate. There are a few kinds of refinement methods: *h*-refinement, *p*-refinement, *r*-refinement and their combinations: *hp*-refinement and *hr*-refinement. The refinement is based on a posteriori error indicator, which may be predicted from the solution gradients of variables: density, velocity pressure or temperature. The error indicator in each element is first calculated. If the indicator is greater than a specific tolerance in an element, the mesh may then be refined in the following ways: (1) the element is subdivided through its midpoints for *h*-refinement, (2) the nodes around the element are rearranged for *r*-refinement and (3) the order of the shape function is increased for *p*-refinement. An example of using *hp*-refinement technique can be found in Robertson and co-workers (1999, 2004) for simulations of nonlinear free surface flows.

It is known that most of the previous work on wave-body interactions is based on the boundary element method. However, it is shown from above-mentioned work that the finite element method is robust and effective in solving nonlinear water wave problems. A comparison between the FEM and the BEM was made by Wu & Eatock Taylor (1995). Their results suggested that the FEM was more efficient in both memory requirement and computational time than the BEM. A main advantage for the BEM is that the discretisation need only be performed on the boundary, which reduces the dimension of the problems by one. In contrast to this, the FEM requires discretisation of the whole fluid domain. Hence, the number of nodes in the FEM is much larger than that in the BEM. Since the solution is calculated in the whole domain for the FEM and only on the boundary for the BEM, it seems that the BEM needs much less computer storage and computer time than the FEM. However, the global coefficient matrix in the FEM is symmetric and sparse, which can be held efficiently in packed storage of only nonzero elements. Therefore, smaller storage and computational resources are required than the BEM, which corresponds to a fully populated matrix. For example, a 3D mesh with 8-node hexahedral elements in a wave tank with 10 intervals in three directions, the number of nodes in the domain is 1331, and the total number of nonzero elements in the coefficient matrix is only 15561. If the same 4-node quadrilateral elements on the boundary are used for the BEM, it will lead to a total number of $231 \times 231 = 53361$, even when the symmetry about the wall and bottom of the tank is considered. In the numerical simulations in this thesis, the number of nodes may sometimes reach hundreds of thousands, but using the advantage of the packed storage scheme, we can finish most of our numerical simulations in a personal computer with 256 MB memory. This would be problematic if the same nodes were distributed on the boundary in the BEM. The finite element equation can be solved by some efficient methods such as the conjugate gradient (CG) method with a symmetric successive over relaxation (SSOR) preconditioner.

1.4 Wave absorption

In numerical simulations, the computational domain is usually truncated at some position which is an artificial boundary. This boundary was differently named as the radiation boundary (Zienkiewicz *et al.*, 1977), the transmitting boundary (Claerbout,

1976), the absorbing boundary (Lysmer & Kuhlemeyer, 1969), the nonreflecting the boundary (Smith, 1974a, b), the silent boundary (Cohen & Jennings, 1983) or the open boundary (Jagannathan, 1986). A radiation condition is required to ensure that the wave reflection from this boundary is minimal. Generally, there are two kinds of approaches for absorbing waves. One is the Sommerfeld-Orlanski radiation condition; the other is the damping zone method.

1.4.1 Active wave absorption in physical tanks

In physical tanks, wave reflection is a very important issue. Waves generated by a wave maker at one end of the tank can be absorbed by another wave maker at the other end. Milgram (1970) presented a method for active wave absorption by a moving boundary of wave-maker type. Wave elevations in front of the absorber were used for controlling the device. A flap type active absorber was implemented in a physical wave flume and was found to give good results. Bullock & Murton (1989) developed and implemented a wedge type absorbing wave maker in physical wave flume experiments. The wedge motion was controlled partly by the requirement of the wave field generation and partly by a feed-back loop connected to two wave gauges mounted on the front face of the wave maker. Some other methods have also been developed. Skourup & Schaffer (1998) studied active absorption of multidirectional waves by a piston type wave absorber and developed a 3D active wave absorption control system called 3DAWACS. Chatry *et al.* (1999) applied the Kalman filter to self-adaptive control of a piston wave absorber. These methods can theoretically be used in numerical wave tanks.

1.4.2 Artificial wave absorption in numerical tanks

In the numerical simulation of water waves, the computational fluid domain is truncated at a finite distance. The boundary should keep the wave outgoing and not reflect it back. The most common methods to achieve this goal are to employ a radiation condition or use a passive wave absorber. One approach based on Sommerfeld's radiation condition was developed by Orlanski (1976) and so is usually called the Sommerfeld-Orlanski radiation condition. In this method, the phase velocity was

calculated numerically at each time step in the vicinity of the boundary. The computation should ensure that the phase velocity smoothly develops with the time. Much work on this subject include that by Chan (1977), Jagannathan(1988), Romate(1992), Isaacson(1991, 1992, 1993), Sen (1993) and Kim, D.J. & Kim, M.H. (1997). Romate (1992) also discussed an extension of the Sommerfeld radiation condition to a higher order, but it has a higher computational demand and may cause numerical instability.

The passive wave absorber uses the so-called damping layer, damping zone, sponge layer or absorbing beach in front of the truncated boundary. The free surface conditions inside the damping zone are modified by adding a dissipative term to absorb outgoing waves as much as possible. This approach can be easily implemented and it is very effective for shorter wave problems (Tsai & Yue, 1996). However, the computational domain must be extended to include the damping zone, which leads to more elements and nodes in numerical simulations.

Baker *et al.* (1981) introduced the damping layer into their study of 2D nonlinear free surface flow. Around at the same time, Israeli & Orszag (1981) employed the sponge layer with the combination of the viscous damping and the Newtonian cooling techniques for a one-dimensional wave equation. This method is widely used now. Cointe (1989) utilised this method in his nonlinear simulation of transient free surface flow based on the boundary element method, in which Newtonian cooling terms were introduced in both the kinematic and the dynamic free surface conditions. However, it was shown by Cao *et al.* (1993) that a dissipative term only added to the dynamic free-surface condition would also give good results for wave absorption. Subramanya & Grilli (1994) and Celebi *et al.* (1998) have used this formulation in their sponge layers. However, other formulations are also possible (eg. Ferrant, 1993 & Wang, 1993). Nakos *et al.* (1993) proposed a damping zone method. They introduced Newtonian cooling term into kinematic condition and excellent performance was obtained. It should be mentioned that the viscous damping and Newtonian cooling terms should be carefully chosen. Otherwise, the absorption effect will be either too strong or too weak. A portion of the energy will be reflected from the radiation boundary for weak absorption or strong absorption. The damping coefficient may be determined by optimisation schemes.

The combination of several different techniques for treating the radiation condition, which was suggested by Israeli & Orszag (1981) and Clement & Domgin (1994), may

be more effective. Ohyama & Nadaoka (1991) combined a sponge layer with the Sommerfeld-Orlanski condition and studied its performance in order to find optimum sponge strength. Boo & Kim (1997) and Boo (2002) combined a sponge layer with a stretching technique for simulations of nonlinear irregular waves. Ma, Wu & Eatock Taylor (2001a, b) used the damping zone and Sommerfeld-Orlanski condition in their 3D interactions of steep waves and structures based on the FEM. More details on the radiation condition will be given in Chapter 3.

1.5 Numerical methods for calculating hydrodynamic forces

The force is a very important factor for the designs of ocean structures. It is easy to obtain the hydrostatics, but the calculation becomes more difficult for the hydrodynamic force. The hydrodynamic force may show strong nonlinearity when the interactions of waves and ocean structures are serious.

A difficult problem for calculating the hydrodynamic force is how to obtain the derivative of the velocity potential with respect to time $\partial\phi/\partial t$. The simplest method is to use a difference scheme. This way is effective for linear or higher order problems based on the perturbation because the mesh nodes are fixed. However, it becomes difficult for fully nonlinear problems since the wetted surface of structures varies with the time.

In the last decades, four methods have been developed to calculate $\partial\phi/\partial t$: (1) iterative method by Sen (1993) and Cao *et al.* (1994), (2) modal decomposition method by Vinje & Brevig (1981a, 1981b) and Cointe *et al.* (1990), (3) implicit boundary condition method by Van Daalen (1993) and Tanizawa (1995), (4) indirect method by Wu & Eatock Taylor (1996, 2003).

Here, we give a brief summary of Wu & Eatock Taylor's (1996, 2003) method. This method introduces some auxiliary functions, which satisfy the Laplace equation in the fluid domain and the corresponding boundary conditions on the free surface and the body surface. The computation of integration of the $\partial\phi/\partial t$ term on the body surface is converted to that on both the body and free surfaces without the $\partial\phi/\partial t$ term. This method was used by Kashiwagi (1998) in his 2D numerical wave tank, and it was also used by Ma *et al.* (2001a, 2001b) in their wave-body interactions in wave tanks, Hu *et*

al. (2002) in radiation problems and Wu *et al.* (2004) in motions of FPSO. The expression of this method will be given in Chapter 3.

1.6 Methods for mesh generation

An essential part for finite element simulations is mesh generation. There are mainly two types of mesh: the structured and the unstructured. A lot of methods can be found in the handbook of mesh generation edited by Thompson *et al.* (1999). For the structured mesh, the connectivity of any node with its neighbouring nodes can be easily recognised. In general, there are two kinds of structured mesh generation: algebraic method and partial differential equation (PDE) mapping method which needs to solve elliptic, hyperbolic, or parabolic partial differential equations. The structured mesh has been widely used in the field of CFD.

The unstructured mesh generation, on the other hand, allows any number of elements to meet at a single node. Triangle and tetrahedral meshes are by far the most common forms of the unstructured mesh generation, although quadrilateral and hexahedral meshes can also be unstructured. Most current methods for triangle and tetrahedral mesh have three main categories: quadtree/octree methods, Delaunay triangulation methods and advancing front methods.

The quadtree/octree method was primarily developed by Yerry & Shepherd (1984). In this method, squares or cube boxes containing the geometric model are recursively subdivided until the desired mesh is obtained. Irregular elements are usually created near the boundary, and it often requires a significant number of surface intersection calculations. In order to improve element shapes, smoothing and cleanup operations may be employed.

The most popular triangular and tetrahedral meshing technique is the Delaunay triangulation method, in which the Delaunay criterion is obeyed. The Delaunay criterion has the property that the circumcircle (circumsphere) of every triangle (tetrahedron) does not contain any points of the triangulation. A circumcircle (circumsphere) can be defined as the circle (sphere) passing through all three (four) vertices of a triangle (tetrahedron). Although the Delaunay criterion has been known for many years, it was not until the work of Lawson (1977) and Watson (1981) that the criterion was utilised for developing algorithms to triangulate a set of nodes. There are two main and very

similar Delaunay triangulation methods: the Watson algorithm (Watson, 1981) and the Bowyer algorithm (Bowyer, 1981). The triangulation process of the Watson algorithm has the following steps:

1. Initialize the triangulation by discretising boundaries and giving an initial mesh surrounding all nodes on boundaries.
2. Introduce a new point.
3. Search all the triangles and identify those whose circumcircles contain the new point.
4. With the union of all such triangles, an insertion polygon is formed, and then we connect the vertices of the polygon to the new point by straight line.
5. Repeat step 2 through step 4 until all nodes have been inserted.

Another very popular method for triangle and tetrahedral mesh generation is the advancing front method (AFM). In this method, the triangles (tetrahedrons) are built progressively inward from the triangulated surface. An active front is maintained where new triangles (tetrahedrons) are formed, and it will be updated to create new triangles (tetrahedrons) to fill the remainder of the area. The process is pursued until the front is not empty.

It has been in some reports that unstructured meshes have been used in flow problems. For example, Greaves (1995) used a quadtree method together with an adaptive technique to model laminar separated flow and standing wave interaction with bodies and this method has also been used in moving boundary problems (Greaves *et al.*, 1997 & Greaves, 2004a, b). Zhu *et al.* (2001) also used the same meshing procedure to simulate interactions of submerged cylinders and viscous flow with a free surface. Hu, Greaves & Wu (2002) improved the tri-tree method and applied it in laminar separated flows, and then Wu & Hu (2004) used a hybrid mesh based on the tri-tree algorithm to simulate a floating structure in large amplitude motion. Turnbull *et al.* (2003) adopted a coupled structured and Delaunay algorithm based unstructured mesh technique to simulate 2D wave-body interactions.

1.7 Objectives of the study

The previous studies based on the finite element method such as Ma, Wu & Eatock Taylor (2001a, b), Hu, Wu & Ma (2002) and Wu & Hu (2004) are all on wall-sided

structures. However, FPSOs (Floating Production, Storage and Offloading vessel) usually have large bows with pronounced flare above the still waterline. The flare may limit the green water but may cause larger hydrodynamic forces on FPSOs. With such a change in design, it is necessary to develop new numerical approaches to predict the interactions of waves and flared FPSOs. Another interesting topic is interactions of waves and multiple structures such as bridges, tension leg platforms and floating airports, most previous work is based on the frequency-domain method. A time-domain approach may be easier to observe the development of the waves and forces with the time and the mutual effect of structures on the development. To solve these problems, we develop the corresponding numerical methods based on the finite element method. The main tasks are: (1) to develop a numerical scheme for 3D simulations of the interaction of nonlinear waves with an array of cylinders based on the second order theory in the time domain. A semi-structured or semi-unstructured 3D mesh with prism elements based on the 2D unstructured mesh is presented; (2) to develop a numerical method based on unstructured meshes for fully nonlinear 2D simulations of interactions between waves and non-wall-sided structures. The 2D simulation is helpful to 3D study in this thesis and may probably be useful in extending it to full 3D unstructured mesh based cases, although this work is not included in this thesis; (3) to develop a numerical method to study fully nonlinear interactions between waves and structures with flare. A numerical tank with flared structures inside will be investigated. The effect of flare on waves and forces will be discussed; (4) to simulate interactions between waves and multiple structures including numerical wave tank and radiation problems based on the fully nonlinear wave theory, and the influence of the interference on waves and hydrodynamic forces will be discussed.

1.8 Outline of the thesis

This thesis has nine chapters. A review of previous work about interactions between waves and ocean structures has been presented in this chapter. In Chapter 2, the mathematical formulation used to solve wave-structure interaction problems is described. In Chapter 3, the numerical methods are described. It includes the finite element discretisation, time marching schemes, computation of velocity, remeshing and smoothing techniques and numerical radiation conditions. The method of 3D mesh

generation is proposed in Chapter 4. In Chapter 5 a time-domain second order numerical algorithm based on the finite element method is developed and used to study interactions of waves and an array of vertical cylinders. In Chapter 6 a 2D fully nonlinear simulation of wave-structure interactions based on unstructured meshes is presented. The fully nonlinear simulations of interactions between waves and vertical flared cylinders and multiple wall-sided cylinders in a tank are given in Chapter 7; a radiation problem about multiple cylinders in an open sea is calculated in Chapter 8 followed by the conclusion and recommendations for the future work in Chapter 9.

2. MATHEMATICAL FORMULATION

2.1 Introduction

The mathematical formulation of the nonlinear water wave problem is derived from the mass and momentum conservation laws. It consists of equations which are valid in the fluid domain, and the conditions which should be satisfied on the boundaries. Together they define the nonlinear wave problem. For potential flow problems, the nonlinearity comes from the boundary conditions on the free surface and the body surface.

In this chapter, we will give the mathematical description of the governing equation and the boundary conditions. The computational expression of the hydrodynamic force will be given as well.

2.2 Governing equation

With constant density assumed, the fundamental mass conservation law can be described by the following continuity equation

$$\nabla \cdot \vec{u} = 0, \tag{2.2.1}$$

and the momentum conservation by the Navier-Stokes equation:

$$(\frac{\partial}{\partial t} + \vec{u} \cdot \nabla)\vec{u} = \nabla(\frac{p}{\rho} + gz) + \nu\nabla^2\vec{u}, \tag{2.2.2}$$

where $\vec{u} = (u, v, w)$ is the velocity vector, p the pressure, ρ the density, g the gravitational acceleration, ν the constant kinematic viscosity, and z is a coordinate in the vertical direction which is positive upwards.

When the fluid is assumed to be inviscid, equation (2.2.2) is simplified as the Euler equation

$$(\frac{\partial}{\partial t} + \vec{u} \cdot \nabla)\vec{u} = -\nabla(\frac{p}{\rho} + gz). \tag{2.2.3}$$

Furthermore, if the fluid motion is assumed to be irrotational, that is, the vorticity

$$\nabla \times \vec{u} = 0, \tag{2.2.4}$$

a potential ϕ exists and we can define it as $\vec{u} = \nabla\phi$, and then equation (2.2.1) will become the Laplace equation

$$\nabla \cdot \vec{u} = \nabla \cdot \nabla\phi = \nabla^2\phi = 0. \tag{2.2.5}$$

This is the governing equation for the fluid that is incompressible and inviscid and its motion is irrotational. Correspondingly, the Euler equation (2.2.3) will become the Bernoulli equation

$$-\frac{p}{\rho} = \frac{\partial\phi}{\partial t} + \frac{1}{2}|\nabla\phi|^2 + gz + C(t), \tag{2.2.6}$$

where $C(t)$ is a constant.

2.3 Boundary conditions for numerical wave tanks

In this section, we consider the boundary conditions with the fluid assumed incompressible and inviscid, and the flow irrotational. In simulations of interactions between nonlinear water waves and structures, the boundary of the fluid domain consists of: the free surface, the body surface and the artificial control surface at the far field. On these surfaces, the dynamic and kinematic conditions, impenetrable condition and the radiation condition are satisfied respectively. In addition, an initial condition should be given since the problem is solved in the time domain.

The full nonlinear boundary value problem defining the motion of a body such as a floating vertical cylinder in a numerical tank is first considered here. A wave maker which is in horizontal motion is at the left end of the tank. With reference to Figure 2.3.1, the three-dimensional problem is defined with respect to a right-handed Cartesian coordinate system $oxyz$, in which x and y are measured horizontally and z is measured vertically upwards form the still water level, and the plane oxy is coincident with the still water surface.

The body surface is denoted by S_b, the free surface S_f, the surface of the wave maker S_w, the wall of the tank S_{wall}, the fluid domain $\forall$ and the unit normal vector of the boundary directed outward from the fluid region $\vec{N} = (N_x, N_y, N_z)$. Let t denote time and η the free surface elevation relative to the still water level. The seabed S_{bed} is assumed horizontal along the plane $z = -h$.

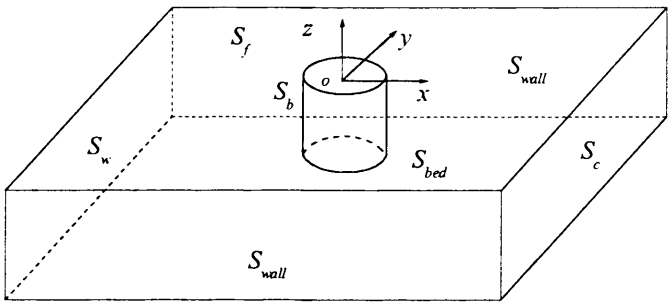

Figure 2.3.1 Coordinate system and fluid domain

2.3.1 Free surface conditions

The free surface is a moving boundary with two conditions satisfied on it. The first condition is the kinematic condition. The instantaneous free surface equation may be defined as

$$z = \eta(x,y,t) \text{ or } F(x,y,z,t) = z - \eta(x,y,t) = 0 . \tag{2.3.1}$$

The kinematic boundary condition can be derived as

$$\frac{DF}{dt} = \frac{\partial F}{\partial t} + \vec{u} \cdot \nabla F = 0 . \tag{2.3.2}$$

We can write equation (2.3.2) in the following form

$$\frac{\partial \phi}{\partial z} - \frac{\partial \eta}{\partial t} - \frac{\partial \phi}{\partial x}\frac{\partial \eta}{\partial x} - \frac{\partial \phi}{\partial y}\frac{\partial \eta}{\partial y} = 0 \qquad \text{on } S_f . \tag{2.3.3}$$

The second is the dynamic boundary condition, and it can be derived from equation (2.2.6) by setting the pressure to be zero on the free surface

$$\frac{\partial \phi}{\partial t} + g\eta + \frac{1}{2}|\nabla \phi|^2 = 0 \qquad \text{on } S_f . \tag{2.3.4}$$

Equations (2.3.3) and (2.3.4) are the free surface conditions in the Eulerian form, and they can also be written in the Lagrangian form

$$\frac{Dx}{Dt} = \frac{\partial \phi}{\partial x}, \quad \frac{Dy}{Dt} = \frac{\partial \phi}{\partial y}, \quad \frac{Dz}{Dt} = \frac{\partial \phi}{\partial z}, \tag{2.3.5}$$

$$\frac{D\phi}{Dt} = -g\eta + \frac{1}{2}\nabla\phi\nabla\phi , \tag{2.3.6}$$

where $\frac{D}{Dt}$ is the substantial derivative and is defined as $\frac{D}{Dt} = \frac{\partial}{\partial t} + \nabla\phi \cdot \nabla$.

2.3.2 Body surface boundary condition

This condition is used on the rigid surfaces of structures, which states that the fluid particles cannot penetrate or depart from the rigid surfaces and can only move tangentially. On solid fixed boundaries such as the bottom S_{bed} and the wall of the tank S_{wall}, the normal velocity is zero

$$\frac{\partial \phi}{\partial N} = 0 \qquad \text{on } S_{bed} \,\&\, S_{wall}. \tag{2.3.7}$$

On the moving boundaries such as a floating body and the wave maker, the velocity potential satisfies

$$\frac{\partial \phi}{\partial N} = \begin{cases} \vec{N} \cdot \vec{V} & \text{on } S_w \\ \vec{N} \cdot (\vec{V} + \vec{\Omega} \times \vec{r}) & \text{on } S_b \end{cases}, \tag{2.3.8}$$

where $\vec{V}$ is the translational oscillatory velocity of the cylinder or the wave maker, $\vec{\Omega}$ is the rotational velocity about a point on the body, which may be chosen as the mass centre of the body and $\vec{r}$ is the position vector from a point on the body surface to the mass centre.

2.3.3 Open boundary condition

In numerical simulations of nonlinear wave problems, the computational capacity is limited even though the real fluid domain may be very large. We need to truncate the fluid domain at some distance from the area of interest. The open boundary condition can be used at the truncation to minimise the effect of reflecting waves. In addition, when modelling practical problems within finite fluid domains such as experiments in physical tanks, active absorbers for absorbing reflection waves are usually used. The numerical simluations of these problems also need artifical open boundary conditions in numerical tanks.

As shown in Figure 2.3.1, an appropriate open boundary condition must be imposed on the control surface S_c in order to simulate a sufficiently long duration in the finite computational domain. In numerical computation, there are two main schemes. One is to apply the Sommerfeld radiation condition on S_c. This idea was first used by Orlanski (1976)

$$\frac{\partial \phi}{\partial t} + c\frac{\partial \phi}{\partial N} = 0 . \qquad (2.3.9)$$

Some successful results are reported such as that by Sen (1993). In this method, it is important to decide the phase velocity c described in Chapter 3. The other scheme is to apply an artificial damping zone on the free surface near the control surface S_c, which means that damping terms are added to dynamic and/or kinematic free surface conditions. For example, Cointe *et al.* (1990) added a dissipative term to the dynamic boundary condition

$$\frac{D\phi}{Dt} = -g\eta + \frac{1}{2}|\nabla\phi|^2 - \nu\phi \qquad \text{on } S_f . \qquad (2.3.10)$$

The parameter ν is specified, which increases from zero at the beginning of the damping zone to a positive value at the end of the zone. The magnitude of ν and the length of the damping zone are chosen empirically. More details of these two schemes will be discussed in the next chapter.

2.3.4 Initial conditions

Since the fully nonlinear water wave problem is solved in the time domain, the initial conditions including the velocity potential and the position of the free surface should also be given. They can be expressed as

$$\phi(x, y, z = \varsigma, t = 0) = \varphi(x, y), \eta(x, y, t = 0) = \varsigma(x, y), \qquad (2.3.11)$$

2.4 Boundary conditions in the moving system for an oscillatory floating body at constant forward speed in an open sea

The full nonlinear boundary value problem defining the fluid motion of a floating body undergoing specified oscillatory motions at forward speed in an open sea is considered here. With reference to figure 2.4.1, the three-dimensional problem is defined with respect to two right-handed Cartesian coordinate systems: one is the inertial (space-fixed) coordinate system $o_0x_0y_0z_0$, and the other is the coordinate system

$oxyz$ which moves along the o_0x_0 axis with the floating body at a constant speed $\vec{U} = (U,0,0)$.

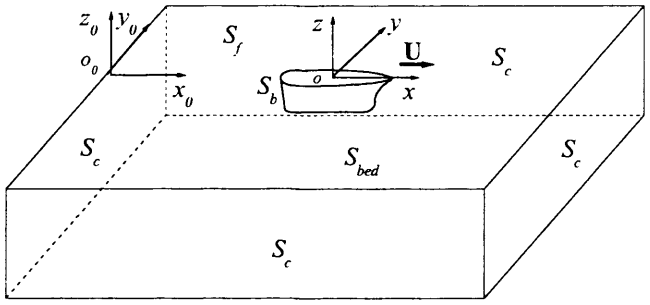

Figure 2.4.1 Coordinate system and fluid domain
for an oscillatory floating body at constant forward speed

On the surface of the floating body, the velocity potential satisfies

$$\frac{\partial \phi}{\partial N} = \vec{N} \cdot \vec{V}' \qquad \text{on } S_b, \tag{2.4.1}$$

where $\vec{V}'$ is the velocity of the body surface in coordinate system $o_0x_0y_0z_0$ and $\vec{V}' = \vec{U} + \vec{V} + \vec{\Omega} \times \vec{r}$.

On the free surface $z_0 = \eta(x_0, y_0, t)$, the kinematic and dynamic conditions should be satisfied:

$$\frac{\partial \phi}{\partial z_0} - \frac{\partial \eta}{\partial t} - \frac{\partial \phi}{\partial x_0}\frac{\partial \eta}{\partial x_0} - \frac{\partial \phi}{\partial y_0}\frac{\partial \eta}{\partial y_0} = 0 \qquad \text{on } S_f, \tag{2.4.2}$$

$$\frac{\partial \phi}{\partial t} + g\eta + \frac{1}{2}|\nabla \phi|^2 = 0 \qquad \text{on } S_f. \tag{2.4.3}$$

The free surface elevation can be more easily described in the moving system $oxyz$:

$$(\nabla)_{x_0,y_0,z_0} = (\nabla)_{xyz}, \tag{2.4.4}$$

$$(\frac{\partial}{\partial t})_{x_0,y_0,z_0} = (\frac{\partial}{\partial t} - \vec{U} \cdot \nabla)_{xyz}, \tag{2.4.5}$$

and so equations (2.4.2) and (2.4.3) become:

$$[\frac{\partial}{\partial t} - (\vec{U} - \nabla \phi) \cdot \nabla]\eta = \frac{\partial \phi}{\partial z} \qquad \text{on } S_f, \tag{2.4.6}$$

$$[\frac{\partial}{\partial t} - \vec{U} \cdot \nabla]\phi + \frac{1}{2}\nabla \phi \cdot \nabla \phi = -g\eta \qquad \text{on } S_f. \tag{2.4.7}$$

If the forward speed of the floating body is zero, that is, U=0, equations (2.4.6) and (2.4.7) will become equations (2.3.3) and (2.3.4), respectively. Meanwhile, the body surface boundary condition (2.4.1) will become equation (2.3.8).

In addition, the radiation condition and initial condition should be given.

2.5 Second order solution

One of the major difficulties in solving above-mentioned fully nonlinear free surface potential flow problems is the treatment of the free surface boundary conditions (2.3.3) and (2.3.4), which are both nonlinear and defined on the free surface which is not known prior to solving the problem. Here we will consider the problem to the second order. The second order approach for predicting floating structures has been given by Ogilvie (1983) in the frequency domain and then used by Isaacson, Ng & Cheung (1993) in the time domain.

Besides the coordinate system *oxyz* shown in Figure 2.3.1, we define another coordinate system $\overline{oxyz}$, which is fixed on the body and the origin $\bar{o}$ is located at the mass centre of the body $\vec{x}_g = (x_g, y_g, z_g)$. The coordinates in systems *oxyz* and $\overline{oxyz}$ are denoted as $\vec{x} = (x, y, z)$ and $\bar{\vec{x}} = (\bar{x}, \bar{y}, \bar{z})$ respectively. The unit normal vector of the mean body surface $S_b^{(0)}$ directed outward from the fluid region is denoted by $\vec{n} = (n_x, n_y, n_z)$. The motion of the rigid body can be described in terms of a translational motion vector $\vec{X} = (X, Y, Z)$ along the axis x, y and z and a rotational motion vector $\vec{\Theta} = (\Theta_x, \Theta_y, \Theta_z)$ around the mass centre. The displacement vector of a point on the body surface is denoted by $\vec{\Xi}$ and it can be expressed as

$$\vec{\Xi} = \vec{x} - \vec{x}_g - \bar{\vec{x}}. \tag{2.5.1}$$

With the assumptions that the wave amplitude is small compared to the wavelength and the body motion is small compared to a principal body dimension, it is possible to apply Taylor series expansions to transform the free surface and body surface conditions, originally defined on the instantaneous surfaces, to conditions evaluated at the corresponding mean positions (Isaacson, Ng & Cheung, 1993)

$$\left(\frac{\partial\phi}{\partial z}-\frac{\partial\eta}{\partial t}-\frac{\partial\phi}{\partial x}\frac{\partial\eta}{\partial x}-\frac{\partial\phi}{\partial y}\frac{\partial\eta}{\partial y}\right)$$
$$+\eta\frac{\partial}{\partial z}\left(\frac{\partial\phi}{\partial z}-\frac{\partial\eta}{\partial t}-\frac{\partial\phi}{\partial x}\frac{\partial\eta}{\partial x}-\frac{\partial\phi}{\partial y}\frac{\partial\eta}{\partial y}\right)+\cdots=0 \qquad \text{on } S_f^{(0)}, \tag{2.5.2}$$

$$\left(\frac{\partial\phi}{\partial t}+g\eta+\frac{1}{2}|\nabla\phi|^2\right)+\eta\frac{\partial}{\partial z}\left(\frac{\partial\phi}{\partial t}+g\eta+\frac{1}{2}|\nabla\phi|^2\right)+\cdots=0 \quad \text{on } S_f^{(0)}, \tag{2.5.3}$$

$$\dot{\vec{\Xi}}\cdot\vec{N}=[\nabla\phi+\vec{\Xi}\cdot\nabla(\nabla\phi)+\cdots]\cdot\vec{N} \qquad \text{on } S_b^{(0)}, \tag{2.5.4}$$

where $S_f^{(0)}$ is the still water surface, $\dot{\vec{\Xi}}=\vec{V}+\vec{\Omega}\times\vec{r}$, where the over-dot indicates the time derivative. The boundary conditions may now be applied on $S_f^{(0)}, S_b^{(0)}$ and other mean boundaries. Using the Stokes expansion procedure, quantities at first and second order are separated by introducing perturbation series for ϕ , η , $\vec{X}$ and $\vec{\Theta}$

$$\phi=\varepsilon\phi^{(1)}+\varepsilon^2\phi^{(2)}+\cdots, \tag{2.5.5}$$

$$\eta=\varepsilon\eta^{(1)}+\varepsilon^2\eta^{(2)}+\cdots, \tag{2.5.6}$$

$$\vec{X}=\varepsilon\vec{X}^{(1)}+\varepsilon^2\vec{X}^{(2)}+\cdots, \tag{2.5.7}$$

$$\vec{\Theta}=\varepsilon\vec{\Theta}^{(1)}+\varepsilon^2\vec{\Theta}^{(2)}+\cdots, \tag{2.5.8}$$

where ε is a perturbation parameter related to the wave slope which is small, and the superscripts (1) and (2) indicate respectively components at the first- and second-order. With assuming the motion to be harmonic and specified, $\vec{X}$ and $\vec{\Theta}$ may be considered to first order only, so that

$$\vec{X}=\varepsilon\vec{X}^{(1)}, \tag{2.5.9}$$

$$\vec{\Theta}=\varepsilon\vec{\Theta}^{(1)}, \tag{2.5.10}$$

which means $\vec{X}=(X^{(1)},Y^{(1)},Z^{(1)})$ and $\vec{\Theta}=(\Theta_x^{(1)},\Theta_y^{(1)},\Theta_z^{(1)})$. For convenience, the superscript (1) will be omitted, so $(X^{(1)},Y^{(1)},Z^{(1)})$ and $(\Theta_x^{(1)},\Theta_y^{(1)},\Theta_z^{(1)})$ can be denoted by (X,Y,Z) and $(\Theta_x,\Theta_y,\Theta_z)$ respectively.

Since we consider only small amplitude motions, the displacement $\vec{\Xi}$ can be expressed using the translational motion $\vec{X}$ and the rotational motion $\vec{\Theta}$ by the following equation

$$\vec{\Xi}=(\vec{X}+\vec{\Theta}\times\vec{\bar{x}})+\tilde{H}\vec{\bar{x}}, \tag{2.5.11}$$

where matrix $\tilde{H}$ is given as

$$\tilde{H} = \begin{bmatrix} -\frac{\Theta_y^2 + \Theta_z^2}{2} & 0 & 0 \\ \Theta_x\Theta_y & -\frac{\Theta_x^2 + \Theta_z^2}{2} & 0 \\ \Theta_x\Theta_z & \Theta_y\Theta_z & -\frac{\Theta_x^2 + \Theta_y^2}{2} \end{bmatrix}.$$

Equation (2.5.11) is valid up to second order. Similar to equation (2.5.11), the unit normal vector $\vec{N}$ is given by

$$\vec{N} = \vec{n} + \vec{\Theta} \times \vec{n} + \tilde{H}\vec{x} \qquad (2.5.12)$$

By a time differentiation of equation (2.5.11), we obtain the velocity on the body surface

$$\dot{\vec{\Xi}} = (\dot{\vec{X}} + \dot{\vec{\Theta}} \times \vec{\bar{x}}) + \dot{\tilde{H}}\vec{x} \,. \qquad (2.5.13)$$

Upon substituting the Stokes perturbation expansions of ϕ, η and $\vec{\Xi}$ into the Laplace equation and the boundary conditions and collecting terms of equal order, it yields the corresponding boundary-value problems for ε and ε^2 terms in the power series expansions, and so the boundary value problem at each order is now linear. In the k-th order wave radiation problem (with k=1, 2 in turn), the potential satisfies the Laplace equation in the fluid domain

$$\nabla^2\phi^{(k)} = 0 \qquad \text{in} \quad \forall^{(0)}, \qquad (2.5.14)$$

and is subject to the boundary conditions applied on the still water surface, the mean body surface and the seabed, given respectively as

$$\frac{\partial\phi^{(k)}}{\partial z} - \frac{\partial\eta^{(k)}}{\partial t} = f_k' \qquad \text{on} \quad S_f^{(0)}, \qquad (2.5.15)$$

$$\frac{\partial\phi^{(k)}}{\partial t} + g\eta^{(k)} = f_k'' \qquad \text{on} \quad S_f^{(0)}, \qquad (2.5.16)$$

$$\frac{\partial\phi^{(k)}}{\partial n} = f_k \qquad \text{on} \quad S_b^{(0)}, \qquad (2.5.17)$$

$$\frac{\partial\phi^{(k)}}{\partial z} = 0 \qquad \text{on} \quad z = -h, \qquad (2.5.18)$$

where $\forall^{(0)}$ is a time-independent fluid domain bounded by the seabed, the mean body surface $S_b^{(0)}$, the still water surface $S_f^{(0)}$ and the open boundary S_c. The terms f_k', f_k'' and f_k are given respectively as

$$f_k' = \begin{cases} 0 & (k=1) \\ \dfrac{\partial \phi^{(1)}}{\partial x}\dfrac{\partial \eta^{(1)}}{\partial x} + \dfrac{\partial \phi^{(1)}}{\partial y}\dfrac{\partial \eta^{(1)}}{\partial y} - \eta^{(1)}\dfrac{\partial^2 \phi^{(1)}}{\partial z^2} & (k=2) \end{cases},$$

$$f_k'' = \begin{cases} 0 & (k=1) \\ -\dfrac{1}{2}\left|\nabla \phi^{(1)}\right|^2 - \eta^{(1)}\dfrac{\partial^2 \phi^{(1)}}{\partial z \partial t} & (k=2) \end{cases},$$

$$f_k = \begin{cases} (\dot{\vec{X}} + \dot{\vec{\Theta}} \times \vec{\bar{x}}) \cdot \vec{n} & (k=1) \\ (\dot{\vec{H}}\vec{\bar{x}}) \cdot \vec{n} - [(\vec{X} + \vec{\Theta} \times \vec{\bar{x}}) \cdot \nabla(\nabla \phi^{(1)})] \cdot \vec{n} & \\ + (\vec{\Theta} \times \vec{n}) \cdot [(\dot{\vec{X}} + \dot{\vec{\Theta}} \times \vec{\bar{x}}) - \nabla \phi^{(1)}] & (k=2) \end{cases}.$$

For the first order solution, the problem corresponds to the linear wave radiation problem; for the second order solution, the boundary problem is inhomogeneous and f_2', f_2'' & f_2 represent quadratic forcings of the corresponding free surface and body surface conditions which can be determined from the first order solution.

2.6 Hydrodynamic forces

The hydrodynamic forces on the body can be obtained by carrying out a direct integration of the pressure over the instantaneous wetted body surface S_b. The pressure in the fluid can be determined by the Bernoulli equation (2.2.6) with taking $c(t)$ to be zero and we rewrite equation (2.2.6) as

$$p = -\rho\left(\frac{\partial \phi}{\partial t} + \frac{1}{2}|\nabla \phi|^2 + gz\right). \tag{2.6.1}$$

For a structure with a constant forward speed $\vec{U}$, the pressure can be expressed as

$$p = -\rho\left(\frac{\partial \phi}{\partial t} - \vec{U} \cdot \nabla \phi + \frac{1}{2}|\nabla \phi|^2 + gz\right). \tag{2.6.2}$$

The hydrodynamic force and moment acting on body can be expressed as

$$\vec{F} = \iint_{S_b} p\vec{N} ds, \tag{2.6.3}$$

$$\vec{M} = \iint_{S_b} p(\vec{r} \times \vec{N}) ds, \tag{2.6.4}$$

where $\vec{r} = \vec{x} - \vec{x}_g$ is the vector from the point on the body surface to the mass centre. The numerical method for calculating equations (2.6.3) and (2.6.4) will be given in the next chapter.

For the second order problem, the pressure on the instantaneous body surface can consistently be expanded about the mean body surface

$$(p)_{S_b} = (p + \vec{\Xi} \cdot \nabla p + \cdots)_{S_b^{(0)}}, \tag{2.6.5}$$

Substituting equation (2.5.11) into equation (2.6.5) and retaining terms to second order, we obtain

$$\begin{aligned} p = & -\rho \frac{\partial \phi}{\partial t} - \frac{1}{2}\left|\nabla \phi^{(1)}\right|^2 - \rho g z - \rho g (Z + \Theta_x \bar{y} - \Theta_y \bar{x}) \\ & - \rho g \tilde{H} \bar{\bar{x}} - \rho (\dot{\bar{X}} + \bar{\Theta} \times \bar{\bar{x}}) \cdot \nabla (\frac{\partial \phi^{(1)}}{\partial t}) \qquad \text{on } S_b \end{aligned} \tag{2.6.6}$$

The integration over the exact wetted body surface may be expressed as the sum of the integration over the mean wetted body surface and the correction integral defined at the still waterline *WL*. The hydrodynamic force contains three components

$$\vec{F} = \vec{F}^{(1)} + \vec{F}^{(2)} + \bar{\vec{F}}^{(2)}, \tag{2.6.7}$$

where $\vec{F}^{(1)}, \vec{F}^{(2)}$ and $\bar{\vec{F}}^{(2)}$ are the first order oscillatory force at the excitation frequency, the second order oscillatory force at twice the excitation frequency and the second order mean force, respectively. $\vec{F}^{(1)}$ and $\vec{F}^{(2)}$ may be finally expressed as (Isaacson, Ng & Cheung, 1993)

$$\vec{F}^{(1)} = -\rho \iint_{S_b^{(0)}} \frac{\partial \phi^{(1)}}{\partial t} \vec{n} ds - \rho g A_w (Z^{(1)} + y_f \Theta_x - x_f \Theta_y) \vec{k} \tag{2.6.8}$$

$$\begin{aligned} \vec{F}^{(2)} = & -\rho \iint_{S_b^{(0)}} \frac{\partial \phi^{(2)}}{\partial t} \vec{n} ds - \frac{1}{2} \rho \iint_{S_b^{(0)}} \left|\nabla \phi^{(1)}\right|^2 \vec{n} ds + \frac{\rho g}{2} \oint_{WL} (\eta_r^{(1)})^2 \vec{n}_l dl \\ & - \rho \iint_{S_b^{(0)}} [(\dot{\bar{X}} + \bar{\Theta} \times \bar{\bar{x}}) \cdot \nabla (\frac{\partial \phi^{(1)}}{\partial t})] \vec{n} ds - \rho \iint_{S_b^{(0)}} \frac{\partial \phi^{(1)}}{\partial t} (\Theta \times \vec{n}) ds, \\ & - \rho g A_w [(y_f \Theta_y \Theta_z + x_f \Theta_z \Theta_x) + \frac{1}{2} (\Theta_x^2 + \Theta_y^2) z_g] \vec{k} - \bar{\vec{F}}^{(2)} \end{aligned} \tag{2.6.9}$$

where A_w is the mean waterplane area, (x_f, y_f) is the centre of floatation in the system *oxyz* when the body is at rest, *WL* denotes the waterline. $\eta_r^{(1)} = \eta^{(1)} - Z - \Theta_x \bar{y} + \Theta_y \bar{x}$ is the relative wave height at the waterline and $\vec{n}_l = \vec{n} / \sqrt{1 - n_z^2}$. In equation (2.6.9), the first term is the contribution from the second order potential, the second term is associated with the velocity squared term of the Bernoulli equation, and the third term is

related to the correction for the hydrodynamic forces on the instantaneous body surface. The fourth, the fifth and the sixth terms account for the change in pressure due to first order motions, change in directions of forces due to first order rotation and the second order hydrostatic forces associated with the displacements of the body motions from its equilibrium position, respectively. The mean force $\bar{\vec{F}}^{(2)}$ may be obtained by time averaging the part due to the first order potential in equation (2.6.9) over one period

$$\begin{aligned}\bar{\vec{F}}^{(2)} = & -\rho\overline{\iint_{S_b^{(0)}} \frac{\partial\phi^{(1)}}{\partial t}(\vec{\Theta}\times\vec{n})ds} + \frac{\rho g}{2}\overline{\oint_{WL}(\eta_r^{(1)})^2\vec{n}_l dl} \\ & -\rho\overline{\iint_{S_b^{(0)}}[\frac{1}{2}\left|\nabla\phi^{(1)}\right|^2 + (\vec{X}+\vec{\Theta}\times\vec{\bar{x}})\cdot\nabla(\frac{\partial\phi^{(1)}}{\partial t})]\vec{n}ds} \\ & -\rho g\overline{A_w[(y_f\Theta_y\Theta_z + x_f\Theta_x\Theta_z) + \frac{1}{2}(\Theta_x^2+\Theta_y^2)z_g]\vec{k}}\end{aligned} \quad . \qquad (2.6.10)$$

The corresponding moment components $\vec{M}^{(1)}$, $\vec{M}^{(2)}$ and $\bar{\vec{M}}^{(2)}$ may be obtained in the similar way

$$\begin{aligned}\vec{M}^{(1)} = & -\rho\iint_{S_b^{(0)}}\frac{\partial\phi^{(1)}}{\partial t}(\vec{\bar{x}}\times\vec{n})ds \\ & -\rho g\{ZA_w y_f + \Theta_x[\forall(z_b - z_g) + L_{yy}] - \Theta_y L_{xy} - \Theta_z\forall x_b\}\vec{i} \\ & -\rho g\{-ZA_w x_f + \Theta_y[\forall(z_b - z_g) + L_{xx}] - \Theta_x L_{xy} - \Theta_z\forall y_b\}\vec{j}\end{aligned} \quad , \qquad (2.6.11)$$

$$\begin{aligned}\vec{M}^{(2)} = & -\rho\iint_{S_b^{(0)}}\frac{\partial\phi^{(2)}}{\partial t}(\vec{\bar{x}}\times\vec{n})ds - \frac{1}{2}\rho\iint_{S_b^{(0)}}(\vec{\bar{x}}\times\vec{n})\left|\nabla\phi^{(1)}\right|^2 ds \\ & + \frac{\rho g}{2}\oint_{WL}(\eta_r^{(1)})^2(\vec{\bar{x}}\times\vec{n}_l)dl - \rho\iint_{S_b^{(0)}}(\vec{\bar{x}}\times\vec{n})[(\vec{X}+\vec{\Theta}\times\vec{\bar{x}})\cdot\nabla(\frac{\partial\phi^{(1)}}{\partial t})]ds \\ & -\rho\iint_{S_b^{(0)}}\frac{\partial\phi^{(1)}}{\partial t}[\vec{X}\times\vec{n} + \vec{\Theta}\times(\vec{\bar{x}}\times\vec{n})]ds \\ & -\frac{1}{2}\rho g A_w z_g(\Theta_x^2+\Theta_y^2)(y_f\vec{i} - x_f\vec{j}) - \bar{\vec{M}}\end{aligned} \quad ,(2.6.12)$$

$$\begin{aligned}\bar{\vec{M}}^{(2)} = & -\rho\overline{\iint_{S_b^{(0)}}\frac{\partial\phi^{(1)}}{\partial t}[X\times\vec{n} + \vec{\Theta}\times(\vec{\bar{x}}\times\vec{n})]ds} + \frac{\rho g}{2}\overline{\oint_{WL}(\eta_r^{(1)})^2(\vec{\bar{x}}\times\vec{n})dl} \\ & -\rho\overline{\iint_{S_b^{(0)}}(\vec{\bar{x}}\times\vec{n})[\frac{1}{2}\left|\nabla\phi^{(1)}\right|^2 + (\vec{X}+\vec{\Theta}\times\vec{\bar{x}})\cdot\nabla(\frac{\partial\phi^{(1)}}{\partial t})]ds} \\ & -\frac{1}{2}\rho g A_w z_g\overline{(\Theta_x^2+\Theta_y^2)}(y_f\vec{i} - x_f\vec{j})\end{aligned} \quad , \qquad (2.6.13)$$

where $\forall$ is the displaced volume of the body at its mean position, (x_b, y_b, z_b) is the center of buoyancy and L_{mn} is the water plane area moment of inertia with respect to the m and n axes when the body is in its equilibrium position.

3. FINITE ELEMENT DISCRETISATION AND NUMERICAL PROCEDURES

3.1 Introduction

In this chapter, we will present numerical algorithms for solving the fully nonlinear wave problem described in Chapter 2. In the numerical simulation of the problem, the fluid domain is first discretised and the finite element equation is solved to obtain the velocity potential in the domain. After the potential is obtained, we can calculate the velocity using the Galerkin method and the hydrodynamic forces on the body. We then update the velocity potential and the wave elevation on the free surface and render the boundary information for the next time step. Other numerical techniques such as remeshing and smoothing will also be presented in this chapter.

As mentioned in Chapter 2, with the fluid assumed to be incompressible and inviscid, and the flow irrotational, the fluid motion can be described by the velocity potential ϕ which satisfies the Laplace equation

$$\nabla^2\phi = 0 \tag{3.1.1}$$

within the fluid domain $\forall$ and the following boundary conditions

$$\phi = f_p(x,y,z) \qquad \text{on } S_p, \tag{3.1.2}$$

$$\frac{\partial\phi}{\partial n} = f_n(x,y,z) \qquad \text{on } S_n, \tag{3.1.3}$$

where S_p is the Dirichlet boundary where the potential is known, and S_n represents the Neumann boundary where the normal derivative of the potential is known. Taking the numerical tank shown in Figure 2.3.1 as an example, S_p includes the free surface S_f and the artificial boundary S_c, and S_n includes the body surface S_b, the wave maker surface S_w, the tank wall S_{wall} and the tank bottom S_{bed}. Equations (3.1.1)~(3.1.3) will be solved by the finite element method to obtain the velocity potential in the whole domain.

3.2 Finite element discretisation

In the numerical simulation based on the finite element method, the fluid domain is first discretised with many elements and the details will be discussed in the next chapter. Several methods can be used to transform the problem described in equations (3.1.1)~(3.1.3) to its finite element discrete analogue, and the most popular one is the Galerkin weighted residual method.

3.2.1 Galerkin weighted residual method

The basic idea of the Galerkin weighted residual method is to construct a mathematical process to minimise the residual of the governing equation $R = \nabla^2\phi$ as close to zero as possible. The mathematical process may be expressed in the form of the inner product of the residual R and a weighted function W_i as follows

$$\langle W_i, R\rangle = \iiint_{\forall} W_i R d\forall = 0. \tag{3.2.1}$$

The weighted function W_i may be selected as the variation of the potential $\delta\phi$, and then equation (3.2.1) can be written as

$$\iiint_{\forall} \nabla^2\phi(\delta\phi)d\forall = \iiint_{\forall} (\frac{\partial^2\phi}{\partial x^2} + \frac{\partial^2\phi}{\partial y^2} + \frac{\partial^2\phi}{\partial z^2})\delta\phi dxdydz = 0, \tag{3.2.2}$$

or

$$-\iiint_{\forall} (\nabla\phi\cdot\nabla(\delta\phi)dxdydz + \iiint_{\forall} [\frac{\partial}{\partial x}(\frac{\partial\phi}{\partial x}\delta\phi) + \frac{\partial}{\partial y}(\frac{\partial\phi}{\partial y}\delta\phi) + \frac{\partial}{\partial z}(\frac{\partial\phi}{\partial z}\delta\phi)]dxdydz = 0.$$

It follows, using Green-Gauss's theorem $\iiint_{\forall} \nabla\cdot\vec{x}d\forall = \oiint_{S} \vec{n}\cdot\vec{x}ds$, that

$$-\iiint_{\forall} \nabla\phi\cdot\nabla(\delta\phi)dxdydz + \iint_{S_p+S_n} \frac{\partial\phi}{\partial n}\delta\phi ds = 0. \tag{3.2.3}$$

It is noticed that the variation $\delta\phi$ is zero on the Dirichlet boundary S_p, and so $\iint_{S_p} \frac{\partial\phi}{\partial n}\delta\phi ds = 0$. Thus, equation (3.2.3) becomes

$$\iiint_{\forall} \nabla\phi\cdot\nabla(\delta\phi)dxdydz = \iint_{S_n} f_n\delta\phi ds. \tag{3.2.4}$$

3.2.2 *Shape functions*

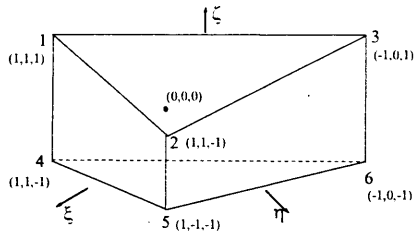

Figure 3.2.1 A triangular prism element with 6 nodes

For 3D simulations, the 6-node triangular prismatic element (see Figure 3.2.1) is used and the fluid domain is divided into many prismatic elements. The shape functions defined in a local coordinate system $\vec{\xi} = (\xi, \eta, \zeta)$ at the six corners of an element e may be expressed as, respectively

$$\begin{aligned} N_1^{(e)} &= \xi(1+\zeta)/2 \\ N_2^{(e)} &= \eta(1+\zeta)/2 \\ N_3^{(e)} &= (1-\xi-\eta)(1+\zeta)/2 \\ N_4^{(e)} &= \xi(1-\zeta)/2 \\ N_5^{(e)} &= \eta(1-\zeta)/2 \\ N_6^{(e)} &= (1-\xi-\eta)(1-\zeta)/2 \end{aligned} \qquad (3.2.5)$$

The local coordinate system can be mapped to a global coordinate system $\vec{\mathrm{x}} = (x,y,z)$ by the following transformation

$$\vec{\mathrm{x}} = \sum_{i=1}^{6} N_i^{(e)} \vec{\mathrm{x}}_i^{(e)} . \qquad (3.2.6)$$

In the same way, the velocity potential at $\vec{\mathrm{x}}$ within element e can be represented as

$$\phi(\vec{\mathrm{x}}) = \sum_{i=1}^{6} N_i^{(e)} \phi_i^{(e)}(\vec{\mathrm{x}}_i) \qquad (3.2.7)$$

3.2.3 *Coefficient matrices and right-hand side vectors*

Due to equation (3.2.7), the following equation holds for a typical finite element

$$\delta\phi = \sum_{i=1}^{6} N_i^{(e)} \delta\phi_i^{(e)} . \qquad (3.2.8)$$

Substituting equations (3.2.6), (3.2.7) and (3.2.8) into (3.2.4), we obtain

$$\sum_{i=1}^{6}(\sum_{j=1}^{6}K_{ij}^{(e)}\phi_j^{(e)})\delta\phi_i^{(e)}=\sum_{i=1}^{6}F_i^{(e)}\delta\phi_i^{(e)}, \tag{3.2.9}$$

where

$$K_{ij}^{(e)}=\iiint_{\forall^{(e)}}\nabla N_i^{(e)}\cdot\nabla N_j^{(e)}d\forall, \tag{3.2.10}$$

$$F_i^{(e)}=\iint_{S_n^{(e)}}f_nN_i^{(e)}ds. \tag{3.2.11}$$

Since all variations $\delta\phi_i^{(e)}(i=1,2,\cdots,6)$ are independent of each other, we have

$$\sum_{j=1}^{6}K_{ij}^{(e)}\phi_j^{(e)}=F_i^{(e)}\quad i=1,2,\cdots,6. \tag{3.2.12}$$

This is the finite element equation in element *e*. We can assemble the global coefficient matrix from equation (3.2.12) through the connectivity information of the element and the node

$$[K]\{\phi\}=\{F\}, \tag{3.2.13}$$

where $[K]$ and $\{F\}$ are the global coefficient matrix and the global right-hand side vector and are assembled by $K_{ij}^{(e)}$ and $F_j^{(e)}$, respectively, over all elements in the fluid domain. They can be expressed as

$$K_{IJ}=\sum_{k=1}^{NK}\iiint_{\forall^{(e_k)}}\nabla N_i^{(e_k)}\cdot\nabla N_j^{(e_k)}d\forall, \tag{3.2.14}$$

$$F_I=\sum_{k=1}^{NK}\iint_{S_n^{(e_k)}}f_nN_i^{(e_k)}ds, \tag{3.2.15}$$

where *I* and *J* are the global numbers of nodes *i* and *j* in element e_k respectively. *NK* is the number of elements that share node *I*. For convenience, we define a global shape function $N_I(\xi,\eta,\zeta)$ by

$$N_I(\xi,\eta,\zeta)=\begin{cases}N_i^{(e_k)}(\xi,\eta,\zeta) & (\xi,\eta,\zeta)\in e_k\\ 0 & (\xi,\eta,\zeta)\notin e_k\end{cases}\quad(k=1,2,\cdots,NK), \tag{3.2.16}$$

and so K_{IJ} and F_I can be rewritten as

$$K_{IJ}=\iiint_{\forall}\nabla N_I\cdot\nabla N_J d\forall, \tag{3.2.17}$$

$$F_I=\iint_{S_n}f_nN_I ds. \tag{3.2.18}$$

Since the potential on the Dirichlet boundary is known, we can incorporate it into equation (3.2.13). Finally, the global coefficient matrix and the right-hand side vector can be written as

$$K_{IJ} = \iiint_{\forall} \nabla N_I \cdot \nabla N_J d\forall \qquad I \notin S_p \text{ and } J \notin S_p, \tag{3.2.19}$$

$$F_I = \iint_{S_n} f_n N_I ds - \iiint_{\forall} \nabla N_I \sum_{J(J \in S_p)} (f_p)_J \nabla N_J d\forall \quad I \notin S_p \text{ and } J \in S_p . \tag{3.2.20}$$

3.2.4 *Numerical integration of the local element coefficient matrix and right-hand side vector*

From the chain rule for partial differentiation, we have

$$\begin{bmatrix} \frac{\partial N_i^{(e)}}{\partial \xi} \\ \frac{\partial N_i^{(e)}}{\partial \eta} \\ \frac{\partial N_i^{(e)}}{\partial \zeta} \end{bmatrix} = [J] \begin{bmatrix} \frac{\partial N_i^{(e)}}{\partial x} \\ \frac{\partial N_i^{(e)}}{\partial y} \\ \frac{\partial N_i^{(e)}}{\partial z} \end{bmatrix}, \tag{3.2.21}$$

where $[J]$ is the Jacobian matrix given by

$$[J] = \begin{bmatrix} \frac{\partial x}{\partial \xi} & \frac{\partial y}{\partial \xi} & \frac{\partial z}{\partial \xi} \\ \frac{\partial x}{\partial \eta} & \frac{\partial y}{\partial \eta} & \frac{\partial z}{\partial \eta} \\ \frac{\partial x}{\partial \zeta} & \frac{\partial y}{\partial \zeta} & \frac{\partial z}{\partial \zeta} \end{bmatrix}.$$

Therefore, we have

$$\begin{bmatrix} \frac{\partial N_i^{(e)}}{\partial x} \\ \frac{\partial N_i^{(e)}}{\partial y} \\ \frac{\partial N_i^{(e)}}{\partial z} \end{bmatrix} = [J]^{-1} \begin{bmatrix} \frac{\partial N_i^{(e)}}{\partial \xi} \\ \frac{\partial N_i^{(e)}}{\partial \eta} \\ \frac{\partial N_i^{(e)}}{\partial \zeta} \end{bmatrix}, \tag{3.2.22}$$

where $[J]^{-1}$ is the inverse matrix of $[J]$ and is calculated by the following equation

$$[J]^{-1}=\frac{1}{|J|}\begin{bmatrix}\frac{\partial y}{\partial \eta}\frac{\partial z}{\partial \zeta}-\frac{\partial y}{\partial \zeta}\frac{\partial z}{\partial \eta} & \frac{\partial y}{\partial \zeta}\frac{\partial z}{\partial \xi}-\frac{\partial y}{\partial \xi}\frac{\partial z}{\partial \zeta} & \frac{\partial y}{\partial \xi}\frac{\partial z}{\partial \eta}-\frac{\partial y}{\partial \eta}\frac{\partial z}{\partial \xi}\\ \frac{\partial x}{\partial \zeta}\frac{\partial z}{\partial \eta}-\frac{\partial x}{\partial \eta}\frac{\partial z}{\partial \zeta} & \frac{\partial x}{\partial \xi}\frac{\partial z}{\partial \zeta}-\frac{\partial x}{\partial \zeta}\frac{\partial z}{\partial \xi} & \frac{\partial x}{\partial \eta}\frac{\partial z}{\partial \xi}-\frac{\partial x}{\partial \xi}\frac{\partial z}{\partial \eta}\\ \frac{\partial x}{\partial \eta}\frac{\partial y}{\partial \zeta}-\frac{\partial x}{\partial \zeta}\frac{\partial y}{\partial \xi} & \frac{\partial x}{\partial \zeta}\frac{\partial y}{\partial \xi}-\frac{\partial x}{\partial \xi}\frac{\partial y}{\partial \zeta} & \frac{\partial x}{\partial \xi}\frac{\partial y}{\partial \eta}-\frac{\partial x}{\partial \eta}\frac{\partial y}{\partial \xi}\end{bmatrix}. \quad (3.2.23)$$

$|J|$ is the determinant of $[J]$ and $K_{ij}^{(e)}$ can be expressed as

$$K_{ij}^{(e)}=\iiint_{\forall^{(e)}}\nabla N_i^{(e)}\cdot\nabla N_j^{(e)}|J|d\xi d\eta d\zeta\,, \quad (3.2.24)$$

where $d\forall = dxdydz = |J|d\xi d\eta d\zeta$ is used and $\nabla N_i^{(e)}$ can be obtained from equation (3.2.22).

The integration of a function $f(\xi,\eta,\zeta)$ in a prismatic element can be obtained by the following equation:

$$\begin{aligned}\iiint_{\forall^{(e)}} f(\xi,\eta,\zeta)d\xi d\eta d\zeta &= \int_{-1}^{1}\{\int_0^1[\int_0^{1-\xi} f(\xi,\eta,\zeta)d\eta]d\xi\}d\zeta\\ &= \sum_{i=1}^{n}\sum_{j=1}^{m} f(\xi_j,\eta_j,\zeta_i)w_i w_j^t\end{aligned} \quad (3.2.25)$$

where ξ_j, η_j and ζ_i are abscissae and w_i, w_j^t are weighted coefficients of the one-dimensional Gauss integration and the numerical integration in a triangle, respectively. The Abscissae and weight coefficients are given in the Appendix A. Thus, Equations (3.2.10) and (3.2.11) can be written as, respectively

$$K_{ij}^{(e)}=\sum_{k=1}^{n}\sum_{l=1}^{m}\nabla N_i^{(e)}\cdot\nabla N_j^{(e)}|J|w_k w_l^t\,, \quad (3.2.26)$$

$$F_i^{(e)}=\begin{cases}\sum_{k=1}^{n}\sum_{l=1}^{n} f_n N_i^{(s)}|J_0|w_k w_l & \text{for quadrilateral elements}\\ \sum_{k=1}^{m} f_n N_i^{(s)}|J_0|w_k^t & \text{for triangular elements}\end{cases}, \quad (3.2.27)$$

where $N_i^{(s)}$ are the shape functions for $S_n^{(e)}$ that is a 4-node quadrilateral or a 3-node triangle and they can be found in Appendix B. $|J_0|$ is the Jacobian determinant that maps surface $S_n^{(e)}$ in the global coordinate system (x,y,z) to an

local system (ξ,η), in which the surface is represented by ζ=constant. It can be expressed as

$$|J_0| = [(\frac{\partial y}{\partial \xi}\frac{\partial z}{\partial \eta} - \frac{\partial z}{\partial \xi}\frac{\partial y}{\partial \eta})^2 + (\frac{\partial z}{\partial \xi}\frac{\partial x}{\partial \eta} - \frac{\partial x}{\partial \xi}\frac{\partial z}{\partial \eta})^2 + (\frac{\partial x}{\partial \xi}\frac{\partial y}{\partial \eta} - \frac{\partial y}{\partial \xi}\frac{\partial x}{\partial \eta})^2]^{\frac{1}{2}}.$$

3.2.5 Solution method for the finite element equation

A simple and efficient iterative method widely used for the solution of sparse systems is the conjugate gradient (CG) method, but its convergence is generally slow. The convergence can be considerably improved by using preconditioning matrices. In this thesis, the CG method with a symmetric successive overelaxlation (SSOR) preconditioner is employed to solve the linear system (3.2.13). The detailed description of this method can be found in the book by Saad (2003). Ma (1998) further took numerical tests for this method in his thesis and suggested it was a good alternative for solving finite element equations in simulations of nonlinear wave problems. This method is summarised below.

Suppose we have a non-singular symmetric positive definite (SPD) matrix $[M]$, whose inverse matrix is denoted by $[M]^{-1}$. We multiply the both sides of equation (3.2.13) by $[M]^{-1}$ as follows

$$[M]^{-1}[K]\{\phi\} = [M]^{-1}\{F\}, \tag{3.2.28}$$

where $[M]$ may be defined as

$$[M] = ([D] + \mu[L])[D]^{-1}([D] + \mu[L]^T)\frac{1}{\mu(2-\mu)},$$

μ is a constant called the relaxation coefficient, $[D]$ is a diagonal matrix formed by the diagonal entries of $[K]$, and $[L]$ is the lower-triangular part of matrix $[K]$ with its diagonal entries equal to zero. For the constant μ, it is in the range $0 < 0 < 2$ and its optimal value may be determined by numerical tests. The original task of solving equation (3.2.13) has now become to solve equation (3.2.28) with faster convergence. The algorithm of the CG method with SSOR preconditioner is given as follows:

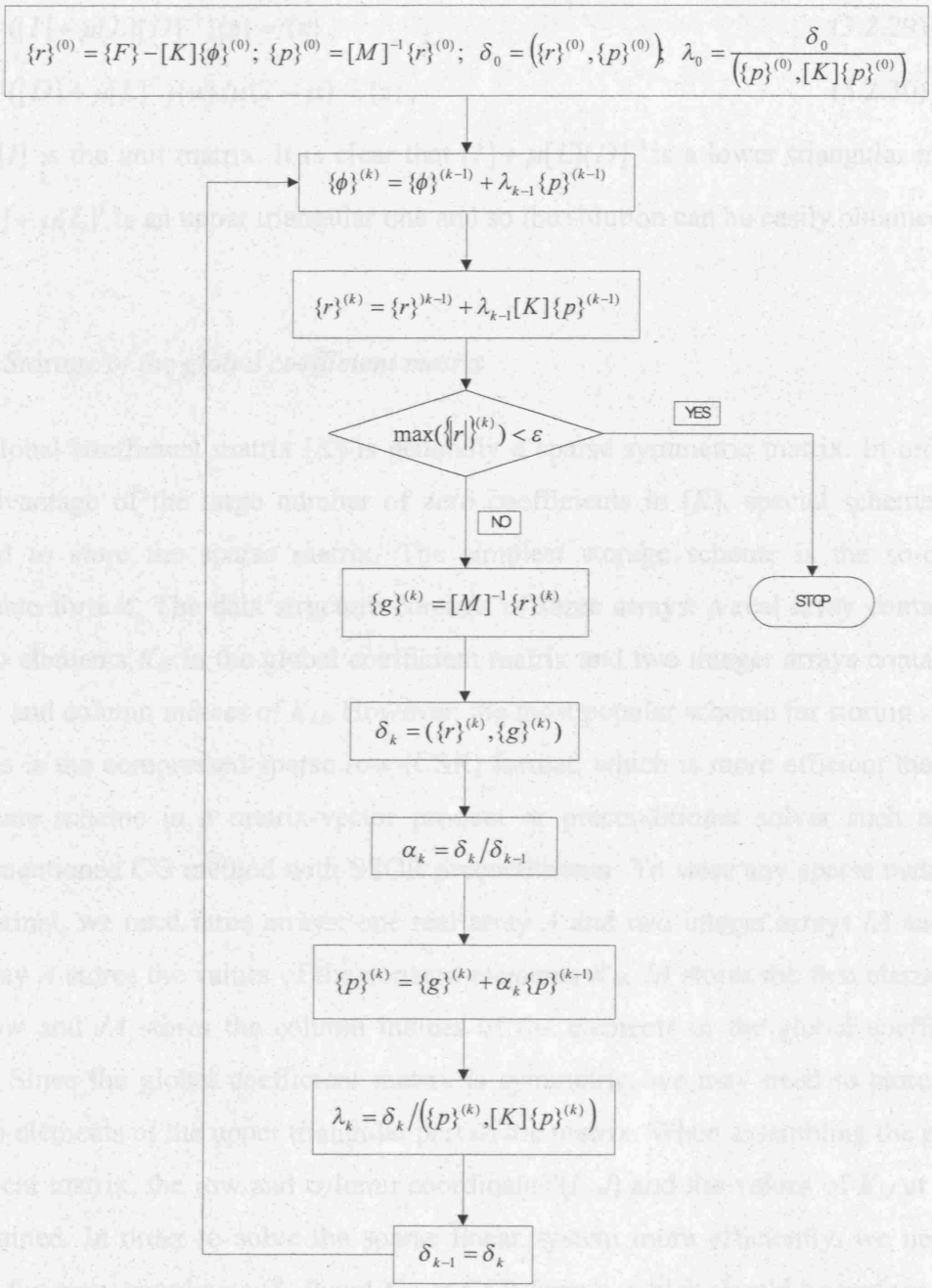

In the above algorithm, $\{r\}$, $\{p\}$ are vectors, δ_k λ_k α_k are scalars, and ε is a tolerance error.

It should be mentioned here that we have to calculate the multiplication of the inverse of the preconditioning matrix $[M]$ and a vector such as $[M]^{-1}\{r\}^{(k)}$ many times when using the CG method with the SSOR preconditioner. However, the inverse matrix of $[M]$ is not necessarily sparse and can even be a full matrix, and so it is not practical to directly calculate $[M]^{-1}$. To compute $\{w\}=[M]^{-1}\{x\}$, we may solve the following two linear systems

$$([I]+\mu[L][D]^{-1})\{z\}=\{x\}, \tag{3.2.29}$$

$$([D]+\mu[L]^{T})\{w\}/\mu(2-\mu)=\{z\}, \tag{3.2.30}$$

where $[I]$ is the unit matrix. It is clear that $[I]+\mu[L][D]^{-1}$ is a lower triangular matrix and $[D]+\mu[L]^{T}$ is an upper triangular one and so the solution can be easily obtained.

3.2.6 Storage of the global coefficient matrix

The global coefficient matrix $[K]$ is generally a sparse symmetric matrix. In order to take advantage of the large number of zero coefficients in $[K]$, special schemes are required to store the sparse matrix. The simplest storage scheme is the so-called coordinate format. The data structure consists of three arrays: a real array containing nonzero elements K_{IJ} in the global coefficient matrix and two integer arrays containing the row and column indices of K_{IJ}. However, the most popular scheme for storing sparse matrices is the compressed sparse row (CSR) format, which is more efficient than the coordinate scheme in a matrix-vector product or preconditioner solver such as the above-mentioned CG method with SSOR preconditioner. To store any sparse matrix in CSR format, we need three arrays: one real array A and two integer arrays IA and JA. The array A stores the values of the nonzero elements K_{IJ}, IA stores the first element in each row and JA stores the column indices of the elements in the global coefficient matrix. Since the global coefficient matrix is symmetric, we may need to store only nonzero elements of the upper triangular part of the matrix. When assembling the global coefficient matrix, the row and column coordinates (I, J) and the values of K_{IJ} at them are obtained. In order to solve the sparse linear system more efficiently, we need to convert the entry coordinate (I, J) and K_{IJ} to CSR format, which should be performed as quickly as possible. We introduce an approach to calculate the global coefficient matrix in CSR format as follows.

Firstly, we store all nonzero elements in the global coefficient matrix using a data structure called a linear linked list (Dale, 1998), which is very convenient for the storage of sparse matrices. A linear linked list is a set of records with a linear relationship between records. The linked list is convenient for recording the row and column coordinate (I, J) and the value at (I, J) although all elements at any row in the sparse matrix are not continuous and the number of elements at each row is not identical. The linked list that we use here contains an integer number called *column* denoting the

column *J*, a double precision real number *val* expressing the value of a nonzero element and a pointer *next* for the address of the next record. A list may be described using a data type called 'struct' as follows in **C** language

```
struct List {
  long column;
  double val;
  List *next;
};
```

The pointer *next* is used for connecting the present record and the next one. A list with *n* records is shown in Figure 3.2.2. Each record includes a data zone and an address zone. At the front of the list, there is a pointer called HEAD pointing to the first record, and a NULL pointer in the last record expressing the end of the list. The data zone contains the data *column* and *val* while the address zone contains the pointer *next*.

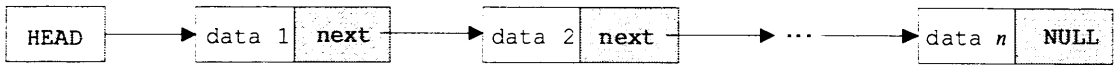

Figure 3.2.2 A linear list

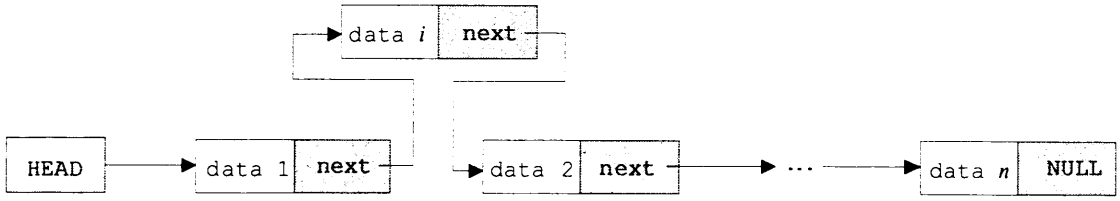

Figure 3.2.3 Insert a record into the list

The nonzero elements at each row in the global coefficient matrix [*K*] are stored using a linked list, so it needs *n* lists for *n* rows. At the same time as assembling the global coefficient matrix, the row and column coordinates (*I, J*) and K_{IJ} are added to the *I*-th list. In each list, the position of K_{IJ} is determined by the value of *J*. The addition can be finished by an insert operation. Suppose we need to insert a record between records one and two, we only need to let the pointer in record one point to the inserted record and meanwhile the pointer in the inserted record points to record two (Figure 3.2.3). The operation is simple. The advantage of using a list is that the length of the list can dynamically increase or decrease with very few operations, which is difficult when using an array expression.

Secondly, we convert the matrix in the format of the linearly linked list to that of CSR. This process is very simple. K_{IJ}, IA and JA can be easily taken out from the list by assignment and addition operations.

This approach for storing sparse matrices in CSR format is fast. A test has been made with an AMD 1800+ personal computer with windows XP system and the result is shown in Figure 3.2.4. It is seen that the time to construct the global coefficient matrix in CSR format nearly linearly increases with the number of nodes or elements.

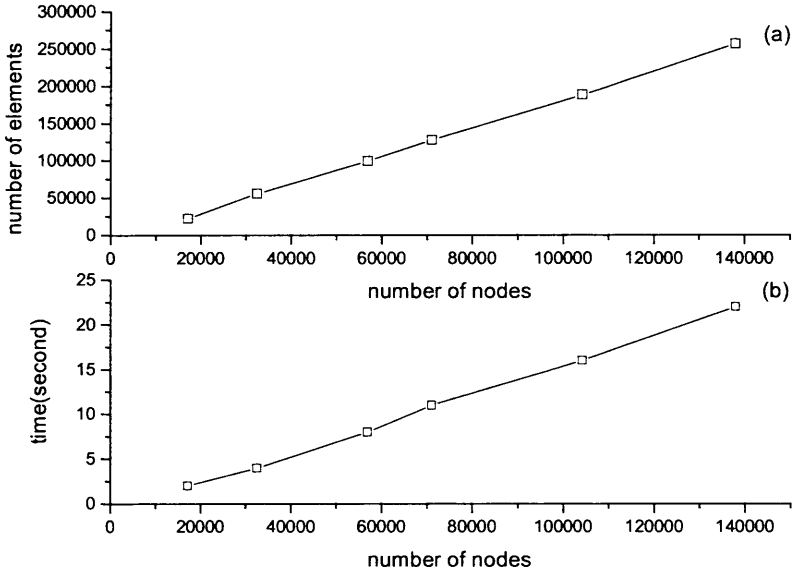

Figure 3.2.4 Time cost for constructing the global coefficient matrix in CSR format

3.3 Numerical procedures

3.3.1 Computation of velocity

For a quadrilateral or a hexahedron isoparametric element, we can directly obtain the velocity at nodes based on the shape function. However, for a linear element with triangular facets such as a triangle, prism or tetrahedron element, the velocity will be constant on the facet. Thus, the result may not be sufficiently accurate.

Ma, Wu & Eatock Taylor (2001a, b) developed a numerical method to calculate the velocity $\vec{u} = (u,v,w)$. They employed a differential formula to obtain the vertical component of the velocity w. Here we employ a cubic polynomial to express the velocity potential along the vertical direction

$$\phi = a + bz + cz^2 + dz^3, \tag{3.3.1}$$

and its first- and second-order derivatives with respect to z are

$$w = \frac{\partial \phi}{\partial z} = b + 2cz + 3dz^2, \tag{3.3.2a}$$

$$\frac{\partial^2 \phi}{\partial z^2} = 2c + 6dz, \tag{3.3.2b}$$

respectively, where a, b, c and d are coefficients and may be determined through solving the following system:

$$\begin{bmatrix} 1 & z_1 & z_1^2 & z_1^3 \\ 1 & z_2 & z_2^2 & z_2^3 \\ 1 & z_3 & z_3^2 & z_3^3 \\ 1 & z_4 & z_4^2 & z_4^3 \end{bmatrix} \begin{bmatrix} a \\ b \\ c \\ d \end{bmatrix} = \begin{bmatrix} \phi_1 \\ \phi_2 \\ \phi_3 \\ \phi_4 \end{bmatrix},$$

where z_i $(i = 1,2,3,4)$ are four successive nodes along the vertical direction, and ϕ_i $(i = 1,2,3,4)$ are the velocity potentials at z_i $(i = 1,2,3,4)$. The vertical velocity is obtained using equation (3.3.2a). The calculation of second order derivative $\partial^2\phi/\partial z^2$ in equation (3.3.2b) is required in the second order problems of the later chapters. After the vertical velocity is obtained by equation (3.3.2a), the following equation is used to obtain the horizontal components u and v:

$$\left.\begin{aligned} u_i l_x^k + v_i l_y^k &= \frac{\partial \phi}{\partial l^k} - w_i l_z^k \\ u_i l_x^m + v_i l_y^m &= \frac{\partial \phi}{\partial l^m} - w_i l_z^m \end{aligned}\right\}, \tag{3.3.2c}$$

where $\frac{\partial \phi}{\partial l^k} = \frac{\phi_{i+k} - \phi_i}{l^k}$, and l_x^k, l_y^k & l_z^k are the components of $\bar{l}^k$ (k=1,2,...), a vector formed by nodes i+k and i. A weighted average was then used to obtain the final velocity. This method requires the node on the free surface and three nodes immediately below the free surface to be on the same vertical line. The method is found to be accurate but it is suitable only for wall-sided cylindrical structures. In this thesis, we will consider interactions of waves and cylinders with flare. The above method will be invalid, and the method developed by Wu & Eatock Taylor (1994) when they considered the 2D problem is adopted. We first expand the velocity in terms of the shape function similar to equation (3.2.2) and then the Galerkin method is used. This means

$$\iiint_{\forall}(\vec{u}-\nabla\phi)N_i d\forall = 0, \tag{3.3.3}$$

or

$$\iiint_{\forall}\vec{u}N_i d\forall = \iiint_{\forall}\nabla\phi N_i d\forall . \tag{3.3.4}$$

The equation to calculate velocity can be finally derived as

$$[A]\{\vec{u}\} = [\vec{B}]\{\phi\}, \tag{3.3.5}$$

where

$$A_{ij} = \iiint_{\forall} N_i N_j d\forall$$

$$\vec{B}_{ij} = \iiint_{\forall} N_i \nabla N_j d\forall$$

A comparison between the two methods is performed. We consider a diffraction problem of interactions between Stokes second order waves and a vertical circular cylinder. The water depth is equal to the radius of the section of the cylinder and a nondimensional wavenumber k_0a=1.0 is chosen to test the two approaches. We only compare the first order waves at the front and back sides of the cylinder. The results are shown in Figure 3.3.1. It can be seen that wave history is graphically identical.

Equation (3.3.5) is suitable for general cases, but the computation needs more time when comparing with equations (3.3.2a) and (3.3.2c).

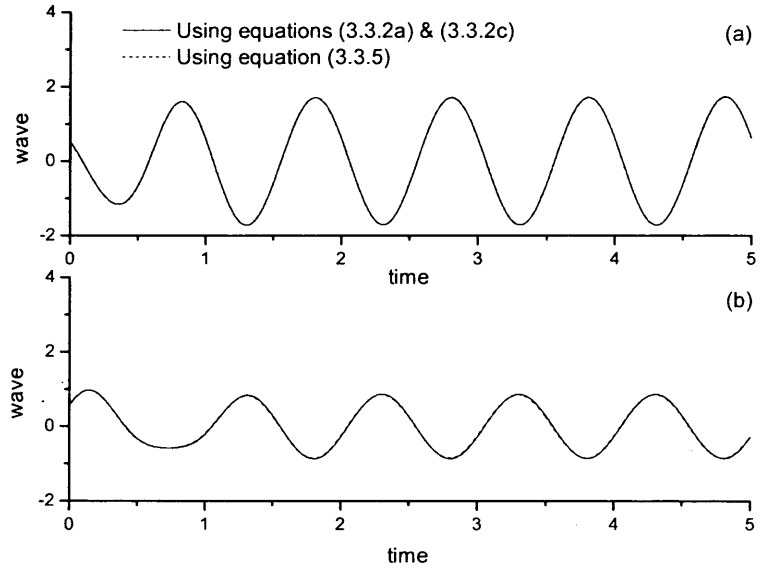

Figure 3.3.1 Comparison of two methods of calculating velocity
(a) at the front side; (b) at the back side

3.3.2 *Time-integral of free surface boundary conditions*

After the velocity potential and velocity are obtained by equations (3.2.13) and (3.3.5), we can use (2.3.3) and (2.3.4) for Eulerian form or (2.3.5) and (2.3.6) for Lagrangian form to update the information on the free surface. For the fully nonlinear wave problems, the wave elevation and the velocity potential on the free surface should be updated at each time step by

$$f(t+\Delta t) = f(t) + \int_t^{t+\Delta t} f'(t)dt\,, \tag{3.3.6}$$

where $f(t)$ represents either the coordinate of the free surface or the velocity potential and f' is its derivative with respect to time t.

A time integration scheme should be adopted for equation (3.3.6) in numerical simulations. A simple integration scheme is the second order Adams-Bashforth equation

$$f(t+\Delta t) = f(t) + \frac{\Delta t}{2}[3f'(t) - f'(t-\Delta t)]\,. \tag{3.3.7}$$

Other higher order time integral methods such as the fourth order Adams-Bashforth equation

$$\begin{aligned} f(t+\Delta t) &= f(t) + \\ &\frac{\Delta t}{24}[55f'(t) - 59f'(t-\Delta t) + 37f'(t-2\Delta t) - 9f'(t-3\Delta t)], \end{aligned} \tag{3.3.8}$$

and the fourth order Runge-Kutta method (Engeln-Müllges & Uhlig, 1996)

$$f(t+\Delta t) = f(t) + \frac{\Delta t}{8}(k_1 + 3k_2 + 3k_3 + k_4) \tag{3.3.9}$$

are also usually employed. In equation (3.3.9), $k_i = f'(t + \frac{i-1}{3}\Delta t, Q^{n+\frac{i-1}{3}})\ (i = 1, 2, 3, 4)$.

At time steps $n\Delta t + \frac{i-1}{3}\Delta t$ $(i = 2,3,4)$, the position of the free surface and the corresponding velocity potential can be computed by the following equations respectively,

$$f(t + \frac{\Delta t}{3}) = f(t) + \frac{\Delta t}{3}k_1\,, \tag{3.3.10a}$$

$$f(t + \frac{2}{3}\Delta t) = f(t) + \Delta t(-\frac{1}{3}k_1 + k_2)\,, \tag{3.3.10b}$$

$$f(t+\Delta t) = f(t) + \Delta t(k_1 - k_2 + k_3)\,. \tag{3.3.10c}$$

One advantage of the Runge-Kutta method is that it does not need the information at previous time steps but only depends on the position of free surface and the corresponding potential within the present time step. It does however need additionally to calculate equations (3.3.10a, b, c) and the corresponding derivative f' at mini steps $n\Delta t + \frac{i-1}{3}\Delta t$ $(i = 2,3,4)$, which means that three additional linear systems should be solved at these time steps. Thus it will increase the CPU time. In 2D fully nonlinear simulations, we use the fourth order Runge-Kutta method to update the free surface since the computational cost is acceptable. In 3D simulations, the fourth order Runge-Kutta method is generally time-consuming and the Adams-Bashforth methods will be used. The second order Adams-Bashforth method will be utilised for the fully nonlinear problem and the fourth order for the second order calculation. A consideration to this is that the derivatives f' at previous time steps t-Δt, t-$2\Delta t$ and t-$3\Delta t$ are obtained through interpolation when remeshing is performed. The interpolation is only required for steps t-Δt for the second order Adams-Bashforth method but required at t-Δt, t-$2\Delta t$ and t-$3\Delta t$ for the fourth order method. More interpolations require more computation and may cause numerical errors. However, the cost is that a smaller time interval is needed. For the second order perturbation solution, since the nodes on the free surface do not vary with time, no additional computation of interpolation is required at the previous three time steps t-Δt, t-$2\Delta t$ and t-$3\Delta t$ when equation (3.3.8) is used.

3.3.3 Remeshing the free surface

When the simulation is over a substantial period of time, the nodes on the free surface may cluster and cause elements to be distorted. In order to avoid this, nodes on the free surface should be rearranged every few time steps i.e. remeshing should be performed. We first present a 2D remeshing method. Suppose there are n+1 nodes $\mathbf{P}_i(x_i, z_i)$ $(i = 0,1,\cdots,n)$ on a curve. We may interpolate any point on the curve between nodes $\mathbf{P}_i$ and $\mathbf{P}_{i+1}$ using B-splines. We use the uniform cubic B-spline to express the point as

$$\mathbf{P}(u) = \sum_{j=0}^{3} B_{j,3}(u)\mathbf{V}_{i+j} \quad (i = 0,1,\cdots,n), \tag{3.3.11}$$

where u is a parameter and $0 \le u \le 1$, $B_{j,3}(u)$ $(j = 0,1,2,3)$ are cubic B-spline functions and may be expressed as

$$\left.\begin{aligned} B_{0,3}(u) &= \frac{1}{6}(1-u)^3 \\ B_{1,3}(u) &= \frac{1}{6}(3u^3 - 6u^2 + 4) \\ B_{2,3}(u) &= \frac{1}{6}(-3u^3 + 3u^2 + 3u + 1) \\ B_{3,3}(u) &= \frac{1}{6}u^3 \end{aligned}\right\}; \tag{3.3.12}$$

and $\mathbf{V}_{i+j}$ $(i = 0,1,\cdots,n)$ are control points. We can obtain the following equation according to equations (3.3.11) and (3.3.12)

$$\mathbf{P}_i(0) = \frac{1}{6}(\mathbf{V}_i + 4\mathbf{V}_{i+1} + \mathbf{V}_{i+2}) \quad (i = 0,1,\cdots,n). \tag{3.3.13}$$

In matrix from, this becomes

$$[A][\mathbf{V}] = [\mathbf{P}], \tag{3.3.14}$$

where $[A]$ is a tridiagonal matrix, $[\mathbf{V}]$ and $[\mathbf{P}]$ are vectors consisting of the control points $\mathbf{V}_i$ and nodes $\mathbf{P}_i$ respectively

$$[A] = \begin{bmatrix} 6 & 0 & & & & \\ 1 & 4 & 1 & & & \\ & 1 & \ddots & \ddots & & \\ & & \ddots & \ddots & 1 & \\ & & & \ddots & 4 & 1 \\ & & & & 0 & 6 \end{bmatrix}, \quad [\mathbf{V}] = \begin{bmatrix} \mathbf{V}_0 \\ \mathbf{V}_1 \\ \vdots \\ \\ \mathbf{V}_{n+2} \end{bmatrix}, \quad [\mathbf{P}] = 6\begin{bmatrix} \mathbf{P}_{-1} \\ \mathbf{P}_0 \\ \vdots \\ \\ \mathbf{P}_{n+1} \end{bmatrix}.$$

The boundary points $\mathbf{V}_0$ and $\mathbf{V}_{n+2}$ are set to be $\mathbf{P}_{-1}$ and $\mathbf{P}_{n+1}$, respectively, and $\mathbf{P}_{-1}$ and $\mathbf{P}_{n+1}$ may be obtained through linear extrapolation

$$\mathbf{P}_{-1} = 2\mathbf{P}_0 - \mathbf{P}_1,$$

$$\mathbf{P}_{n+1} = 2\mathbf{P}_n - \mathbf{P}_{n-1}.$$

The arc length from node $\mathbf{P}_i$ to $\mathbf{P}_0$ may be calculated by the following equation:

$$S_i = \sum_{k=0}^{i} \int_0^1 \left(\frac{ds}{du}\right)_k du \qquad (i = 0,1,...,n), \tag{3.3.15}$$

where

$$\frac{ds}{du} = \sqrt{\left(\frac{dx}{du}\right)^2 + \left(\frac{dz}{du}\right)^2},$$

and

$$(\frac{dx}{du},\frac{dz}{du}) = \frac{d\mathbf{P}(u)}{du} = \sum_{j=0}^{3} \frac{dB_{j,3}}{du}\mathbf{V}_{i+j}.$$

Suppose there are m segments or m+1 nodes on the curve after remeshing. We denote the nodes as $\mathbf{P}_{i,r}$ $(i = 0,1,\cdots,m)$. The arc length $S_{i,r}$ from node $\mathbf{P}_{0,r}$ to $\mathbf{P}_{i,r}$ may be determined as we require, for example, if we wish to have smaller elements near $\mathbf{P}_0$ and larger elements near $\mathbf{P}_n$, we can adopt the following procedure (Chung, 2002)

$$S_{i,r} = S_n \frac{(\beta+1)-(\beta-1)(\frac{\beta+1}{\beta-1})^{1-i/m}}{(\frac{\beta+1}{\beta-1})^{1-i/m}+1} \quad (i = 0,1,\cdots,m), \tag{3.3.16}$$

where $\beta > 1$ is a constant and it controls distribution of the nodes. A larger value of β will give a more uniform distribution. Equation (3.3.16) will be discussed in more detail in Chapter 4.

For 3D problems, we can employ a 2D horizontal remeshing scheme (Ma, 1998) as we consider single value waves. The detailed remeshing procedure can be found in Ma's thesis (1998). We gave only a summary below.

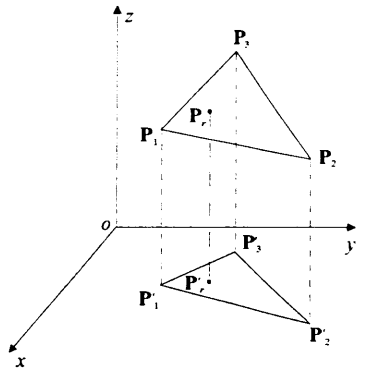

Figure 3.3.2 Projection of a triangle on the free surface to the *oxy* plane

(1) The free surface is projected to the horizontal plane *oxy* and a 2D mesh M_{old} is generated on the plane. The projection of a triangular element $\Delta\mathbf{P}_1\mathbf{P}_2\mathbf{P}_3$ on the free surface is denoted by $\Delta\mathbf{P}_1'\mathbf{P}_2'\mathbf{P}_3'$ on plane *oxy* (Figure 3.3.2). The potential and velocity at nodes $\mathbf{P}_i(x_i, y_i, z_i)$ $(i = 1,2,3)$ are denoted by ϕ_i, $\mathbf{u}_i$, respectively.

(2) A new 2D mesh named M_{new} is generated on the *oxy* plane. The node in M_{new} is denoted as $\mathbf{P}_r'(x_r', y_r')$ and its corresponding node vertically projected to the free surface is $\mathbf{P}_r(x_r, y_r, z_r)$.

(3) A search is performed to find the location of $\mathbf{P}_r'$ in the mesh M_{old}.

(4) Interpolation is performed to obtain the vertical coordinate, the potential and velocity at $\mathbf{P}_r$. We assume that the node $\mathbf{P}_r'$ is in the triangular element $\Delta\mathbf{P}_1'\mathbf{P}_2'\mathbf{P}_3'$ and $\mathbf{P}_r'$ will divide the element into three triangles: $\Delta\mathbf{P}_r'\mathbf{P}_2'\mathbf{P}_3'$, $\Delta\mathbf{P}_r'\mathbf{P}_3'\mathbf{P}_1'$ and $\Delta\mathbf{P}_r'\mathbf{P}_1'\mathbf{P}_2'$. The ratios of areas of $\Delta\mathbf{P}_r'\mathbf{P}_2'\mathbf{P}_3'$, $\Delta\mathbf{P}_r'\mathbf{P}_3'\mathbf{P}_1'$ and $\Delta\mathbf{P}_r'\mathbf{P}_1'\mathbf{P}_2'$ to that of $\Delta\mathbf{P}_1'\mathbf{P}_2'\mathbf{P}_3'$ are denoted by $\chi_i (i = 1,2,3)$. The coordinates, the potential and the velocity at $\mathbf{P}_r$ can be obtained by the following equations:

$$x_r = x_r', y_r = y_r', z_r = \sum_{i=1}^{3} \chi_i z_i', \tag{3.3.17}$$

$$\phi_r = \sum_{i=1}^{3} \chi_i \phi_i, \tag{3.3.18}$$

$$\mathbf{u}_r = \sum_{i=1}^{3} \chi_i \mathbf{u}_i. \tag{3.3.19}$$

(5) Steps (3) and (4) are repeated until all nodes in M_{new} and the potential and the velocity at them are found.

In order to use equation (3.3.7) to update the wave and potential on the free surface, the coordinates, the potential and the velocity at the node at the previous time step $t - \Delta t$ corresponding to node $\mathbf{P}_r$ should be known, and they can obtained by the same method as above.

It should be noticed that an over frequent remeshing may cause a loss of energy. For the numerical wave tank problem, remeshing every 20-30 steps will be adopted in this thesis.

3.3.4 Smoothing technique

Simulations of steep waves sometimes crash due to saw-tooth problems on the free surface. In order to avoid such behaviour we may use a smoothing technique. A simple method is the weighted 5-points smoothing for a curve with equal spacing

$$\bar{f}_i = \frac{1}{16}(-f_{i-2} + 4f_{i-1} + 10f_i + 4f_{i+1} - f_{i+2}), \tag{3.3.20}$$

or

$$\bar{f}_i = \frac{1}{32}(-f_{i-3} + 9f_{i-1} + 16f_i + 9f_{i+1} - f_{i+3}). \tag{3.3.21}$$

This method was first used by Longuet-Higgins & Cokelet (1976) for removing saw-tooth instability. For nonuniform distribution, an energy method introduced by Zhu (2000) is utilised to smooth the free surface for 2D problems in this thesis. Suppose there is a discrete set of nodes defined through position vectors $\mathbf{Q}_i$ (i=0, 1, ..., n) and node $\mathbf{Q}_i$ becomes $\mathbf{P}_i$ after smoothing. We define the energy of all nodes $\mathbf{P}_i$ (i=0,1,...,n) as

$$E_c = \sum_{j=1}^{n-1} \frac{1}{l_i + l_{i+1}} (e_{i+1} - e_i)^2 , \tag{3.3.22}$$

where $l_i = \|\mathbf{Q}_i - \mathbf{Q}_{i-1}\|$ is the distance between $\mathbf{Q}_i$ and $\mathbf{Q}_{i-1}$, e_i is defined as $e_i = \frac{p_i - p_{i-1}}{l_i}$ and $p_i\ (i = 0,1,\cdots,n)$ is either x or z coordinate of node $\mathbf{P}_i$. The smoothing process should ensure that the difference between $\mathbf{P}_i$ and $\mathbf{Q}_i (i = 0,1,\cdots,n)$ is as little as possible. In order to achieve this, we define an objective function as

$$F_c = \alpha E_c + \sum_{j=0}^{n} \beta_j (p_j - q_j)^2 , \tag{3.3.23}$$

where α and β_j are constants, and $q_i\ (i = 0,1,\cdots,n)$ is either x or z coordinate of node $\mathbf{Q}_j$. Substituting equation (3.3.22) into (3.3.23), we obtain

$$F_c = \alpha \sum_{j=1}^{n-1} \frac{1}{l_{j+1} + l_j} \left(\frac{p_{j+1} - p_j}{l_{j+1}} - \frac{p_j - p_{j-1}}{l_j} \right)^2 + \sum_{j=0}^{n} \beta_j (p_j - q_j)^2 . \tag{3.3.24}$$

The first summation of this equation reflects the smoothness while the second summation reflects the difference between the curves before smoothing and after smoothing. Both of them should be minimal, which is achieved through setting the derivatives of F_c with respect to $p_i (i = 0,1,\cdots,n)$ equal to zero, that is

$$\frac{\partial F_c}{\partial p_i} = 0 \quad (i = 0,1,\cdots,n). \tag{3.3.25}$$

This gives

$$[A][\mathbf{P}] = [\mathbf{Q}], \tag{3.3.26}$$

where A is a matrix with bandwidth being five,

$$[A]=\begin{bmatrix} c_0 & d_0 & e_0 & & & \\ b_1 & c_1 & \ddots & \ddots & & \\ a_2 & \ddots & \ddots & \ddots & \ddots & \\ & \ddots & \ddots & \ddots & \ddots & e_{n-2} \\ & & \ddots & \ddots & \ddots & d_{n-1} \\ & & & a_n & b_n & c_n \end{bmatrix}.$$

The coefficients in matrix $[A]$ are given as, respectively,

$$a_i = \alpha \frac{1}{(l_i + l_{i-1}) l_i l_{i-1}} (i = 2, \cdots, n),$$

$$b_i = \begin{cases} -\alpha \dfrac{1}{l_1^2 l_2} & (i = 1) \\ -\alpha \dfrac{1}{l_i^2} \left(\dfrac{1}{l_{i+1}} + \dfrac{1}{l_{i-1}} \right) & (i = 2, \cdots, n-1), \\ -\alpha \dfrac{1}{l_n^2 l_{n-1}} & (i = n) \end{cases}$$

$$c_i = \begin{cases} \beta_0 & (i = 0) \\ \alpha \left[\dfrac{l_2 + l_1}{l_2^2 l_1^2} + \dfrac{1}{(l_3 + l_2) l_2^2} \right] + \beta_1 & (i = 1) \\ \alpha \left[\dfrac{1}{(l_i + l_{i-1}) l_i^2} + \dfrac{l_{i+1} + l_i}{l_{i+1}^2 l_i^2} + \dfrac{1}{(l_{i+2} + l_{i+1}) l_{i+1}^2} \right] + \beta_i & (i = 2, \cdots, n-2), \\ \alpha \left[\dfrac{1}{(l_{n-1} + l_{n-2}) l_{n-1}^2} + \dfrac{l_n + l_{n-1}}{l_n^2 l_{n-1}^2} \right] + \beta_{n-1} & (i = n\text{-}1) \\ \beta_n & (i = n) \end{cases}$$

$$d_i = \begin{cases} -\alpha \dfrac{1}{l_1^2 l_2} & (i = 0) \\ -\alpha \dfrac{1}{l_{i+1}^2} \left(\dfrac{1}{l_i} + \dfrac{1}{l_{i+2}} \right) & (i = 1, \cdots, n-2), \\ -\alpha \dfrac{1}{l_n^2 l_{n-1}} & (i = n-1) \end{cases}$$

$$e_i = \alpha \frac{1}{(l_{i+2} + l_{i+1}) l_{i+2} l_{i+1}} (i = 0, \cdots, n-2).$$

In our simulations, the constants $\beta_j (j = 0,1,\cdots,n)$ are set to be a unit value. The smoothing factor α is related to $l_i (i = 1,2,\cdots,n)$ and may be obtained by numerical tests. We adopt the following procedure. Suppose the minimum value of $l_i (i = 1,2,\cdots,n)$ is l_{min}, we write $\alpha = C l_{\min}^3$ where C is a coefficient. Numerical tests in Figure 3.3.3 show that a

number between 5 and 10 is a good choice for C. It should be mentioned that the boundary nodes $\mathbf{Q}_0$ and $\mathbf{Q}_n$ are constrained and they are equal to $\mathbf{P}_0$ and $\mathbf{P}_n$, respectively, which may be achieved simply by taking $d_0=e_0=a_n=b_n=0$.

At the same time as smoothing the free surface, the velocity potential on the nodes of the free surface should also be smoothed. The same procedure can be used but one of the coordinates is taken as the potential and the other taken to be zero.

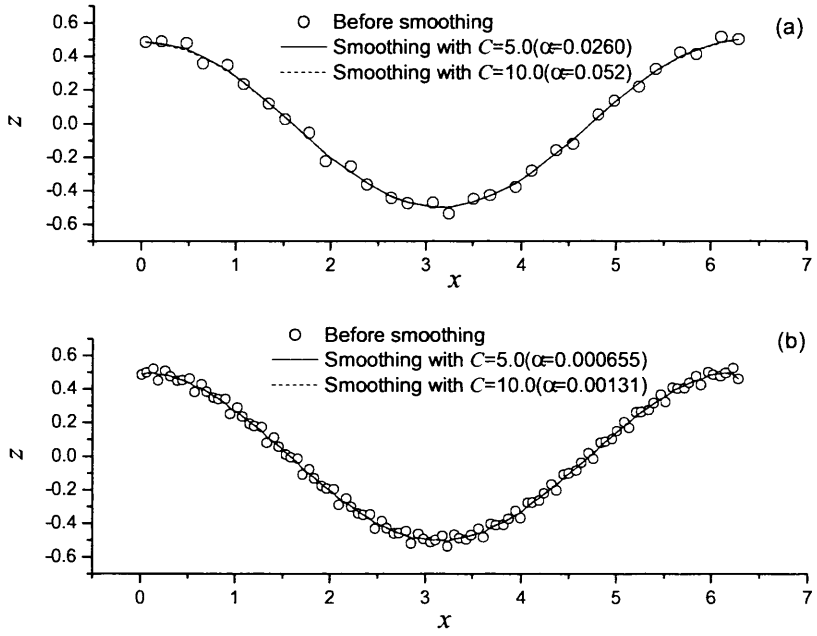

Figure 3.3.3 Curve Smoothing
(a) 30 nodes (l_{min}=0.173); (b) 100 nodes (l_{min}=0.051)

For 3D simulations, the free surface consists of many triangular elements and the distribution of nodes is irregular since the mesh is unstructured. Ideal smoothing techniques should be suitable for an irregular distribution of nodes on a surface, which could be a challenge. Here since the hybrid mesh (see Chapter 4) on the free surface is used, we may utilise the 2D smoothing technique [see equation (3.3.20)] to smooth the wave and potential within the part of the structured mesh as shown in shadow in Figure 3.3.4. The nodes along the y-direction are uniformly distributed after remeshing, which is performed on the whole free surface, and smoothing is then performed along the y-direction within the structured mesh for both the wave elevation and the velocity potential.

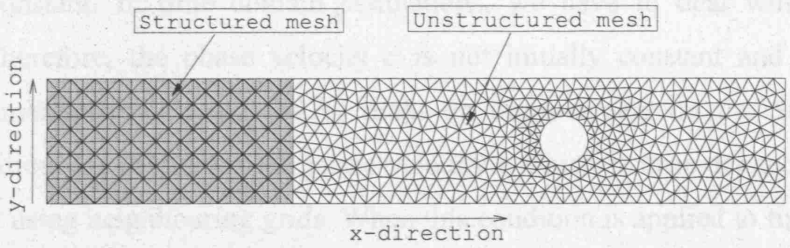

Figure 3.3.4 Smoothing within the structured mesh

3.3.5 Artificial wave absorption

When a wave is produced in a tank by a wave maker or by oscillation of a floating body on water surface, it will propagate outwards. In numerical simulations of nonlinear water waves in the time domain, it is impossible to select a computational domain as large as the physical domain. It is usually truncated at some position called an open boundary denoted by S_c. To avoid wave reflection, an appropriate radiation condition should be imposed at the open boundary. There are usually two methods for wave absorbing in numerical simulations. One is based on the Sommerfeld radiation condition, and the other is through an artificial damping zone.

(1) Sommerfeld-Orlanski radiation condition

When we simulate radiation problems such as oscillations of a floating body in the frequency domain, an appropriate radiation condition is indispensable in obtaining a unique solution. The radiation condition guarantees that waves always propagate away from the oscillating floating body. Although the fluid domain is infinite, Green functions can still be constructed for linear problems to directly satisfy the radiation condition in both situations of finite and infinite water depths. However, in nonlinear time domain simulations, no such a Green's function is available and we can only deal with a finite computational domain. For the problem of a wave generated by a disturbed source such as wave maker in a 2D tank (see Figure 3.3.6), the Sommerfeld radiation condition should be satisfied at the open boundary S_c

$$\frac{\partial \phi}{\partial t} + c\frac{\partial \phi}{\partial x} = 0, \tag{3.3.27}$$

where c is the phase velocity of wave and ϕ is the velocity potential. For a single frequency, periodic and linear wave, the phase velocity in the Sommerfeld radiation

condition is constant. In time domain simulations, we have to deal with transient phenomena. Therefore, the phase velocity c is not initially constant and has to be determined numerically. Orlanski (1976) made an improvement on the Sommerfeld radiation condition. He calculated the phase velocity c which is time-dependent, at the open boundary using neighbouring grids. When this condition is applied to time domain numerical simulations, it is usually called the Sommerfeld-Orlanski radiation condition. Since then, Chan (1977), Jagannathan (1988), Romate (1992) have also used this method in their simulations of interactions of second order waves and bodies in two- and three-dimensions in the time domain.

In nonlinear simulations, c is determined by substituting equation (2.3.4) into equation (3.3.27)

$$c = \frac{(\frac{1}{2}\nabla\phi \cdot \nabla\phi + g\eta)}{\partial\phi/\partial x}, \tag{3.3.28}$$

where η is the wave elevation at S_c . $\partial\phi/\partial x$ may be obtained by differential schemes using grids near S_c. After c is obtained, we integrate $\partial\phi/\partial t$ with respect to time to calculate the potential ϕ on S_c at next time step, and this potential is taken as the boundary condition on S_c for solving the finite element equation. If the phase velocity c calculated using equation (3.3.28) is greater than $\Delta x/\Delta t$ (Δx is the length of neighboring grid), it is set to be $\Delta x/\Delta t$. When it is negative, we set it to be zero. Orlanski (1976) gave the discretisation form of equations (3.3.27) and (3.3.28) in a central difference in time and a leap-frog difference in space

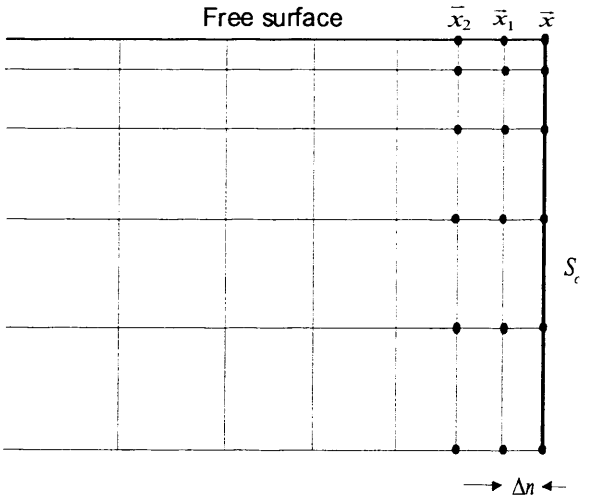

Figure 3.3.5 Discretisation of the Sommerfeld-Orlanski radiation condition

$$\frac{\phi(\vec{x},t+\Delta t)-\phi(\vec{x},t-\Delta t)}{2\Delta t} + \frac{c}{\Delta n}\{\frac{1}{2}[\phi(\vec{x},t+\Delta t)+\phi(\vec{x},t-\Delta t)]-\phi(\vec{x}_1,t)\}=0, \tag{3.3.29}$$

where $\vec{x}$ is a point on S_c, Δn is a small distance from S_c ($\Delta n = \Delta x$ for 2D problems), and $\vec{n}$ the normal vector at $\vec{x}$ as shown in Figure 3.3.5. The celerity c on S_c is calculated by equation (3.3.27) at the previous time step

$$c = -\frac{\Delta n}{\Delta t}\frac{\phi(\vec{x}_1,t)-\phi(\vec{x}_1,t-2\Delta t)}{\phi(\vec{x}_1,t)+\phi(\vec{x}_1,t-2\Delta t)-2\phi(\vec{x}_2,t-\Delta t)}, \tag{3.3.30}$$

where $\vec{x}_1$ and $\vec{x}_2$ are two neighbouring points to $\vec{x}$, $\vec{x}_1 = \vec{x} - \vec{n}\Delta n$ and $\vec{x}_2 = \vec{x} - 2\vec{n}\Delta n$ (see Figure 3.3.5). However, there are numerical difficulties in using equation (3.3.30) as c will become undefined or inaccurate when both $\partial\phi/\partial t$ and $\partial\phi/\partial n$ are zero or very small. In practical commutation, the celerity is usually obtained from

$$c' = \begin{cases} 0 & c \le 0 \\ c & 0 \le c \le \Delta n/\Delta t \\ \Delta n/\Delta t & c \ge \Delta n/\Delta t \end{cases}. \tag{3.3.31}$$

Equations (3.3.29) and (3.3.30) have been used by Isaacson & Cheung (1991, 1992) to simulate second order wave diffraction problems in two- and three-dimensions.

(2) Artificial damping zone

When the Sommerfeld-Orlanski radiation is used in simulations of nonlinear water waves in the time domain, the mesh size near the open boundary must be small enough. Otherwise, the phase velocity at the open boundary obtained by equation (3.3.28) may not be sufficiently accurate. A different method from the Sommerfeld-Orlanski radiation type is based on an artificial damping zone, which is also called a sponge layer or an artificial beach. The artificial damping zone is an absorbing boundary. Outgoing waves will be absorbed through artificial damping terms added to free surface boundary conditions when they arrive at the damping zone.

Cointe *et al.* (1990) developed a damping zone technique for their 2D numerical wave tank. In the damping zone, the following absorbing free surface boundary condition is modified as follows

$$\frac{Dz}{dt} = \frac{\partial \phi}{\partial z} - \nu\eta, \tag{3.3.32}$$

$$\frac{D\phi}{Dt} = -g\eta + \frac{1}{2}\nabla\phi \cdot \nabla\phi - \nu\phi, \tag{3.3.33}$$

with

$$\nu(x) = \begin{cases} \alpha\omega(\dfrac{x - x_0}{\lambda})^2 & x_0 \le x \le x_1 = x_0 + \beta\lambda \\ 0 & 0 < x < x_0 \ \text{ or } x > x_1 \end{cases},$$

where ω is the wave frequency, λ the linear wave length. The damping zone starts from point x_0 and extends for $\beta\lambda$ as shown in Figure 3.3.6. Parameters α and β control the strength and the length of the damping zone respectively, and they may be obtained through numerical experiments. The numerical investigation by Tanizawa (1996) has shown that reflection is minimised when $\alpha = \beta = 1.0$.

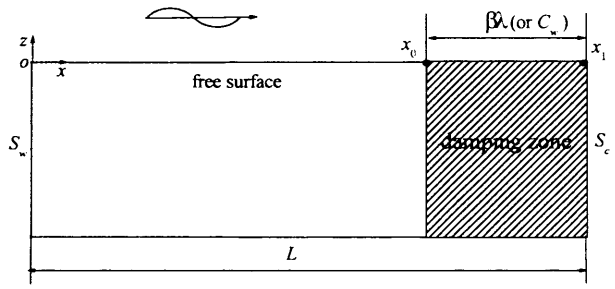

Figure 3.3.6 Artificial damping zone

In linear 3D problems, Nakos *et al.* (1993) claimed the excellent performance of their proposed damping zone. They added a damping term called a Newtonian cooling term only in the kinematic boundary condition

$$\frac{\partial \eta}{\partial t} = \frac{\partial \phi}{\partial z} - 2\nu\eta + \frac{\nu^2}{g}\phi, \tag{3.3.34}$$

$$\frac{\partial \phi}{\partial t} = -g\eta, \tag{3.3.35}$$

where ν is the damping coefficient given by

$$\nu(r) = 3\frac{C_s}{C_w^3}(r - r_0)^2 \quad 0 \le r - r_0 \le C_w.$$

As shown in Figure 3.3.7, L_{dm} is the length of the damping zone, and r is the distance for the point p under consideration to the centre of the body. The damping zone starts from the edge of an inner rectangle $r = r_0(x, y)$ and ends at outer rectangle $r = r_0(x, y) + C_w(x, y)$. C_s in the equation is a constant to control the strength of the damping coefficient and is chosen to be 1.0 in this study, L_{dm} is set to be one wavelength of the linear wave for shorter waves and eight times the typical dimension of the body for longer waves. This method has been extended to 2D fully nonlinear wave simulations by Kashiwagi (1996).

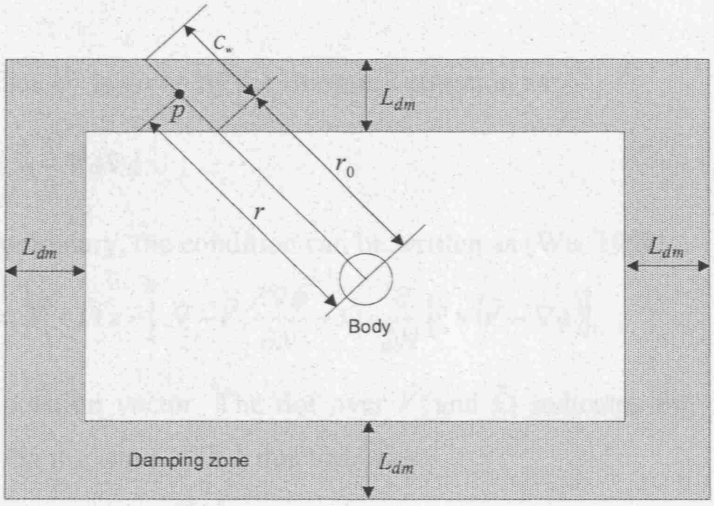

Figure 3.3.7 Damping zone on the free surface

The damping zone method is simple but efficient. Its disadvantage is that an extra domain is needed in the computation. Sometimes the Sommerfeld-Orlanski radiation condition and the artificial damping zone are combined together in numerical simulations (Tsai & Yue, 1996).

3.3.6 Calculation of hydrodynamic forces

In equations (2.6.3) and (2.6.4), the computation of integration of $(\frac{1}{2}|\nabla\phi|^2 + gz)$ on the body surface is not too difficult. There are however some problems with $\partial\phi/\partial t$. It may be calculated using the finite difference method. However, for fully nonlinear problems, this often causes instability and sawteeth in the force history may occur, especially in the case of large amplitude motion. In order to avoid this behaviour, we use the method developed by Wu & Eatock Taylor (1996, 2003) to compute the

hydrodynamic forces, which circumvents the need for the derivative with respect to time directly. We summarise the method below.

We consider a numerical wave tank problem with a floating body in the tank. We denote the translational and angular velocity of the moving body as $\vec{V}$ and $\vec{\Omega}$ respectively. In the fluid domain, the time derivative ϕ_t satisfies the Laplace equation

$$\nabla^2\phi_t = 0. \tag{3.3.36}$$

On the fixed boundary it satisfies

$$\frac{\partial\phi_t}{\partial N} = 0. \tag{3.3.37}$$

On the free surface ϕ_t is given by the Bernoulli equation as

$$\phi_t = -gz - \frac{1}{2}\nabla\phi\nabla\phi \ . \tag{3.3.38}$$

On the moving boundary, the condition can be written as (Wu, 1998)

$$\frac{\partial}{\partial N}(\phi_t) = \left[\dot{\vec{V}} + \dot{\vec{\Omega}}\times\vec{r}\right]\cdot\vec{N} - \vec{V}.\frac{\partial\nabla\phi}{\partial N} + \vec{\Omega}\cdot\frac{\partial}{\partial N}\left[\vec{r}\times\left(\vec{V} - \nabla\phi\right)\right], \tag{3.3.39}$$

where $\vec{r}$ is the position vector. The dot over $\vec{V}$ and $\vec{\Omega}$ indicates the derivatives with respect to time. On the wave maker this becomes

$$\frac{\partial}{\partial N}(\phi_t) = \dot{\vec{V}}_0\cdot\vec{N} - \vec{V}_0.\frac{\partial\nabla\phi}{\partial N}, \tag{3.3.40}$$

where $\vec{V}_0$ is the velocity of the wave maker. If the accelerations in equation (3.3.37) are known, we can solve equations (3.3.36)~(3.3.40) to obtain ϕ_t, otherwise we may introduce some auxiliary functions $\chi_i (i = 1,2,\cdots,6)$, which satisfy the Laplace equation in the fluid domain

$$\nabla^2\chi_i = 0 \tag{3.3.41}$$

with the boundary condition

$$\frac{\partial\chi_i}{\partial N} = N_i \tag{3.3.42}$$

on the body surface and

$$\chi_i = 0 \tag{3.3.43}$$

on the free surface, where $N_i\ (i = 1,2,\cdots,6)$ are the components of $\vec{N}$ and $\vec{r}\times\vec{N}$. The condition on other boundaries is given as

$$\frac{\partial \chi_i}{\partial N} = 0 . \tag{3.3.44}$$

χ_i can then be obtained by solving equations (3.3.41)~(3.3.44). Using Green's identity $\iint_S (\phi_t \frac{\partial \chi_i}{\partial N} - \chi_i \frac{\partial \phi_t}{\partial N}) = 0$ and considering boundary conditions for ϕ_t in equations (3.3.37)~ (3.3.40), we obtain

$$\begin{aligned} \iint_{S_b} \frac{\partial \phi}{\partial t} N_i ds = & \iint_{S_b} \chi_i \{[\dot{\vec{V}} + \dot{\vec{\Omega}} \times \vec{r}] \cdot \vec{N} - \vec{V} \cdot \frac{\partial \nabla \phi}{\partial N} + \vec{\Omega} \cdot \frac{\partial}{\partial N} [\vec{r} \times (\vec{V} - \nabla \phi)]\} ds \\ & + \iint_{S_f} (\frac{1}{2} \nabla \phi \cdot \nabla \phi + gz) \frac{\partial \chi_i}{\partial N} ds + \iint_{S_w} (-\dot{V}_0 + V_0 \phi_{xx}) \chi_i ds. \end{aligned} \tag{3.3.45}$$

The hydrodynamic force on the body can finally be obtained as

$$\begin{aligned} F_i = & -\iint_{S_b} \{\nabla \chi_i [(\vec{V} + \vec{\Omega} \times \vec{r}) \cdot \vec{N}][\nabla \phi - (\vec{V} + \vec{\Omega} \times \vec{r})] + \chi_i (\vec{\Omega} \times \vec{V}) \cdot \vec{N}\} ds \\ & - \iint_{S_f + S_b} (\frac{1}{2} \nabla \phi \cdot \nabla \phi + gz) \frac{\partial \chi_i}{\partial N} ds + \iint_{S_w} (-\dot{V}_0 + V_0 \phi_{xx}) \chi_i ds \\ & - \sum_{j=1}^{6} C_{ij} A_j \qquad (i = 1,2,\cdots,6), \end{aligned} \tag{3.3.46}$$

where $C_{ij} = \iint_{S_b} \chi_i N_j ds$ and $A_j (j = 1,2,\cdots,6)$ are the acceleration components corresponding to the three translations and three rotations of the body. In this equation, there is an integration of second order derivative $\phi_{xx} \chi_i$ on the surface of the wave maker, and it may be calculated by the following equation

$$\begin{aligned} \iint_{S_w} \phi_{xx} \chi_i ds = & -\int_{-h}^{\eta} \int_{-B/2}^{B/2} \phi_{zz} \chi_i dz dy - \int_{-h}^{\eta} \int_{-B/2}^{B/2} \phi_{yy} \chi_i dz dy \\ = & \int_{-B/2}^{B/2} [-\phi_z \chi_i \Big|_{-h}^{\eta} + \int_{-h}^{\eta} \phi_z \frac{\partial \chi_i}{\partial z} dz] dy \\ & + \int_{-B/2}^{B/2} [-\phi_y \chi_i \Big|_{-B/2}^{B/2} + \int_{-B/2}^{B/2} \phi_y \frac{\partial \chi_i}{\partial y} dy] dz \\ = & \iint_{S_w} (\phi_z \frac{\partial \chi_i}{\partial z} + \phi_y \frac{\partial \chi_i}{\partial y}) ds, \end{aligned} \tag{3.3.47}$$

where B is the breadth of the tank. If the body is fixed, we may solve equations (3.3.36)~(3.3.40) to obtain ϕ_t and then the force. For a body in forced motion, although its acceleration is known, we still use equation (3.3.46) to calculate the force. This is because it may be inaccurate to calculate the second order derivative $\partial \nabla \phi / \partial n$ in equation (3.3.39), which can be avoided when equation (3.3.46) is used.

4. MESH GENERATION FOR FLARE STRUCTURES

4.1 Introduction

An essential part of CFD is the mesh generation. The fluid domain should be discretised when the finite element method is used. Two types of mesh are usually used: the structured mesh and the unstructured mesh. The latter is more suitable for complex fluid domains, and it has been successfully used in many areas such as car and plane design, heat conduction and fluid dynamics. However, the application of 3D unstructured meshes to simulations of fully nonlinear water waves presents a considerable challenge. The difficulty is mainly due to the fact that the boundary of the fluid domain including the free surface and the body surface is time-dependent. Meshes have to be generated regularly and so extensive computer resource is required. In this thesis, the mesh employed consists of 6-node prismatic elements. This mesh may be said to be semi-unstructured or semi-structured.

4.2 3D mesh generation

As mentioned in Wu & Hu (2004), a fully 3D grid generator is usually too computationally intensive for this problem, especially when a typical simulation would allow only a few minutes of CPU at each time step. Thus, they adopted a 2D method for cylindrical structures. The mesh is first obtained through the tri-tree method on a horizontal plane and the 3D mesh is then generated by drawing straight lines in the vertical direction. The procedure is efficient but it does not allow variation of cross section in the vertical direction [see Figure 4.2.1(a)], even though the shape of the section can be arbitrary.

When the body is not cylindrical or it has a flare [see figure 4.2.1(b)], substantial change in mesh generation is required. For a cylindrical structure, the projection of the waterline on the free surface will remain the same if the body is in translation only. For a flared structure, the projection will vary considerably. We summarise the mesh generation procedure for a flared structure below.

The wavy free surface is first projected on to the horizontal plane, and a 2D unstructured mesh is generated on the plane. A 2D mesh generator called BAMG

(Hecht, 1998) which is based on the Delaunay algorithm is used here. One of its advantages is that it is less computational intensive than the tri-tree algorithm by Hu *et al.*(2002). A typical triangular mesh generated by BAMG is shown in Figure 4.2.2(a). The mesh generator can also handle holes of arbitrary shape in the domain as shown in Figure 4.2.2(b). Furthermore, BAMG can make a local refinement and Lapacian smoothing. Its preparation of data input is simple, which needs the nodes and element numbers on all boundaries only. A 2D mesh for a circle generated by this method is shown in Figure 4.2.3.

For a flared cylinder, it may seem that the body is a small variation from that without flare in shape. However, the flare will lead to more complexities in mesh generation, and more attention should be paid to handling the intersection line between the free surface and the cylinder. Unlike the situation of a wall-sided cylinder, the shape of the projected waterline of a flared cylinder on the plane changes with time. It can be non-circular for a cylindrical structure. The nodes on the curve need rearranging before the new 2D mesh is generated.

A curve is then drawn from the nodes of the 2D mesh along the depth to form the 3D mesh. We use prism elements instead of tetrahedral elements here. One of the advantages of this element is that its index system is much simpler for this problem. This mesh is therefore semi-unstructured since the mesh is unstructured in the horizontal direction and structured in the vertical direction.

A 3D mesh with prism elements is shown in Figure 4.2.4. The surface mesh around the cylinder is shown in Figure 4.2.5(a).

A 3D mesh for a truncated cylinder with flare is shown in Figure 4.2.5(b), which requires further steps. The 2D mesh on planes below the cylinder consists of two parts: one is obtained from the extension of the 2D mesh on the free surface [Figure 4.2.6(a)], and the other is the 2D mesh generated inside the bottom of the cylinder [Figure 4.2.6(b)]. The two meshes are joined together to form the 2D mesh on all planes below the cylinder [Figure 4.2.6(c)]. Attention should be paid to the index system when the two meshes are combined together.

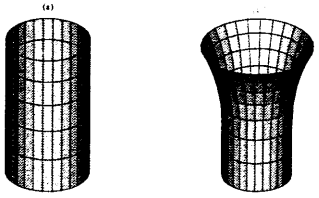

Figure 4.2.1 Cylinders (a) without flare and (b) with flare

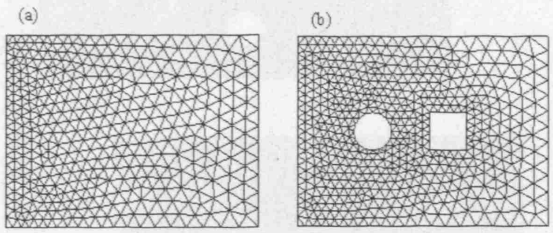

Figure 4.2.2 2D Meshes by BAMG

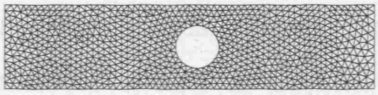

Figure 4.2.3 2D unstructured mesh for a circle

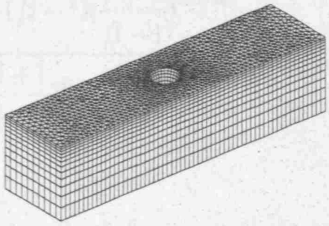

Figure 4.2.4 3D mesh for a cylinder

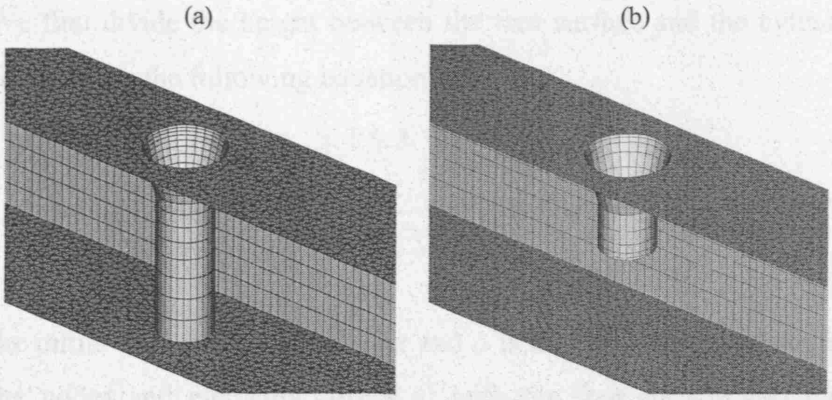

Figure 4.2.5 Bottom mounted and truncated cylinders

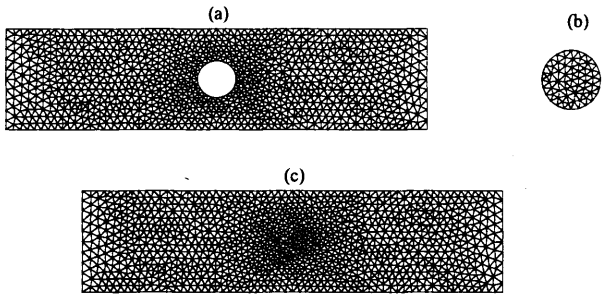

Figure 4.2.6 Combination of two unstructured meshes

When the 3D mesh is constructed, we usually divide the depth of the fluid domain into many layers. The elements should be clustered near the free surface where the fluid motion is largest. We may use the following equation (Chung, 2002) to achieve this

$$z_i = \eta - (h+\eta)\frac{(\beta+1)-(\beta-1)(\frac{\beta+1}{\beta-1})^{1-i/m}}{(\frac{\beta+1}{\beta-1})^{1-i/m}+1} \quad (i=0,1,\cdots,m), \qquad (4.2.1)$$

where z_i is the vertical coordinate of i-th layer, η the wave elevation, h the depth of the fluid domain, m the number of layers along the depth, and β>1 is a constant. A smaller value of β will lead the nodes and elements to cluster at the top of the domain and a larger β will have the nodes and elements more uniformly distributed in the vertical direction (Figure 4.2.7).

Equation (4.2.1) suits for bottom mounted cylinders. For truncated cylinders, we take two steps. We first divide the height between the free surface and the cylinder bottom into m_1 intervals using the following equation

$$z_i = \eta - (d+\eta)\frac{(2\alpha+\beta)(\frac{\beta+1}{\beta-1})^{\frac{i/m_1-\alpha}{1-\alpha}}+2\alpha-\beta}{(2\alpha+1)[(\frac{\beta+1}{\beta-1})^{\frac{i/m_1-\alpha}{1-\alpha}}+1]} (i=0,1,\cdots,m_1), \qquad (4.2.2)$$

where d is the initial drought of the cylinder and α is another constant. Equation (4.2.2) can make the nodes and elements cluster at both the free surface and the cylinder bottom. The influence of β and α on the distribution of nodes is depicted in Figure 4.2.8. The vertical distribution of layers for the truncated cylinder with β=1.05 and α=0.5 for the layers between the cylinder bottom and the tank bottom is shown in Figure 4.2.5(b).

We then divide the height between the cylinder bottom and the tank bottom into m_2 layers using equation (4.2.1) by replacing η with $-d$, we rewrite it as follows

$$z_i = -d - (h-d)\frac{(\beta+1)-(\beta-1)(\frac{\beta+1}{\beta-1})^{1-i/m_2}}{(\frac{\beta+1}{\beta-1})^{1-i/m_2}+1} \quad (i=0,1,\cdots,m_2). \qquad (4.2.3)$$

A test on β is taken in a 3D numerical wave tank with a bottom mounted cylinder without flare inside. There are 14 layers in the vertical direction. The waves at the front side of the cylinder with two motion amplitudes of the wave maker are shown in Figure 4.2.9. Equation (4.2.1) is used to control the nodes distribution along the vertical direction. Three values of β 1.02, 1.05 and 1.08 are tested. The element near the free surface should be smaller than those away from the free surface, which requires a smaller value of β. However, the size of the element should gradually but not abruptly increase from the free surface to the tank bottom. Relatively, a very small β leads the elements neighbouring the free surface to be much smaller and the element far from the free surface much larger, and this may cause numerical errors such as overflow. A compromise with β =1.05 will be taken in this thesis.

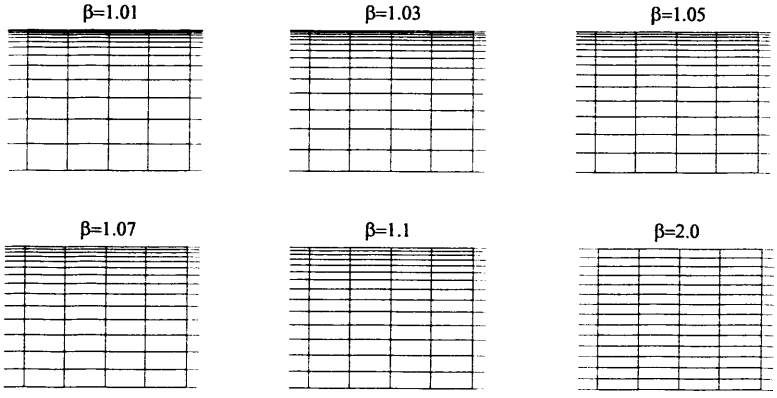

Figure 4.2.7 Influence of β

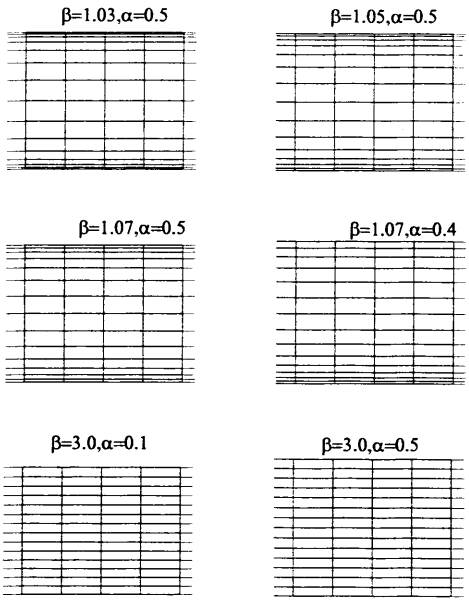

Figure 4.2.8 Influence of β and α

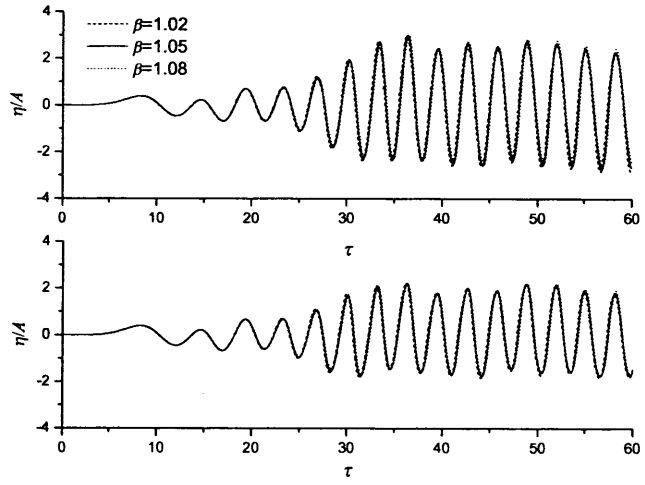

Figure 4.2.9 Waves at the front side of the cylinder
(a) A/h=0.01; (b) A/h=0.03

It should be mentioned that a zone of structured mesh [Figure 4.2.10(a)] near the wave maker may usually be combined with the unstructured mesh to form a hybrid mesh as shown in Figure 4.2.11. One reason of its presence is due to the transverse stability discussed by Wu, Ma & Eatock Taylor (1996). They found that the stability depends very much on the mesh structure used near the wave maker. The structured mesh may improve the numerical stability. It should also be noticed the structured mesh is symmetric about y=0. A symmetric mesh should be more stable than an asymmetric mesh [Figure 4.2.10(b)] when they are used in free surface problems, and this is confirmed by Robertson & Sherwin (1999) when they studied 2D free surface flow

problems. They found that the asymmetric mesh caused some saw teeth on the free surface. The 3D mesh based on this hybrid mesh is shown in Figure 4.2.12.

In this thesis, we also consider the interactions of waves and multiple cylinders. The mesh generation for multi-cylinder cases requires slightly more work on the input information of the boundary than that for a single-cylinder but it will be much more complex if the structured mesh is used. The meshes on seven bottom-mounted and truncated cylinders in a line are given in Figures 4.2.13 and 4.2.14.

(a) (b)

Figure 4.2.10 2D structured mesh

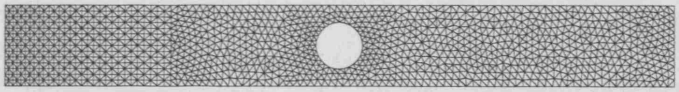

Figure 4.2.11 2D hybrid mesh

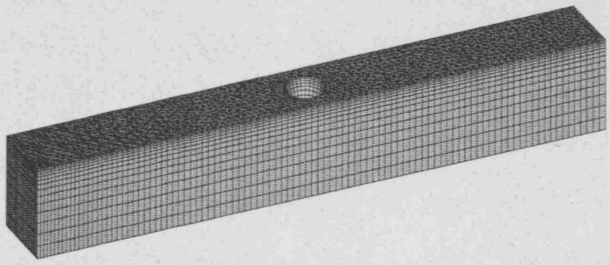

Figure 4.2.12 3D mesh for a cylinder

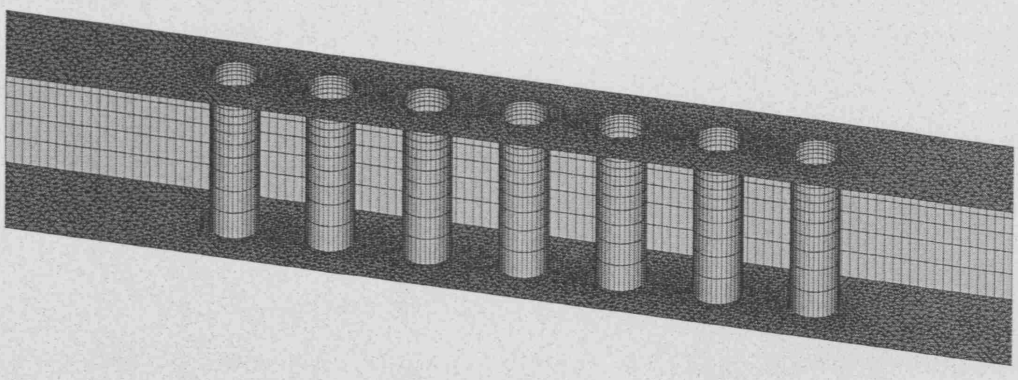

Figure 4.2.13 Seven bottom-mounted cylinders

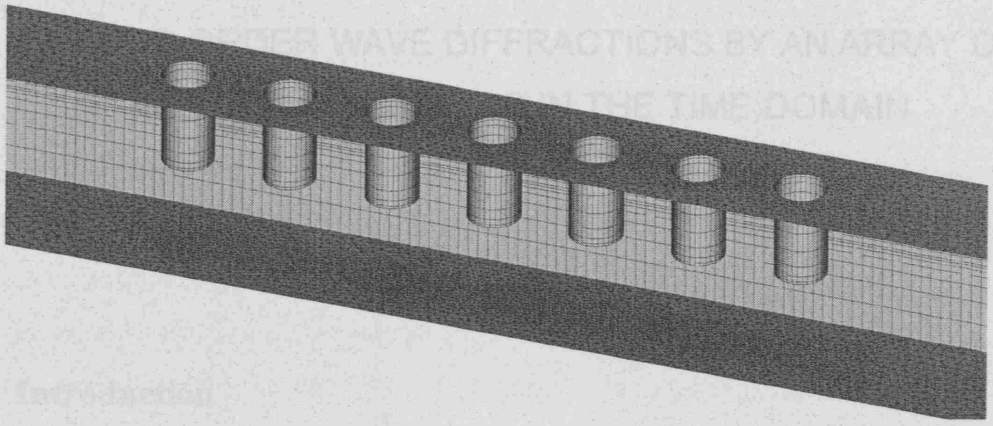

Figure 4.2.14 Seven truncated cylinders

5. SECOND ORDER WAVE DIFFRACTIONS BY AN ARRAY OF VERTICAL CYLINDERS IN THE TIME-DOMAIN

5.1 Introduction

We now move on to the validation and application of the numerical method described in the previous chapters. A few types of problem will be investigated: wave diffraction and radiation for multiple cylinders in open seas and transient waves generated by wave makers in tanks in two- and three-dimensions. In this chapter, we consider the interaction of second order waves and multiple cylinders in the time-domain.

One of the interesting problems in wave-body interactions is an array of vertical cylinders in an incoming wave. This configuration has a wide range of applications, such as bridges and floating airports. Maniar & Newman (1997) considered linear diffraction by an array of 101 cylinders. They found that when the wave number was close to the trapped mode (Ursell, 1951), very large hydrodynamic forces could occur on the cylinders in the middle. Evans & Porter (1997a) also showed that very large force could occur for a small number of cylinders, such as four, especially when they were quite close to each other. Malenica *et al.* (1999) further showed that similar behaviour could occur for the second order result. The wave number for the first order problem chosen by them was far away from the trapped mode and the linear result did not exhibit any unusual behaviour. The corresponding wave number for the second order problem was, however, quite near the trapped mode. As a result, some of the second order results were found to be abnormally large. Other investigations on an array of cylinders include those by Kashiwagi & Ohwatari (2002) and Ohl *et al.* (2001).

The work mentioned above is all based on the frequency domain method. The present work is to use the time domain method to analyse the first and second order wave diffraction by a group or an array of cylinders. One of the advantages of the time domain method is that it can easily capture the transient effect if the motion is not periodic. From the computational point of view, as the domain in the perturbation method is fixed, the global coefficient matrix needs to be worked out only once. This

can then be used at all the time steps during the simulation and be used at any frequency for the periodic motions. The time domain problem is usually solved by the boundary element method (BEM) through two schemes. The first one is to use a Green function which satisfies the free surface boundary condition. As a result, the differential equation can be converted into an integral equation. A typical example of this is the work by Beck *et al.* (1987). Unlike the frequency domain method however, the integral equation contains a term of convolution which includes all the information prior to the current instant, or the memory effect. As time progresses, the memory effect can become too big for practical computation. The other scheme in the time domain method is to use the Rankin source. The Green function in this case does not satisfy the free surface boundary condition and the source distribution is required on the free surface. Typical examples of this scheme include those by Isaacson & Cheung (1990, 1991, 1992) on the second order wave diffraction problems by a single cylinder. The advantage of the Rankin source method is that it removes the explicit memory effect from the equation. Its disadvantage is that it requires sources all over the free surface. As the matrix is fully populated, the storage requirement can also be very big. In the present work, we use the finite element method (FEM). As discussed in Chapter 1, even though the FEM has more unknowns, it corresponds to smaller memory requirement because its matrix is banded. For this reason, it has been widely used in a variety of fully nonlinear problems in the time domain (Wu *et al.* 1998, Ma, *et al.* 20001a, b, Hu, *et al.* 2002, Wu & Hu 2004) and is found to be very effective. Wang & Khoo (2005) simulated fully nonlinear random sloshing problems and the second order results based on the finite element method were also provided for comparison.

Simulation is made first for two cylinders to investigate the effect of the interaction through the comparison with the single cylinder case. Numerical results are provided for both the wave elevation and the force. Simulation is then made for four cylinders, and for both bottom mounted and truncated cylinders. The effect of the trapped mode on the first- and the second-order results is investigated. Simulation is also made for an array of ten cylinders in a line and a double array of eight cylinders in two lines.

5.2 Mathematical formulation for second order diffraction problems

The mathematical formulation of fully nonlinear wave-body interactions has been presented in Chapter 2, and the description of radiation problems based on the second order theory has also been given in the chapter. In this chapter, we first give the mathematical formulation of second order diffraction problems. The Sketch for multi-cylinder is depicted in Figure 5.2.1. In the figure, S_c is the artificial boundary surface, on which a suitable radiation condition should be imposed. A difference of the diffraction problem from the radiation problems is that the normal velocity on the body surface S_b is zero

$$\frac{\partial \phi}{\partial N} = 0 \quad \text{on} \quad S_b . \tag{5.2.1}$$

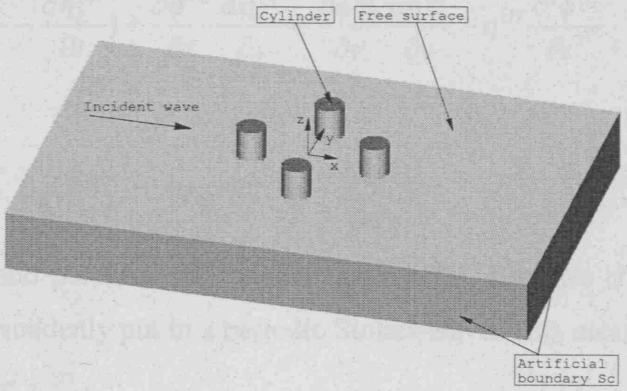

Figure 5.2.1 A sketch of the problem

Based on the second order theory, the velocity potential and wave elevation can be expressed in the first- and second-order components [see equations (2.5.5) and (2.5.6)] using the perturbation expansion procedure. The components of the potential and the wave are further split into the known incident potential $\phi_I^{(k)}$ and wave $\eta_I^{(k)}$, and the unknown diffracted potential $\phi_D^{(k)}$ and wave $\eta_D^{(k)}$, respectively

$$\phi = \varepsilon(\phi_I^{(1)} + \phi_D^{(1)}) + \varepsilon^2(\phi_I^{(2)} + \phi_D^{(2)}) + \cdots, \tag{5.2.2}$$

$$\eta = \varepsilon(\eta_I^{(1)} + \eta_D^{(1)}) + \varepsilon^2(\eta_I^{(2)} + \eta_D^{(2)}) + \cdots. \tag{5.2.3}$$

Similar to the second-order radiation problem given in Chapter 2, the mathematical formulation of the second-order diffraction problem can be derived. The governing equations for $\phi_D^{(k)}$ become

$$\nabla^2 \phi_D^{(k)} = 0 \qquad \text{in} \quad \forall^{(0)}, \tag{5.2.4}$$

and is subject to the boundary conditions applied on the still water surface, the mean body surface, and the seabed, given respectively as

$$\frac{\partial \phi_D^{(k)}}{\partial z} - \frac{\partial \eta_D^{(k)}}{\partial t} = f_k' \qquad \text{on } S_f^{(0)}, \tag{5.2.5}$$

$$\frac{\partial \phi_D^{(k)}}{\partial t} + g\eta_D^{(k)} = f_k'' \qquad \text{on } S_f^{(0)}, \tag{5.2.6}$$

$$\frac{\partial \phi_D^{(k)}}{\partial n} = -\frac{\partial \phi_I^{(k)}}{\partial n} \qquad \text{on } S_b^{(0)}, \tag{5.2.7}$$

$$\frac{\partial \phi_D^{(k)}}{\partial z} = 0 \qquad \text{on } z = -h\ . \tag{5.2.8}$$

The terms f_k' and f_k'' in these equations can be written as

$$f_1' = 0,$$

$$f_2' = -\left(\frac{\partial \phi_I^{(2)}}{\partial z} - \frac{\partial \eta_I^{(2)}}{\partial t}\right) + \frac{\partial \phi^{(1)}}{\partial x}\frac{\partial \eta^{(1)}}{\partial x} + \frac{\partial \phi^{(1)}}{\partial y}\frac{\partial \eta^{(1)}}{\partial y} - \eta^{(1)}\frac{\partial^2 \phi^{(1)}}{\partial z^2},$$

$$f_1'' = 0,$$

$$f_2'' = -\left(\frac{\partial \phi_I^{(2)}}{\partial t} + g\eta_I^{(2)}\right) - \frac{1}{2}\left|\nabla \phi^{(1)}\right|^2 - \eta^{(1)}\frac{\partial^2 \phi^{(1)}}{\partial z \partial t}\ .$$

The incident wave and potential are transient in general. Here we consider the case in which a structure is suddenly put in a periodic Stokes wave. This means

$$\begin{aligned}\eta_I &= \varepsilon \eta_I^{(1)} + \varepsilon^2 \eta_I^{(2)} \\ &= \frac{H}{2}\cos k_0(x - ct) \\ &\quad + \left(\frac{H}{2}\right)^2 \frac{k_0}{4}\frac{\cosh k_0 h(\cosh 2k_0 h + 2)}{\sinh^3 k_0 h}\cos 2k_0(x - ct)\end{aligned}, \tag{5.2.9}$$

$$\begin{aligned}\phi_I &= \varepsilon \phi_I^{(1)} + \varepsilon^2 \phi_I^{(2)} \\ &= \frac{H}{2}c\frac{\cosh k_0(z + h)}{\sinh k_0 h}\sin k_0(x - ct) \\ &\quad + \frac{3}{8}\left(\frac{H}{2}\right)^2 k_0 c\frac{(\cosh 2k_0(z + h)}{\sinh^4 k_0 h}\sin 2k_0(x - ct)\end{aligned}, \tag{5.2.10}$$

where H is the wave height, c the wave celerity, k_0 the wavenumber, h is the water depth, and $\omega = k_0 c$ is obviously the frequency and is also linked to the wave number through $k_0 \tanh k_0 h = \omega^2/g$.

For second order problems, the hydrodynamic forces on the cylinder can be expressed as

$$F_j = \iint_{S_b^{(0)}} p n_j ds + \frac{1}{2}\rho g \oint_{WL} (\eta^{(1)})^2 n_j dl \quad (j = 1,2,\cdots,6), \tag{5.2.11}$$

where p is the pressure up to second order. The normal vector $(n_1, n_2, n_3, n_4, n_5, n_6) = (n_x, n_y, n_z, yn_z - zn_y, zn_x - xn_z, xn_y - yn_x)$, $j = 1,2,3$ corresponding to the force and $j = 4,5,6$ to the moment. The total force on the cylinder may be expressed as a sum of three components: the first order oscillatory force $F_j^{(1)}$, the second order oscillatory force $F_j^{(2)}$ and the second order mean force $\overline{F}_j^{(2)}$. The first order oscillatory force is given as

$$F_j^{(1)} = -\rho \iint_{S_b^{(0)}} \frac{\partial \phi^{(1)}}{\partial t} n_j ds \quad (j = 1,2,\cdots,6). \tag{5.2.12}$$

The second order oscillatory force may be expressed as

$$F_j^{(2)} = F_j^{(21)} + F_j^{(22)} - \overline{F}_j^{(2)} \quad (j = 1,2,\cdots 6), \tag{5.2.13}$$

where $F_j^{(21)}$ and $F_j^{(22)}$ are the second order force components due to the first- and second-order potentials respectively, and they are defined as

$$F_j^{(21)} = -\frac{1}{2}\rho \iint_{S_b^{(0)}} \left|\nabla \phi^{(1)}\right|^2 n_j ds + \frac{1}{2}\rho g \int_{WL} (\eta^{(1)})^2 n_j dl \quad (j = 1,2,\cdots,6), \tag{5.2.14}$$

$$F_j^{(22)} = -\rho \iint_{S_b^{(0)}} \frac{\partial \phi^{(2)}}{\partial t} n_j ds \quad (j = 1,2,\cdots,6). \tag{5.2.15}$$

By time averaging equation (5.2.14) over one period when the problem has become periodic, we obtain the second order mean force

$$\overline{F}_j^{(2)} = -\frac{1}{2}\rho \overline{\iint_{S_b^{(0)}} \left|\nabla \phi^{(1)}\right|^2 n_j ds} + \frac{1}{2}\rho g \overline{\int_{WL} (\eta^{(1)})^2 n_j dl} \quad (j = 1,2,\cdots,6). \tag{5.2.16}$$

5.3 Computational considerations

5.3.1 Meshes for multi-cylinders

As presented in Chapter 4, the 2D mesh generator BAMG (Hecht, 1998) is used to generate a 2D unstructured mesh on the plane first (see Figure 5.3.1). It is then extended along the vertical direction to form the 3D mesh with prismatic elements (see Figure 5.3.2). When equations (4.2.1) and (4.2.2) are used to divide the water depth into many

layers, the wave elevations η in them are zero since the second order problem is considered on the mean water level.

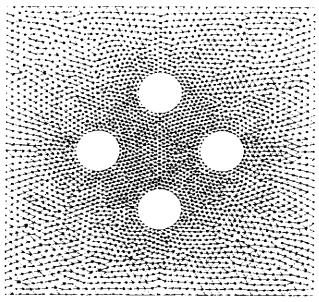

Figure 5.3.1 A 2D unstructured mesh for four circles

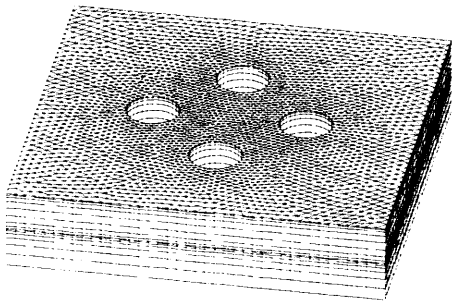

Figure 5.3.2 A 3D mesh for four truncated cylinders

5.3.2 Computations of derivatives in time and space

In equation (5.2.6), we need to calculate the derivative $\frac{\partial^2\phi^{(1)}}{\partial z\partial t}$. We first calculate velocity $(\frac{\partial\phi}{\partial x},\frac{\partial\phi}{\partial y},\frac{\partial\phi}{\partial z})$ using equations (3.3.2a) and (3.3.2c) since we only consider wall-sided structures. The Galerkin method may be an alterative, but the former will need much less time. We then use a back difference formula to obtain the derivative $\frac{\partial^2\phi^{(1)}}{\partial z\partial t}$

$$\frac{\partial^2\phi^{(1)}}{\partial z\partial t}=\frac{\partial}{\partial t}(\frac{\partial\phi^{(1)}}{\partial z})=(\frac{\partial\phi^{(1)}(t)}{\partial z}-\frac{\partial\phi^{(1)}(t-\Delta t)}{\partial z})/\Delta t. \qquad (5.3.1)$$

For the second order derivative $\partial^2\phi/\partial^2 z$, equation (3.3.2b) is utilised. The two spatial derivatives $\partial\eta^{(1)}/\partial x$ and $\partial\eta^{(1)}/\partial y$ in equation (5.2.5) may also be obtained through equation (3.3.2c) by replacing the potential ϕ with the first-order wave elevation $\eta^{(1)}$.

5.3.3 Computations of velocity on the surface of cylinders

When using equation (5.2.14) to obtain the second order force, we need to calculate the integration of the square of velocity $|\nabla\phi|^2$ over the body surface. We may have two approaches to calculate the integration. One is to directly evaluate the integration, in which the velocity at all nodes on the body surface is needed; the other one is to calculate the integration based on the shape function, in which only the potential is needed. We will adopt the latter. The velocity in an element may be obtained from the following equation

$$\begin{bmatrix} \frac{\partial\phi}{\partial x} \\ \frac{\partial\phi}{\partial y} \\ \frac{\partial\phi}{\partial z} \end{bmatrix} = \begin{bmatrix} \frac{\partial x}{\partial\xi} & \frac{\partial y}{\partial\xi} & \frac{\partial z}{\partial\xi} \\ \frac{\partial x}{\partial\eta} & \frac{\partial y}{\partial\eta} & \frac{\partial z}{\partial\eta} \\ n_x & n_y & n_z \end{bmatrix}^{-1} \begin{bmatrix} \frac{\partial\phi}{\partial\xi} \\ \frac{\partial\phi}{\partial\eta} \\ \frac{\partial\phi}{\partial n} \end{bmatrix}, \tag{5.3.2}$$

where (ξ,η) is a local coordinate corresponding to a global coordinate (x,y,z), which is the node coordinates of the quadrilateral element on the body surface, (n_x,n_y,n_z) is the outside normal vector and $\frac{\partial\phi}{\partial n}$ is the normal velocity at (x,y,z). The derivatives of x, y, z and ϕ with respect to ξ and η can be easily obtained through the shape function in an element with n nodes

$$\begin{aligned} \frac{\partial q}{\partial\xi} &= \sum_{i=1}^{n} \frac{\partial N_i}{\partial\xi} q_i \\ \frac{\partial q}{\partial\eta} &= \sum_{i=1}^{n} \frac{\partial N_i}{\partial\eta} q_i \end{aligned}, \tag{5.3.3}$$

where q denotes the coordinates x, y, z or potential ϕ. The normal vector can be calculated by the following equations

$$n_x = \frac{|J_1|}{|J|}, n_y = \frac{|J_2|}{|J|}, n_z = \frac{|J_3|}{|J|}, \tag{5.3.4}$$

where

$$|J_1| = \frac{\partial y}{\partial\xi}\frac{\partial z}{\partial\eta} - \frac{\partial z}{\partial\xi}\frac{\partial y}{\partial\eta},$$

$$t|J_2| = \frac{\partial z}{\partial \xi}\frac{\partial x}{\partial \eta} - \frac{\partial x}{\partial \xi}\frac{\partial z}{\partial \eta},$$

$$|J_3| = \frac{\partial x}{\partial \xi}\frac{\partial y}{\partial \eta} - \frac{\partial y}{\partial \xi}\frac{\partial x}{\partial \eta},$$

$$|J| = (|J_1|^2 + |J_2|^2 + |J_2|^2)^{\frac{1}{2}}.$$

5.3.4 Numerical radiation conditions

For long time simulations, an appropriate numerical radiation condition should be imposed on the boundary S_c. We used a combination of the Sommerfeld-Orlanski radiation condition and the damping zone method to absorb reflection waves. The discretised Sommerfeld-Orlanski radiation condition equations (3.3.29) and (3.3.30) are used. It should be noticed that points $\vec{x}_1$ and $\vec{x}_2$ are generally not the nodes of the mesh, and they are obtained through interpolation.

We adopt the damping zone method in Nakos *et al.* (1993). This method has been given in equations (3.3.34) and (3.3.35). Nakos *et al.* (1993) used it in linear wave problems, and we now extend it to our second order simulations and they may expressed as

$$\frac{\partial \eta^{(k)}}{\partial t} = \frac{\partial \phi^{(k)}}{\partial z} - f_k' - 2\nu\eta^{(k)} + \frac{\nu^2}{g}\phi^{(k)} \quad (k=1,2) \quad \text{on } S_f^{(0)}, \tag{5.3.5}$$

$$\frac{\partial \phi^{(k)}}{\partial t} = -g\eta^{(k)} + f_k'' \quad (k=1,2) \quad \text{on } S_f^{(0)}, \tag{5.3.6}$$

where $f_k', f_k''(k=1,2)$ are the same as those in equations (5.2.5) and (5.2.6) for the diffraction problem and the same as those in equations (2.5.16) and (2.5.17) for the radiation problem, respectively.

5.3.5 Modulation/ramp function

In order to let the diffracted wave develop gradually, we applied a modulation function $M(t)$ in equation (5.2.7) (Isaacson & Cheung, 1992)

$$\frac{\partial \phi_D^{(k)}}{\partial n} = -M(t)\frac{\partial \phi_I^{(k)}}{\partial n} \quad (k=1,2), \tag{5.3.7}$$

where

$$M(t)=\begin{cases}\frac{1}{2}[1-\cos(\frac{\pi t}{T})] & t<T\\ 1 & t\geq T\end{cases}$$

and $T=2\pi/\omega$ is the period of the first order incident wave. The modulation function is necessary for the development of the wave and force with time. A comparison between results with and without the modulation function is shown in Figure 5.3.3. The first- and second-order diffracted waves for a single cylinder are depicted in the figure. It is clearly seen that the first order wave without the modulation function is not good and the second order wave is very bad. The modulation function has a tremendous influence on the second order wave.

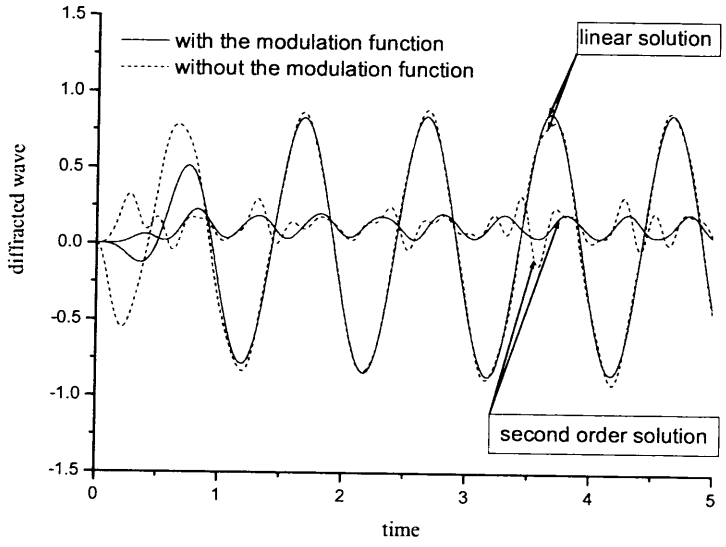

Figure 5.3.3 Comprasion of waves between with and without modulation function

5.4 Simulations for single-cylinder case

Before simulating multi-cylinder cases, we first consider the diffraction by a single isolated cylinder to verify the accuracy of the present numerical method. A case with k_0a=1, h=a and H/λ=0.1 is considered here (a is the radius of the cross section of cylinder and λ the wave length of the first order incident wave). The same case was also studied by Isaacson & Cheung (1992) and their results are used for comparison. The wave histories at the front and the back sides of the cylinder are shown in Figure 5.4.1, in which A denotes the amplitude of the first order incident wave and hereinafter for the subsequent figures. It is seen that the waves develop well. The amplitude of the first order wave and the maximum of the linear plus second order wave at the front side are

about 1.75 and 2.67 times the incident wave amplitude, respectively, which are in very good agreement with the results at ka=1 in Figure 5.4.2 given by Isaacson & Cheung (1992). The force and moment shown in Figure 5.4.3 are also in very good agreement both in amplitude and phase compared with those in Figure 5.4.4 given by Isaacson & Cheung (1992). A further comparison between second order forces obtained through the present method and the frequency-domain results by Eatock & Hung (1987) at different frequencies is given in Figure 5.4.5, which further confirms that the present numerical method is accurate.

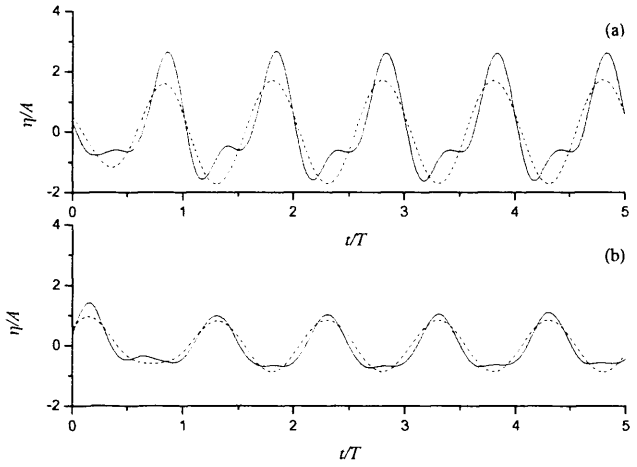

Figure 5.4.1 Wave histories at the front and back sides of the cylnider
(a) Front; (b) back
····· Linear; —— linear plus second order

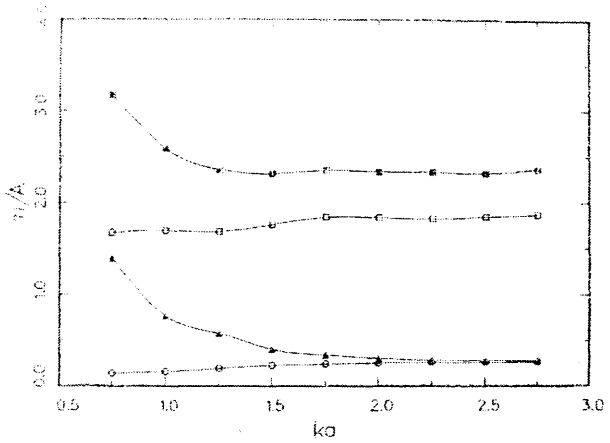

Fig 5.4.2 Wave amplitudes at the front of the cylinder versus the nondimensional wavenumber (Isaacson & Cheung, 1992)

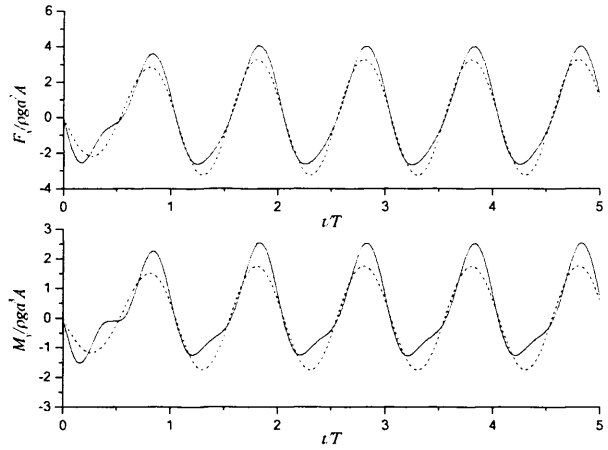

Figure 5.4.3 Histories of force and moment
····· Linear; —— linear plus second order

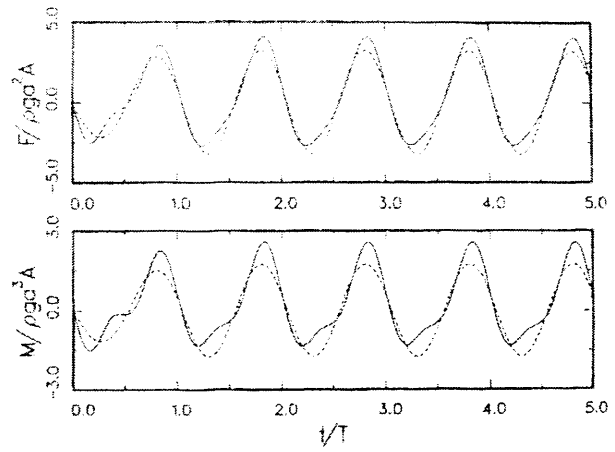

Figure 5.4.4 Histories of forces and moment ((Isaacson & Cheung, 1992)

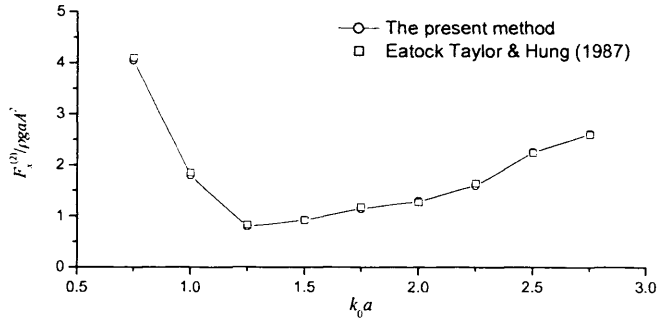

Figure 5.4.5 The amplitude of the total second order force versus $k_0 a$

5.5 Simulations for two- and three-cylinder cases

In all the simulation from this section, the cylinders are identical and all have radius a. The water depth is taken as $3a$. The ratio of the wave height to wavelength is taken is H/λ=0.05 and $A = H/2$.

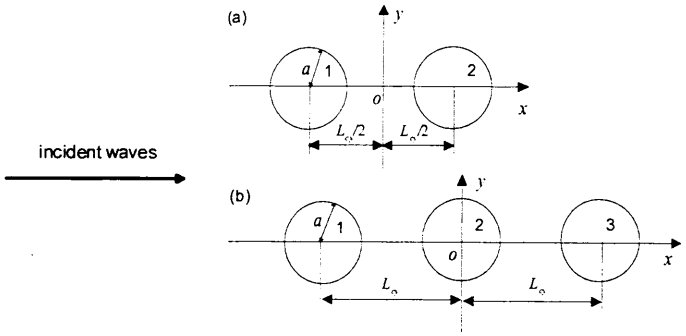

Figure 5.5.1 Two- and three-cylinder cases

A two cylinder configuration is the simplest multi-cylinder case. Figure 5.5.1(a) shows that two bodies are placed along the line of the wave direction. The centres of the two cylinders are located at $(-L_{cy}/2,0)$ and $(L_{cy}/2,0)$. The simulation corresponds to $L_{cy} = 4a$ and $k_0 a = 0.754$.

The convergence study is first undertaken. In this case, the fluid domain on the free surface is of rectangular shape with length $50a$ and width $40a$, which are divided into 60 and 50 intervals respectively. This corresponds to a mesh with 8706 nodes and 17122 triangular elements on the free surface. The waterline of one cylinder is divided into 36 uniform segments and the time step is taken as $\Delta t = T/200$. Three different vertical meshes with NH=10, 14 and 18 are used and their corresponding results for second order waves are shown in Figure 5.5.2. The three curves are in good agreement and the results at NH=14 and 18 are almost graphically identical. The simulation is made on a Pentium 4 personal computer with 3.40 GHz Intel CPU, windows XP system and Open Watcom C++ complier v1.1. The maximum memory is about 74 MB at NH=14 and 93 MB at NH=18. The CPU required is about 10 seconds per time step at NH=14 and 14 seconds at NH=18, respectively.

Convergence study is further undertaken with horizontal elements. The numbers of nodes and elements on the free surface used above have been increased to 15024 nodes and 29658 elements receptively. The simulation is performed with NH=14 and $\Delta t = T/200$. The results are shown in Figure 5.5.3, and the agreement from the two meshes is quite good. Convergence study is also undertaken with the time steps using $\Delta t = T/200$ and $\Delta t = T/400$ at NH=14. The result is shown in Figure 5.5.4 and the agreement is again quite good.

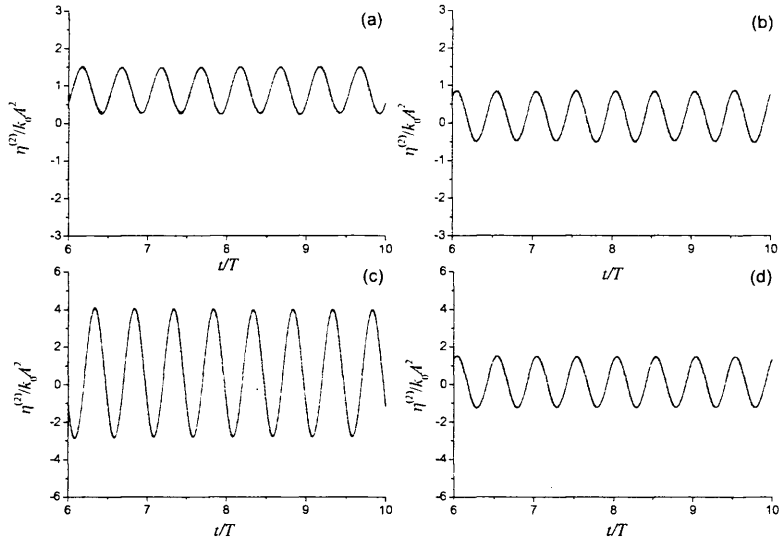

Fig. 5.5.2 Convergence of second order waves with mesh variation in vertical direction
(a) front side of cylnider one; (b) back side of cylnider one;
(c) front side of cylnider two; (d) back side of cylnider two
····· NH=10; —— NH=14; —— NH=18

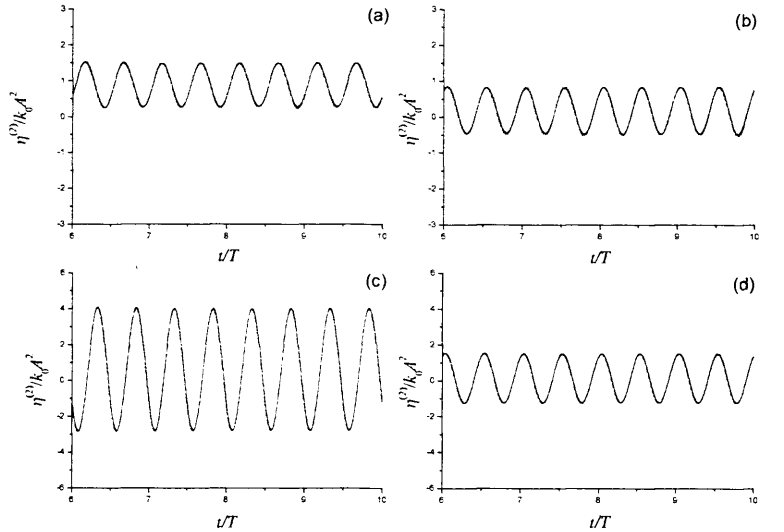

Figure 5.5.3 Convergence of second order waves with mesh variation in horizontal direction
(a) front side of cylnider one; (b) back side of cylnider one;
(c) front side of cylnider two; (d) back side of cylnider two
—— mesh with 15024 nodes and 29658 elements
····· mesh with 8706 nodes and 17122 elements

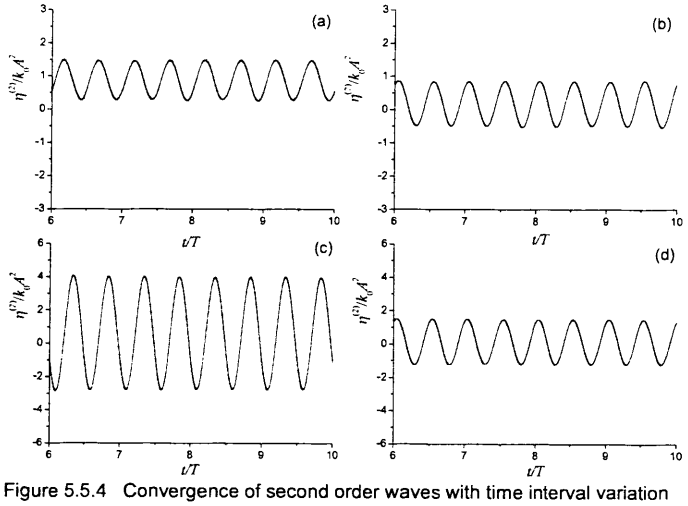

Figure 5.5.4 Convergence of second order waves with time interval variation
(a) front side of cylnider one; (b) back side of cylnider one;
(c) front side of cylnider two; (d) back side of cylnider two
····· Δt=T/200; —— Δt=T/400

Further comparisons between single- and two-cylinder cases at NH=14 and $\Delta t = T/200$ are made and results are included in Figs. 5.5.5 and 5.5.6. The single cylinder is placed at the location of cylinder 1 in Figure 5.5.5 and at the location of cylinder 2 in Figure 5.5.6. As the body surface boundary condition is modulated through $M(t)$, the wave runup becomes periodic after one wave period for the single cylinder case, as in Isaacson & Cheung (1992). The transition to periodic state, however, takes much longer in the two cylinder case, especially for the second order results, as can be seen from the figures. The interaction effect on the first order wave is evidently visible, but the major effect is on the second order. In fact, the amplitudes of the first order waves at both the front and the back sides of cylinder one are generally larger than those in the single-cylinder case and it is about 13% larger at the front side. However, the amplitudes of first order waves are slightly less than those in the single-cylinder case for cylinder two. It is also observed that the amplitude of $\eta^{(2)}$ at the front side of cylinder two is about 3.7 times that of a single cylinder. Generally, the first- and second-order waves between the two cylinders are affected by the existence of the other cylinder in both amplitude and phase, and the influence on the second order wave is even more evident.

The corresponding histories of the force and moment are shown in Figures 5.5.7 and 5.5.8. Similar to the wave runup, the results for the two-cylinder case take a longer time to become periodic, especially for the second order force and moment. The interference leads the first order force and moment to increase by 17% for cylinder one and decrease

by 10% for cylinder two compared with those in the single-cylinder case. For the second order force and moment, their mean values are greater than those in a single-cylinder case, in which the peaks of the force and moment cannot even reach these mean values. This indicates larger mean drift force and moment in the two-cylinder case. We can also observe that the second order force and moment on cylinder two have significant increase in amplitude. The total wave elevations and forces are shown in Figures 5.5.9 and 5.5.10. The linear solutions are also given in the two figures to show the nonlinearities of the waves and forces.

Besides difference in amplitudes, the phases of wave and force may be different from those in single-cylinder cases as shown in Figures 5.5.5~5.5.8.

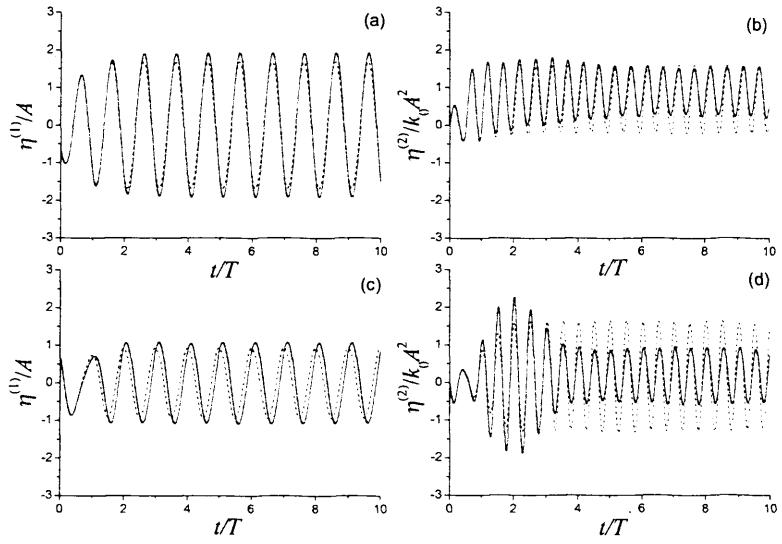

Figure 5.5.5 Wave histories for cylinder one at k_0a=0.754
(a) first order & (b) second order at the front side;
(c) first order & (d) second order at the back side
····· single-cylinder; —— two-cylinder

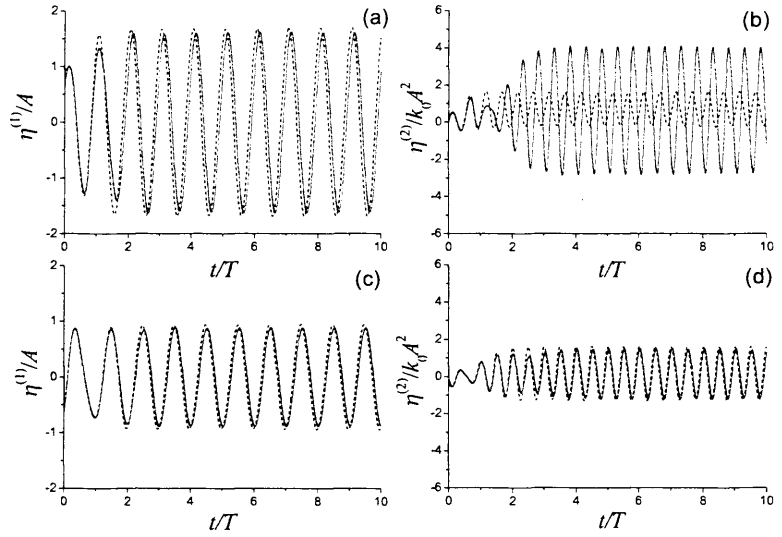

Figure 5.5.6 Wave histories for cylinder two at k_0a=0.754
(a) first order & (b) second order at the front side;
(c) first order & (d) second order at the back side
····· single-cylinder; —— two-cylinder

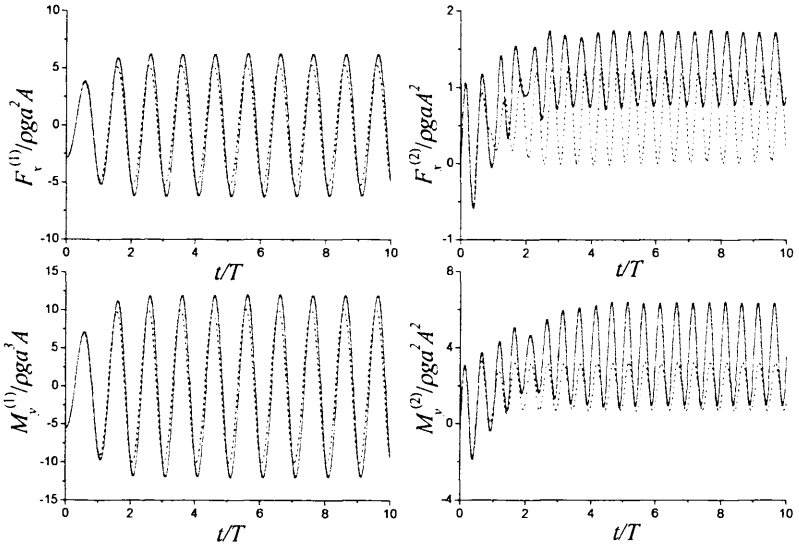

Figure 5.5.7 Histories of force and moment on cylinder one at k_0a=0.754
····· single-cylinder; —— two-cylinder

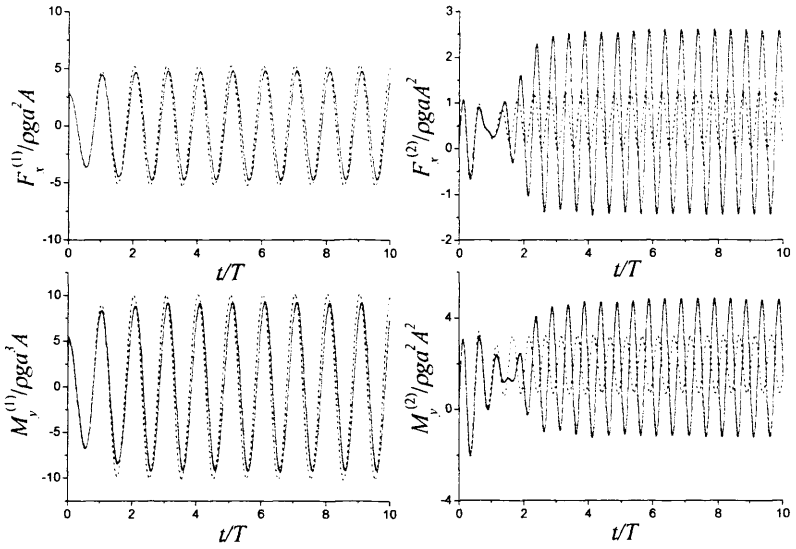

Figure 5.5.8 Histories of force and moment on cylinder two at $k_0 a$=0.754
····· single-cylinder; —— two-cylinder

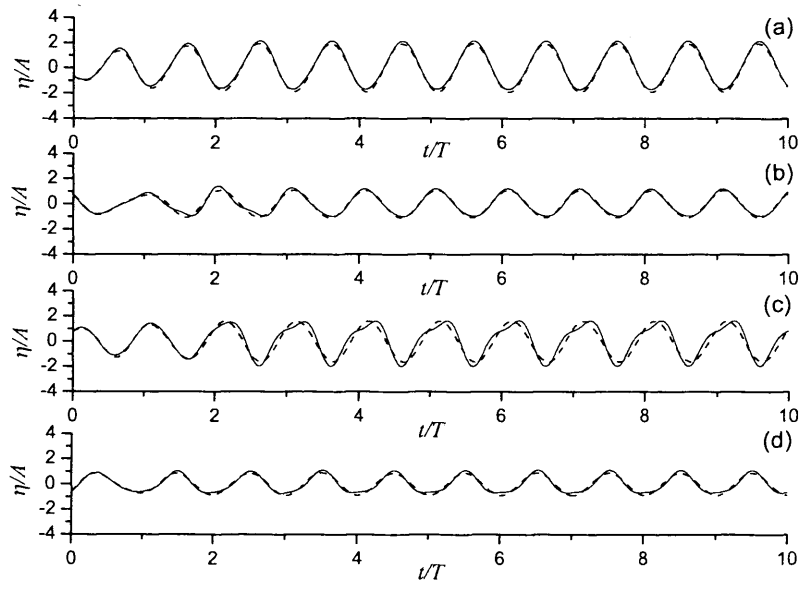

Figure 5.5.9 Wave histories at $k_0 a$=0.754
(a) front of cylinder one; (b) back of cylinder one;
(c) front of cylinder two; (d) back of cylinder two
----- linear; —— linear plus second order

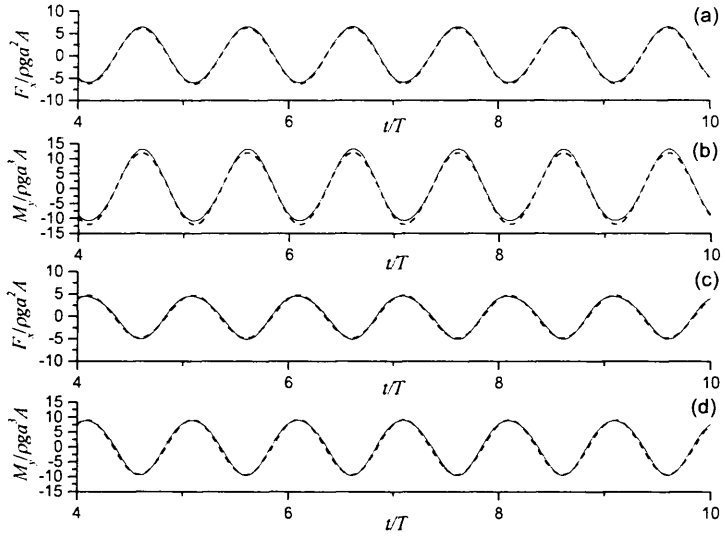

Figure 5.5.10 Histories of forces and moments on
(a), (b) cylinder one and (c), (d) cylinder two at k_0a=0.754

A case with L_{cy}=4a and a larger wavenumber $k_0a = 2.0$ is also investigated. In this case, the fluid domain may be chosen to be smaller than that in the case of k_0a=0.754 since the wavelength is smaller. However, more elements are needed around each cylinder. There are 52 intervals on the waterline for each cylinder in this case. The wave histories are shown in Figures 5.5.11 and 5.5.12. The nonlinearity of the wave at the front side of each cylinder is clear but weak at the back sides, and this may be explained through Figure 5.5.13. The two second order wave components are shown, $\eta^{(21)}$ and $\eta^{(22)}$, which are the waves due to the first order potential and the second order potential, respectively. It is seen that $\eta^{(21)}$ and $\eta^{(22)}$ are almost out of phase and the amplitudes are close, which leads the total second order wave to be very small. The wave at the back side of cylinder two is similar to this.

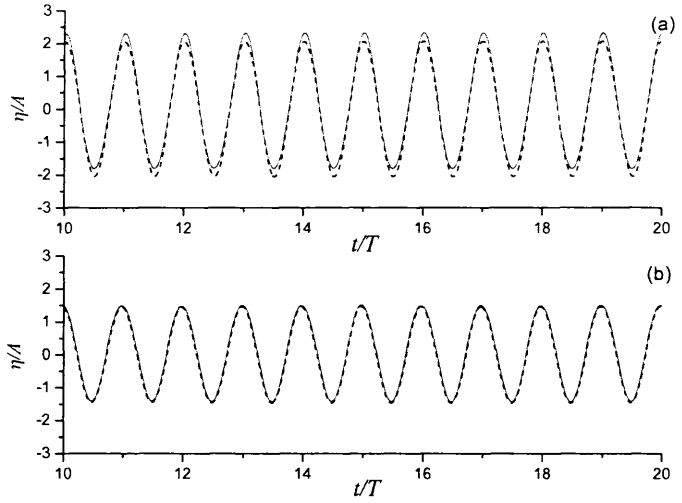

Figure 5.5.11 Wave histories for cylinder one at k_0a=2.0
(a) front; (b) back
----- linear; —— linear plus second order

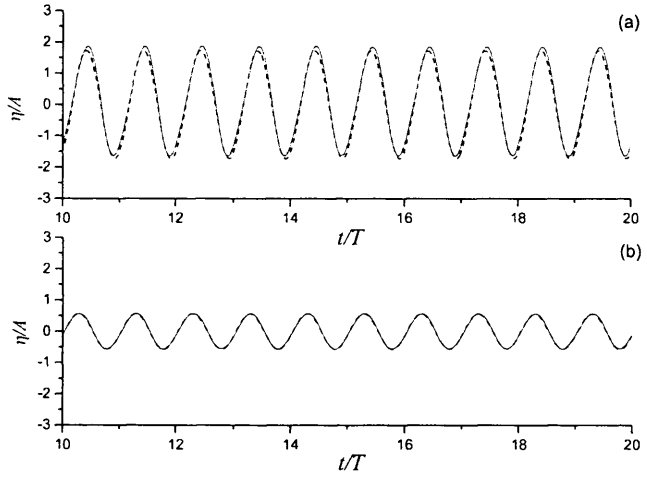

Figure 5.5.12 Wave histories for cylinder two at k_0a=2.0
(a) front; (b) back
----- linear; —— linear plus second order

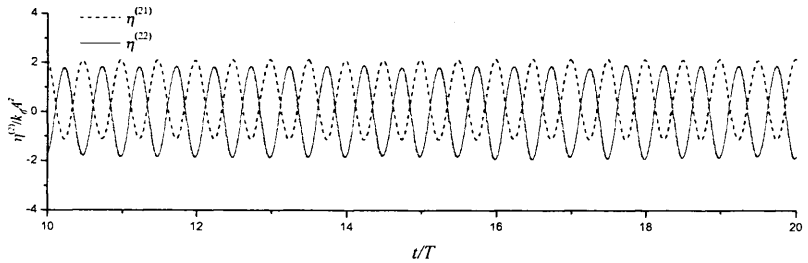

Figure 5.5.13 Second order wave components at the back side of cylinder one

The wave profiles for the above mentioned two-cylinder configuration with k_0a=0.754 and 2.0 are shown in Figures 5.5.14 and 5.5.15. The wave profile is generally

smoother at k_0a=0.754 than that at k_0a=2.0, and more wave peaks and troughs can be observed for the latter. The nonlinear effect of the waves around the cylinders is clear especially for k_0a=0.754 since the second order wave has more influence on the whole wave runup in this case.

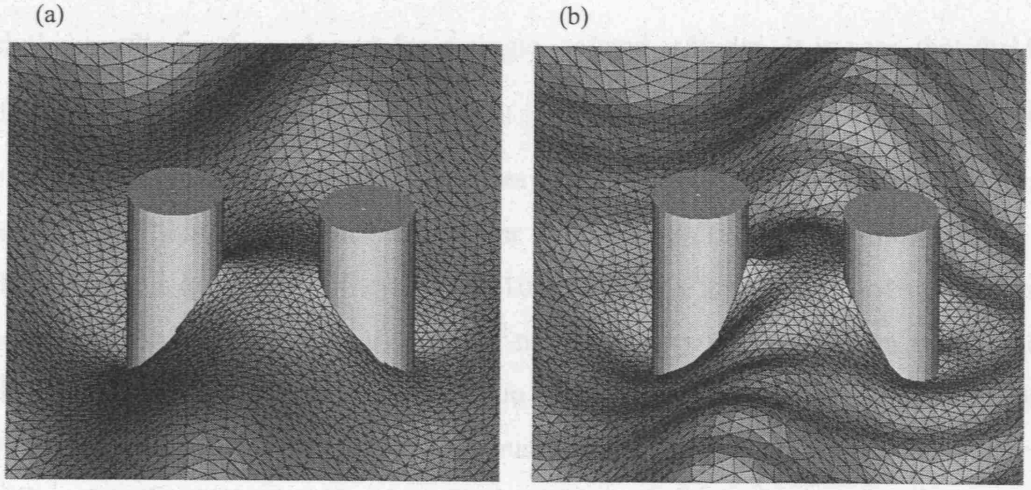

Figure 5.5.14 Free surface profiles around cylinders at t=6T with k_0a=0.754
(a) linear; (b) linear plus second order

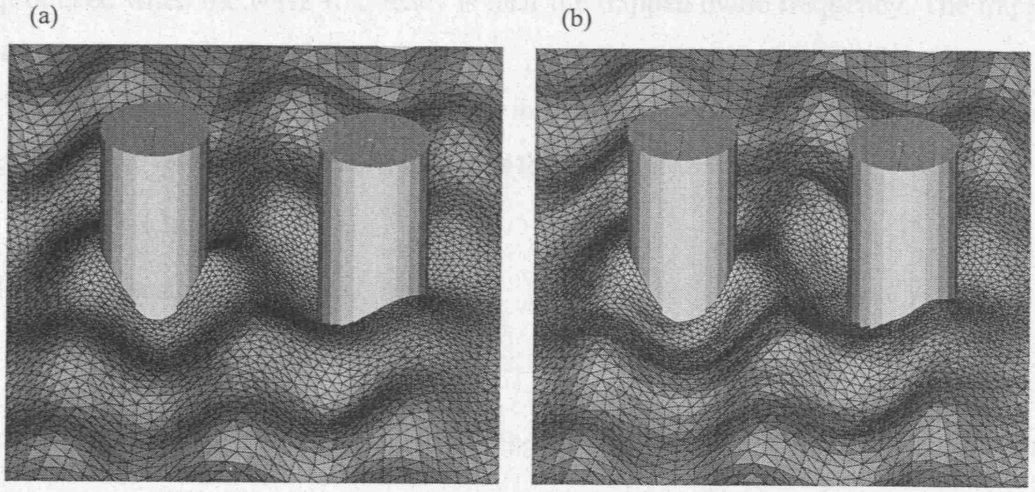

Figure 5.5.15 Free surface profiles around cylinders at t=6T with k_0a=2.0
(a) linear; (b) linear plus second order

Three-cylinder cases are also considered. The centres of the three cylinders are located at $(-L_{cy},0)$, $(0,0)$ and $(L_{cy},0)$, respectively, as shown in Figure 5.5.1(b). A case with $L_{cy}=4a$ and $k_0a=0.754$ is first simulated. The forces on the three cylinders are

given in Figure 5.5.16. It is shown that the largest first- and second-order forces are on cylinders one and two respectively. Two other cases with L_{cy}=4a and 7a at a smaller wavenumber $k_0 a = 0.57$ are also considered. Figure 5.5.17 shows the histories of the first- and second-order forces when L_{cy}=4a. The largest first order force is on cylinder two. The forces on cylinder two in case $L_{cy} = 7a$ are given in Figure 5.5.18 which also includes results for $L_{cy} = 4a$ and for a single isolated cylinder. It is seen that the first order force at $L_{cy} = 4a$ is the largest and is smallest at $L_{cy} = 7a$. The cylinder on which the maximum linear force acts in an array of cylinders may depend on the wave frequency and this is confirmed by Maniar & Newman (1997) when they studied the diffraction by a long array of cylinders (101 cylinders) in a line based on the linear theory. The results about a small array of nine cylinders was also given by them and further results about a double array of 2×9 in two lines was presented by Evans & Porter (1997a). Their results show that the maximum force will occur on the cylinders near the middle rather than at both ends when the frequency is near the Neumann trapped mode. The trapped mode is a localized phenomenon with finite energy which does not propagate into infinity (Ursell, 1951). Very large waves and hydrodynamic forces can be produced when the wave frequency is near the trapped mode frequency. The trapped mode may be described as follows:

An array of cylinders is located in the midway between the two parallel walls of a long tank. The velocity potential ϕ satisfies the Helmholtz equation,

$$\nabla^2\phi + k_0^2\phi = 0, \tag{5.5.1}$$

and the body surface condition

$$\frac{\partial\phi}{\partial n} = 0 \tag{5.5.2}$$

on surfaces of all cylinders. On the wall of the tank, if the normal velocity is zero, that is,

$$\frac{\partial\phi}{\partial n} = 0, \tag{5.5.3}$$

it is in the Neumann mode and if the velocity potential is zero

$$\phi = 0, \tag{5.5.4}$$

it is in the Dirichlet mode. Here we focus on the computation of waves and hydrodynamic forces. Some work on the trapped mode can be found in many publications. Maniar & Newman (1997) calculated the nondimensional wavenumbers

k_0l ($l=L_{cy}/2=2a$) in trapped modes for more than 10 cylinders in a line. The nondimensional wavenumber in the Neumann trapped mode is about 1.346 for the ten-cylinder case. The nondimensional wavenumber will gradually increase with increase in number of cylinders, but there is only a small difference between a ten-cylinder case and an infinite-cylinder case, in which the nondimensional wavenumber in the Neumann trapped mode is about 1.391. Kashiwagi (2002) calculated the diffraction by four truncated cylinders with $L_{cy}=4a$ based on the second order theory in the frequency domain and his calculation showed that the nondimensional wavenumber $k_0l=1.2$ or $k_0a=0.6$ was near the Neumann trapped mode. The nondimnesional wavenumber in the three-cylinder case in a trapped mode should be smaller than that in the four-cylinder case according to the study by Maniar & Newman (1997). Therefore, this three-cylinder case with $k_0a=0.57$ or $k_0l=1.14$, which is smaller and very close to that ($k_0l=1.2$) in the four-cylinder case, is probably near the Neumann trapped mode, and so the hydrodynamic force on cylinder two in case $L_{cy}=4a$ is larger than that on a single cylinder. However, the force in case $L_{cy}=7a$ is smaller than that on the single cylinder since the frequency is far from the Neumann trapped mode.

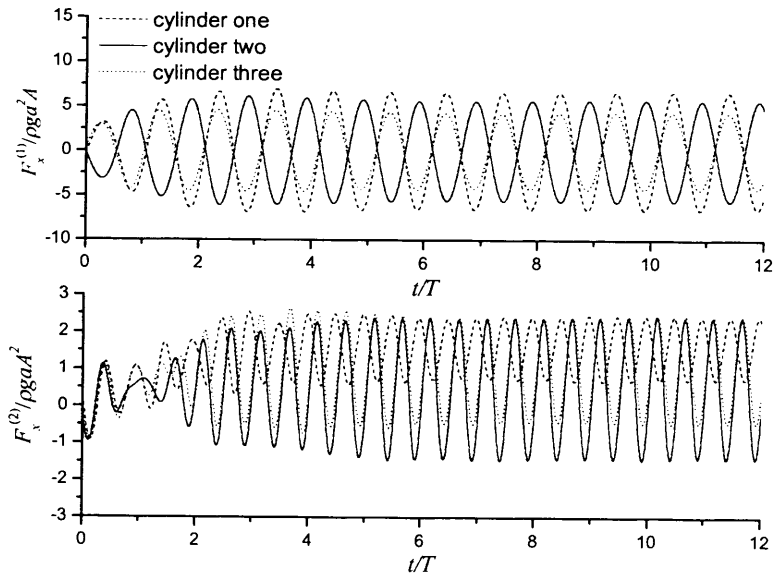

Figure 5.5.16 Histories of first- and second-order forces on the three cylinders with $L_{cy}=4a$ at $k_0a=0.754$

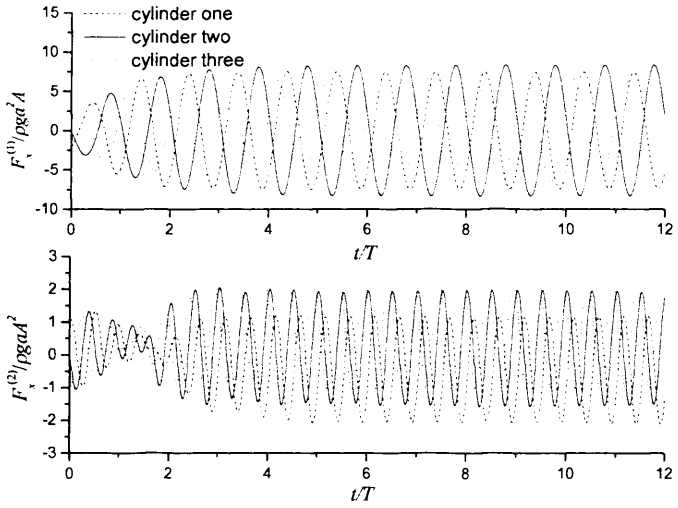

Figure 5.5.17 Histories of first- and second-order forces on the three cylinders with $L_{cc}=4a$ at $k_0a=0.57$

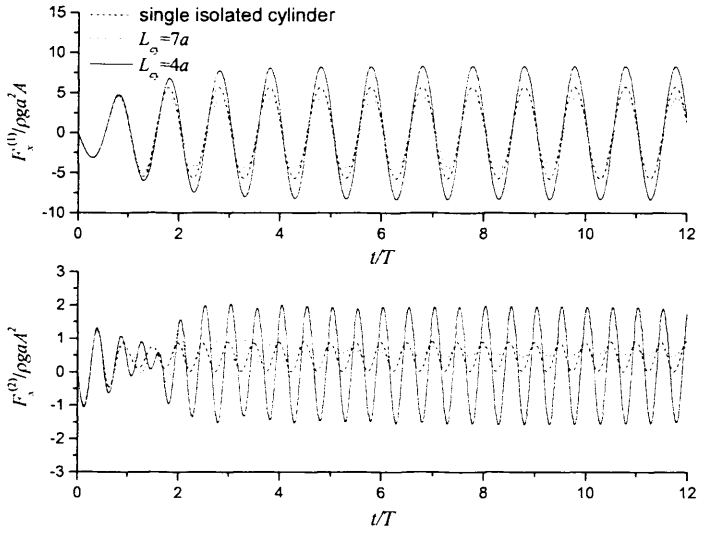

Figure 5.5.18 Histories of first- and second-order forces on the middle cylinder at $k_0a=0.57$

5.6 Simulations for four-cylinder case

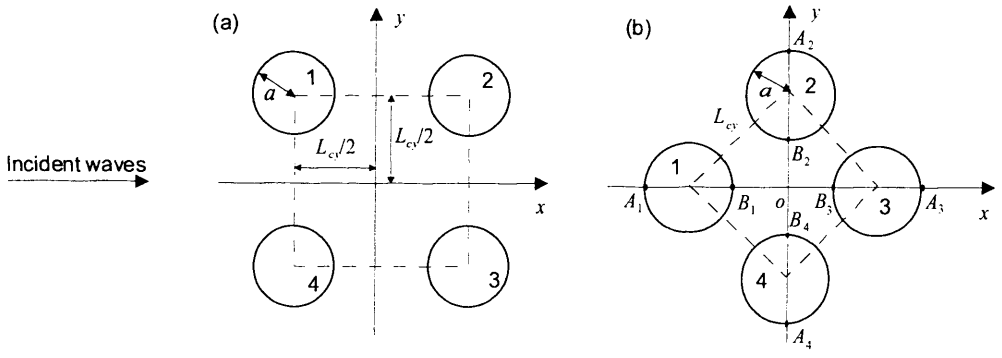

Figure 5.6.1 Four-cylinder cases

Two configurations of four cylinder cases with $L_{cy} = 4a$ are considered in this section, as shown in Figure 5.6.1. They are both symmetric about x and y axes. The simulation is first made for configuration 5.6.1(a). The results for k_0a=0.754 are given in Figures 5.6.2 ~5.6.4. We focus on the wave at the back side of cylinder one and the front side of cylinder two, and the result is given in Figure 5.6.2. The double frequency effect is particularly obvious at the back of cylinder one. Force and moment are given in Figures 5.6.3 and 5.6.4. The second order effect on the force in the x-direction and the moment in the y-direction does not seem to be evident at this wave amplitude, but it is highly significant on the transverse force F_y.

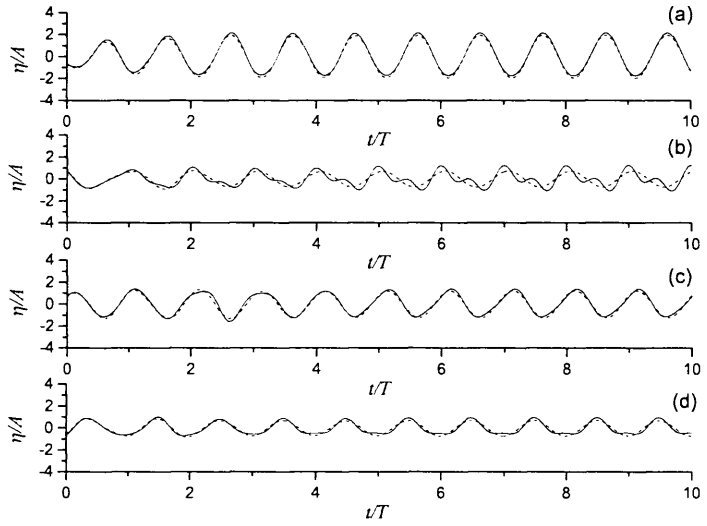

Figure 5.6.2 Wave histories for cylinders in figure 5.6.1(a) at k_0a=0.754
(a) front of cylinder one; (b) back of cylinder one;
(c) front of cylinder two; (d) back of cylinder two
····· linear; —— linear plus second order

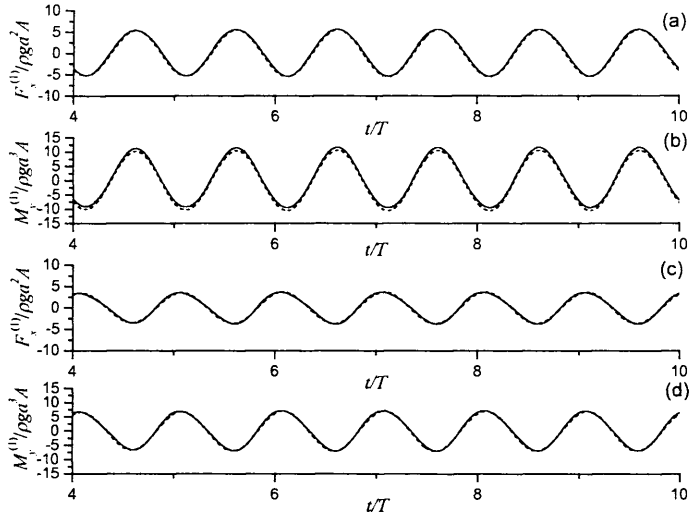

Figure 5.6.3 Histories of forces and moments on cylinders in figure 5.6.1(a) at k_0a=0.754
(a),(b) cylinder one; (c),(d) cylinder two
····· linear; —— linear plus second order

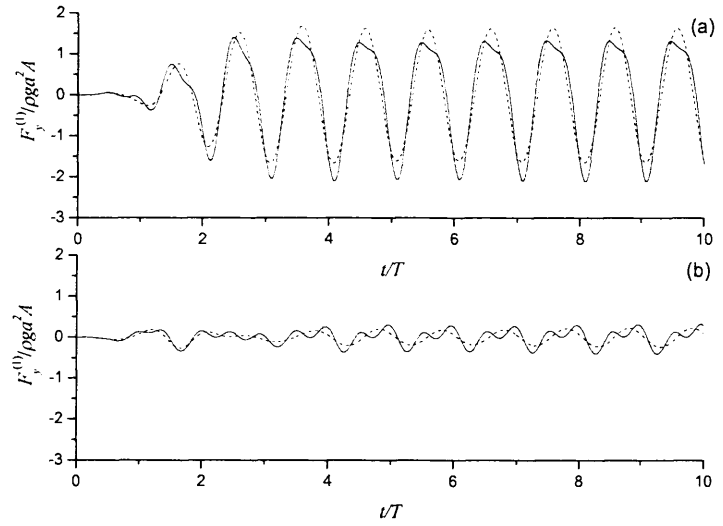

Figure 5.6.4 Transverse forces on cylinders in figure 5.6.1(a) at k_0a=0.754
(b) cylinder one; (b) cylinder two
····· linear; —— linear plus second order

The configuration in Figure 5.6.1(b) can be obtained through rotating that in Figure 5.6.1(a) by 45°. This is the case considered by Evans & Porter (1997b) based on the linear theory and by Malenica *et al.* (1999) based on the second order theory in the frequency domain. When $k_0a = 1.66$, it is very close to the trapped mode. Simulation is made and the wave histories for the four cylinders are shown in Figure 5.6.5, with the locations of points A_i, B_i $(i = 1,2,3,4)$ given in Figure 5.6.1(b). It can be seen that the maximum ratio of η / A is around 4 which is much larger than 1.85 for the single-

cylinder case. It ought to be pointed out that the maximum ratio will increase dramatically when L_{cy}/a is reduced, as observed in the frequency domain analysis (Evans & Porter, 1997b). We do not undertake extensive simulation for the cases with a small gap between cylinders, as their practical interest is limited.

When the first order result is large, one would expect that the second order result would be even larger because of those product terms in equation (5.2.6) when $k=2$. We give the second order waves in Figure 5.6.6 together with their components $\eta^{(21)}$ due to the product terms of the first order result and $\eta^{(22)}=-\frac{1}{g}\frac{\partial\phi^{(2)}}{\partial t}$ due to the second order potential. It is seen that the wave runups at B_i $(i=2,3,4)$ have large components $\eta^{(21)}$ and $\eta^{(22)}$. The magnitudes of $\eta^{(21)}$ and $\eta^{(22)}$ are close but their phases are almost opposite to each other. Thus $\eta^{(2)}$ itself is not particularly big at these points. The situation at B_1 is somewhat different. There is a bigger difference between the magnitudes of $\eta^{(21)}$ and $\eta^{(22)}$ even though their phases are almost opposite to each other, and as a result $\eta^{(2)}$ is much bigger. Thus whether the big first order result will lead to a big second order result depends also on the behaviour of each individual component.

The corresponding hydrodynamic forces and moments at $k_0a=1.66$ are shown in Figures 5.6.7~5.6.9. Generally, the dominant part of the total result at this frequency and this wave height is the linear one. However, the second order effect is quite noticeable in some cases. It is interesting to see that the transition of the force to the periodic state progresses rather slowly. This behaviour is similar to that of waves sloshing in a tank near to resonance (Wu *et al.*, 1998), where the transition of the amplitude envelope is dominated by the difference between the natural frequency and excitation frequency. When the difference is small, the development of the envelope can be very slow.

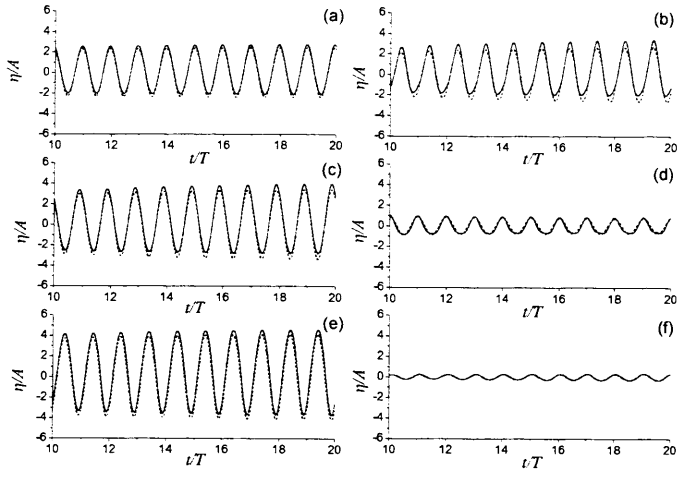

Figure 5.6.5 Wave histories at (a) A_1, (b) B_1, (c) B_2 & B_4, (d) A_2 & A_4, (e) B_3 and (f) A_3 in Figure 5.6.1(b) at k_0a=1.66

····· linear; —— linear plus second order

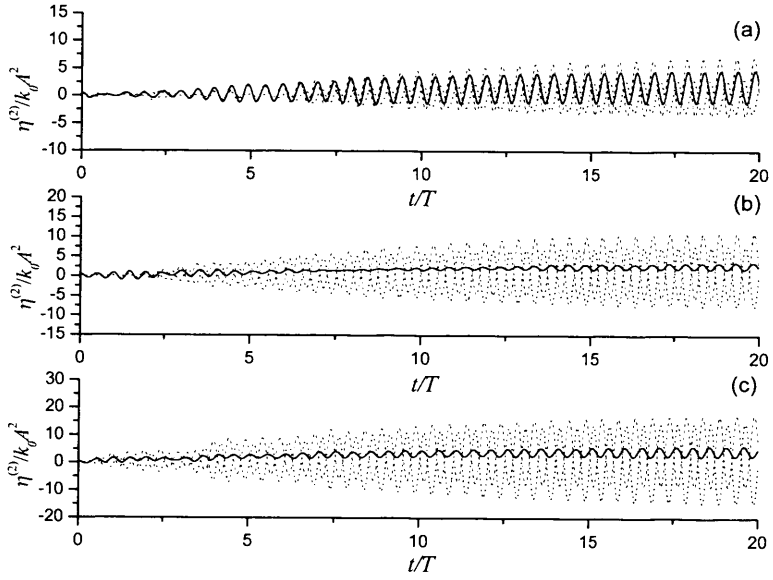

Figure 5.6.6 Second order wave histories at (a) B_1, (b) B_2 & B_4 and (c) B_3 in figure 5.6.1(b) at k_0a=1.66

····· $\eta^{(21)}$; ····· $\eta^{(22)}$; —— $\eta^{(2)}$

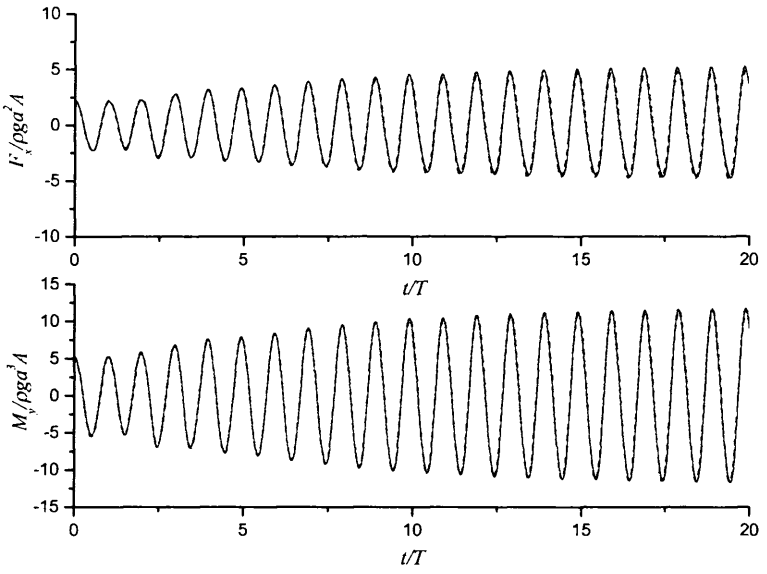

Figure 5.6.7 Histories of force and moment on cylinder one in figure 5.6.1(b) at $k_0 a$=1.66
----- linear; —— linear plus second order

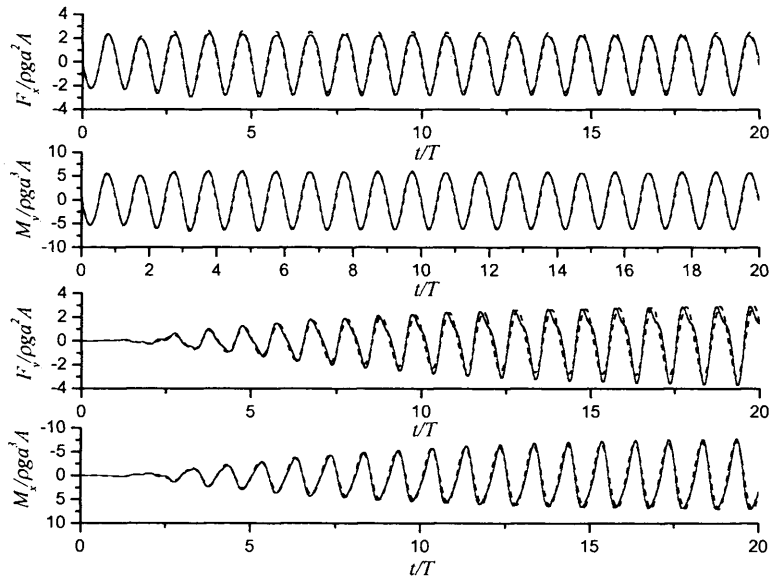

Figure 5.6.8 Histories of force and moment on cylinder two in figure 5.6.1(b) at $k_0 a$=1.66
----- linear; —— linear plus second order

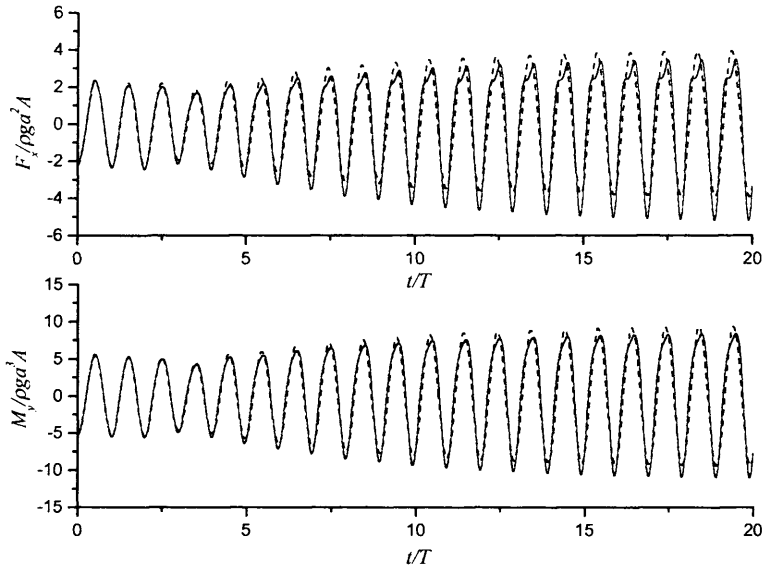

Figure 5.6.9 Histories of force and moment on cylinder three in figure 5.6.1(b) at $k_0 a$=1.66
----- linear; —— linear plus second order

We then consider a case at $k_0 a = 0.468$ for the same configuration. The trapped mode is far away from this wave number and its effect on the first order result is not expected to have any significance. At this wave number however, the second order wave corresponds to a wave number which is very close to the trapped mode. For this reason, the case was chosen by Malenica, *et al.* (1999) in their second order analysis based on the frequency domain method. The results for the second order wave from the present simulation are shown in Figures 5.6.10~5.6.12. As expected, these results have a large component $\eta^{(22)}$ due to the second order potential whose wave number is near the trapped mode. By contrast, $\eta^{(21)}$ is very small because the trapped mode virtually has no effect on the first order result. A comparison of second-order wave amplitudes at points B_1, B_3 is given in Table 5.5.1. The frequency-domain results were taken from the paper by Malenica, et al. (1999). The results are generally in a good agreement.

Location	$\lvert\eta^{(21)}\rvert/k_0A^2$		$\lvert\eta^{(22)}\rvert/k_0A^2$		$\lvert\eta^{(2)}\rvert/k_0A^2$	
	Present method	Frequency-domain	Present method	Frequency-domain	Present method	Frequency-domain
B_1	1.41	1.44	8.87	9.12	7.93	8.05
B_3	1.74	1.72	15.96	16.68	17.10	17.72

Table 5.5.1 Comparisons of second order waves and components

The linear and linear plus second order waves are given in Figure 5.6.13. It is interesting to see from Figures 5.6.13(d) and (e) that the amplitude of $\eta^{(2)}$ is even larger than that of $\eta^{(1)}$. By contrast, the amplitude of the second order wave at the front of the single cylinder is only about 20% that of the first order at $k_0 a = 0.468$ and H/λ=0.05. The results here of course may raise the question whether the perturbation method is valid in this case, but it nevertheless shows some interesting behaviour near the trapped mode.

The corresponding forces and moments at $k_0 a = 0.468$ are shown in Figures 5.6.14~5.6.19 together with the components $F^{(21)}$ due to the product of the first order result and $F^{(22)}$ due to the second order potential. Once again, $F^{(22)}$ is much larger than $F^{(21)}$ for the same reason discussed above. The second order force is a much bigger or even a dominant component in the total force, compared with those results at $k_0 a = 1.66$. The free surface wave profiles around the cylinders at $k_0 a = 0.468$ are shown in Figure 5.6.20. The inclusion of the second order component has changed the wave pattern completely.

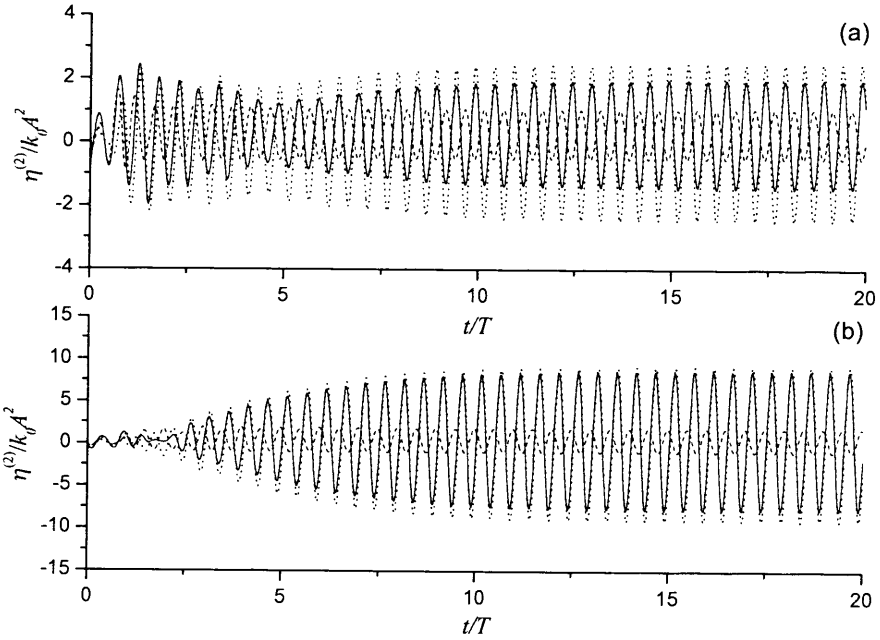

Figure 5.6.10 Second order wave histories at (a) A_1 and (b) B_1 in Figure 5.6.1(b) at k_0a=0.468

------ $\eta^{(21)}$; ..... $\eta^{(22)}$; —— $\eta^{(2)}$

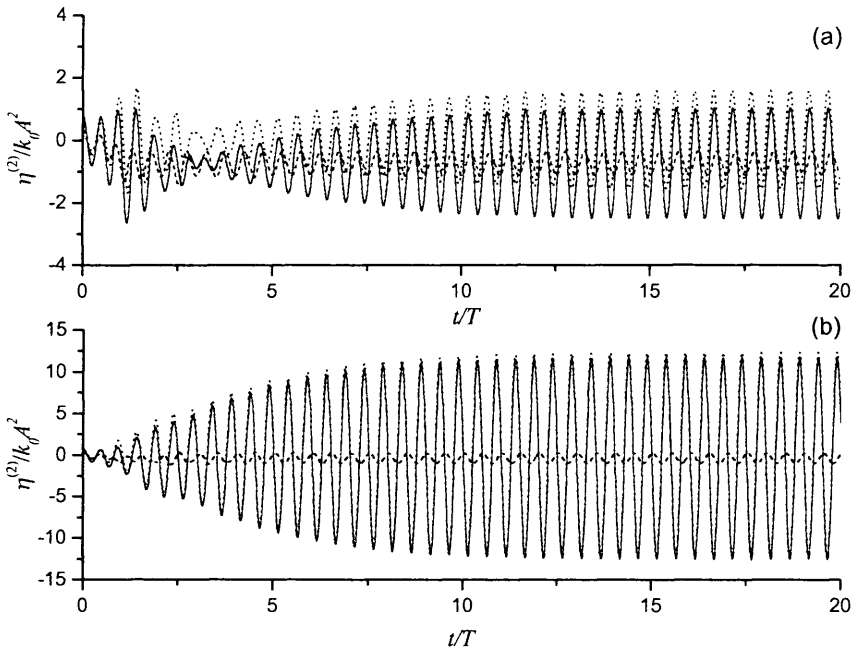

Figure 5.6.11 Second order wave histories at (a) A_2 and (b) B_2 in Figure 5.6.1(b) at k_0a=0.468

..... $\eta^{(21)}$; ..... $\eta^{(22)}$; —— $\eta^{(2)}$

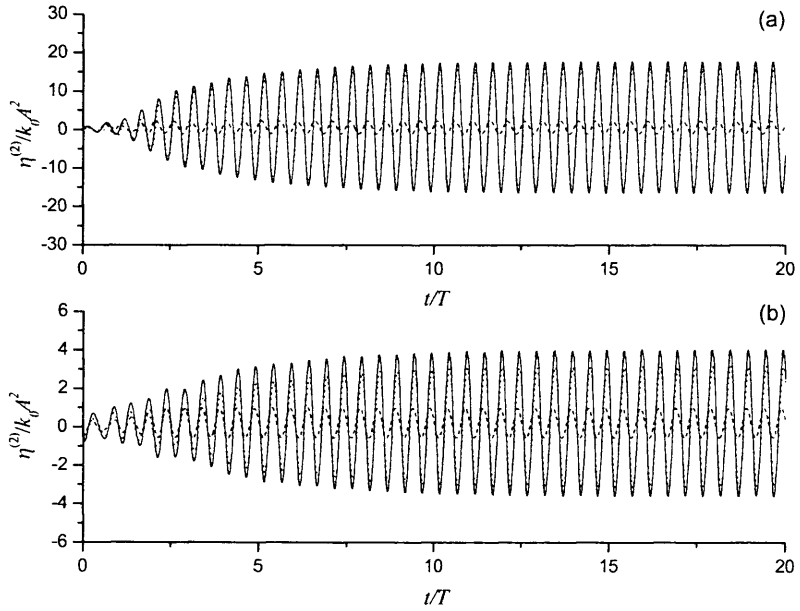

Figure 5.6.12 Second order wave histories at (a) B_3 and (b) A_3 in Figure 5.6.1(b) at k_0a=0.468

..... $\eta^{(21)}$; ..... $\eta^{(22)}$; —— $\eta^{(2)}$

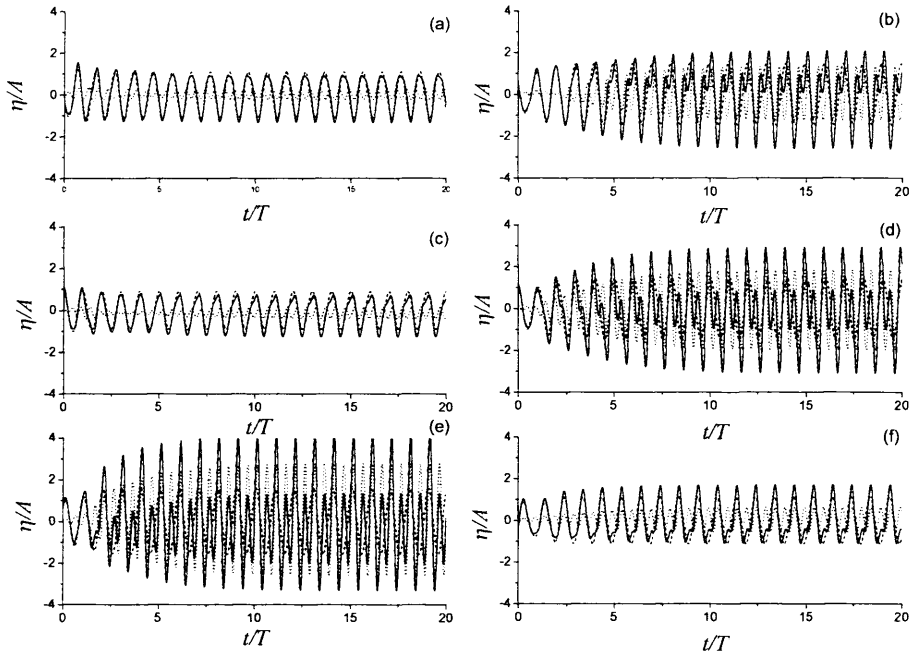

Figure 5.6.13 Wave histories for cylinders one, two and three in Figure 5.6.1(b) at k_0a=0.468
(a) A_1; (b) B_1; (c) A_2; (d) B_2; (e) B_3; (f) A_3
------ linear; ..... second order; —— linear plus second order

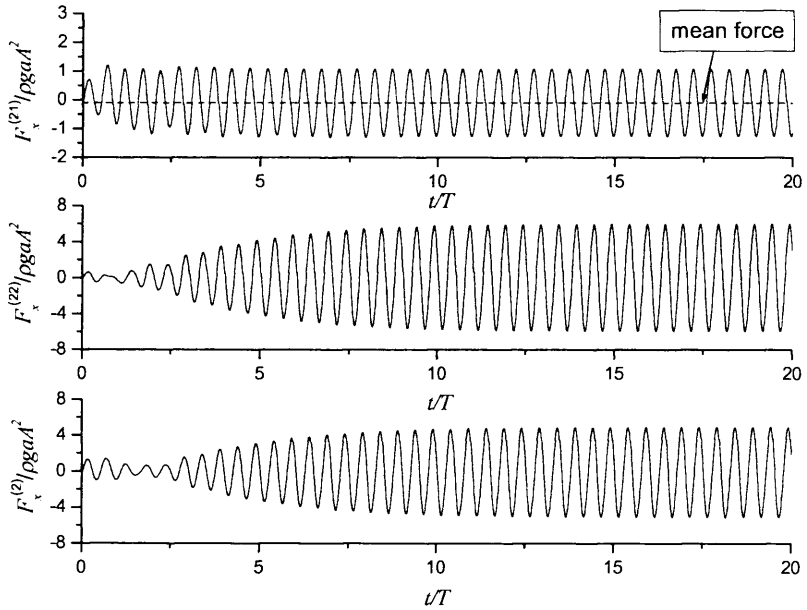

Figure 5.6.14 Second order force and its components
on cylinder one in Figure 5.6.1(b) at k_0a=0.468

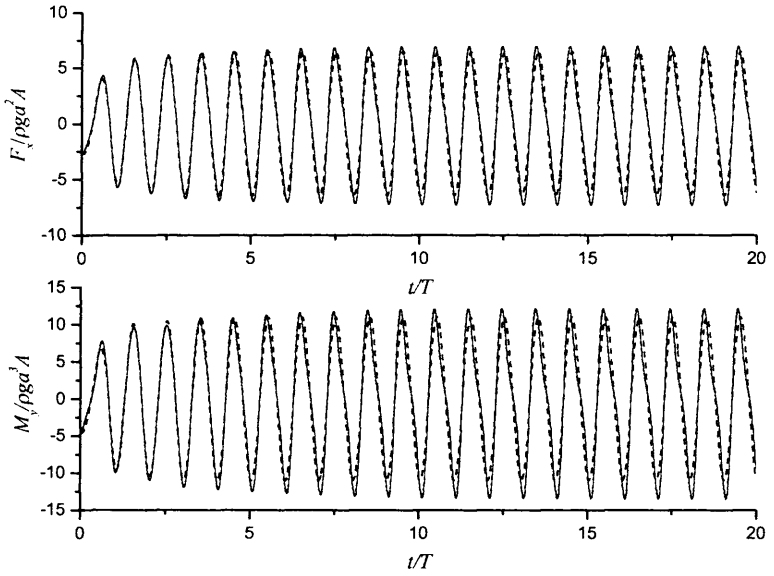

Figure 5.6.15 Histories of force and moment on cylinder one in Figure 5.6.1(b) at $k_0 a$=0.468
----- linear; —— linear plus second order

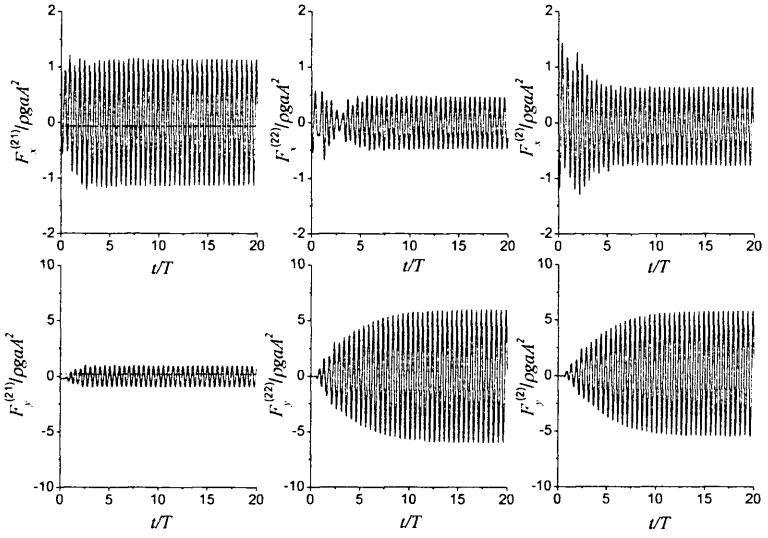

Figure 5.6.16 Second order force and its components
on cylinder two in Figure 5.6.1(b) at $k_0 a$=0.468

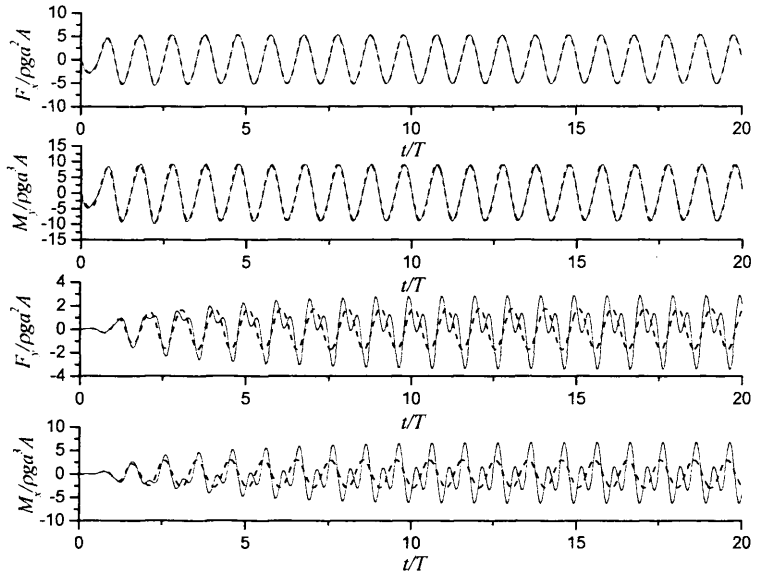

Figure 5.6.17 Histories of force and moment on cylinder two in Figure 5.6.1(b) at $k_0 a$=0.468
----- linear; —— linear plus second order

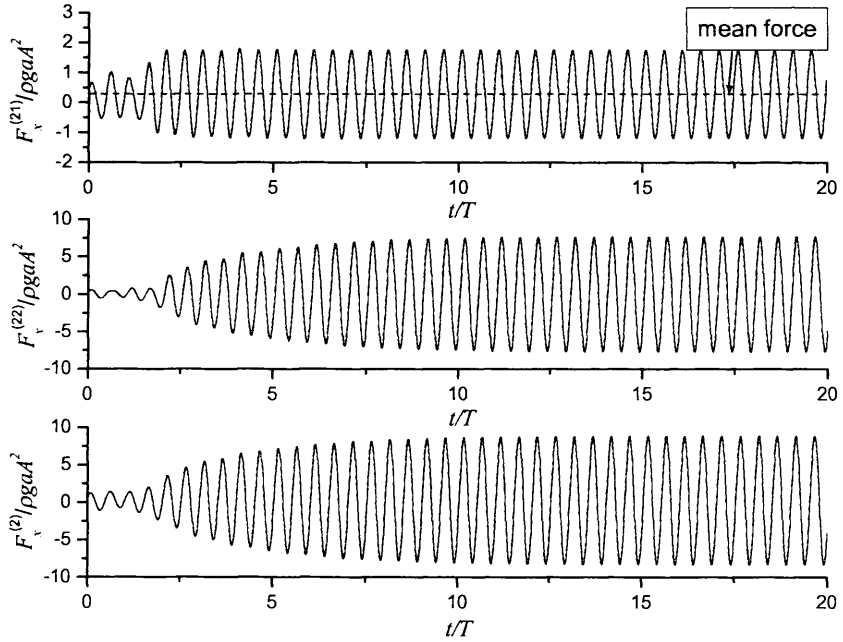

Figure 5.6.18 Second order force and its components on cylinder three in Figure 5.6.1(b) at $k_0 a$=0.468

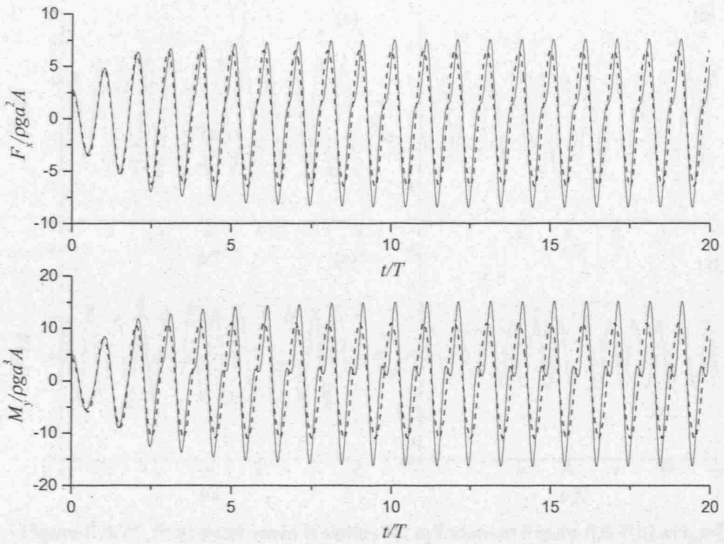

Figure 5.6.19 Histories of force and moment on cylinder three in Figure 5.6.1(b) at k_0a=0.468
----- linear; —— linear plus second order

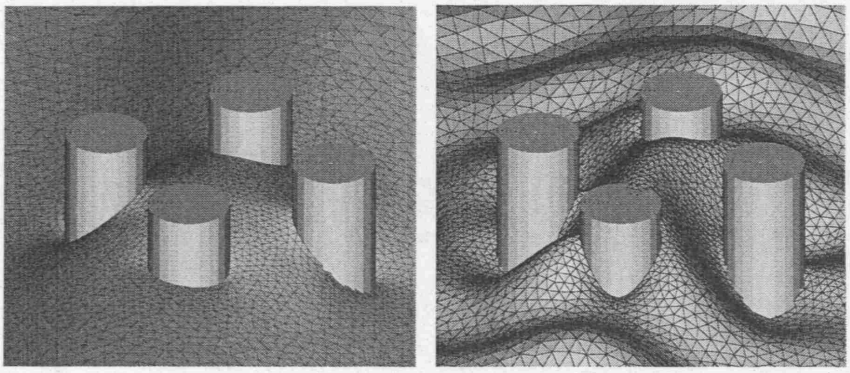

Figure 5.6.20 Wave profiles at t=16T
(a) linear; (b) linear plus second order

A case at k_0a=0.754 is also simulated. The trapped mode is away from both the first and the second order wave numbers. The results in Figures 5.6.21 and 5.6.22 therefore do not show similar behaviour as occurred at $k_0a = 1.66$ or at $k_0a = 0.468$.

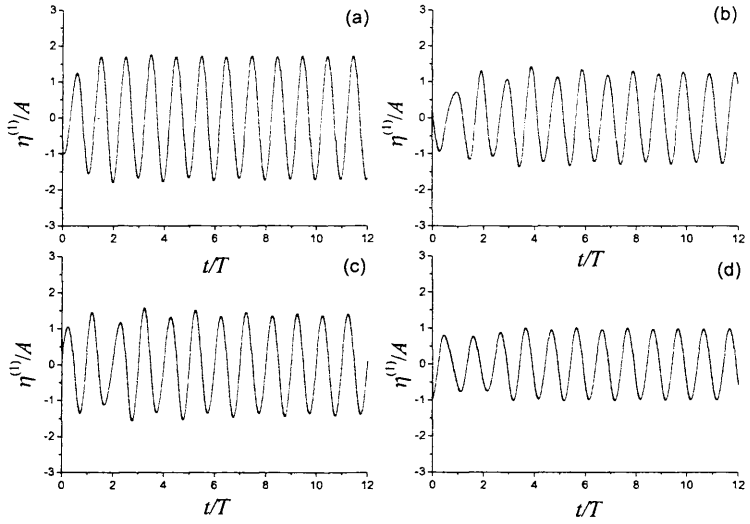

Figure 5.6.21 First order wave histories for cylinders in Figure 5.6.1(b) at k_0a=0.754
(a) front of cylinder one; (b) back of cylinder one;
(c) front of cylinder three; (d) back of cylinder three

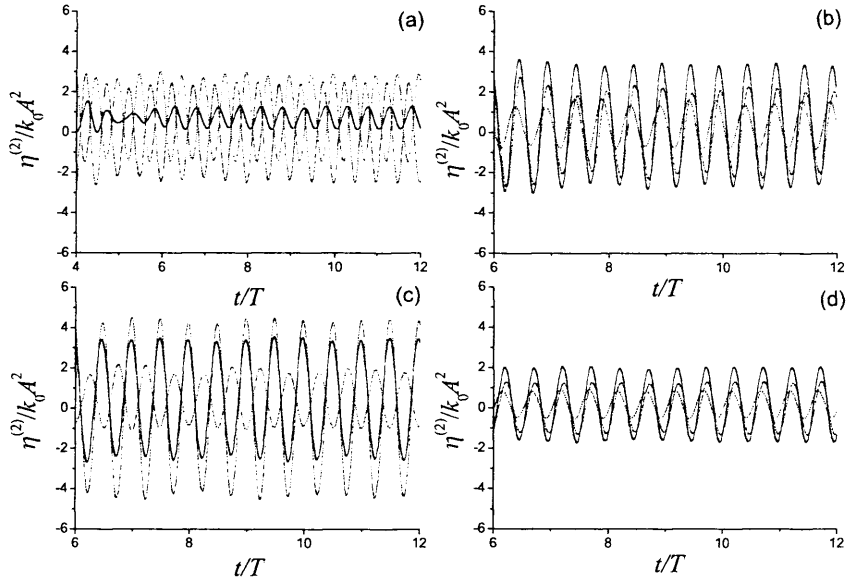

Figure 5.6.22 Second order wave histories for cylinders in Figure 5.6.1(b) at k_0a=0.754
(a) front of cylinder one; (b) back of cylinder one;
(c) front of cylinder three; (d) back of cylinder three
..... $\eta^{(21)}$; —— $\eta^{(22)}$; —— $\eta^{(2)}$

To demonstrate the flexibility of the present numerical procedure, we next consider truncated cylinders in the same configuration as that in Figure 5.6.1(b). The cylinders all have the identical draught d=0.5h and $L_{cy} = 4a$. The wave histories at $k_0a = 1.66$ are given in Figure 5.6.23 for cylinder one and Figure 5.6.24 for cylinder three. The results are hardly different from those for the bottom mounted cylinders. This is

expected as the main component in this case is the linear one and the major action of the linear wave at this frequency is near the free surface. The change near the seabed usually does not affect too much the results near the free surface. Figures 5.6.25~5.6.28 give waves at k_0a=0.468. The difference between waves for the bottom mounted cylinder and the truncated cylinder becomes more evident as the disturbance decays more slowly along the depth at lower frequency. A big difference can be seen in the second order waves. This is because the second order potential decays much more slowly than the first order one along the depth, which was observed by Eatock Taylor *et al.* (1989) and then discussed in detail by Newman (1990). The forces on truncated cylinders one and three at k_0a=0.468 are given in Figures 5.6.29 and 5.6.30. The figures show the highly significant effect of the second order component. Another difference between the truncated cylinder and the bottom mounted cylinder is that there is a vertical force on the former, which is also included in the figures.

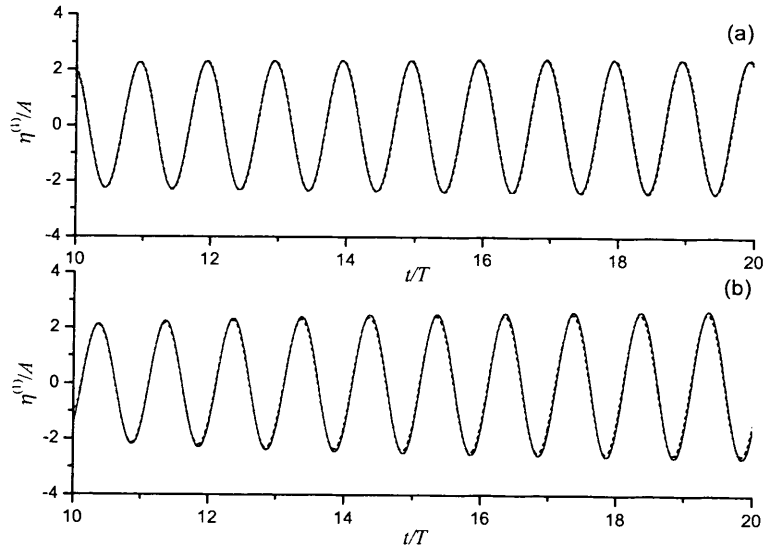

Figure 5.6.23 First order wave histories for cylinder one in Figure 5.6.1(b) at k_0a=1.66
(a) front; (b) back
------ bottom mounted; —— truncated

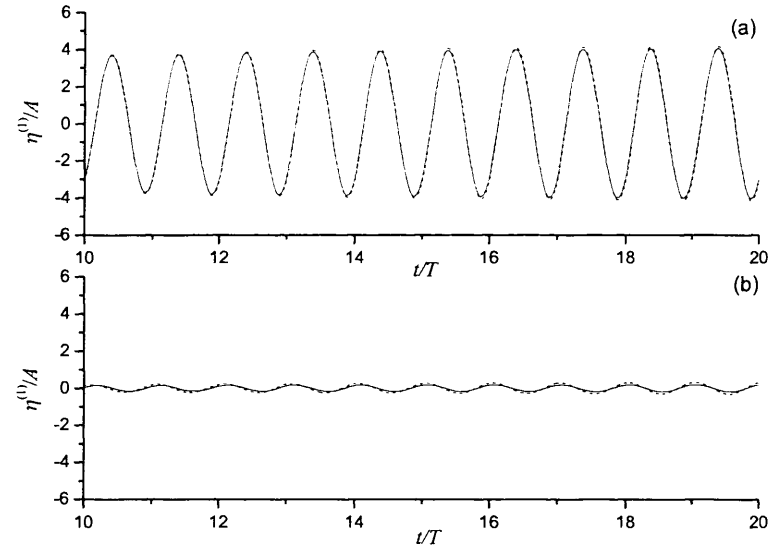

Figure 5.6.24 First order wave histories along cylinder three in Figure 5.6.1(b) at k_0a=1.66
(a) front; (b) back
····· bottom mounted; —— truncated

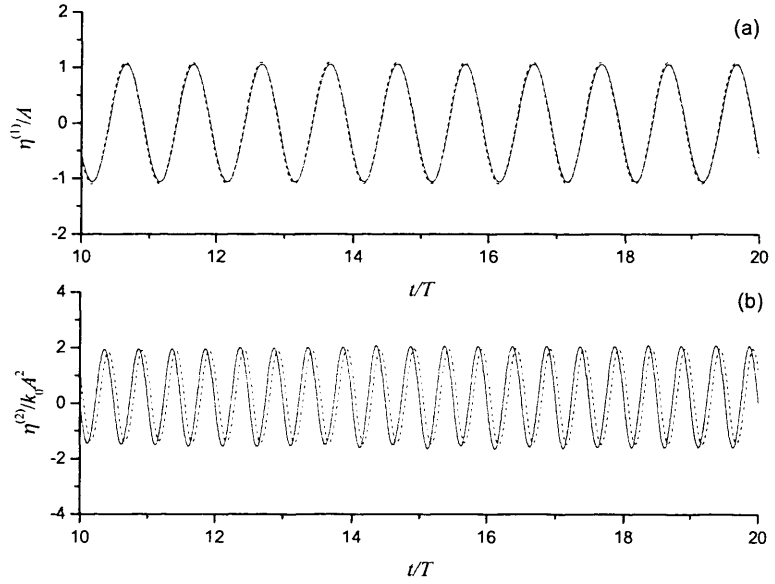

Figure 5.6.25 Wave histories at the front of cylinder one in Figure 5.6.1(b) at k_0a=0.468
(a) linear; (b) second order
····· bottom mounted; —— truncated

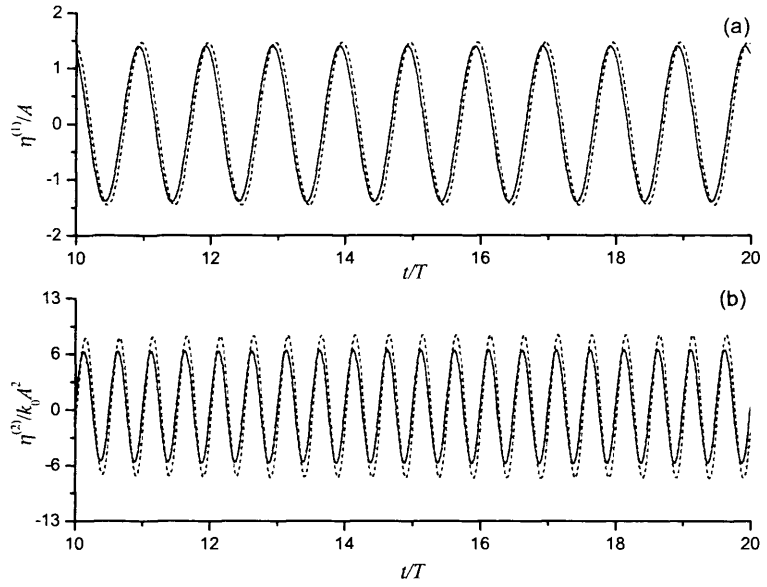

Figure 5.6.26 Wave histories at the back of cylinder one in Figure 5.6.1(b) at k_0a=0.468
(a) linear; (b) second order
------ bottom mounted; —— truncated

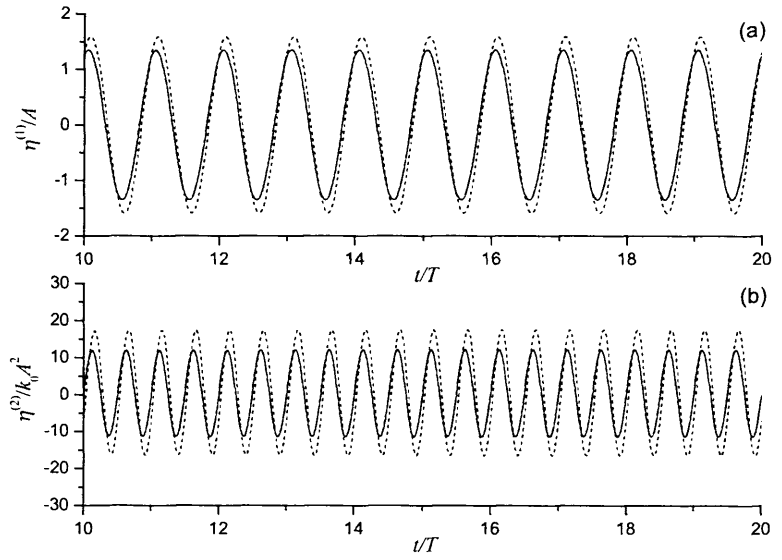

Figure 5.6.27 Wave histories at the front of cylinder three in Figure 5.6.1(b) at k_0a=0.468
(a) linear; (b) second order
------ bottom mounted; —— truncated

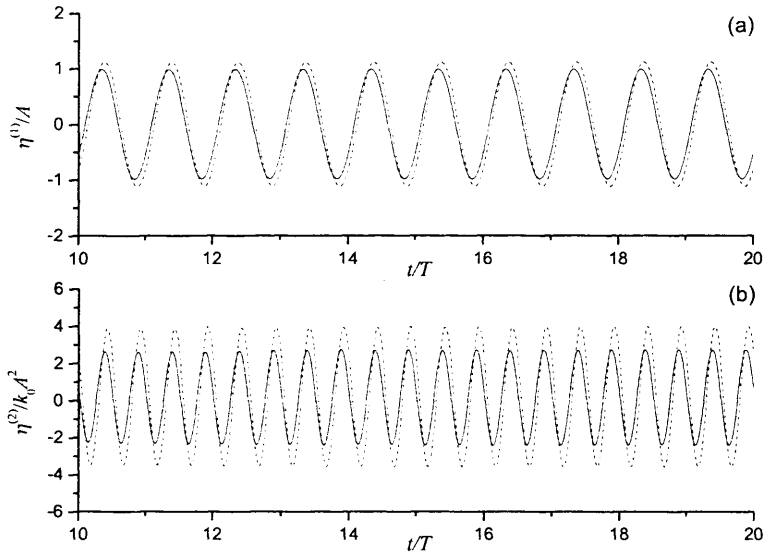

Figure 5.6.28 Wave histories at the back of cylinder three in Figure 5.6.1(b) at k_0a=0.468
(a) linear; (b) second order
····· bottom mounted; —— truncated

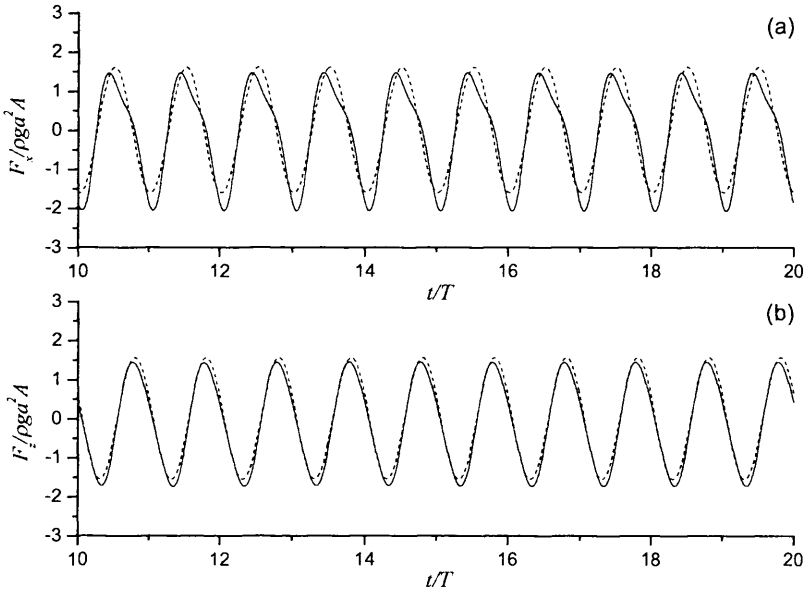

Figure 5.6.29 Histories of forces on cylinder one in Figure 5.6.1(b) at k_0a=0.468
····· linear; —— linear plus second order

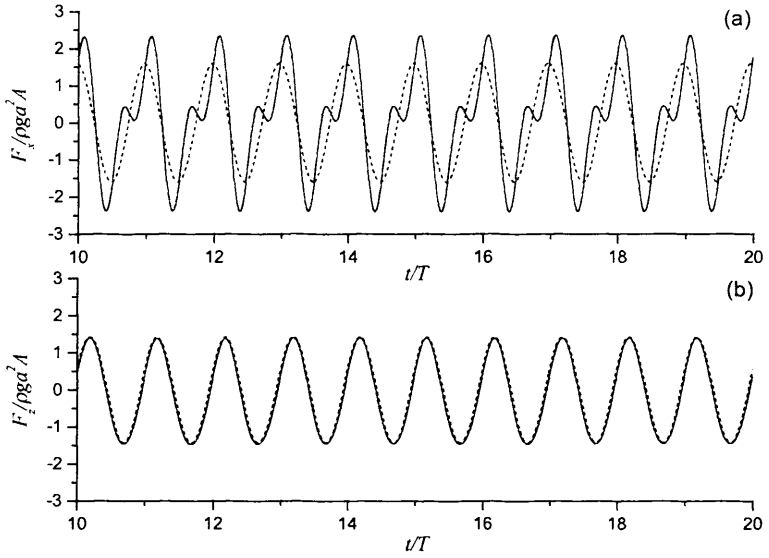

Figure 5.6.30 Histories of forces on cylinder three in Figure 5.6.1(b) at $k_0 a$=0.468
····· linear; —— linear plus second order

5.7 Simulations for an array of cylinders

The case simulated in this section is given in Figure 5.7.1. The cylinders are placed along the line $y = 0$ with an identical distance L_{cy} between two adjacent bodies. The configuration is symmetric about $x = 0$. In the simulation, $L_{cy} = 4a$ and $k_0 a$=0.673 which is near the Neumann trapped mode given by Maniar & Newman (1997). The waves along the two cylinders at two ends and two cylinders in the middle are given in Figure 5.7.2. It can be seen that the result corresponding to cylinders 5 and 6 are larger than those corresponding to 1 and 2. This is consistent with the linear results of Maniar & Newman (1997) from the frequency domain method. Figure 5.7.3 gives the second order wave elevation. As in the four-cylinder case, the components may be big but the total result is much smaller due to cancellation. Figure 5.7.4 gives the linear forces on all the cylinders. It is seen that the force tends to be greater towards the middle cylinders. It is also interesting to see the envelope of the amplitude does not seem to have stabilised even after 30 periods, similar to the behaviour in Figures 5.6.7~5.6.9. Wave profiles at $t = 25T$ are given in Figure 5.7.5, in which the contribution from the second order component is quite evident.

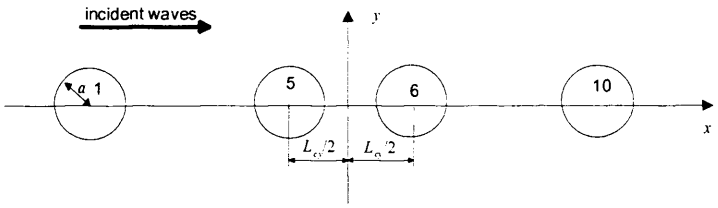

Figure 5.7.1 Ten-cylinder case

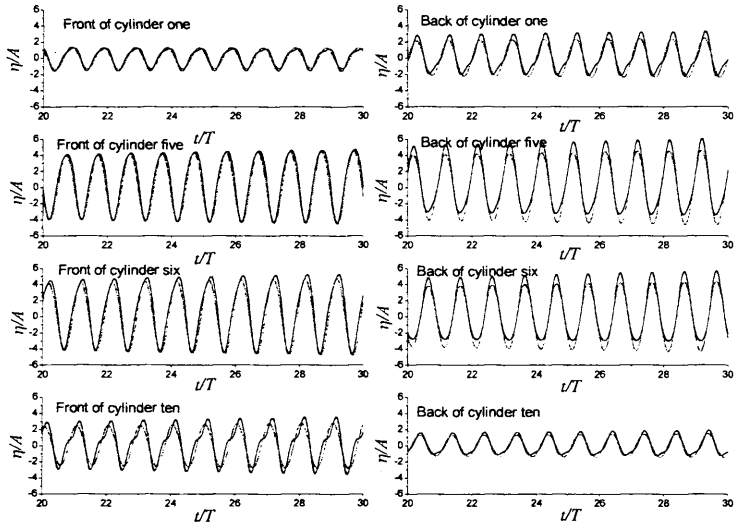

Figure 5.7.2 Wave histories for cylinders one, five, six and ten
—— linear; —— linear plus second order

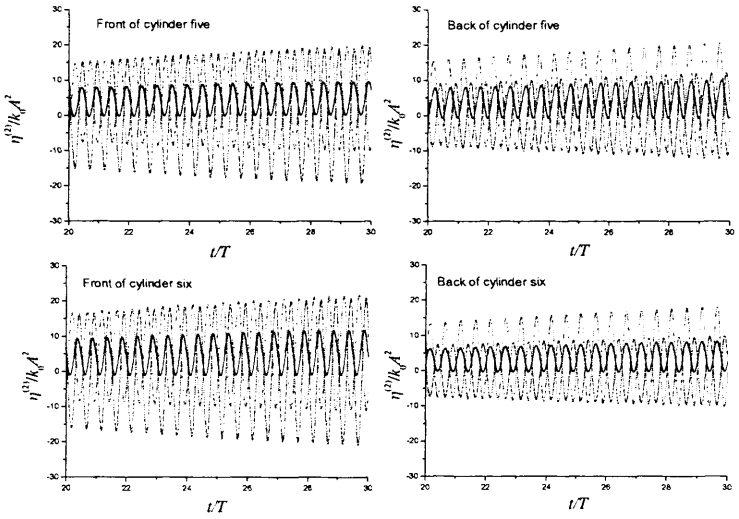

Figure 5.7.3 Histories of secod order wave and components for cylinders five and six
—— $\eta^{(21)}$; —— $\eta^{(22)}$, —— $\eta^{(2)}$

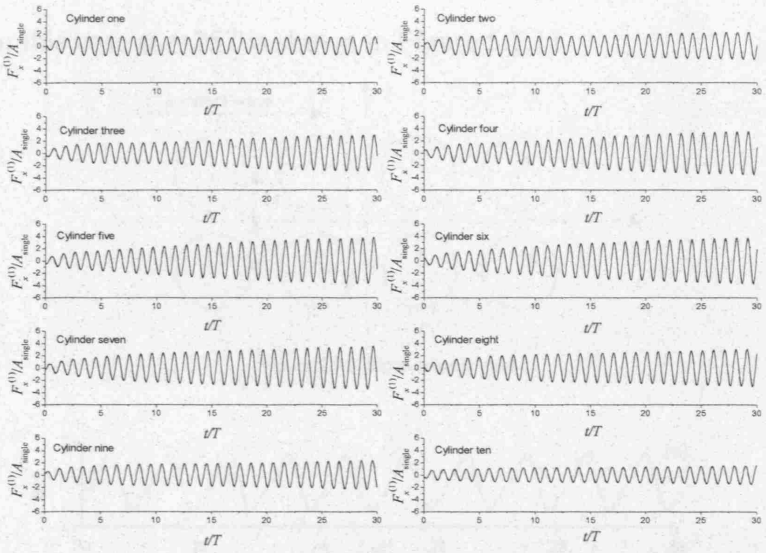

Figure 5.7.4 Histories of forces on the ten cylinders

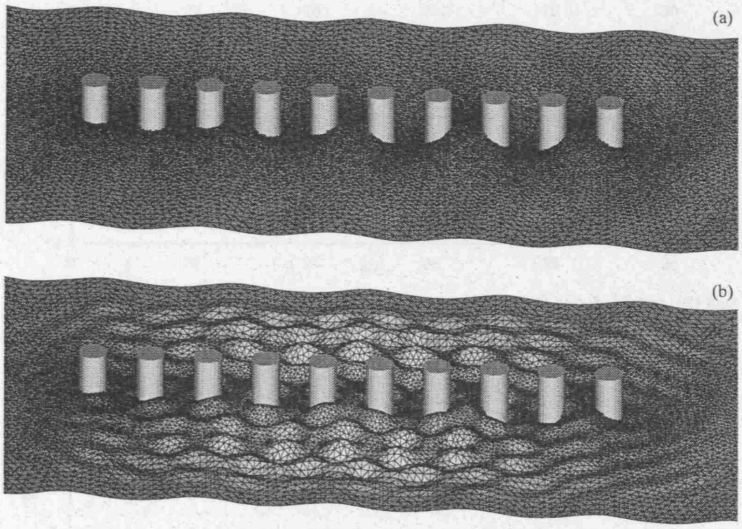

Figure 5.7.5 Free surface profiles at t=25T. (a) linear; (b) linear plus second order

The diffraction by eight truncated cylinders in double lines with $d = 0.5h$ shown in Figure 5.7.6 is also simulated. This case resembles the columns of a floating airport, although the total number 8 is relatively low. The distance between two neighbouring cylinders is $L_{cy} = 4a$ and the distance between the two lines is also $4a$. We provide results for cylinders 1, 2, 3 and 4 only because of symmetry. The waves at $k_0 a = 0.456$ are given in Figures 5.7.7 and 5.7.8. Generally, the waves at the front sides of cylinders are larger than those on their back sides and show stronger nonlinearities, and the amplitude of the second order wave is about 44.6% that of the first order for cylinder two while it is 53% for cylinder three. The horizontal and vertical forces are given in

Figures. 5.7.9 and 5.7.10 while F_y has been ignored as it is small. A snapshot of the wave profile for this case at t=25T is shown in Figure 5.7.11.

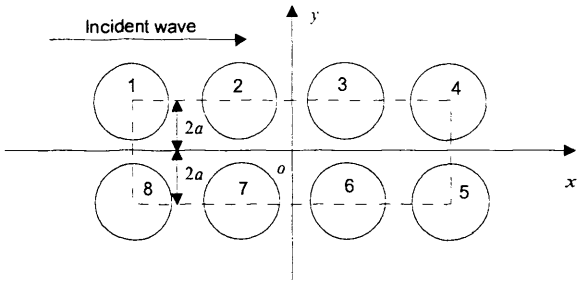

Figure 5.7.6 Eight-cylinder case

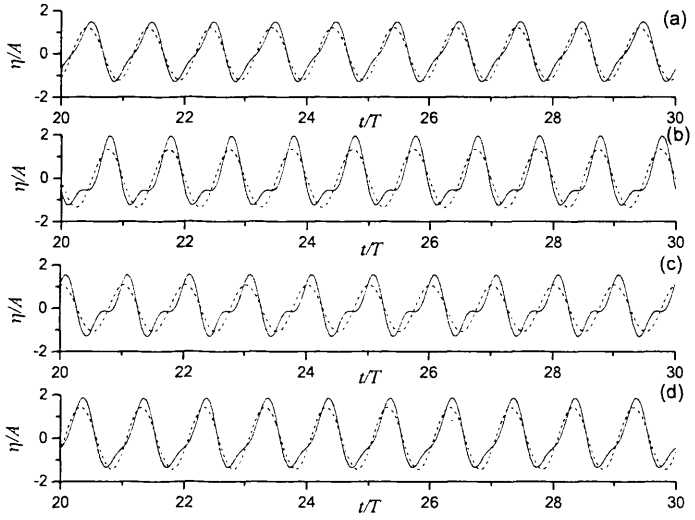

Figure 5.7.7 Wave histories at the fronts of cylinders (a) one, (b) two, (c) three, (d) four
····· linear; —— linear plus second order

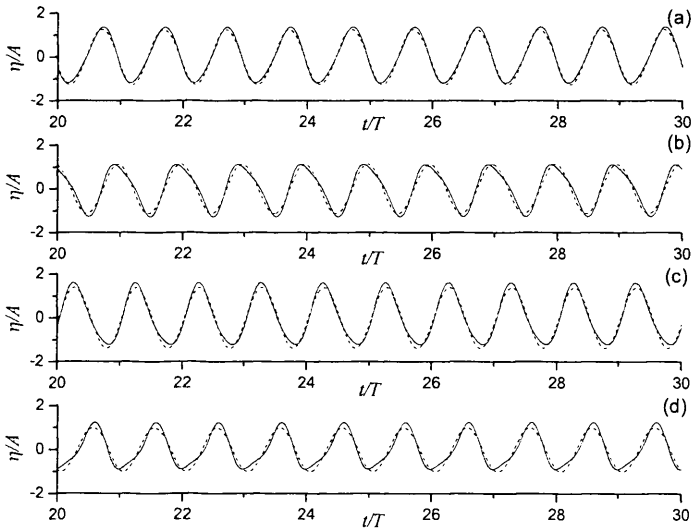

Figure 5.7.8 Wave histories at the backs of cylinders (a) one, (b) two, (c) three, (d) four
····· linear; —— linear plus second order

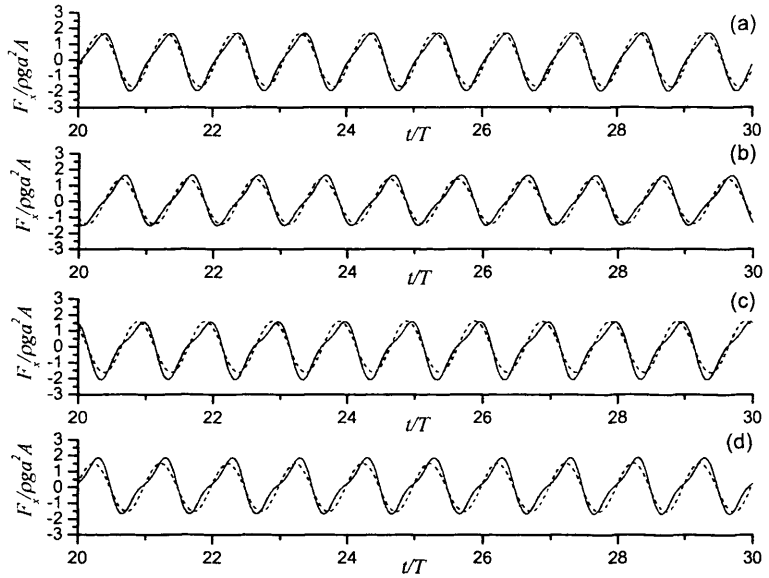

Figure 5.7.9 Histories of horizontal forces on cylinders (a) one, (b) two, (c) three and (d) four
····· linear; —— linear plus second order

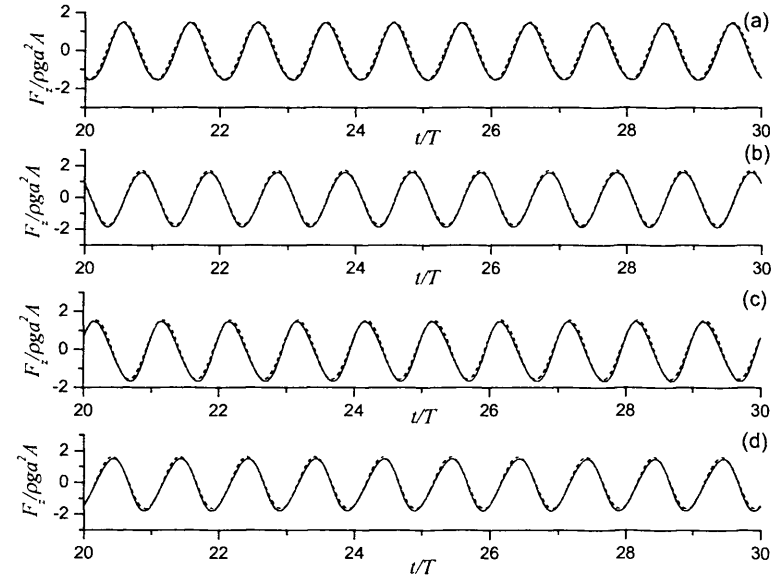

Figure 5.7.10 Histories of vertical forces on cylinders (a) one, (b) two, (c) three and (d) four
····· linear; —— linear plus second order

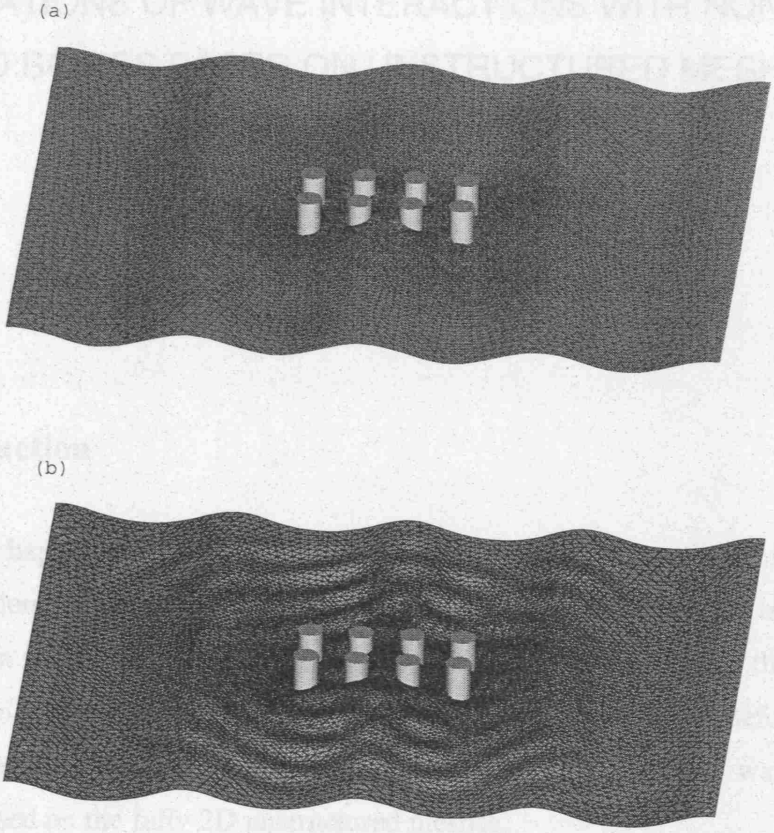

Figure 5.7.11 Free surface profiles at t=25T
(a) linear; (b) linear plus second order

6. SIMULATIONS OF WAVE INTERACTIONS WITH NON-WALL-SIDED BODIES BASED ON UNSTRUCTURED MESHES IN TWO-DIMENSIONS

6.1 Introduction

In the last chapter, we gave a second order simulation of interactions of waves and multiple cylinders. For large amplitude waves or large amplitude motions of structures, the perturbation method will be invalid. In these cases, the fully nonlinear theory should be used. We will consider fully nonlinear problems from this chapter. Before 3D fully nonlinear simulations, we give some 2D numerical results about wave-structure interactions based on the fully 2D unstructured meshes.

As mentioned in Chapter 1, there have been extensive applications of the FEM to fully nonlinear wave-body interaction problems in the last decade. For example, Wu & Eatock Taylor (1994) used both the FEM and the mixed FEM to analyse the 2D nonlinear transient water wave problems. Wu & Eatock Taylor (1995) subsequently made detailed comparison between the FEM and the BEM for the nonlinear free surface flow problem and found that the former was more efficient in terms of both CPU and memory requirement. Later, Ma, Wu & Eatock Taylor (2001a, b) extended the technique to simulate interactions between waves and three dimensional fixed structures in numerical tanks and Hu, Wu & Ma (2002) to the case of a vertical cylinder in forced motions. Other FEM based simulations include those by Clauss & Steinhagen (1999), Robertson *et al.* (1999, 2004), Westhuis (2001) and Wang & Khoo (2005).

The publications mentioned above mainly used structured meshes. A structured mesh is easier to generate but may become ineffective if the fluid domain is complex due to the geometry of the body or large motion of the boundaries. In this case, an unstructured mesh will be more suitable, such as that use by Greaves *et al.* (1997), Zhu *et al.* (2001) and Turnbull *et al.* (2003) in 2D and Wu & Hu (2004) in 3D.

All these applications are either for submerged bodies or for wall-sided or non-flared floating bodies where the body surface at the moving waterline is always vertical to the still water level. In fact, the nonlinear effect will become more significant for a body with flare. From the computational point of view, the presence of the flare makes the mesh generation more complex, especially in the local area. The slope or the curvature of the body near the waterline also makes it more difficult to trace the movement of the waterline in the nonlinear simulation. In this chapter, we use BAMG (Hecht, 1998) to generate the unstructured mesh in the fluid domain (see Figure 6.1.1). Simulations are first made for wave motions in a rectangular tank and for progressive waves in a numerical tank, and results are compared with published data for validation. The focus of this work is on a wedge either in forced large amplitude motion or in nonlinear waves in a numerical tank, and on twin wedges. The wedge has been widely investigated in the water entry problem and extensive survey of the work in this area has been given in Wu, Sun & He (2004). This is a good example of a non-walled body, and results for this case can provide valuable information on the nature of wave interactions with some complicated body shapes.

In the simulations, some numerical algorithms presented in Chapter 3 will be utilised in this chapter. The velocity is obtained using the Galerkin method and the free surface information is updated using the fourth order Runge-Kutta method. The free surface is regularly remeshed and smoothed using the B-spline and the energy method respectively. The damping zone method is employed to absorb the incoming wave and minimize the reflection. The second order theory is also used in several cases for comparison.

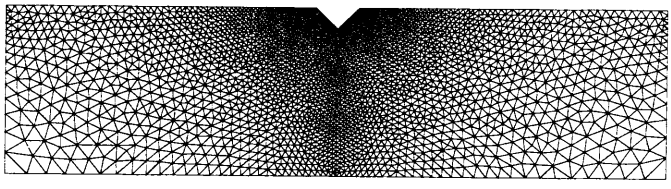

Figure 6.1.1 An unstructured mesh for a floating wedge

6.2 Free oscillation problems

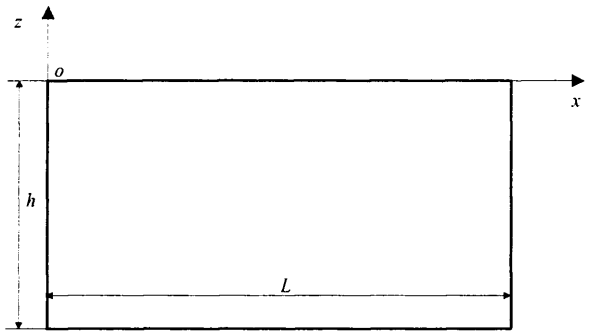

Figure 6.2.1 Sketch of a container

The first validation case concerns a free oscillation problem in a rectangular container with length L and depth h=L/2, as shown in Figure 6.2.1. The initial wave elevation and the velocity potential on the free surface are given as, respectively

$$\eta(x, t = 0) = A\cos(2\pi x/L),$$

$$\phi(x, \eta(x,0), t = 0) = 0,$$

where A is the wave amplitude. The analytical solutions of first and second order wave elevations at $x = L/2$ for this case have been given by Wu & Eatock Taylor (1994)

$$\eta^{(1)}(x, t) = a\cos(\omega_2 t)\cos(k_2 x), \tag{6.2.1}$$

$$\eta^{(2)}(x = L/2, t) = \frac{1}{8g}[2(\omega_2 A)^2 \cos 2\omega_2 t) + \frac{A^2}{\omega_2^2}(k_2^2 g^2 + \omega_2^4) - \frac{A^2}{\omega_2^2}(k_2^2 g^2 + 3\omega_2^4)\cos\omega_4 t)], \tag{6.2.2}$$

where

$$k_i = i\pi/L \quad (i = 1, 2, 3, \ldots),$$

$$\omega_i = [k_i g \tanh(k_i h)]^{1/2} \quad (i = 1, 2, 3, \ldots).$$

This result will be used for validation below.

In the simulation, the finite element nodes are uniformly distributed along the free surface and the bottom of the container. Equation (4.2.1) is used to control the distribution of nodes on the side walls along the depth to have smaller elements near the free surface. An initial mesh is shown in Figure 6.2.2 with NF=120 uniform segments on the free surface, NB=NF/2 uniform segments on the bottom and NH=40 non-uniform segments on the side walls. Two cases at A/h=0.05 and 0.1 are considered. The step of nondimensional time $\tau = t/\sqrt{h/g}$ is set to be 0.05 for the former and 0.025 for the latter, respectively. It is found that smoothing needs to be applied regularly. The mesh at

$\tau = 4.9$ without smoothing is shown in Figure 6.2.3, and the simulation crashes subsequently. When smoothing is applied every 20 time steps, the result becomes stable and the mesh at $\tau = 12$ is shown in Figure 6.2.4. The numerical results with two different meshes are shown in Figure 6.2.5, together with the linear solution plus the second order solution obtained from equations (6.2.1) and (6.2.2). The figure suggests that the numerical simulation is convergent and provides good accuracy.

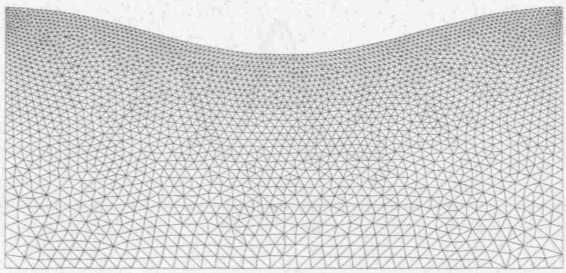

Figure 6.2.2 An initial mesh for a container with 2807 nodes and 5372 elements

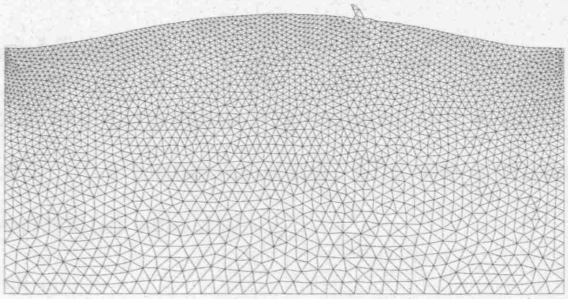

Figure 6.2.3 Mesh at τ=4.9 without smoothing

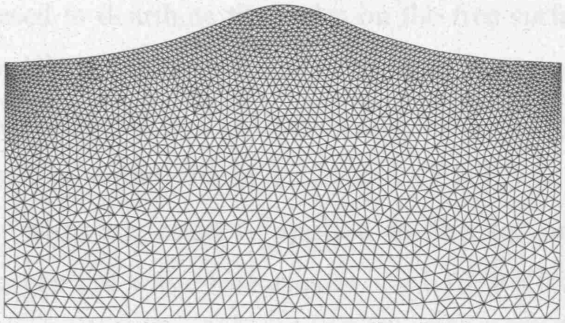

Figure 6.2.4 Mesh at τ=12 with smoothing

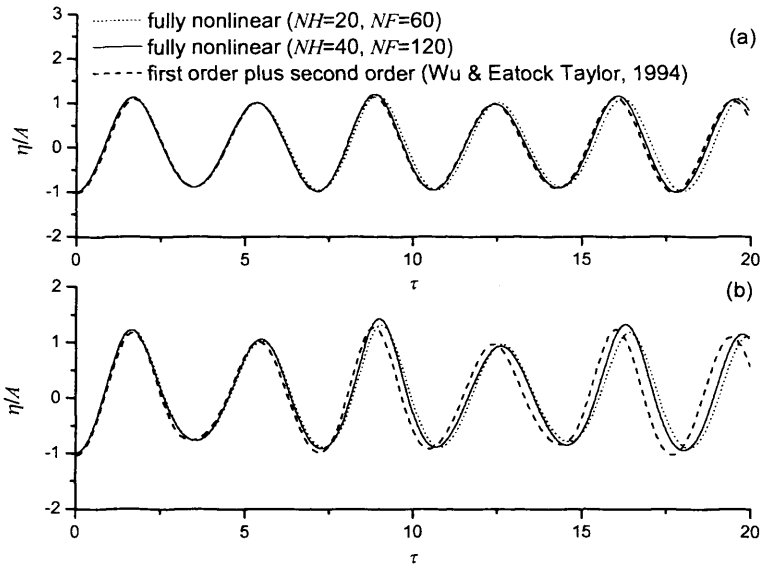

Figure 6.2.5 Wave histories in the container at x/L=0.5
(a) A/h=0.05; (b) A/h=0.1

6.3 Wave tank problems

We next consider wave propagation generated by a piston-type wave maker installed at the left side of a numerical tank. The wave maker undergoes motion with the following horizontal velocity

$$U(t) = \omega A \cos \omega t, \tag{6.3.1}$$

where ω and A are the motion frequency and amplitude of wave maker, respectively. The case chosen is that studied by Lin *et al.* (1984). In our simulation, $h = 0.6m$, $L = 9m$, $A = 0.05h$ and $\omega = 1.5539\sqrt{g/h}$. A similar procedure to equation (4.2.1) is used to distribute the nodes on the free surface. An initial mesh with NF=200, NB=150, NH=20 on the left side of the tank and 16 on the right is shown in Figure 6.3.1. This corresponds to 2423 nodes and 4458 elements. The damping zone method expressed in equations (3.3.32) and (3.3.33) is used to avoid the wave reflection. The damping zone is applied at the far end over one wave length. Figure 6.3.2 gives the wave histories at $x = 1.167h = 0.078L$, where again x is measured from the left hand end of the tank, with two different time steps, where $T = 2\pi/\omega$. It clearly shows that convergence in the time discretisation has

been achieved. The results have been compared visually with those by Lin *et al.* (1984) and no visible difference is found.

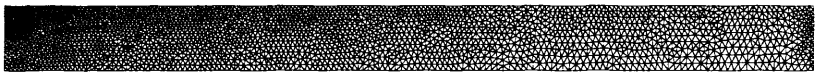

Figure 6.3.1 An initial mesh with 2423 nodes and 4458 elements

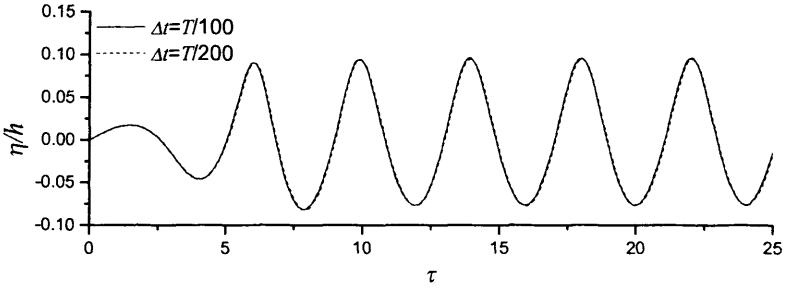

Figure 6.3.2 Wave histories in the tank at x=1.167h

Further validation is made by making comparison between the present fully nonlinear result and the solutions obtained from the perturbation method. In this method the first- and second-order velocity potentials satisfy the Laplace equation in the fluid domain

$$\nabla^2\phi^{(k)} = 0 \quad (k=1,2) \qquad \text{in} \quad \forall^{(0)}, \tag{6.3.2}$$

and they are subject to the conditions on the mean positions of the boundaries. They can be given as

$$\frac{\partial\phi^{(k)}}{\partial z} - \frac{\partial\eta^{(k)}}{\partial t} = f_k' \qquad \text{on } S_f^{(0)}, \tag{6.3.3}$$

$$\frac{\partial\phi^{(k)}}{\partial t} + g\eta^{(k)} = f_k'' \qquad \text{on } S_f^{(0)}, \tag{6.3.4}$$

$$\frac{\partial\phi^{(k)}}{\partial n} = f_k \qquad \text{on } S_w^{(0)}, \tag{6.3.5}$$

$$\frac{\partial\phi^{(k)}}{\partial z} = 0 \qquad \text{on } z=-h, \tag{6.3.6}$$

where $\forall^{(0)}$ is a time-independent fluid domain bounded by the tank bottom, the mean surface of the wave maker $S_w^{(0)}$, the still water surface $S_f^{(0)}$ and the far end of the tank. The terms f_k', f_k'' and f_k are given respectively as

$$f_k' = \begin{cases} 0 & (k=1) \\ \dfrac{\partial\phi^{(1)}}{\partial x}\dfrac{\partial\eta^{(1)}}{\partial x} - \eta^{(1)}\dfrac{\partial^2\phi^{(1)}}{\partial z^2} & (k=2) \end{cases},$$

$$f_k'' = \begin{cases} 0 & (k=1) \\ -\frac{1}{2}\left|\nabla\phi^{(1)}\right|^2 - \eta^{(1)}\frac{\partial^2\phi^{(1)}}{\partial z\partial t} & (k=2) \end{cases},$$

$$f_k = \begin{cases} -U & (k=1) \\ X\frac{\partial^2\phi^{(1)}}{\partial x^2} & (k=2) \end{cases},$$

where $X = A\sin\omega t$ is due to the motion of the wave maker. The closure of this problem can be achieved by including the initial and the radiation conditions. It is then solved through the quadrilateral element based the FEM with quadratic shape functions. An advantage of using the quadratic shape functions is that the second order derivatives can be obtained directly. For the wave tank problem, 80 segments in the horizontal direction and 7 in the vertical direction are used, which corresponds to 1855 nodes and 560 elements. The results are shown in Figure 6.3.3 together with the fully nonlinear solution and the experiment result given by Lin *et al.* (1984). It can be seen that the linear plus second order solution is in very good agreement with the fully nonlinear result and the experiment result for this case.

It should be noticed that no modulation function is used for the second-order body surface condition [see equation (6.3.5)] which seems to contradict the conclusion made in Chapter 5 that the modulation function is very important for the second order solution. Actually, like the modulation function, the smoothing is also helpful to improve the numerical result. In order to demonstrate this, we make a comparison of waves in three cases. In Case one, smoothing is used but without modulation function; In Case two, both smoothing and modulation are used and in Case three neither smoothing nor modulation function is used. The results are shown in Figure 6.3.4. It is seen that the development of the first order waves in the three cases is very good. For second order waves, they are also good in Cases one and two but very bad in Case three. In general, the first- and second-order waves in Cases one and two are graphically identical when they reach the period state. Therefore, the smoothing is very important for the second order waves if no modulation function is used.

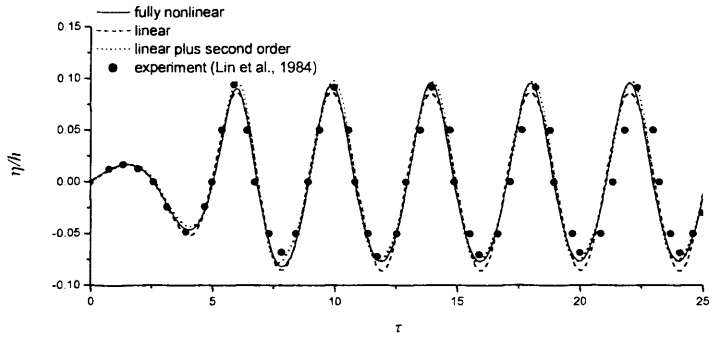

Figure 6.3.3 Comparison of wave histories at x=1.167h

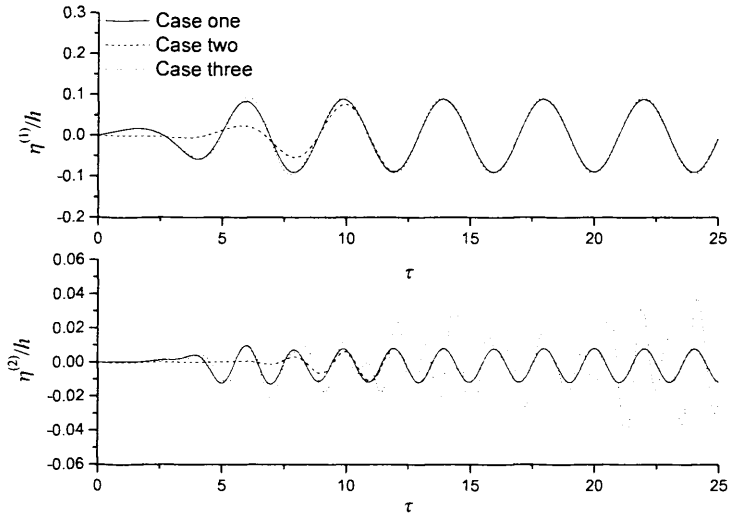

Figure 6.3.4 Influence of smoothing and modulation function on first- and second-order waves

After these comparisons, fully nonlinear simulations are made for the wave maker at larger amplitude. A case at $A/h = 0.1$ is considered. The wave history at the same location as above is shown in Figure 6.3.5 and the wave profile at $\tau = 24.26$ is shown in Figure 6.3.6. As expected, the nonlinear features in these figures become more evident.

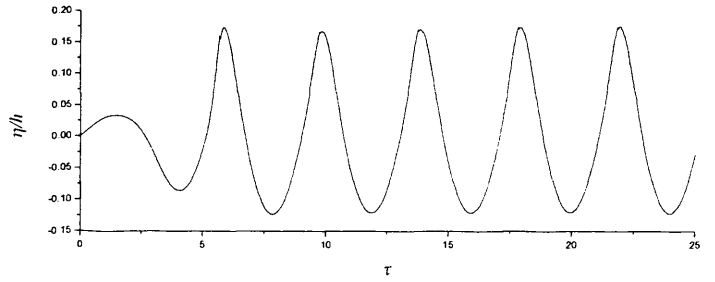

Figure 6.3.5 Wave history in the tank with A/h=0.1

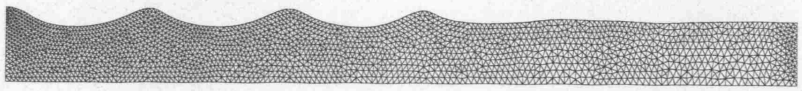

Figure 6.3.6 Wave profile in the tank at τ=24.26 (A/h=0.1)

We now put a wedge in the tank at x=10h. The body is symmetric about a vertical line and Figure 6.3.7 shows half of the wedge. The case considered corresponds to d=0.4h and θ=75°. The motion of the wave maker still follows that defined in equation (6.3.1). The motion amplitude is taken as A=0.05h and the frequency remains the same. The wave profile at τ=58.63 is shown in Figure 6.3.8. In the simulation, the wetted surface of the body may vary significantly with the time, and the number of nodes on the surface will follow this change to ensure the sizes of the elements attached to the body will remain more or less the same.

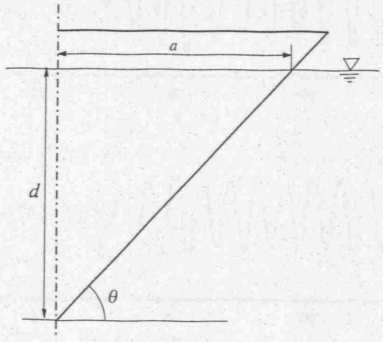

Figure 6.3.7 Sketch of a floating wedge

The wave history at x=1.167h is shown in Figure 6.3.9. The difference between this case and that in Figure 6.3.2 is that waves will be reflected from the body after several periods. The corresponding hydrodynamic forces without the contribution of initial buoyancy are shown in Figure 6.3.10, and they are obtained using equation (3.3.46) from Wu & Eatock Taylor (1996, 2003).

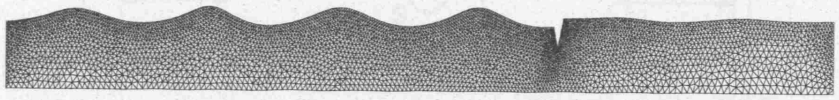

Figure 6.3.8 Wave profile at τ=58.63

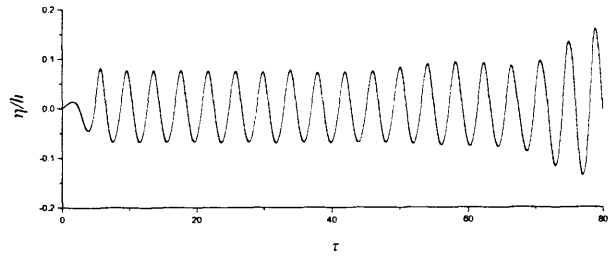

Figure 6.3.9 Wave history at x=1.167h

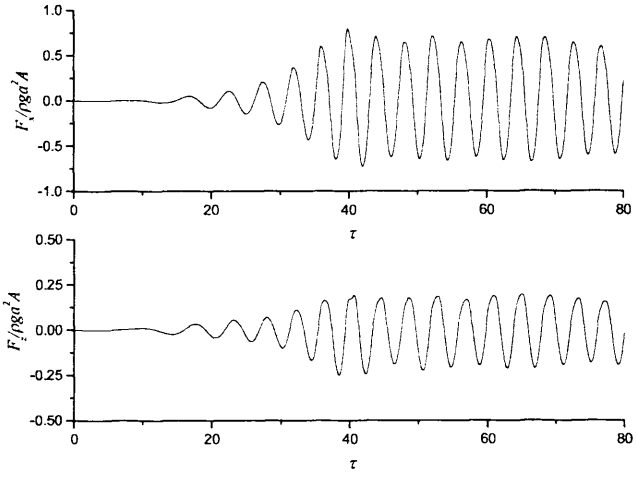

Figure 6.3.10 History of force on a wedge in the tank

6.4 Forced oscillations of floating wedge-shaped bodies

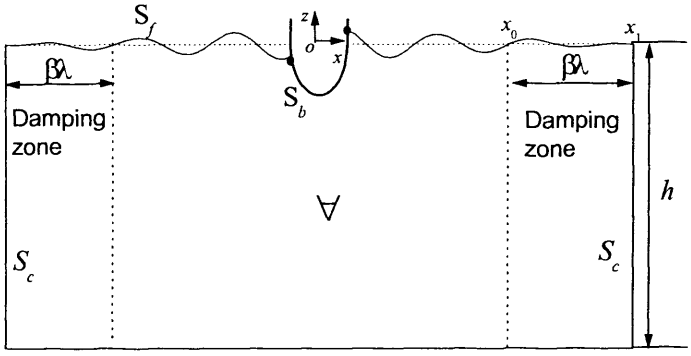

Figure 6.4.1 Coordinate system

We consider floating bodies in forced motions on the free surface in an open sea as shown in Figure 6.4.1. The damping zone is set at the both ends of the computational domain. A symmetric wedge-shaped body is considered here. The initial draught of the wedge is d=1m and width $2a$ as shown in Figure 6.3.7. The body is assumed to be subject to the following sinusoidal horizontal or vertical displacement

$$X = A\sin\omega t \text{ or } Z = A\sin\omega t\,. \tag{6.4.1}$$

The centre line of the wedge is taken as the z axis. In order to avoid an abrupt start and allow a gradual development of the radiated potential, the body surface boundary condition is multiplied by the following modulation function, as used by Isaacson *et al.* (1993)

$$M(t) = \begin{cases} \frac{1}{2}[1-\cos(\pi t/2T)] & t < 2T \\ 1 & t \geq 2T \end{cases} \quad (T = \frac{2\pi}{\omega}). \tag{6.4.2}$$

We take $d = h/8$, θ=60° and A/d=0.5, which is relatively large motion. Two cases of vertical motion at $\omega = 2\sqrt{g/h}$ and $\omega = 3\sqrt{g/h}$ are calculated and the wave elevation at $x = -2d$ is shown in Figure 6.4.2, where $\overline{\omega} = \omega/\sqrt{g/h}$. The length of the computational domain on each side of the body is 3λ (λ is the wave length) and is divided into 100 intervals. 20 intervals are used along the depth. On the seabed, the number of intervals is only two-fifths of that on the free surface. It should be noticed that the node numbers on the free surface and the body surface vary with time. The time step is taken as T/100. Smoothing and remeshing are applied every 20 steps. The nonlinearity at $\omega = 3\sqrt{g/h}$ is stronger, because this corresponds to a shorter wave.

Another simulated case corresponds to a wedge of θ=45° in vertical motion at A/d=0.5 and $\omega = 2\sqrt{g/h}$. The wave histories are shown in Figure 6.4.3. For the heaving motion, the flow should be symmetric about the centre line of the wedge. However, due to the asymmetric nature of the unstructured mesh, symmetry in results may not be achieved because of insufficient accuracy. We plotted the results at $x = \pm 2d$ in Figure 6.4.3a and $x = \pm 3d$ in Figure 6.4.3b. The figures clearly show that the symmetry is accurately maintained. For the linear problem, the wave histories near and away from the body should all be sinusoidal when the motion has become fully periodic, even though their amplitudes may be different. When nonlinear effects are strong, the higher order components become significant. The wave histories at different

locations will have not only different amplitudes but also different shapes, as shown in Figure 6.4.3.

To compare the present simulation with the result from the corresponding perturbation solution, the wedge with $\theta = 45^\circ$ in vertical motion is calculated here with several amplitudes. In this case, the second order body surface boundary condition may be expressed as

$$\frac{\partial \phi^{(k)}}{\partial n} = f_k \qquad \text{on } S_b^{(0)}, \qquad (6.4.3)$$

where $S_b^{(0)}$ is the mean body surface and f_k (k=1,2) are given as

$$f_k = \begin{cases} \dfrac{dZ}{dt} n_z & (k=1) \\ -Z(n_z \dfrac{\partial^2 \phi^{(1)}}{\partial z^2} + n_x \dfrac{\partial^2 \phi^{(1)}}{\partial x \partial z}) & (k=2) \end{cases}.$$

We consider a case with $\omega = 3\sqrt{g/h}$ at $A/d = 0.1, 0.2$ and 0.4. The waves at $x = -2d$ are given in Figure 6.4.4. The figure shows that the results from the fully nonlinear solution and the perturbation theory are in good agreement at A/d=0.1. Noticeable differences appear at A/d=0.2 and become significant at A/d=0.4. Further results from the nonlinear simulation for wave elevation at $x = -3d$ and for force are given in Figure 6.4.5. The nonlinear features become very strong when the amplitude increases. Further simulation is made for a wedge of $\theta = 60^\circ$ in the identical condition. The results are shown in Figure 6.4.6. The nonlinear features are still quite visible but weaker than the those corresponding to $\theta = 45^\circ$, as the waterline is more 'wall-sided' in this case.

The case of a wedge of θ=45° in sway motion at A/d=0.5 and $\omega = 2\sqrt{g/h}$ is also considered. The wave elevation and forces are shown in Figures 6.4.7 and 6.4.8. It can be seen from Figure 6.4.7 that the difference between phases of the wave histories at $x = -2d$ and $x = 2d$ is about half a period. In fact, strictly speaking, after sufficiently long period of time, these two curves should become identical if one of them is moved along the horizontal direction. This can be explained using the argument made by Wu (1993, 2000). We can define y pointing out of the paper. One can view the same problem either along or against the y direction. The difference between these two cases is that there will be a phase difference of half a period when the problem becomes

periodic. As a result, the horizontal force will have components at $(2n+1)\omega$, while the vertical force components will be at $2n\omega$, $(n = 0, 1, 2...)$ This can be seen in Figure 6.4.8. In fact we may write

$$\frac{F}{\rho g d A} = \frac{a_0}{2} + \sum_{i=1}^{\infty}[A_i \cos(i\omega t) + B_i \sin(i\omega t)]. \qquad (6.4.4)$$

The results using the Fourier analysis are shown in Figure 6.4.9. It can be seen that the horizontal force is dominated by the component corresponding to $i = 1$, while the vertical force by $i = 0$ and $i = 2$.

A wedge in large heaving motion relative to the water depth is also considered. In this case, the elements below the body can be squeezed or stretched, similar to the 3D case considered by Wu & Hu (2004). It is vital that remeshing is applied regularly to avoid any over distorted elements. We consider the case at A/d=0.4, $\omega = 2\sqrt{g/h}$, h=$2d$ and θ=75°. This means that the distance from the tip of the wedge to the bottom of the fluid changes from $0.6d$ to$1.4d$. The wave history at x=$2d$ is shown in Figure 6.4.10 and the corresponding hydrodynamic force is given in Figure 6.4.11. The wave is highly nonlinear. Some snapshots of the mesh at different time steps are shown in Figure 6.4.12 and the result of remeshing is evident.

Twin-wedges are also considered here. Recently Wu (2006) solved the water entry problem for this case through a three stage approach. He found that the pressure between the wedges can increase significantly as the wedges move into the water. Here both wedges have θ=75°. The symmetry line of the two wedges is taken as the the z axis and the centre lines of the two bodies are located at $x = -1.5d$ and $x = 1.5d$. The results for heaving motion at $\omega = 2\sqrt{g/h}$, A/d=0.1 and h=$2d$ are shown in Figures 6.4.13, 6.4.14 and 6.4.15. The wave at x=0 is much larger than those at x=±$2d$, ±$3d$. The envelope of its amplitude is also very different. In fact it resembles to some extent the motion of sloshing waves in a tank, which is clearly because the location is confined within two bodies. The forces on both wedges should be identical and therefore the results are given only for one wedge. A difference between the twin-wedge and the single wedge in heaving motion is that there is a horizontal force here, as shown in Figure 6.4.15.

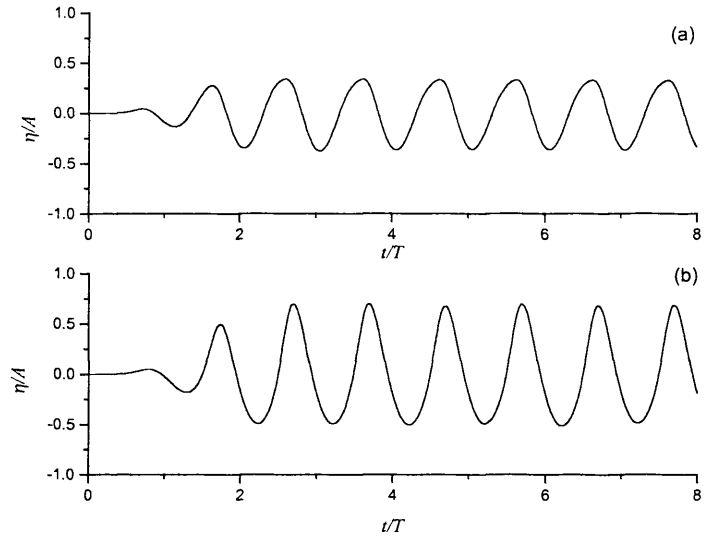

Figure 6.4.2 Wave histories near the wedge with θ=60° in vertical motion (x=-2d and A/d=0.5)
(a) $\bar{\omega}$=2.0; (b) $\bar{\omega}$=3.0

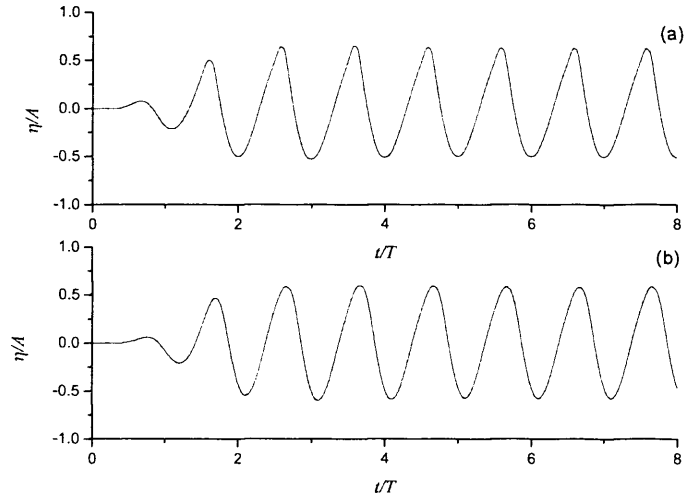

Figure 6.4.3 Wave histories near the wedge with θ=45° in vertical motion ($\bar{\omega}$=2.0 and A/d=0.5)
(a) $x=\pm 2d$ (b) $x=\pm 3d$

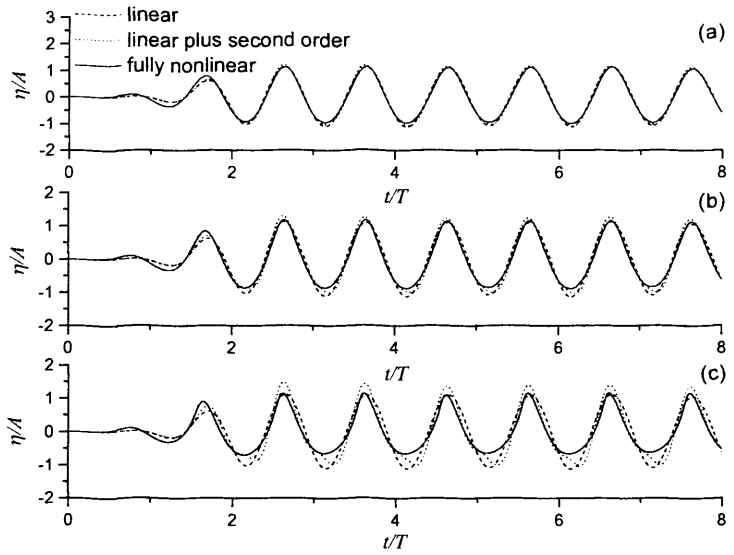

Figure 6.4.4 Comparison of wave histories near the wedge with θ=45° in vertical motion (x=-2d and $\bar{\omega}$=3.0)
(a) A/d=0.1; (b) A/d=0.2; (c) A/d=0.4

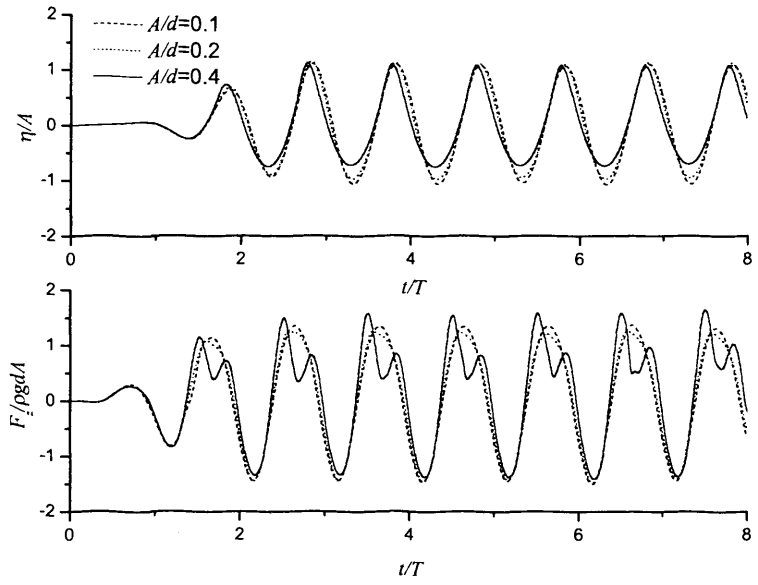

Figure 6.4.5 Wave histories at x=-3d and force histories for a wedge with θ=45° and $\bar{\omega}$=3.0 in vertical motion

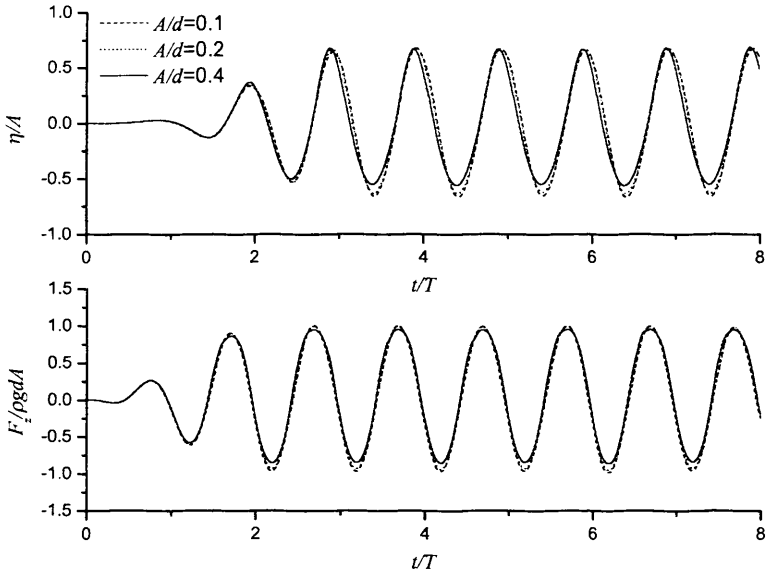

Figure 6.4.6 Wave histories at x=-3d and force histories for a wedge with θ=60° and $\bar{\omega}$=3.0 in vertical motion

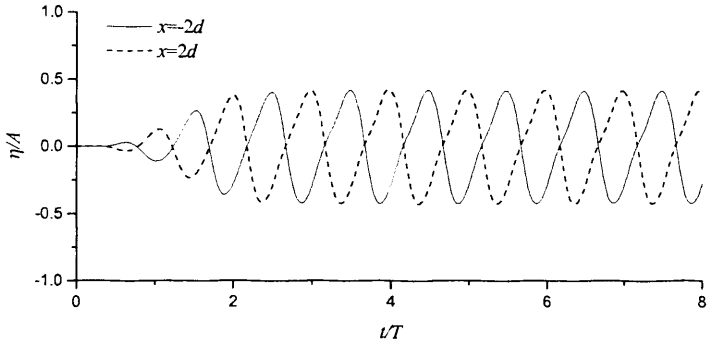

Figure 6.4.7 Wave histories near the wedge in sway motion ($\bar{\omega}$=2.0 and A/d=0.5)

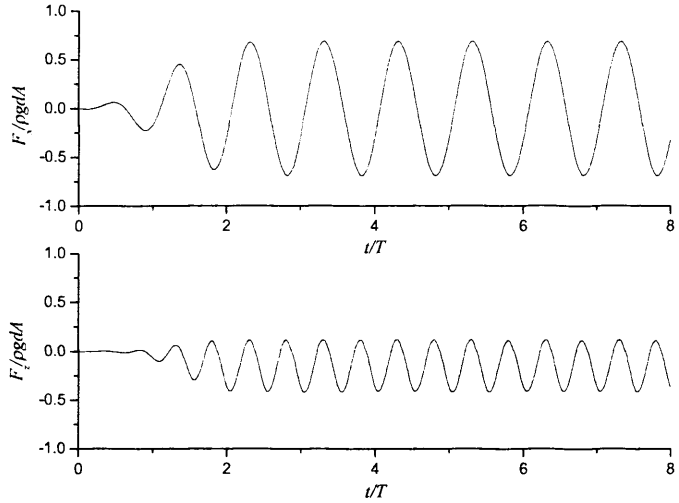

Figure 6.4.8 Hydrodynamic forces on the wedge in sway motion ($\bar{\omega}$=2.0 and A/d=0.5)

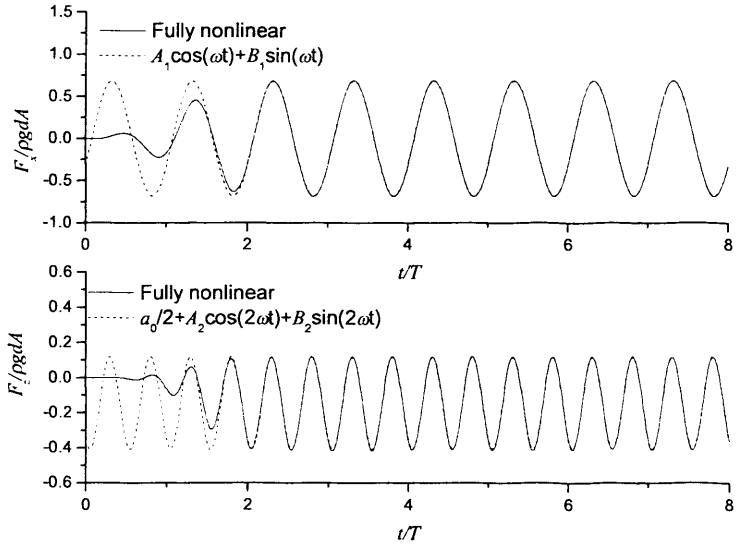

Figure 6.4.9 Fully nonlinear results and Fourier components of the force

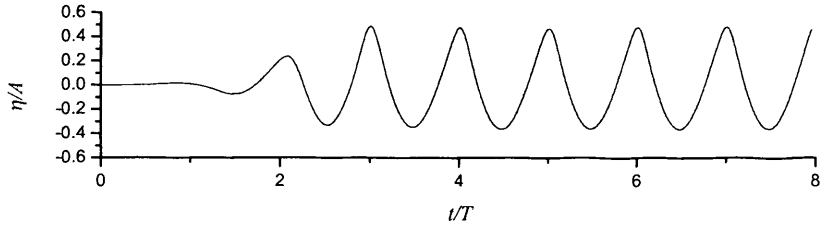

Figure 6.4.10 Wave history at x=2d

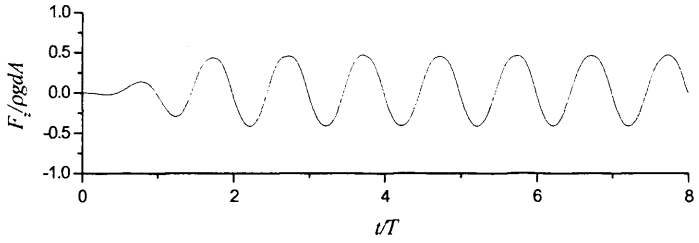

Figure 6.4.11 Force history

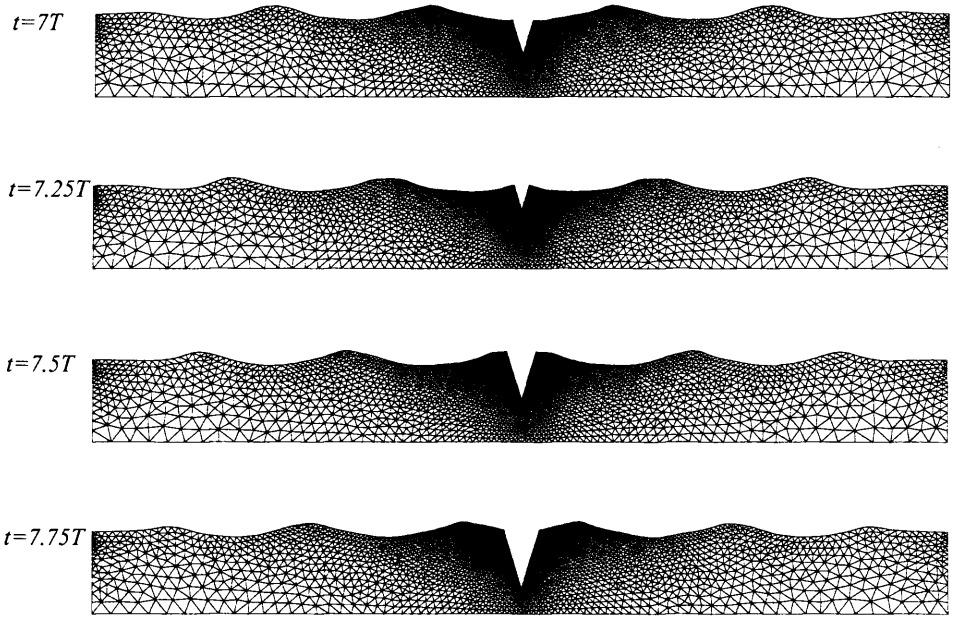

Figure 6.4.12 Meshes in the case of $h=2d$ and $A/d=0.4$

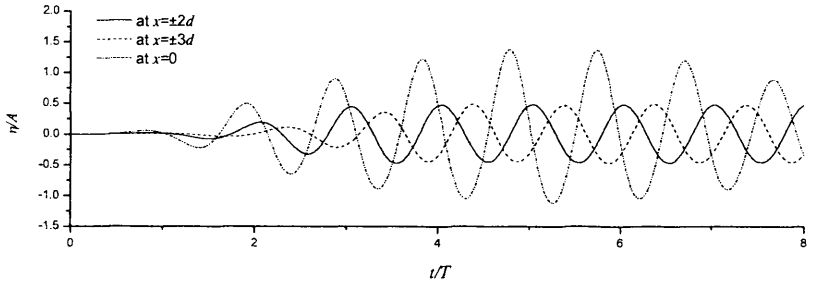

Figure 6.4.13 Wave histories during heave of twin-wedges

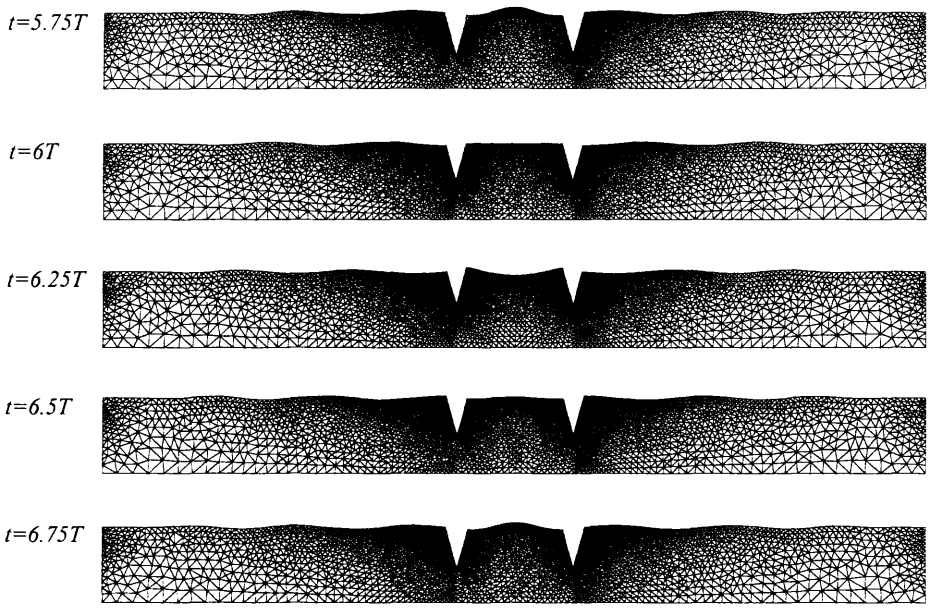

Figure 6.4.14 Meshes for the twin-wedges at different time steps

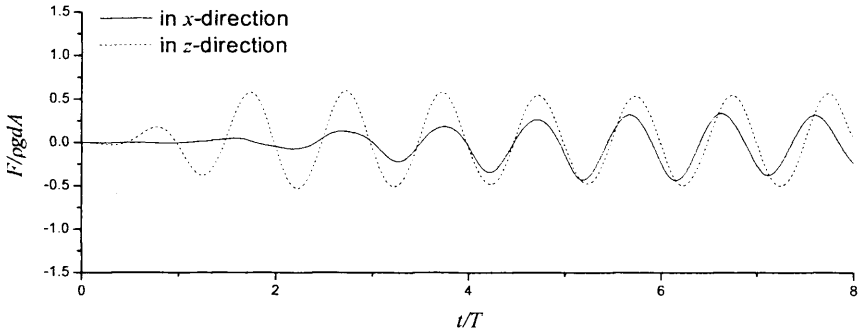

Figure 6.4.15 Force history for wedge one in heave

7. INTERACTIONS BETWEEN FULLY NONLINEAR WATER WAVES AND STRUCTURES IN A WAVE TANK

7.1 Introduction

In Chapter 6, we applied the numerical method for the interactions of fully nonlinear waves and non-wall-sided (flared) bodies based on the unstructured mesh in two-dimensions. There is extensive work on the 3D problem. For example, Ma, Wu & Eatock Taylor (2001a, b) simulated the interaction between waves and fixed cylinders in numerical tanks. Hu, Wu & Ma (2002) extended this method to the case of a cylinder in forced motion. Both of these two works are based on structured meshes. Even though remeshing is applied regularly, connectivity between nodes remains unchanged during the simulation. More recently, Wu & Hu (2004) considered a floating structure in large amplitude motion. A hybrid mesh, with the unstructured part near the body and the structured region away from the body, is used. A completely new grid is generated regularly and information is transported from one mesh to another. All these works, however, are for cylindrical structures with no variation of the cross section in the vertical direction.

For the problem of interactions between steep waves and structures, an interesting topic is wave impact at the bows of FPSOs, which may cause green water loading. A noticeable feature in FPSO design is the large bow with pronounced flare above the still waterline. A greater flare can improve the performance of ships by increasing local reserve of buoyancy and limiting the green water on deck (Schneekluth & Bertram, 1998). With such a change in design, traditional prediction methods become less reliable and direct numerical simulations would be more appropriate. However, flare can cause a rapid variation in pressure especially when the relative angle between the structure and the free surface is small, and the hydrodynamic forces on the flared structure may have stronger nonlinearity than those without flare. This will make the simulation more difficult and complex.

An application of flare in offshore structures is the Draugen platform as shown in Figure 7.1.1. The Draugen platform is used to produce oil in the North Sea, it was built

in 1984. The platform has a concrete monotower base structure with a flare above the mean sea level to more efficiently support the integrated topside facilities.

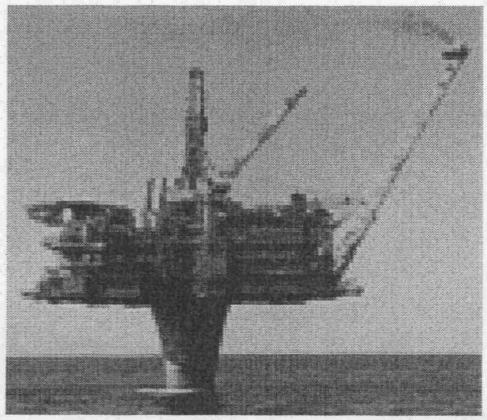

Figure 7.1.1 The Draugen platform

Another interesting problem is the interaction of waves and multiple cylinders. The diffraction by an array of cylinders in the open sea has been studied based on the second order theory in the time domain in Chapter 5, and the mutual influence of cylinders on waves and hydrodynamic forces has been discussed and the trapped modes have been observed. However, a fully nonlinear simulation of this problem has not yet been undertaken.

In this chapter, we will first utilise the numerical method and mesh generation method presented in Chapters 3 and 4 to study the interaction of waves and single-structure with flare based on the fully nonlinear wave potential theory. This work is an extension of the previous ones for 2D non-wall-sided and 3D wall-sided bodies. The mesh generation is different from that in Wu & Hu (2004) and needs more work since it is for flared structures, and has been presented in Chapter 4. We summarise it as follows: A 2D unstructured mesh is generated on a horizontal surface using BAMG (Hecht, 1998), and then it is extended along the vertical direction following a curve rather than a line. Thus, a 3D mesh with prism elements has been generated. Similar to the 2D problem on flared bodies presented in Chapter 6, the Galerkin method (equation 3.3.5) will be utilised to calculate the velocity in the fluid domain for this 3D problem. Numerical results will be provided to show the nonlinear features of waves and forces/moments. Comparisons of waves and forces/moments between bottom mounted and truncated cylinders will be made, and the influence of flare on waves and forces/moments will be discussed. And then, we give some simulations for interactions of irregular waves and a cylinder. Finally, we will investigate interactions of waves and

multiple cylinders through the fully nonlinear wave theory, and the effect of the nearly trapped mode will be discussed.

7.2 Simulations of interactions between waves and a single cylinder with flare

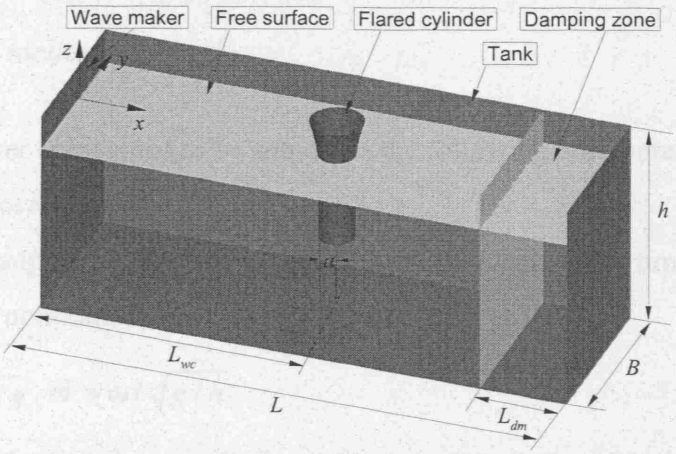

Figure 7.2.1 Computational domain for a numerical tank

A numerical wave tank with length L, width B and depth h is shown in Figure 7.2.1. The x-axis of the coordinate system is along the longitudinal direction of the tank, z-axis is positive upwards and the origin is on the undisturbed free surface. A wave maker is initially located at the left end of the tank (x=0) and a structure such as a cylinder with flare is placed on the plane y=0 and it is L_{wc} away from the left end.

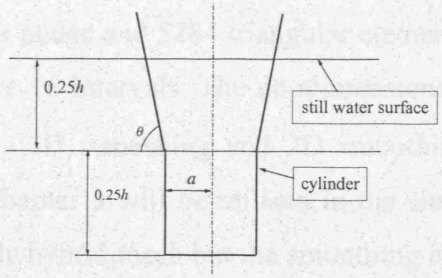

Figure 7.2.2 Dimension of the truncated cylinder with flare

In all the simulations, the water depth h is set to be 1.0m, length L =12h, and breadth B= 0.72h. The radius of the cylinder without flare is a=0.1416h. When the cylinder has flare, the variation of the cross section starts from z=-0.25h, and the angle between the

flare and the horizontal plane is denoted as θ. The dimensions of a truncated cylinder are shown in Figure 7.2.2. For the single-cylinder case, the cylinder is located at a distance of $L_{wc}=7h$ away from the left end of the tank. The Sommerfeld-Orlanski radiation condition and the damping zone method [see equations (3.3.32) and (3.3.33)] are used with the length of damping zone $L_{dm}=\lambda$ (λ is the wavelength of the linear wave).

7.2.1 Regular motions

The wave maker is assumed to be subject to the following horizontal harmonic motion

$$X = -A\cos\omega t, \tag{7.2.1}$$

where A is the amplitude of motion, and ω is the frequency. The time t and oscillatory frequency ω are nondimensionalized as follows:

$$\tau = t/\sqrt{h/g}\,,\ \overline{\omega} = \omega/\sqrt{g/h}\,.$$

We first consider some cases of a bottom mounted cylinder with $\theta=80^{\circ}$, in which the nodimensional frequency $\overline{\omega}$ is set to be 2.0. In all the simulations for flared cylinders, the location at which wave history will be provided is selected at $x=L_{wc}-2a$. The wave history with a small oscillatory amplitude $A=0.01h$ for a bottom mounted cylinder is shown in Figure 7.2.3. We use a 2D hybrid mesh on the horizontal plane (see Figure 4.2.11). The structured mesh is within the range $x\leq 2.1h$ and the unstructured within $2.1h\leq x\leq L$. There are 200 intervals for hybrid mesh in the x-direction (40 for the structured mesh and 160 for the unstructured mesh) and 14 intervals in y-direction, which corresponds to 2869 nodes and 5284 triangular elements for the 2D hybrid mesh. In the z-direction, there are 16 intervals. The nondimensional time interval is set to be $\overline{T}/100$ ($\overline{T}=2\pi/\overline{\omega}$). The 3D remeshing and 2D smoothing [see equation (3.3.20)] techniques presented in Chapter 3 will be utilised in the simulation. The remeshing is performed within the whole hybrid mesh but the smoothing is only along the y-direction within the structured mesh for both the wave elevation and the velocity potential every 20 time steps. The corresponding force and moment are shown in Figure 7.2.4. The force is calculated by first solving equations (3.3.36)~(3.3.40) to obtain ϕ_t and then integrating the pressure on the cylinder surface since the cylinder is fixed. The initial buoyancy is excluded from the vertical force and hereinafter in other figures. The

vertical force is absent for a wall-sided cylinder but it is quite significant here. In fact the figure indicates that it has more high frequency components than the horizontal force.

Figure 7.2.5 shows the wave histories for the bottom mounted cylinder with three different amplitudes A=0.01h, 0.02h and 0.04h, and the corresponding force and moment are provided in Figure 15. It is clearly seen that the nonlinear effect is noticeable for the wave, force and moment. There is a 12.3% or so reduction of the maximum value of η / A (at $\tau \approx 52.15$) from the case at A/h=0.01 to that with 0.02 and a 28.5% reduction from A/h=0.02 to 0.04. This suggests that the effect of the nonlinearity evolves much faster from A/h=0.02 to 0.04 than it does from A/h=0.01 to 0.02. This is of course expected as a function can be normally approximated by the linear term in the Taylor expansion when the variable is small. When the variable increases, the higher order terms become more important. Similar behaviour can also be found for the force and moment in Figure 7.2.6. In this particular case, the fact that the nonlinear effects associated with flare cause a reduction compared to the linear wave loading is in marked contrast with the general findings for wall-sided bodies.

We give a comparison of the wave between the bottom mounted cylinder and a truncated cylinder with the same angle $\theta = 80^\circ$. The wave history corresponding to $\overline{\omega} = 2.0$ and $A = 0.02h$ is shown in Figure 7.2.7 and there is hardly any visible difference between these two cases. The corresponding time histories of force and moment are shown in Figure 7.2.8. The force component in the x-direction and the moment on the bottom mounted cylinder is larger than those on the truncated cylinder but their difference is small. This is expected as the wave effect is significant mainly near the free surface. The peaks of the vertical force on the truncated cylinder are visibly larger than those of the force on the bottom mounted cylinder. This is partly because for the truncated cylinder the bottom of the cylinder also provides a contribution to the vertical force.

Similar comparison is made for cylinders with θ=75° with all the other parameters remaining the same as above. Figure 7.2.9 gives the wave elevation. The difference in results for the truncated cylinder and the bottom mounted cylinder is more significant

than the corresponding results for $\theta = 80°$. Part of the reasons is that θ=75° corresponds to a larger water plane area. Relative to the diameter of the water plane, the draught of the cylinder is smaller in the case of θ=75°. The change at the bottom of the cylinder therefore has a larger effect on the results. Further results at θ=75° are given for $A = 0.04h$ in Figures 7.2.10 and 7.2.11. The difference between the results for the truncated cylinder and the bottom mounted cylinder is even more significant. Part of the reason is due to the larger degree of nonlinearity at $A = 0.04h$. While the nonlinear components decay more slowly along the depth (Eatock Taylor, Hung & Chau, 1989), the change at the bottom of the cylinder has even greater effect.

Comparison is also made for bottom mounted cylinders with $\theta = 75°$ and $\theta = 80°$. The amplitude of the wave maker is set to be $A = 0.04h$. The wave histories are shown in Figure 7.2.12, and the corresponding force and moment in Figure 7.2.13. It is seen that the wave near the body is generally smaller for the cylinder with $\theta = 75°$ than that for the cylinder with $\theta = 80°$. This suggests that a flare with smaller value of θ may be more effective to suppress the wave near the body. However, the force and moment on the cylinder with $\theta = 75°$ are larger than those on the cylinder with $\theta = 80°$. A typical wave profile around a flared cylinder is shown in Figure 7.2.14.

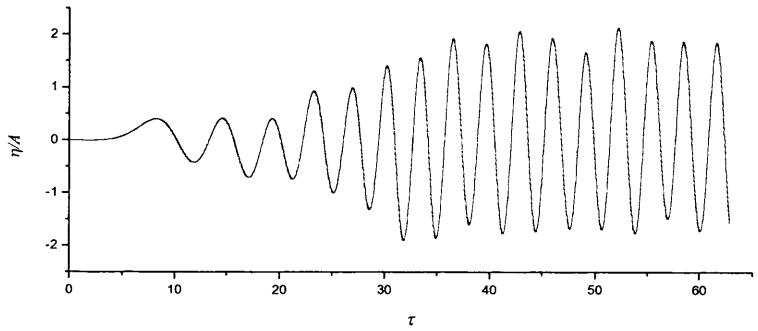

Figure 7.2.3 Wave history at $x=L_c-2a$ at A/h=0.01 for a bottom mounted cylinder with θ=80°

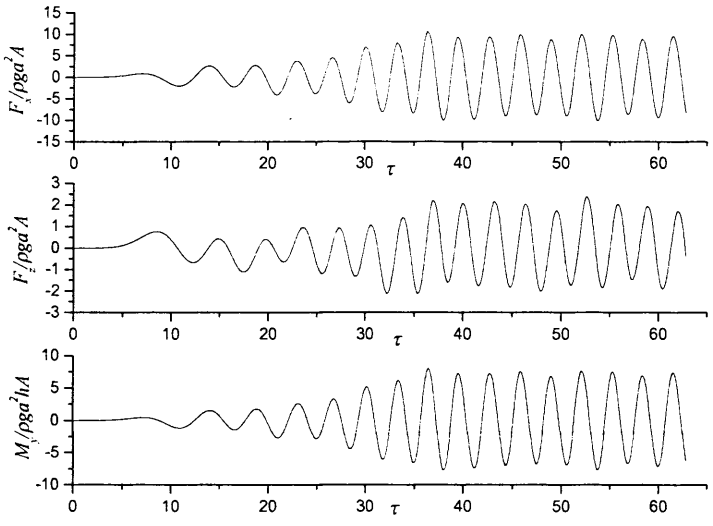

Figure 7.2.4 Histories of force and moment on a bottom mounted cylinder with θ=80° at A/h=0.01

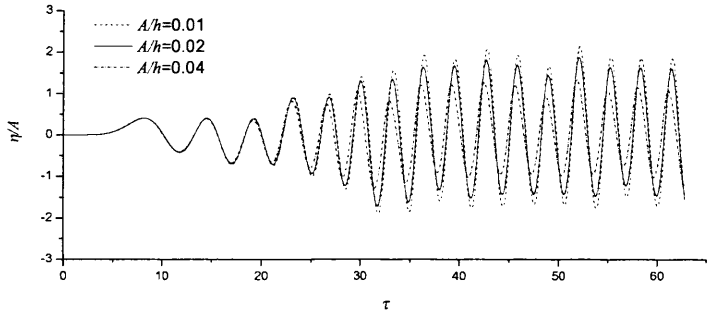

Figure 7.2.5 Comparison of wave histories for a bottom mounted cylinder with θ=80°

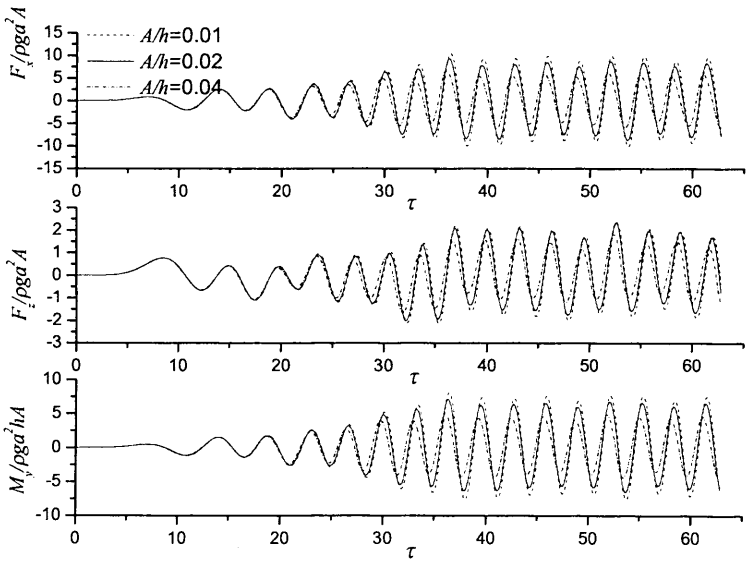

Figure 7.2.6 Comparison of force and moment on a bottom mounted cylinder with θ=80°

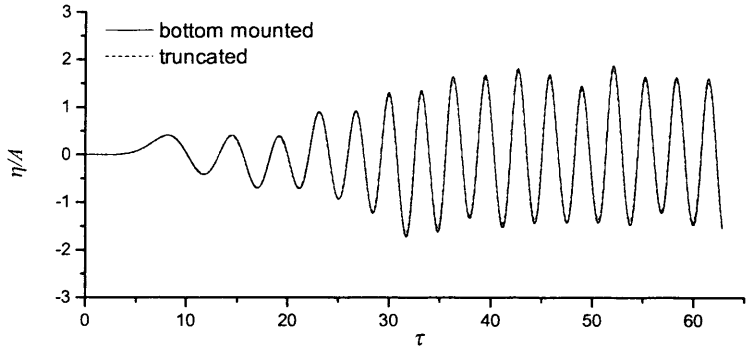

Figure 7.2.7 Comparison of wave histories for a bottom mounted cylinder and a truncated cylinder with θ=80° at A/h=0.02

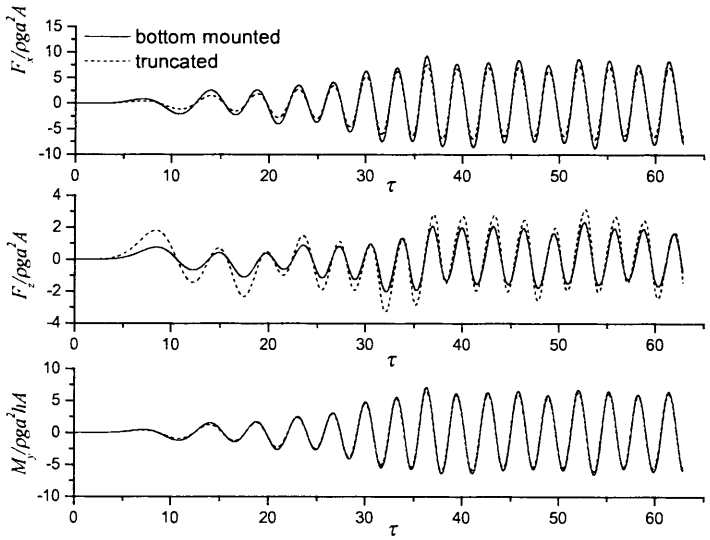

Figure 7.2.8 Comparison of force and moment on a bottom mounted cylinder and a truncated cylinder with θ=80 ° at A/h=0.02

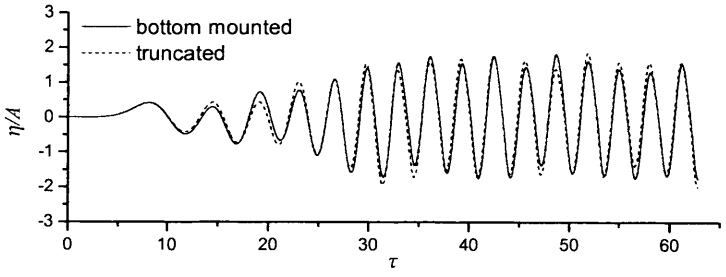

Figure 7.2.9 Comparison of wave histories for a bottom mounted cylinder and a truncated cylinder with θ=75° at A/h=0.02

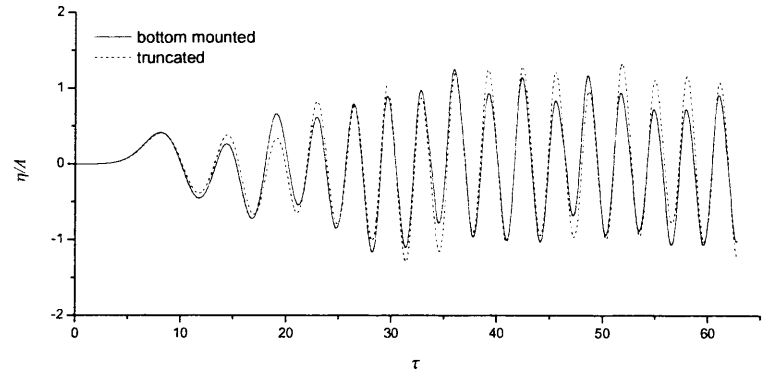

Figure 7.2.10 Comparison of wave histories for a bottom mounted cylinder and a truncated cylinder with θ=75° at A/h=0.04

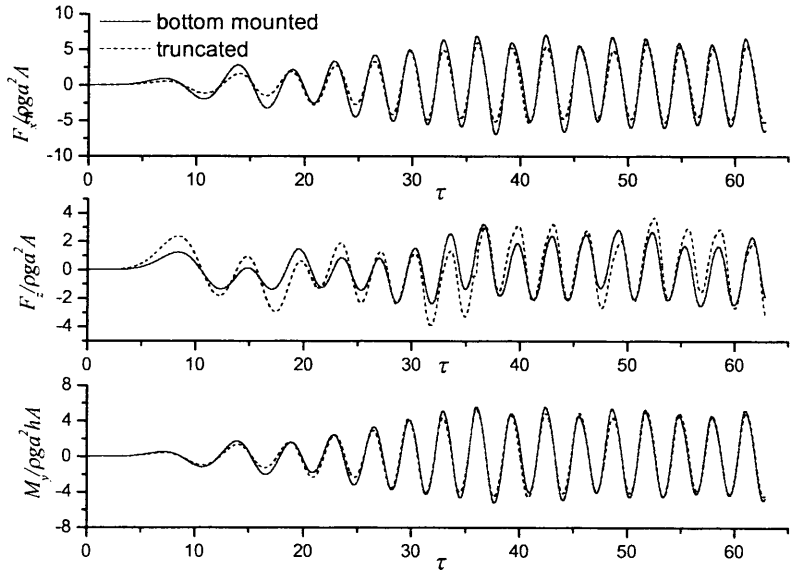

Figure 7.2.11 Comparison of force and moment on a bottom mounted cylinder and a truncated cylinder with θ=75° at A/h=0.04

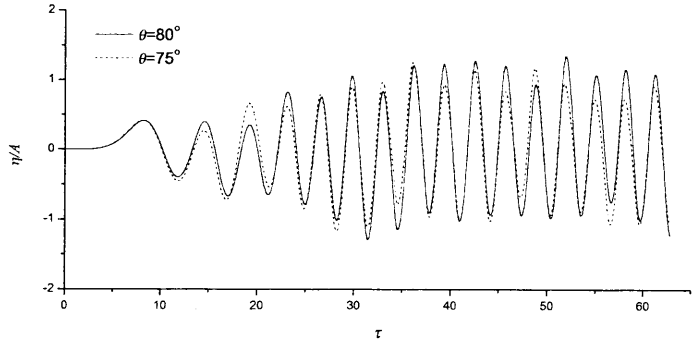

Figure 7.2.12 Comparison of wave histories for two bottom mounted cylinders at A/h=0.04

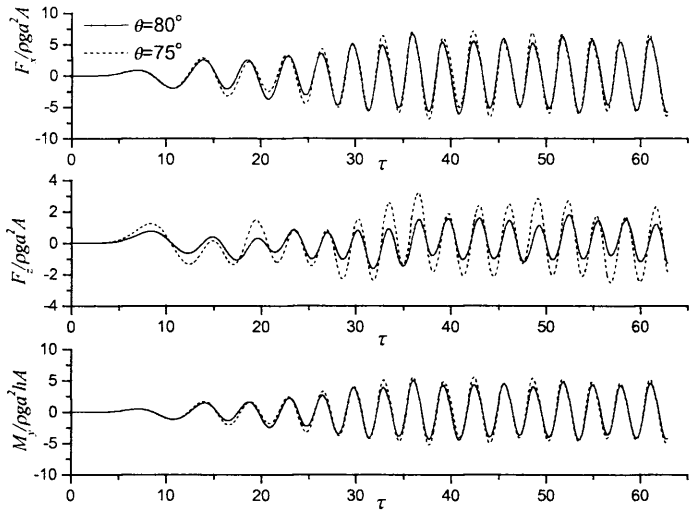

Figure 7.2.13 Comparison of force and moment on two bottom mounted cylinders at A/h=0.04

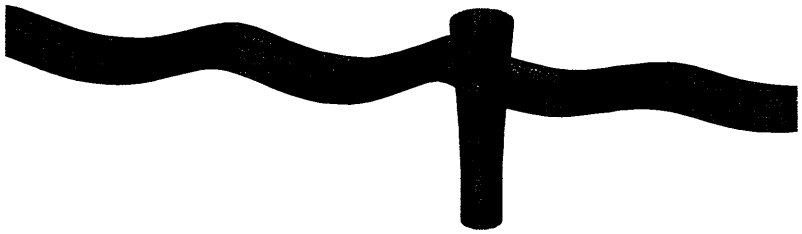

Figure 7.2.14 Wave profile around the cylinder of θ=75° with A/h=0.04 at τ=61.2

7.2.2 Irregular motions

The above simulations are limited to regular motions of the wave maker. Waves in the actual sea environment are generally random. The corresponding hydrodynamic forces on ocean structures and their responses are also random. Therefore, a study on interactions of the random waves with structures is important but difficult since the random wave has a lot of components at different frequencies. In this section, we consider the irregular wave, which has only a few components of frequencies. Most studies on irregular waves are based on the linear or perturbation theories. For examples, Forristall (1985) estimated the kinematics of irregular waves. Longuet-Higgins (1963) and Dean & Sharmar (1981) developed the Stokes second-order irregular wave model for deep and finite water depth, respectively. Pierson (1993) proposed a theory of the Stokes third-order nonlinear irregular waves in deep water. A recent simulation of irregular waves is the work of Boo (2002) based on the fully nonlinear wave potential theory. In this section, we will undertake some simulations for

irregular waves, which are generated by linear superposition of a series of monochromatic linear motions of the wave maker

$$X = \sum_{i=1}^{n} (-A_i \cos \omega_i t), \tag{7.2.2}$$

where X denotes the horizontal displacement of the wave maker, A_i and ω_i are the oscillatory amplitude and frequency of each monochromatic motion, respectively, and n is the number of total monochromatic motions. In the simulations below, we select four monochromatic motions, whose corresponding frequencies ω_i (i=1, 2, 3, 4) are selected as 5.25, 5.55, 6.73 and 7.46 (*rad/s*), respectively. These four frequencies have been used by Boo (2002) to simulate linear and nonlinear irregular waves in a numerical tank. When the damping zone method in equations (3.3.32) and (3.3.33) is used, the frequency is chosen as the lowest one of the four monochromatic motions, at which the corresponding wavelength is longest. This gives a longer damping zone and the wave may be absorbed more effectively. The motion of the wave maker is shown in Figure 7.2.15 with four amplitudes A_i (i=1, 2, 3, 4) equal to 0.003885h, 0.003489h, 0.002381h and 0.001938h, respectively. We consider a flared cylinder with $\theta = 80°$ at the same location as the regular motions. The histories of wave and force are shown in Figures 7.2.16 and 7.2.17 with a time interval $\Delta\tau = 0.025057$. It is seen that the wave and force have typical irregular features and there are about three wave envelopes during the whole simulation. Each wave envelope has a nondimensional period about 65.6 (corresponding to 20.94 seconds) due to a minimum frequency interval $\Delta\omega$=(ω_2-ω_1)=0.3 (*rad/s*).

A comparison between three cases has also been made. Case one corresponds to those A_i above, Case two to $2A_i$ and Case three to $4A_i$. The results are shown in Figures 7.2.18 and 7.2.19. In the Figures, $\overline{A} = \sum_{i=1}^{4} A_i \Big/ 4$ is the average amplitude. The nonlinear feature is captured, which is similar to that in the regular motions of the wave maker. For the random wave, the typical linear elevation has a Normal distribution. However, the nonlinear wave will deviate from the Normal distribution. In order to relate how the nonlinearity of the irregular wave affects the magnitude of the deviation, we first calculate the standard deviations of wave elevations in these three cases. The wave data is recorded starting from $\tau = 56$ over two wave envelope periods. The three standard

deviations are founded to be 0.0122, 0.0199 and 0.0277, respectively. We then calculate the so-called skewness λ_3 to explain the nonlinear feature of the irregular wave

$$\lambda_3 = \frac{1}{\sigma^3}\frac{1}{n}\sum_{i=1}^{n}(\eta_i - \overline{\eta})^3, \tag{7.2.3}$$

where n is the total number of time steps, σ the standard deviation, η_i the wave elevation at i-th time step, and $\overline{\eta}$ the mean of all $\eta_i (i = 1,2,\cdots,n)$. For the linear wave, the skewness will be zero. For the nonlinear wave, its distribution is asymmetrical about the mean water surface. A wave with stronger nonlinearity will be more asymmetrical about the mean water surface. The skewness may be used to describe the asymmetry. A larger skewness means that the wave peaks are greater than troughs and so more asymmetrical about the mean water surface. The three skewnesses are obtained to be 0.0614, 0.0788 and 0.119, respectively, which indicates that the wave nonlinear feature becomes stronger with increase of the amplitude of the wave maker. Some wave profiles in Case one are given in Figure 7.2.20, which shows the feature of the irregular wave in space and time.

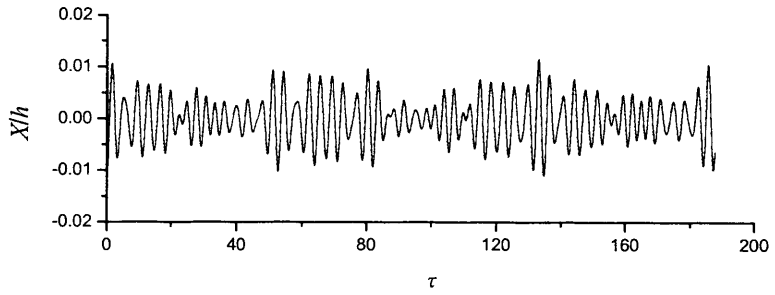

Figure 7.2.15 Motion of the wave maker

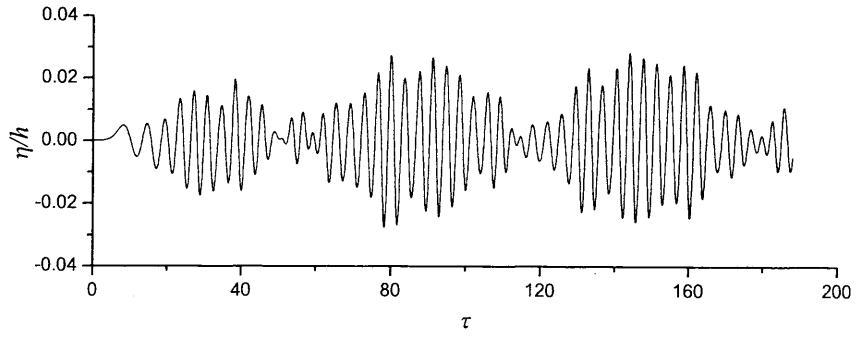

Figure 7.2.16 Wave history at $x=L_{wg}-2a$

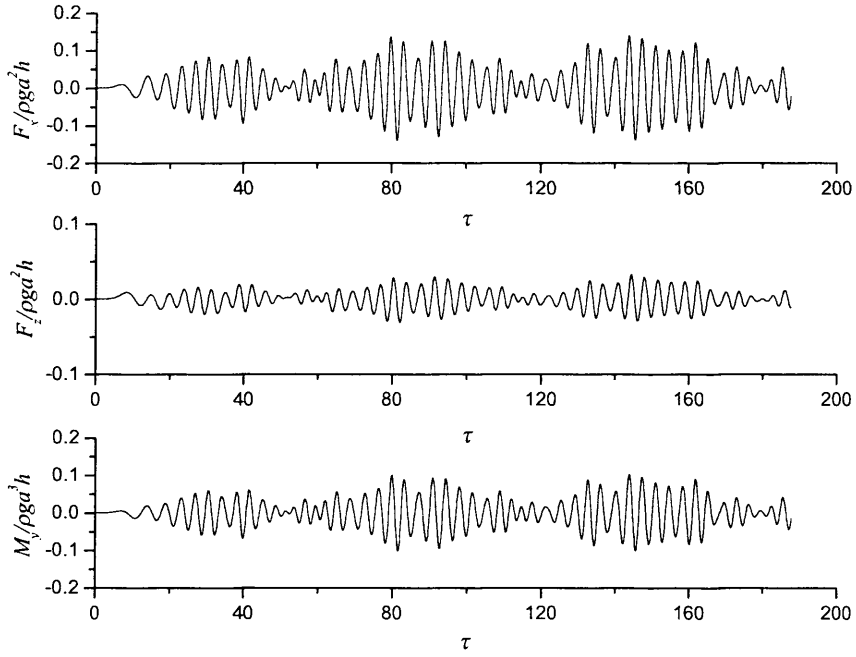

Figure 7.2.17 Histories of force and moment on the cylinder in Case one

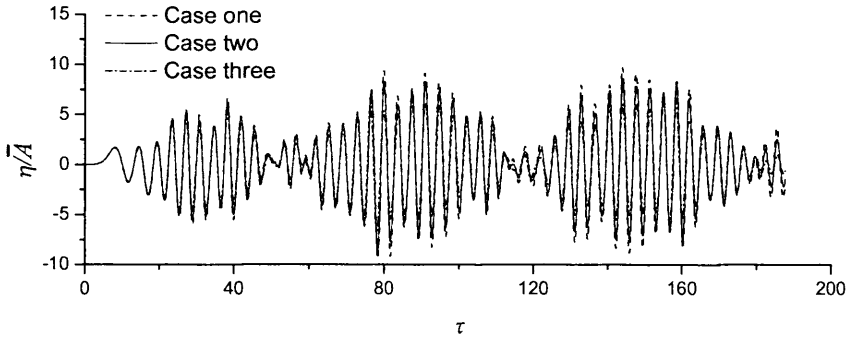

Figure 7.2.18 Wave histories at $x=L_{wc}-2a$

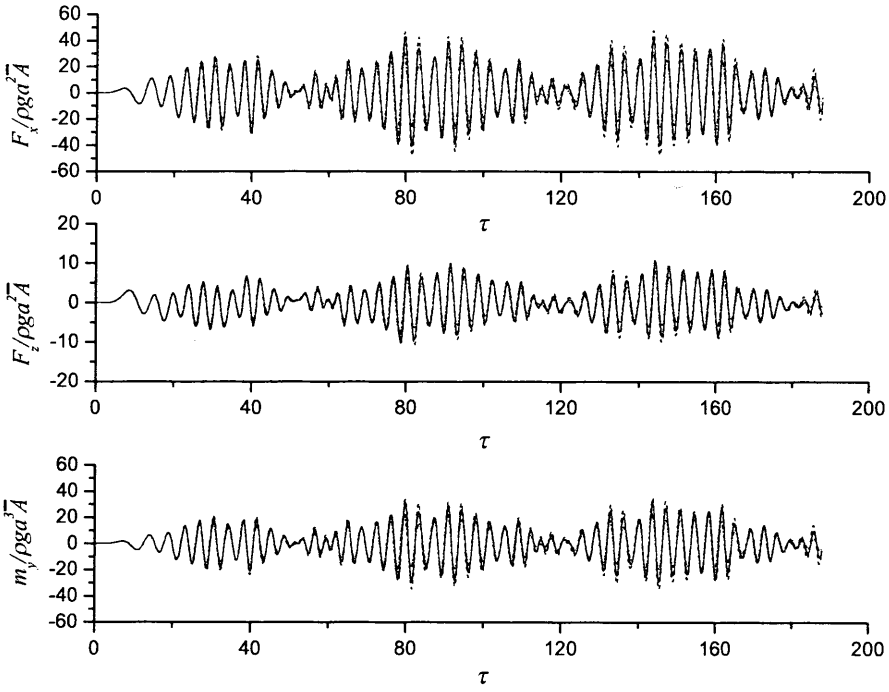

Figure 7.2.19 Comparison of forces and moments on the cylinder
-------- Case one; —— Case two; -------- Case three

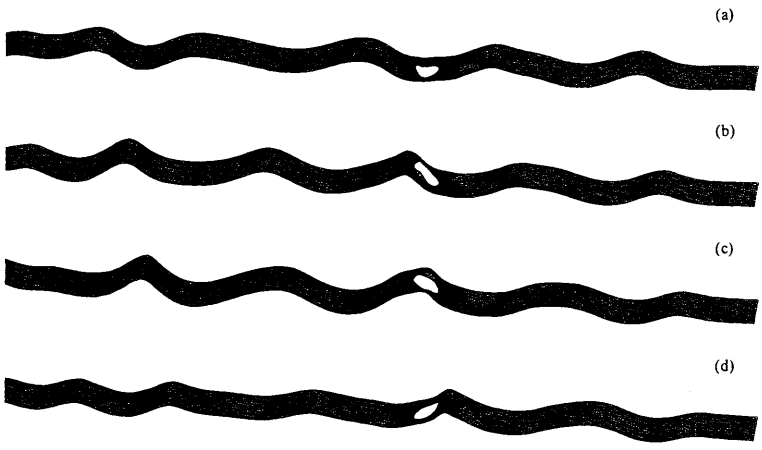

Figure 7.2.20 Irregular wave profiles at time steps (a) 6000, (b) 6050, (c) 6100, (d) 6150

7.3 Simulations for multiple cylinders

In Chapter 5, we presented some numerical results for diffraction by an array of vertical cylinders based on the second order theory in the time domain. In this section, we will investigate fully nonlinear interactions of waves and multiple cylinders without flare in a numerical wave tank, which may have not been considered in previous

publications. Ma (1998) considered a case of two cylinders in a numerical wave tank based on the structured mesh. For an array of cylinders the advantage of the unstructured mesh becomes more obvious.

The motion of the wave maker is subject to the harmonic motion given in equation (7.2.1). We first consider a case of three bottom mounted cylinders. The cylinders are placed on the plane y=0 and the second cylinder is located at a distance from the left end of the tank $7h$ and the distance between two neighboring cylinders is L_{cy}=$7a$. The configuration is shown in Figure 7.3.1. In the simulation, we choose equations (3.3.2a) and (3.3.2c) rather than the Galerkin method [equation (3.3.5)] to calculate the velocity since the cylinder is wall-sided. Both smoothing and remeshing are performed every 20 time steps. The amplitude of the wave maker is A=$0.01h$ and the nondimensional frequency $\overline{\omega}$ is still set to be 2.0. The wave histories are shown in Figure 7.3.2. The waves at the front sides are generally larger than those at the back sides for cylinders two and three, but not one. For cylinder one, the wave at the front side is also larger than that at the back side when $\tau < 33$ but it then becomes smaller, which is very different from that in the single isolated cylinder case as shown in Figure 7.3.3. The hydrodynamic forces and moments on the three cylinders are given in Figure 7.3.4. Generally, the peaks and troughs of the force and moment on cylinder one are the largest and those on cylinder two are the smallest. The wave histories for cylinder two with three different motion amplitudes A=$0.01h$, $0.02h$ and $0.04h$ are provided in Figure 7.3.5 for comparison and it still shows the same nonlinear feature as that in a single-cylinder case although there is interference between cylinders.

Comparisons of waves and forces between bottom mounted and the corresponding truncated cylinders are also made and the results are given in Figures 7.3.6 and 7.3.7. The amplitude of the wave maker is $0.01h$. The waves and forces on bottom mounted cylinders are generally larger than those on truncated cylinders. The difference of waves between the two cases is very clear and it is even more evident than that in a single-cylinder case reported by Wu & Hu (2004) at a larger amplitude A=$0.02h$.

We then run another three-cylinder case with L_{cy}=$4a$, and the nondimensional frequency remain the same as above, which corresponds to a nondimensional wavenumber k_0l=1.14 (k_0 is the wavenumber and l=L_{cy}/2). In Chapter 5, we consider two cases L_{cy}=$4a$ and $7a$ at k_0l=1.14 and compare the results with that for a single isolated cylinder, and we found the case at L_{cy}=$4a$ is probably near the trapped mode. We further compare the result between two cases L_{cy}=$4a$ and $7a$ at k_0l=1.14 here. The

results for cylinder two are given in Figure 7.3.8, in which the result for a single isolated cylinder at the same location is also included. It is seen that the force and moment at L_{cy} =7a are even smaller than those on the single cylinder. However, they are noticeably larger at L_{cy}=4a. The result is consistent with those obtained in Chapter 5 and so the case L_{cy}=4a may be near the trapped mode.

We further consider a seven-cylinder case with $\overline{\omega}$ = 2.0 and L_{cy}=4a, which may also be close to the trapped mode. The middle cylinder is located at (x, y)=(7h,0). The wave histories for cylinder four is shown in Figure 7.3.9. It is clearly seen that the wave at the back side increases with the increase of the number of cylinders. For seven- and three-cylinder cases, the wave amplitude still shows an increase trend at the end of the simulation time. The maximum value of the wave peak within the whole simulation in the seven-cylinder case is about 2.1 times that in the single-cylinder case. The hydrodynamic force and moment show behaviour similar to the wave (see Figure 7.3.10). These results suggest a long array of cylinders in a wave tank may probably produce very large wave and hydrodynamic force in the Neumann trapped mode, and this is consistent with the result obtained by Maniar & Newman (1997) and Evans & Porter (1997a). The histories of forces on the seven cylinders are shown in Figure 7.3.11. The maximum force on cylinder five is nearly the same as that on cylinder four but noticeably smaller for the other cylinders. It should be mentioned that the waves and hydrodynamic forces would be much smaller than the prediction by the linear potential theory due to the viscous damping and nonlinear effects (Maniar & Newman, 1997), so the results calculated through fully nonlinear theory are probably smaller than those obtained through the linear theory in magnitudes. A typical wave profile around the seven cylinders is shown in Figure 7.3.12.

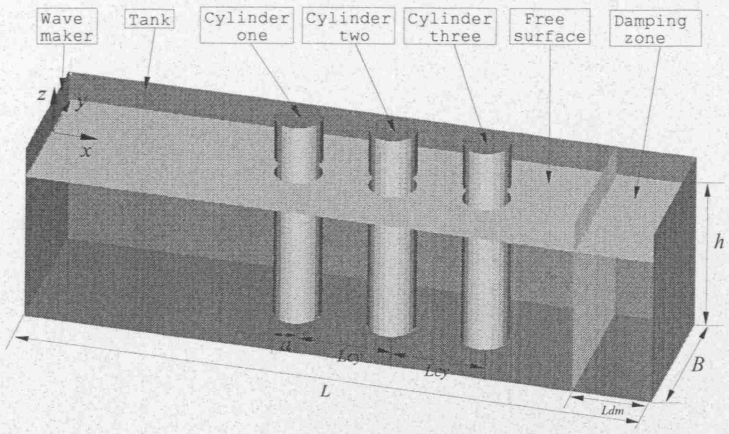

Figure 7.3.1 An array of three wall-sided cylinders in a numerical tank

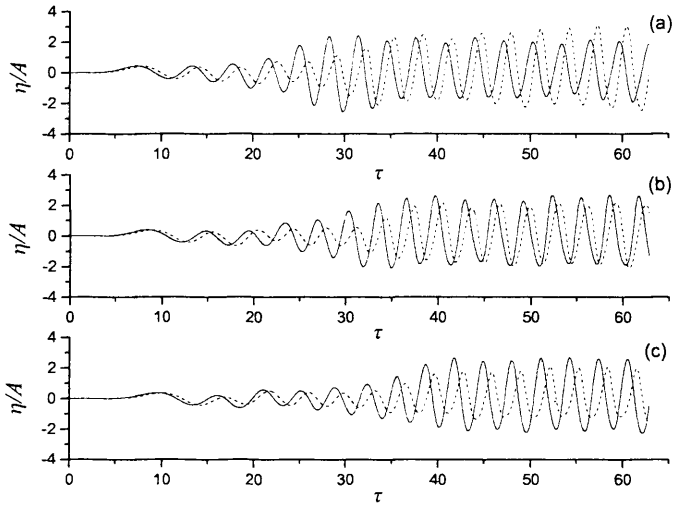

Figure 7.3.2 Wave histories for cylinders (a) one; (b) two; (c) three
—— front; ····· back

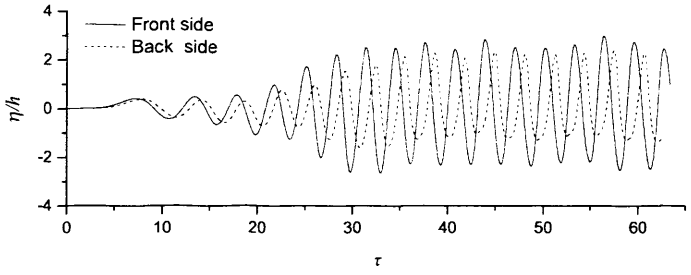

Figure 7.3.3 Wave histories for an isolated single cylinder

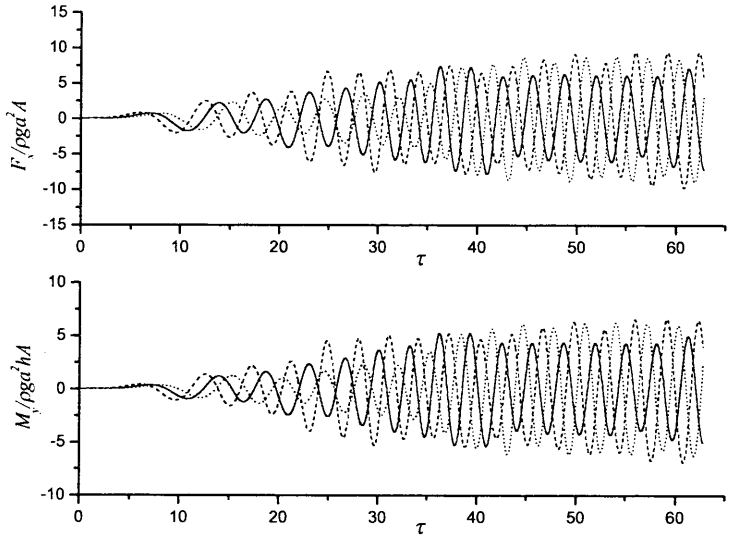

Figure 7.3.4 Hydrodynamic forces and moments on the three cylinders
------ cylinder one; —— cylinder two; ····· cylinder three

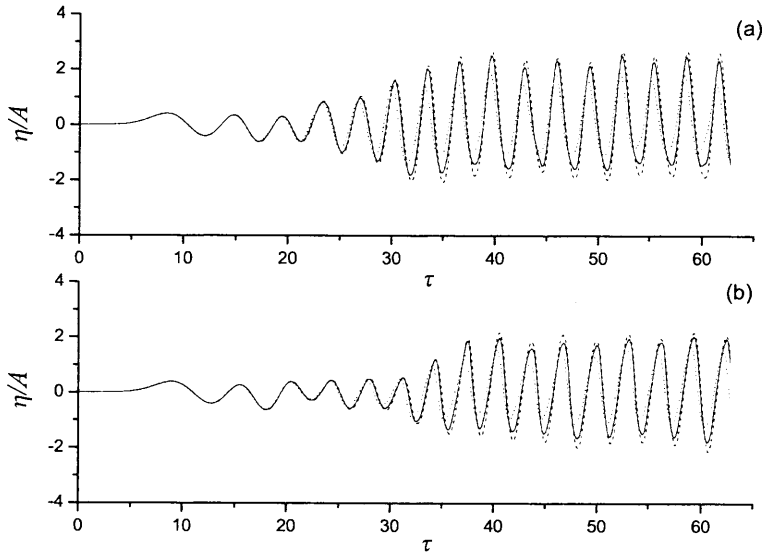

Figure 7.3.5 Wave histories for cylinder two
(a) front; (b) back
····· A/h=0.01; —— A/h=0.02; ····· A/h=0.04

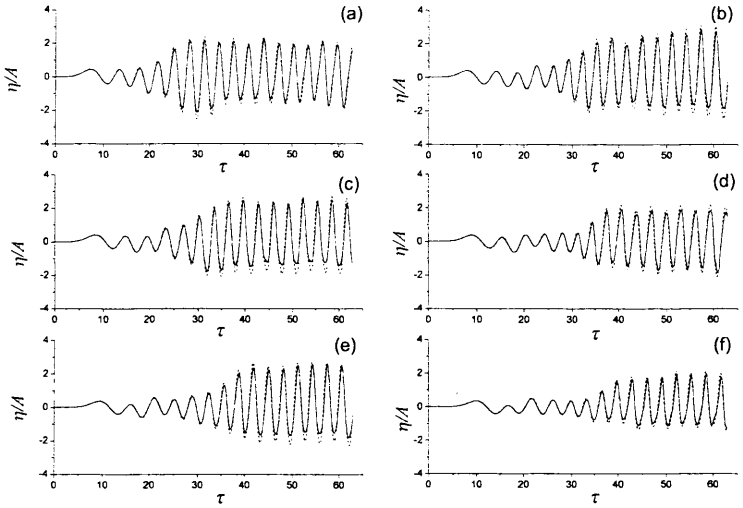

Figure 7.3.6 Wave histories for bottom mounted and truncated cylinders
(a) front of cylinder one; (b) back of cylinder one;
(c) front of cylinder two; (d) back of cylinder two;
(e) front of cylinder three; (f) back of cylinder three
····· bottom mounted; —— truncated

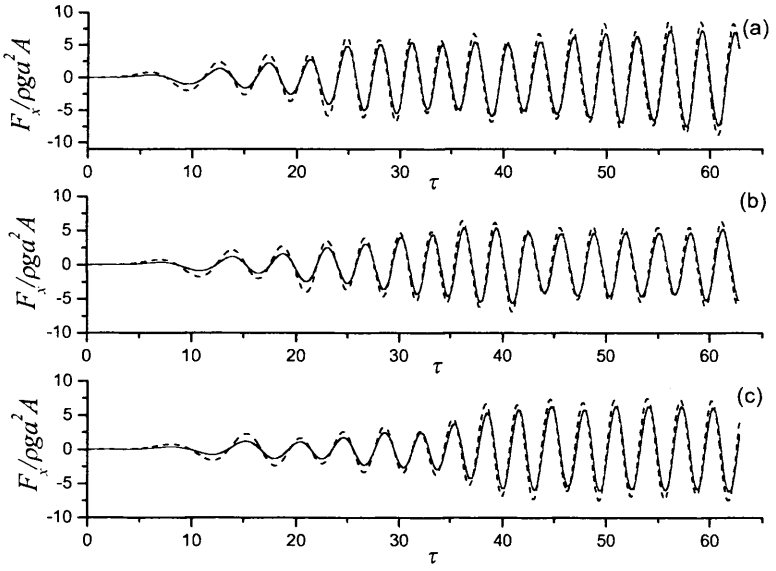

Figure 7.3.7 Comparison of forces on bottom mounted and truncated cylinders
(a) cylinder one; (b) cylinder two; (c) cylinder three
----- bottom mounted; —— truncated

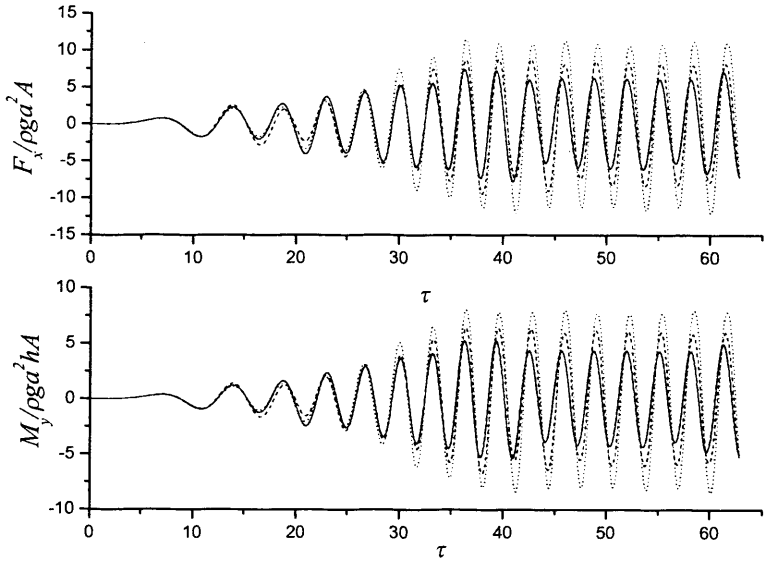

Figure 7.3.8 Comparison of forces and moments on cylinder two
····· single-cylinder case;
—— three-cylinder case with L_{cy}=7a;
····· three-cylinder case with L_{cy}=4a;

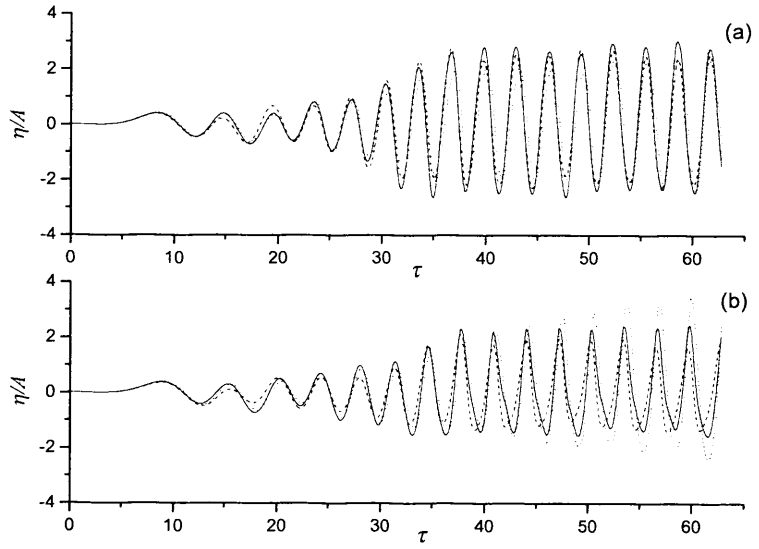

Figure 7.3.9 Wave histories for cylinder four
(a) front; (b) back
····· single-cylinder; —— three-cylnider; ····· seven-cylnider

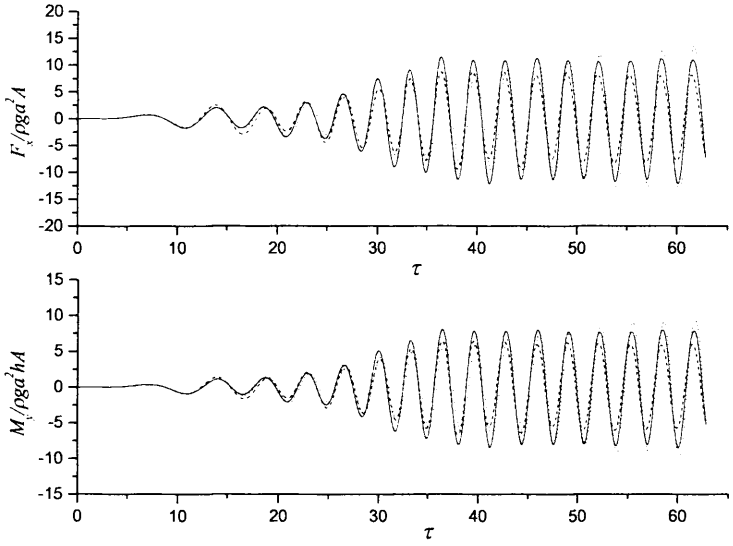

Figure 7.3.10 Hydrodynamic force and moment on cylinder four
····· single-cylinder; —— three-cylinder; ····· seven-cylnider

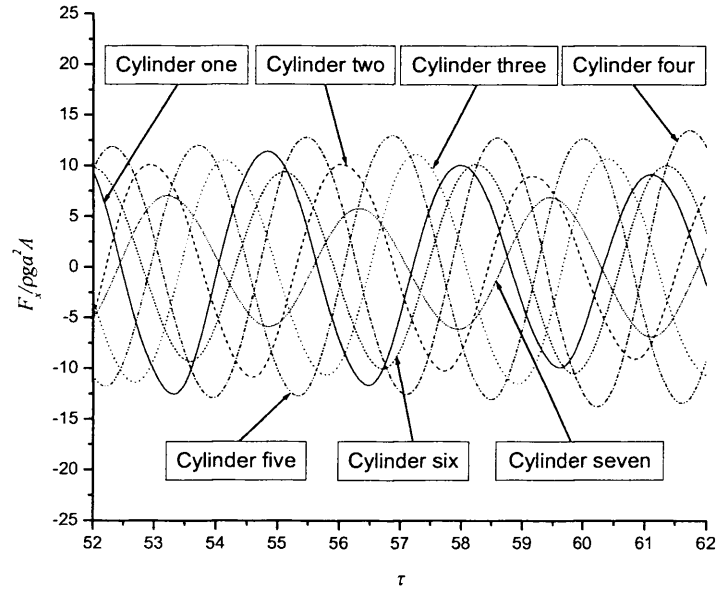

Figure 7.3.11 Histories of forces on the seven cylinders

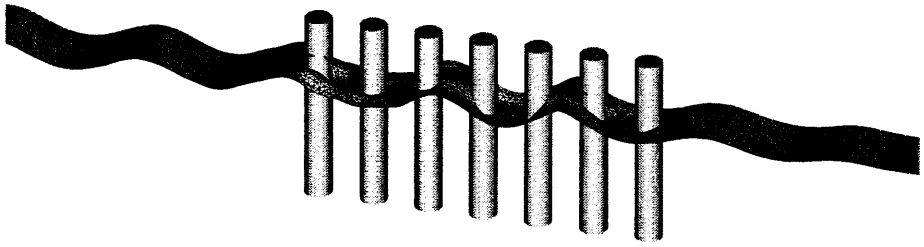

Figure 7.3.12 Wave profile at τ=55.29

8. RADIATION BY MULTIPLE CYLINDERS IN AN OPEN SEA

8.1 Introduction

In Chapter 5, we simulated the wave diffractions by an array of vertical cylinders based on the second order theory. A further simulation of interactions between fully nonlinear waves and multiple cylinders in a numerical tank has been presented in Chapter 7, in which the cylinders are all fixed. However, some ships and offshore structures with multi-hull such as catamarans, tension leg platforms (TLPs), semi-submersibles and drilling ships will be in motions due to the actions of waves, winds and currents. This chapter will focus on forced motions of multiple bodies in the open sea.

Most of previous work on nonlinear wave-structure interactions is on the diffraction problems. There is, however, some work on bodies in motions based on either the second order theory or the fully nonlinear theory. The wave radiation by a single cylinder in 3D was considered by Li (1995) and Goren (1996) based on the second order theory in the frequency domain. The time-domain simulations of second order wave radiation by 2D horizontal single cylinders were undertaken by Isaacson & Ng (1993) and Isaacson, Ng & Cheung (1993) further solved the second order time domain problem in three-dimensions. For fully nonlinear simulations of radiation problems, Yeung & Wu (1989) calculated the motions of a floating body in a closed domain. Sen (1993) studied heaving and rolling motions of floating bodies. Other publications on the 2D problems include those by Kashiwagi (1996), Berkvens (1998), Tanizawa (1996) and Koo & Kim (2004). For the 3D problem, a fully nonlinear numerical simulation of vertical cylinders in swaying or surging motion motions was taken by Hu, Wu & Ma (2002). The experimental studies on a vertical cylinder in horizontal motion have been undertaken by Chaplin *et al.* (1999) and Retzler *et al.* (2000).

For motions of multi-hull structures, the earliest work is that by Ohkusu (1969) on the heaving motion of two circular cylinders on free surface in two-dimension. Williams & Abul-Azm (1989) simulated wave radiation by a group of truncated cylinders, in which one cylinder underwent forced motions but others were fixed. They found the

added mass and the damping coefficient of the cylinder are very different from that of a single isolated cylinder. Both these two works are based on the linear theory. Recently, Wu & Hu (2004) reported fully nonlinear simulations of two bottom mounted vertical cylinders in forced horizontal motions with large amplitudes but no detailed results about waves and forces were given.

The interactions between second-order waves, fully nonlinear waves and fixed multiple cylinders have been studied in Chapters 5 and 7 respectively. The results have shown that the interference between the cylinders may have significant effect on the wave runups and forces on some cylinders. In this chapter, we investigate these effects when a group of truncated cylinders are in forced motions.

8.2 Simulations for single cylinders in horizontal and vertical motions

Single-cylinder cases are considered in this section. We focus on forced motions of cylinders with or without flare. We first consider a wall-sided truncated cylinder (Figure 8.2.1) in heaving motion in an open sea. The initial draught of the cylinder is denoted as d and the radius of its cross section is a. The fully nonlinear result will be compared with the second order solution. The cylinder is subject to the following harmonic motion in the vertical direction

$$Z = A\sin\omega t\,. \tag{8.2.1}$$

A case with water depth $h=a$, initial draught $d=a/2$, amplitude $A=0.1a$ and a nondimensional wavenumber $k_0 a = 1.0$ is first considered. This case has been studied by Li (1995) and Goren (1996) based on the second order theory in the frequency domain. The mesh on the surface of the cylinder is shown in Figure 8.2.1. Since both the free surface and the wetted cylinder surface change with the time, remeshing may be required regularly. The elements near the free surface and the bottom of the cylinder along the vertical direction should be smaller than other parts of the fluid domain by using equations (4.2.2) and (4.2.3). We divide the height of the cylinder into 10 layers using equation (4.2.2), and then divide the gap between the cylinder bottom and the seabed into 6 layers according to equation (4.2.3). In the simulation, the modulation function (see equation 6.4.2) will be used. The computational domain is a square of length $L=30a$ and width $B=30a$, and both the length and width are divided into 50 intervals, which corresponds to 6730 nodes and 13212 triangular elements on the initial

free surface. There are 48 intervals along the waterline. The time interval is $T/150$ ($T=2\pi/\omega$). The radiation condition is the same as that in the second-order diffraction problem in Chapter 5, and the length of the damping zone is set to be one linear wavelength. The remeshing is performed every 15 time steps. We focus on the computation of the vertical force. The force is obtained using equation (3.3.46). The result is shown in Figure 8.2.2, in which the linear and linear plus second order solutions are also given for comparison. Since we only consider the vertical motion, the second order body surface condition may be written as

$$\frac{\partial \phi^{(k)}}{\partial n} = \begin{cases} \dfrac{dZ}{dt} n_z & (k=1) \\ -Z[\dfrac{\partial^2 \phi^{(1)}}{\partial x \partial z} n_x + \dfrac{\partial^2 \phi^{(1)}}{\partial y \partial z} n_y + \dfrac{\partial^2 \phi^{(1)}}{\partial z^2} n_z] & (k=2) \end{cases} \quad \text{on } S_b^{(0)} . \quad (8.2.2)$$

On the lateral surface of the cylinder, $\partial \phi^{(k)} / \partial n \, (k=1,2)$ are zero and on the bottom of the cylinder this equation is reduced to

$$\frac{\partial \phi^{(k)}}{\partial n} = \begin{cases} \dfrac{dZ}{dt} n_z & (k=1) \\ -Z \dfrac{\partial^2 \phi^{(1)}}{\partial z^2} n_z & (k=2) \end{cases} \quad \text{on the bottom of the cylinder} . \quad (8.2.3)$$

The second order derivative $\partial^2 \phi / \partial z^2$ in the above equation is obtained using equation (3.3.2b). The comparison shows the fully nonlinear result is in good agreement with the linear plus second order solution in this case.

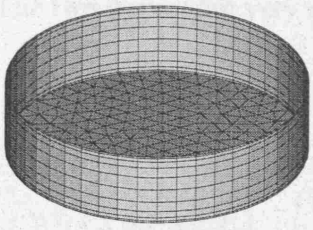

Figure 8.2.1 Surface mesh for a truncated cylinder without flare

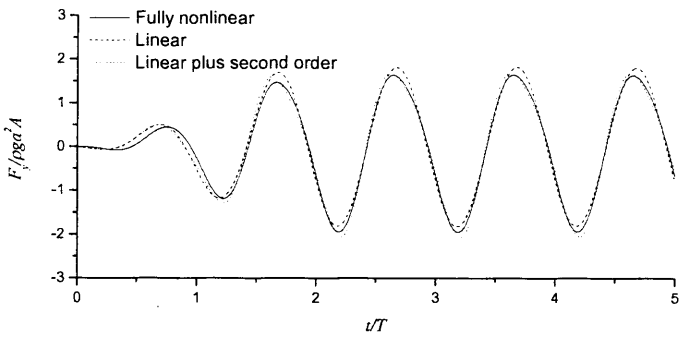

Figure 8.2.2 Comparison of hydrodynamic forces between linear solution, linear plus second order solution and fully nonlinear result

We then consider some cases of cylinders with flare (see Figure 7.2.2) in forced heaving motions. The water depth is h=3a, the initial draught is d=1.5a and the variation of the cross section also starts from z=-0.75a. The cases with $\theta = 80°$ at k_0a=1.0 and three amplitudes A=0.15a, 0.3a and 0.6a are calculated. The force histories are shown in Figure 8.2.3. The nonlinear feature is evident, and the shape of the peaks at A=0.6a is very different from those at A=0.15a and 0.3a, which may be due to the effect of the flare. Difference at peaks may also be seen from the comparison of hydrodynamic forces between the flared cylinder ($\theta = 80°$) and that without flare ($\theta = 90°$) shown in Figure 8.2.4. It shows that the nonlinearity of the force on the cylinder with $\theta = 80°$ is stronger than that on the cylinder without flare and this is consistent with the 2D results in Chapter 6.

A higher frequency case with $k_0a = 2.0$ is also considered. We calculate the force on two cylinders with $\theta = 90°$ and $\theta = 80°$ respectively. The motion amplitude is 0.6a. The result is given in Figure 8.2.5. The two curves are very different near the peaks but only slightly different at the troughs.

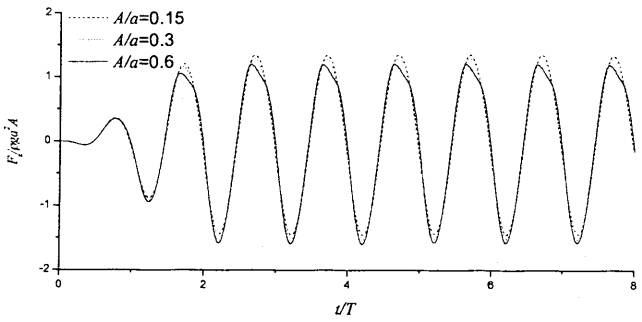

Figure 8.2.3 Histories of forces on the cylinder with θ=80° at k_0a=1.0

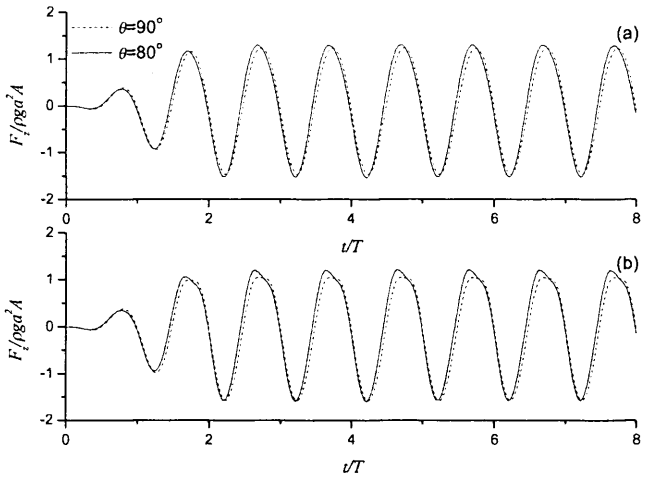

Figure 8.2.4 Histories of forces on cylinders with and without flare at k_0a=1.0
(a) A/a=0.3; (b) A/a=0.6

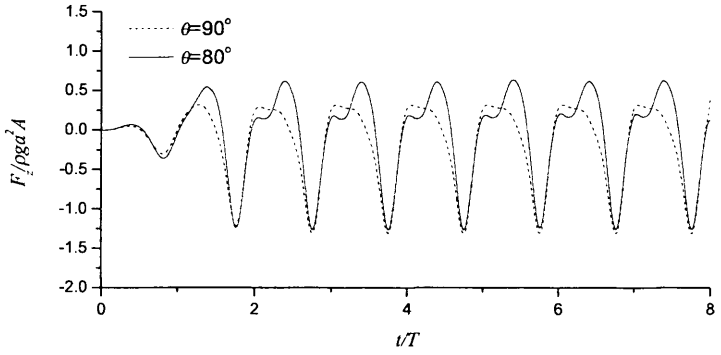

Figure 8.2.5 Histories of forces on cylinders at k_0a=2.0

A case of a bottom-mounted cylinder without flare moving in a circular path around the origin at k_0a=1.0 is also simulated. The water depth is h=3a. The motion of the cylinder is defined as

$$\begin{cases} X = R\cos\omega t \\ Y = R\sin\omega t \end{cases}, \tag{8.2.3}$$

where R is the radius of the path and R=0.015a. The fluid flow should become steady in the system moving with the cylinder after a transition period (Wu & Eatock Taylor, 1990c). The results are given in figures 8.2.6~8.2.8. It is seen that the waves at the front and the back sides of the cylinder are constants (Figure 8.2.6). The force history is given in Figure 8.2.7. The force components in both x- and y-direction are harmonic. However, the force in the normal direction of the motion is a constant. The wave profile at t=8T is given in Figure 8.2.8.

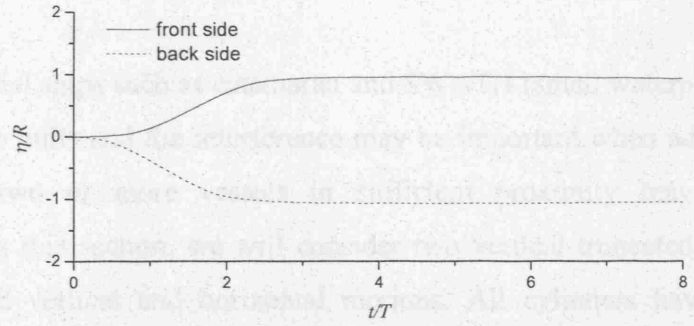

Figure 8.2.6 Wave histories at the front and back sides of the cylinder at k_0a=1.0

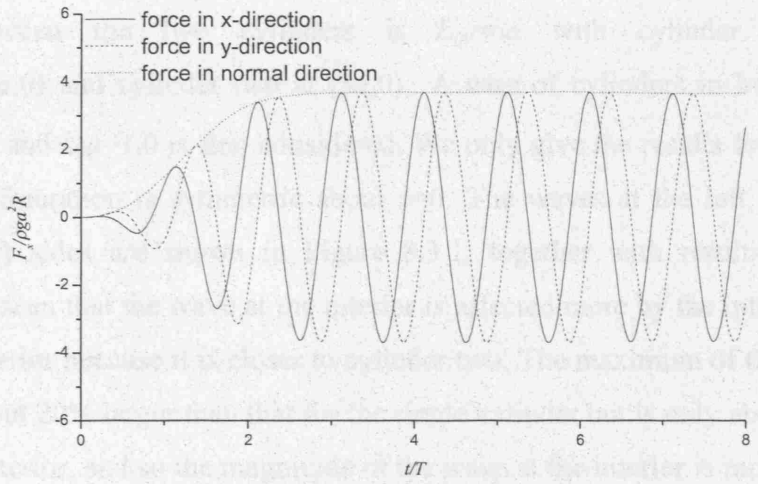

Figure 8.2.7 Hydrodynamic force on the cylinder at k_0a=1.0

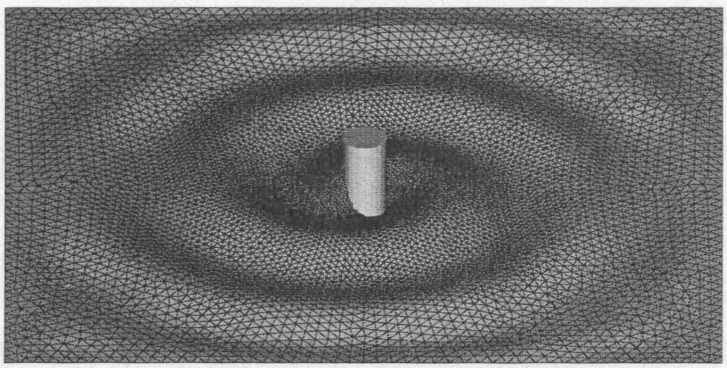

Figure 8.2.8 Wave profile at t=8T

8.3 Simulations for two cylinders in horizontal and vertical motions

Some special ships such as catamaran and SWATH (small waterplane area twin hull ship) have two hulls and the interference may be important when advancing in waves. In addition, two or more vessels in sufficient proximity may have significant interactions. In this section, we will consider two vertical truncated cylinders without flare in forced vertical and horizontal motions. All cylinders have no flare in the following analyses.

In the simulation, the water depth is h=3a and the initial draught of the cylinder is d=1.5a. The vertical motion of both cylinders is described by equation (8.2.1). The distance between the two cylinders is L_{cy}=6a with cylinder one located at $(x, y) = (-3a, 0)$ and cylinder two at $(3a, 0)$. A case of cylinders in heaving motion with A=0.15a and k_0a=1.0 is first considered. We only give the results for cylinder one since the configuration is symmetric about x=0. The waves at the left (exterior) and right (interior) sides are shown in Figure 8.3.1, together with results for a single cylinder. It is seen that the wave at the interior is affected more by the interference than that at the exterior because it is closer to cylinder two. The maximum of the wave at the exterior is about 20% larger than that for the single cylinder but is only about half of the wave at the interior, and so the magnitude of the wave at the interior is more affected by cylinder two. Furthermore, we can observe more evident difference in phase for the wave at the interior than that at the exterior. The corresponding hydrodynamic forces are shown in Figure 8.3.2. For multi-cylinder cases, equation (3.3.46) is modified to the following form to obtain the force on the k-th cylinder

$$F_{i,k} = -\sum_{j=1}^{n} \iint_{S_{b,j}} \{\nabla\chi_{i,j}[(\vec{V} + \vec{\Omega}\times\vec{r})\cdot\vec{N}][\nabla\phi - (\vec{V} + \vec{\Omega}\times\vec{r})] + \chi_{i,j}(\vec{\Omega}\times\vec{V})\cdot\vec{N}\}ds$$
$$- \iint_{S_f + S_{b,k}} (\frac{1}{2}\nabla\phi\cdot\nabla\phi + gz)\frac{\partial\chi_{i.k}}{\partial N}ds - \sum_{j=1}^{6} C_{ij,k}A_{j,k} \qquad (i = 1,2,\cdots,6) \qquad ,(8.3.1)$$

where n is the number of cylinders, $S_{b,k}$ is the surface of the k-th cylinder, $C_{ij.k} = \iint_{S_{b,k}} \chi_{i,k}N_j ds$ and $A_{j,k}$ is the acceleration of the k-th cylinder. A difference between two-cylinder and single-cylinder cases is that there are horizontal forces on cylinders for the former. There is no obvious difference for the vertical forces in the two cases.

We now consider the influence of distance L_{cy} on waves and forces. The amplitude is still A=0.15a, and four different distances L_{cy}=0.5λ, λ, 1.5λ and 2λ are considered (λ is the linear wave length). The results for cylinder one are given in figures 8.3.3 and 8.3.4. It is seen that the waves corresponding to L_{cy}=λ and 2λ are close and are very different from those corresponding to L_{cy}=0.5λ and 1.5λ at both the left and right sides. This is mainly because the phases of the radiated waves by the motions of the two cylinders are almost identical for the former but more different for the latter. The waves at the right (interior) side at L_{cy}=0.5λ and 1.5λ are much larger than those at L_{cy}=λ and 2λ, and the difference between L_{cy}=0.5λ and 1.5 λ or L_{cy}=λ and 2λ are more evident than those at the left (exterior) side since they are more affected by the interference. The variations of the horizontal forces with the time are very similar to the waves at the right (interior) side. However, the effect of the distance L_{cy} on the vertical forces is weak.

The wave at the symmetry line of the cylinders, or point (0,0) is given in Figure 8.3.5. It is seen that the wave amplitude decreases as the distance L_{cy} increases. The wave at L_{cy}=0.5λ is about four times as large as that at L_{cy}=2λ. The waves at (0, 0) produced by the motion of the two cylinders have an identical phase and so the amplitude of the wave is larger than that produced by a single isolated cylinder. The waves with smaller values of L_{cy} will have larger amplitudes since the radiated wave becomes weaker with the increase of the distance between the cylinder and the location where the wave is calculated.

Three amplitudes A=0.15a, 0.3a and 0.6a with L_{cy}=6a and 4a at k_0a=1.0 are considered next. The results for cylinder one are given in figures 8.3.6~8.3.9. Generally, the nonlinearity of the wave is not strong but it is noticeable for the force. It is also noticed that the horizontal force at L_{cy}=4a has stronger nonlinearity than that at L_{cy}=6a and the corresponding maximum for the former is over twice the latter.

We then consider a larger nondimensional wavenumber k_0a=2.5. Two cases at L_{cy}=2λ and 2.5λ are calculated. The wave and force are given in figures 8.3.10 and 8.3.11 respectively. It is seen that the wave is more affected at L_{cy}=2λ and there is no variation in phase for both cases. Similar to the results at k_0a=1, the horizontal forces in these two cases are very different. The magnitude of the horizontal force in L_{cy}=2.5λ is significantly smaller than that in L_{cy}=2λ. The wave profiles for $k_0a = 1.0$ and $k_0a = 2.5$ around the two cylinders with L_{cy}=6a at t=8T are shown in Figure 8.3.12.

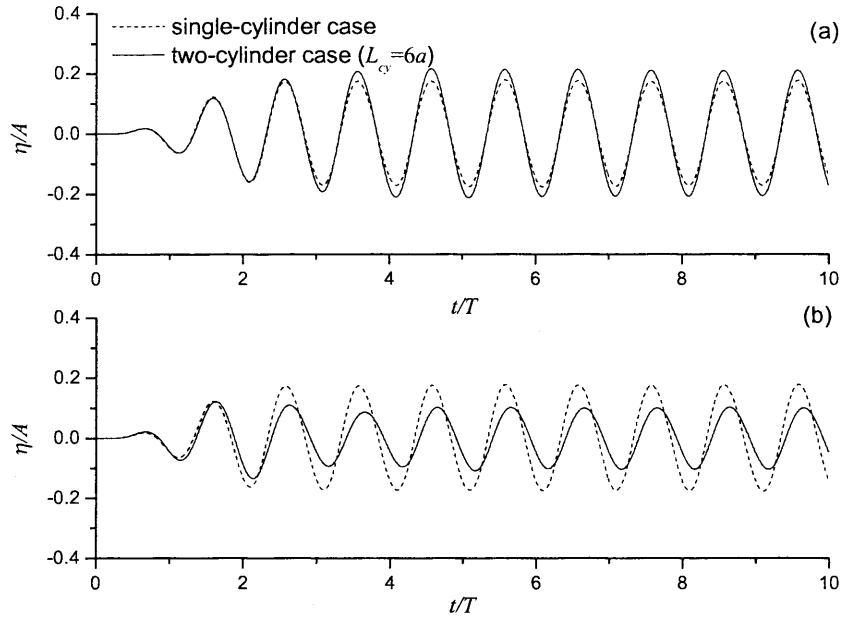

Figure 8.3.1 Wave histories at k_0a=1.0 and A/a=0.15
(a) left side; (b) right side

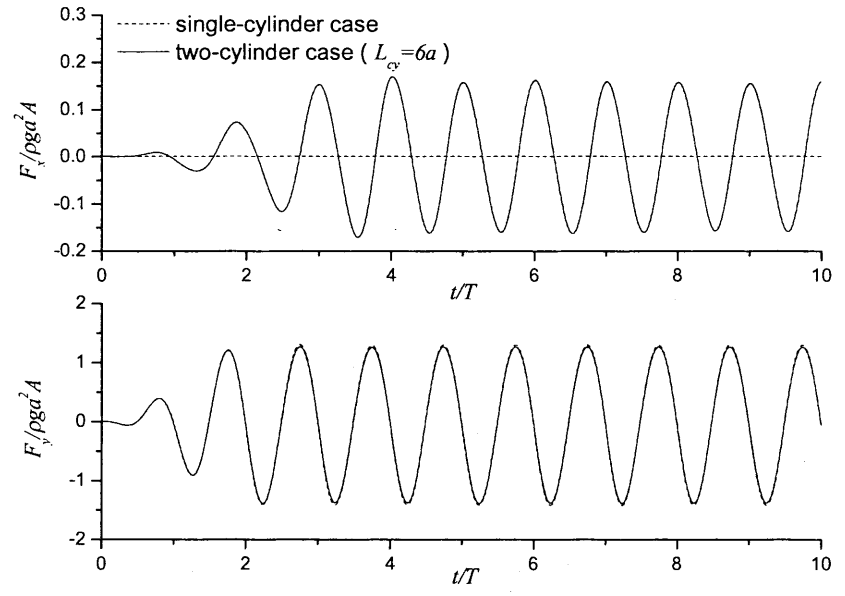

Figure 8.3.2 Histories of forces at k_0a=1.0 and A/a=0.15

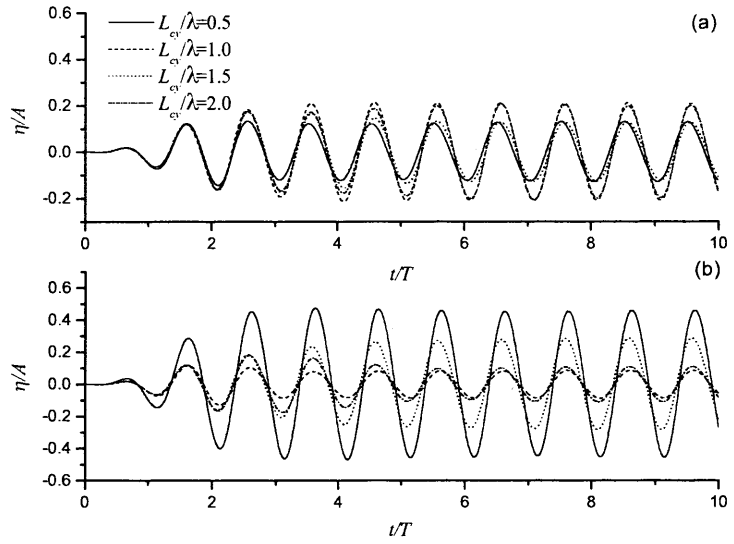

Figure 8.3.3 Wave histories at k_0a=1.0 and A/a=0.15
(a) left side; (b) right side

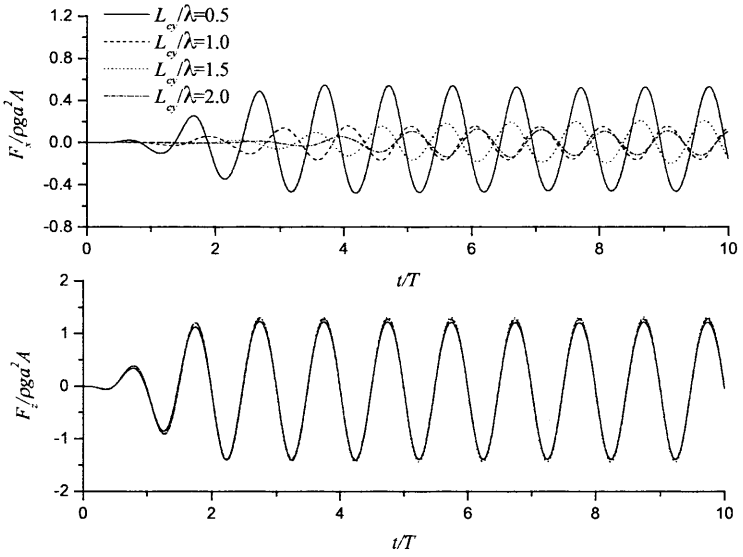

Figure 8.3.4 Histories of forces at k_0a=1.0 and A/a=0.15

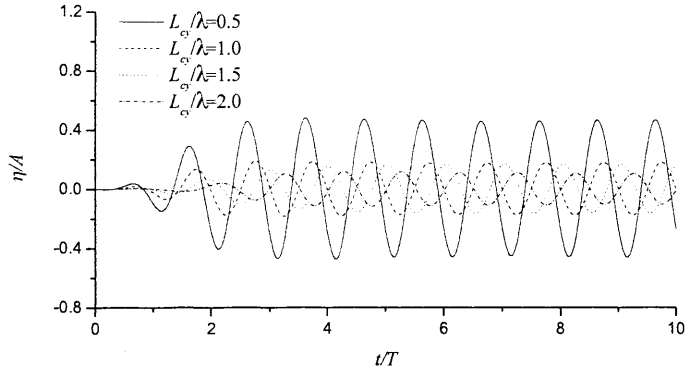

Figure 8.3.5 Wave histories at the symmetry line of the two cylinders (point (0,0)) at k_0a=1.0 and A/a=0.15

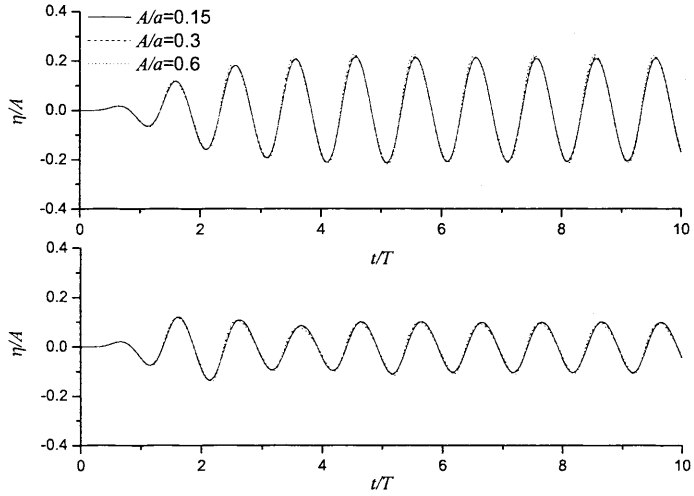

Figure 8.3.6 Wave histories for cylinder one with L_{cy}=6a at k_0a=1.0
(a) left side; (b) right side

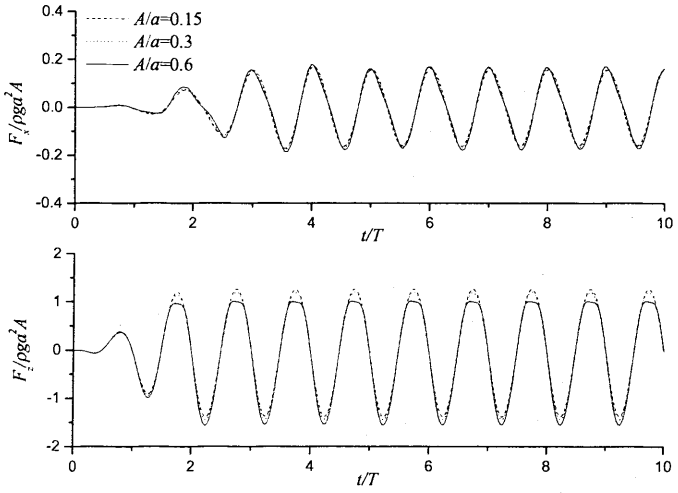

Figure 8.3.7 Histories of forces with L_{cy}=6a at k_0a=1.0

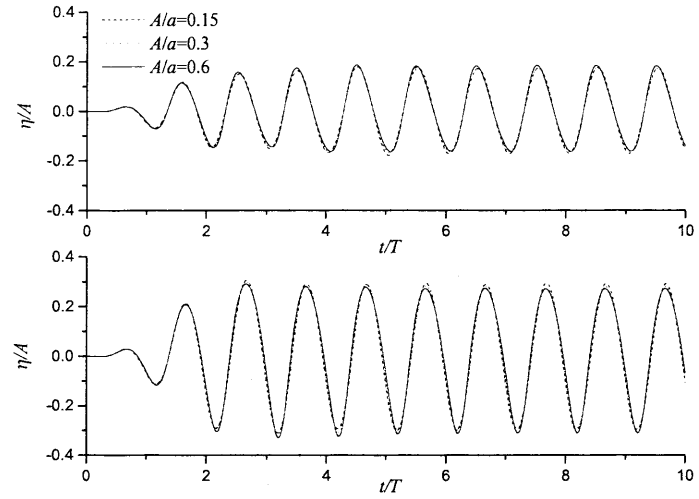

Figure 8.3.8 Wave histories with $L_{cy}=4a$ at $k_0a=1.0$
(a) left side; (b) right side

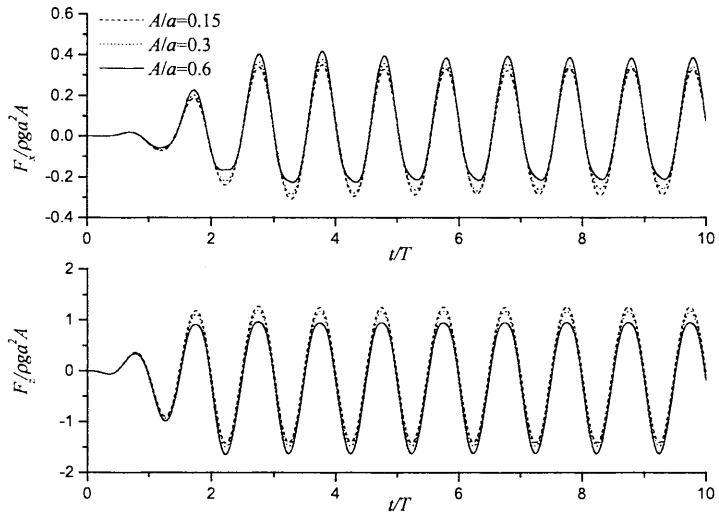

Figure 8.3.9 Histories of forces with $L_{cy}=4a$ at $k_0a=1.0$

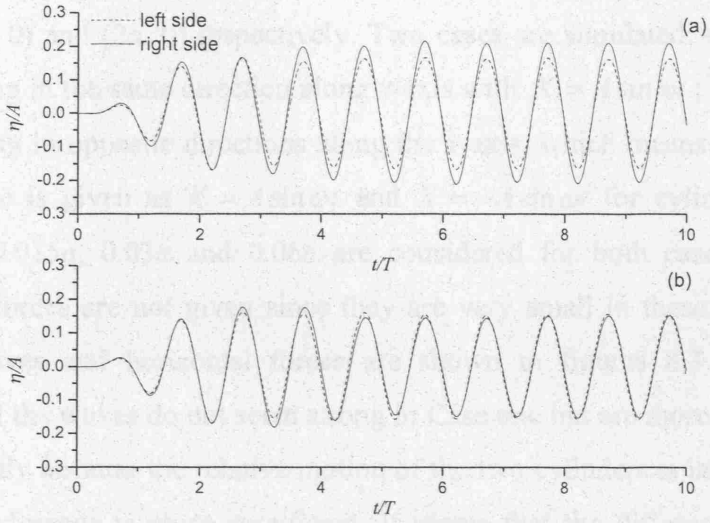

Figure 8.3.10 Wave histories at k_0a=2.5 and A/a=0.15
(a) L_{cy}/λ=2.0 ; (b) L_{cy}/λ=2.5

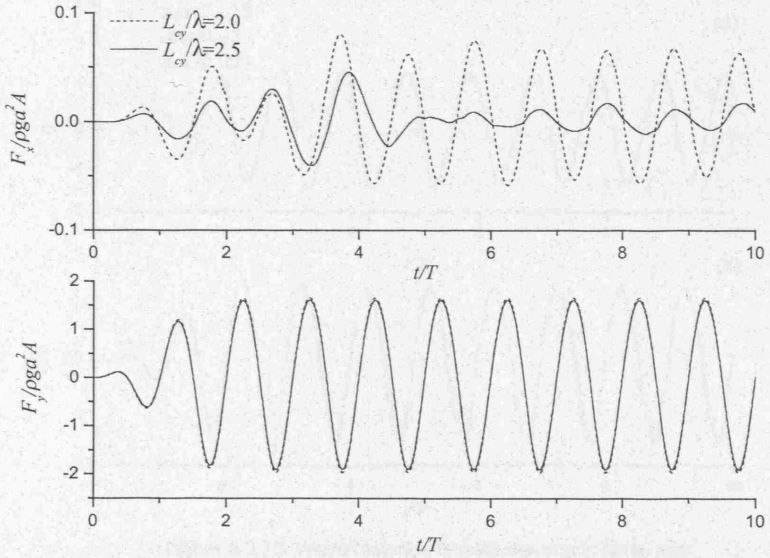

Figure 8.3.11 Histories of forces at k_0a=2.5 and A/a=0.15

(a) (b)

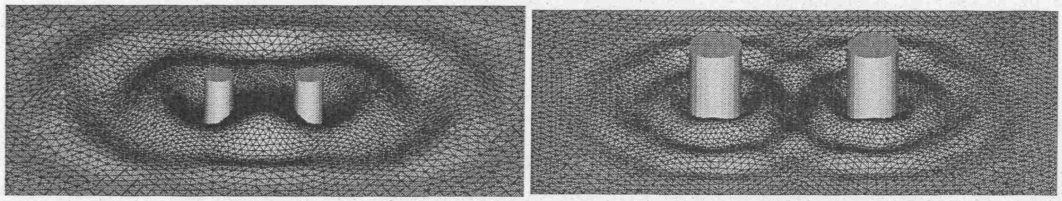

Figure 8.3.12 Wave profile at t=8T with L_{cy}=6a, A/a=0.6 and (a) k_0a=1.0 (b) k_0a=2.5

We then consider some cases of horizontal motions. The two cylinders are initially located at (-2a, 0) and (2a, 0) respectively. Two cases are simulated: Case one is two cylinders moving in the same direction along x-axis with $X = A\sin\omega t$; Case two is two cylinders moving in opposite directions along the x-axis, which means that the motion for cylinder one is given as $X = A\sin\omega t$ and $X = -A\sin\omega t$ for cylinder two. Three amplitudes A=0.015a, 0.03a and 0.06a are considered for both cases. The vertical hydrodynamic forces are not given since they are very small in these two cases. The histories of waves and horizontal forces are shown in figures 8.3.13~8.3.16. The nonlinearities of the waves do not seem strong in Case one but are more evident in Case two. This is partly because the relative motion of the two cylinders is larger in case two and so the interference is more significant. It seems that the difference between the forces at the three different amplitudes in both cases is not significant and the forces are generally linear. The wave profiles at t=8T for both cases are shown in Figure 8.3.17.

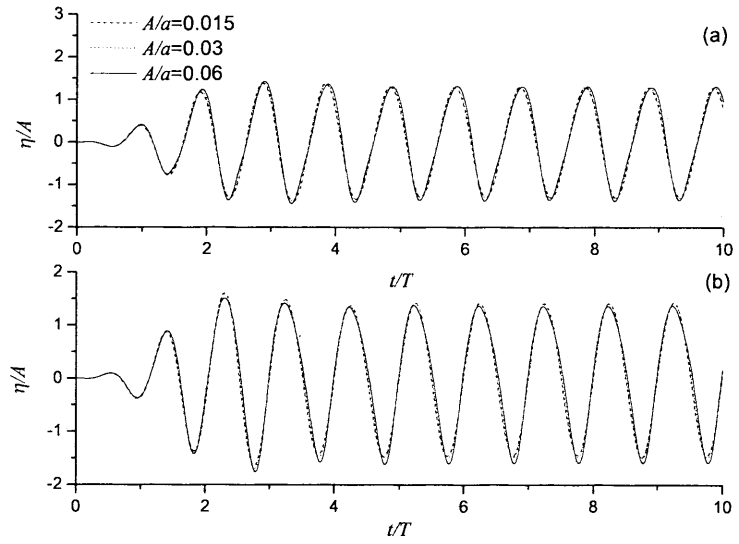

Figure 8.3.13 Wave histories for cylinder one in Case one
(a) left side; (b) right side

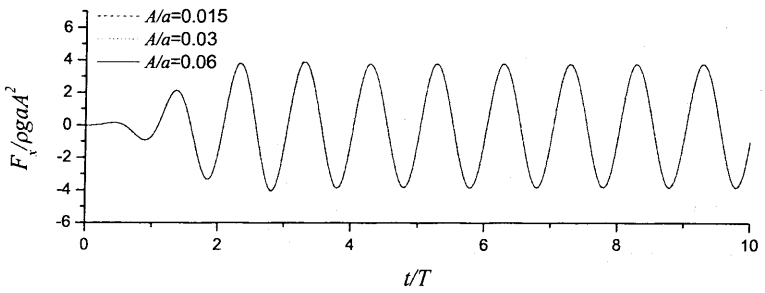

Figure 8.3.14 Horizontal forces on cylinder one in Case one

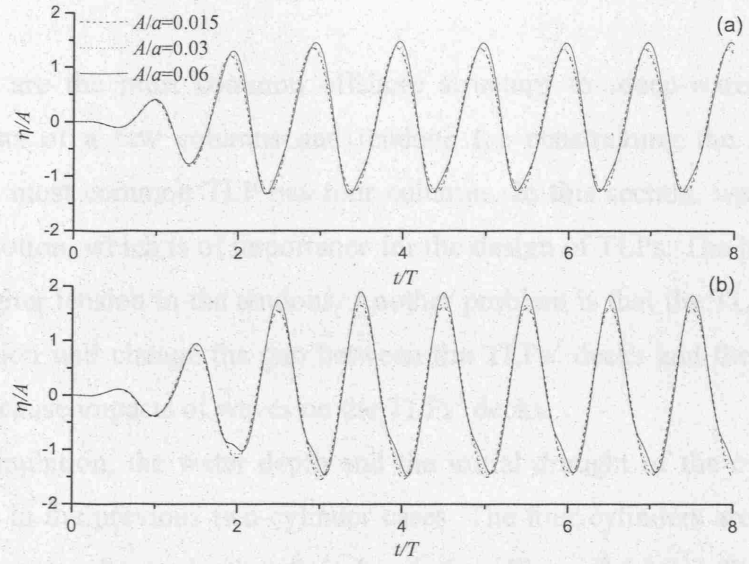

Figure 8.3.15 Wave histories for cylinder one in Case two
(a) left side; (b) right side

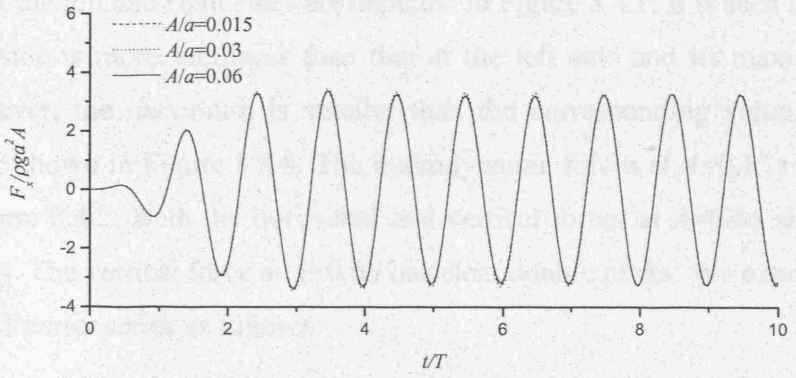

Figure 8.3.16 Horizontal force on cylinder one in Case two

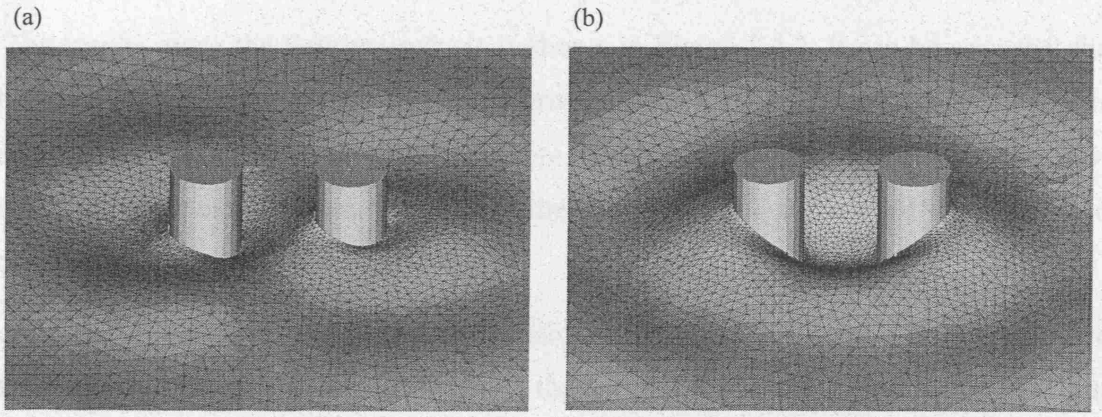

Figure 8.3.17 Wave profiles at $t=8T$ in (a) Case one & (b) Case two

8.4 Simulations for four cylinders in vertical motions

The TLPs are the most common offshore structure for deep-water operation. It mainly consists of a few columns and tendons for constraining the motion of the platform. The most common TLP has four columns. In this section, we only consider the heaving motion, which is of importance for the design of TLPs. The heaving motion may cause higher tension in the tendons. Another problem is that the TLPs' motions in vertical direction will change the gap between the TLPs' decks and the water surface and so it may cause impacts of waves on the TLPs' decks.

In the simulation, the water depth and the initial draught of the cylinder are the same as those in the previous two-cylinder cases. The four cylinders are located at the vertices of a square whose edge length is $L_{cy}=4a$ [see Figure 5.6.1(a)]. Firstly, the cases at $k_0a=1.0$ and three amplitudes $A=0.15a$, $0.3a$ and $0.6a$ are considered here. We only give results for cylinder one since the configuration is symmetric about x- and y-axis. The waves at the left and right sides are depicted in Figure 8.4.1. It is seen that the wave at the right side is more nonlinear than that at the left side and its maximum is also larger. However, the maximum is smaller than the corresponding value in the two-cylinder case shown in Figure 8.3.8. The hydrodynamic forces at $A=0.15a$ and $0.6a$ are given in Figure 8.4.2. Both the horizontal and vertical forces at $A=0.6a$ show stronger nonlinearities. The vertical force at $A=0.6a$ has clear double peaks. We express the force at $A=0.6a$ in Fourier series as follows

$$\frac{F}{\rho g a^2 A}=\frac{a_0}{2}+\sum_{i=1}^{\infty}[A_i\cos(i\omega t)+B_i\sin(i\omega t)]. \qquad (8.4.1)$$

The results using the Fourier analysis is shown in Figure 8.4.3. It can be seen that the horizontal force has a major component corresponding to $i=1$. The component of i=2 is also significant but i=3 and 4 are negligible. For the vertical force, the components of i=3 and 4 are also important because the double peaks are caused by these two components.

We further consider a larger nondimensional wavenumber k_0a=2.5. The results are shown in figures 8.4.4~8.4.5. In this case, the nonlinearity is not strong in the wave but very evident in force. It is also seen that the horizontal forces are smaller than those at k_0a=1.0 and vertical forces are larger than those at k_0a=1.0.

The wave at the centre of the four vertices is given in Figure 8.4.6 for k_0a=1.0 and 2.5. The maximum value of the wave is about twice that at the right side for k_0a=1.0 (see Figure 8.4.1) but is only about half of that at the right side for k_0a=2.5 (see Figure 8.4.4). This is because the wave at k_0a=2.5 becomes much weaker than that at k_0a=1.0 when they arrive at the centre. Some wave profiles are shown in Figure 8.4.7 at k_0a=2.5 and A=0.6a. The variations of the wave profiles and the positions of the four cylinders can be clearly observed.

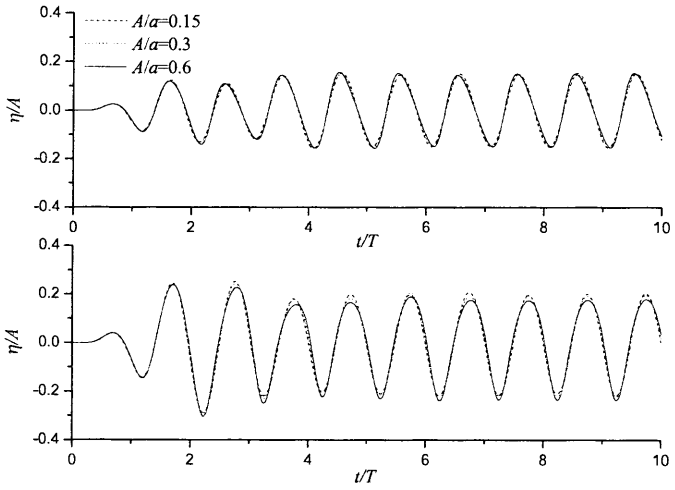

Figure 8.4.1 Wave histories with L_{cx}=4a at k_0a=1.0
(a) left side; (b) right side

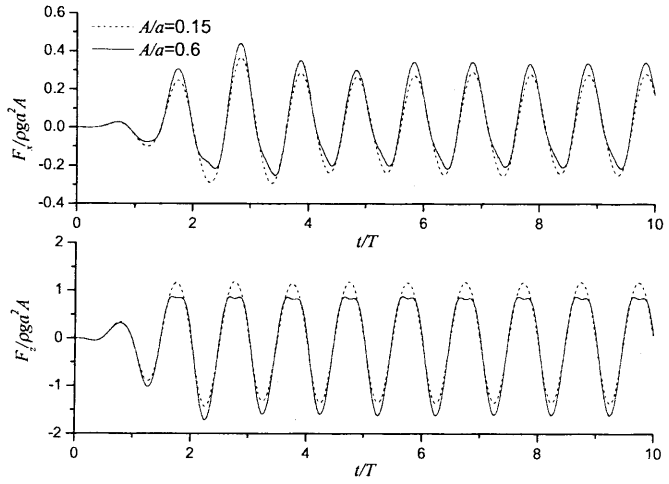

Figure 8.4.2 Histories of forces with L_{cy}=4a at k_0a=1.0

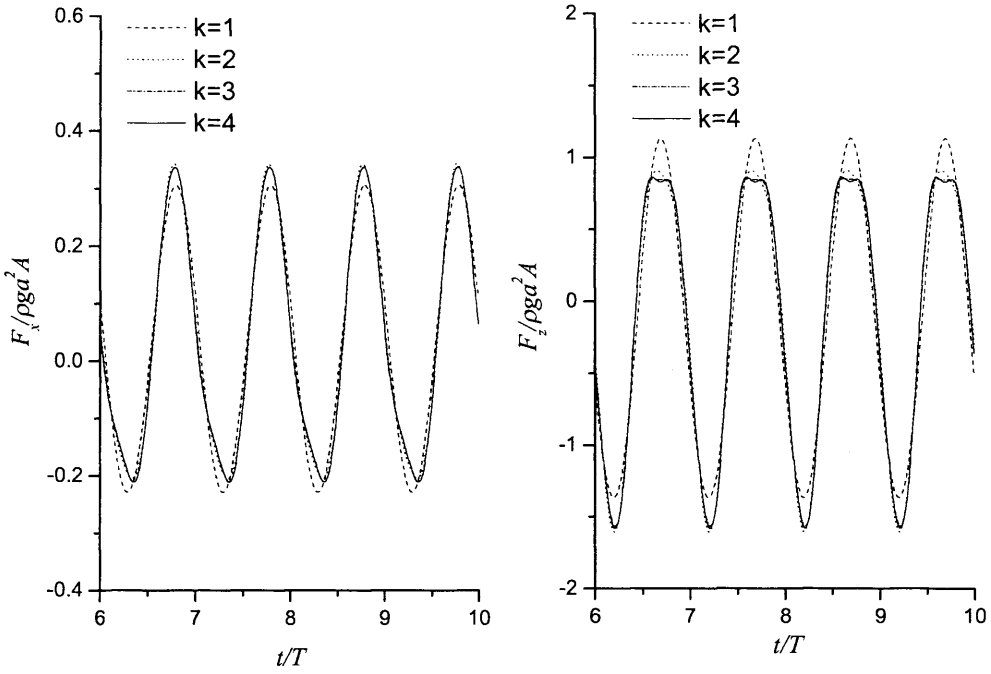

Figure 8.4.3 Fourier components $a_0/2+\Sigma(A_i\cos(i\omega t)+B_i\sin(i\omega t))$ (i=1,k) of the force at A/a=0.6

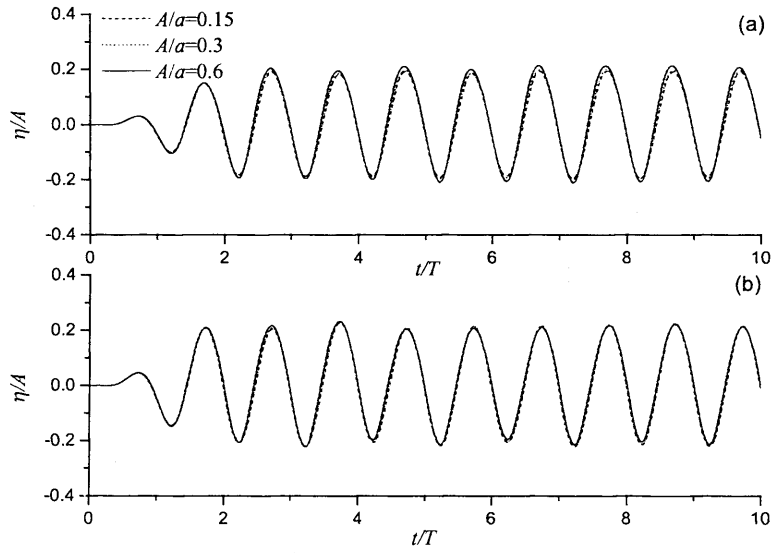

Figure 8.4.4 Wave histories with L_{cy}=4a at k_0a=2.5
(a) left side; (b) right side

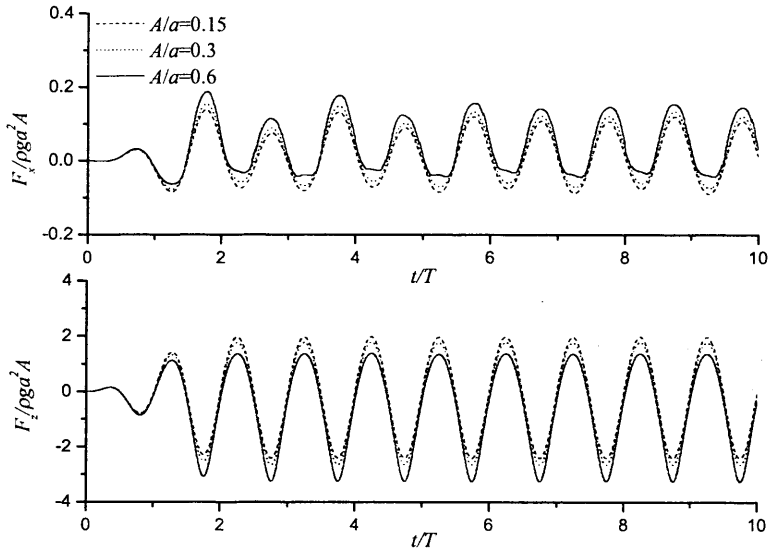

Figure 8.4.5 Histories of forces with $L_{cy}=4a$ at $k_0a=2.5$

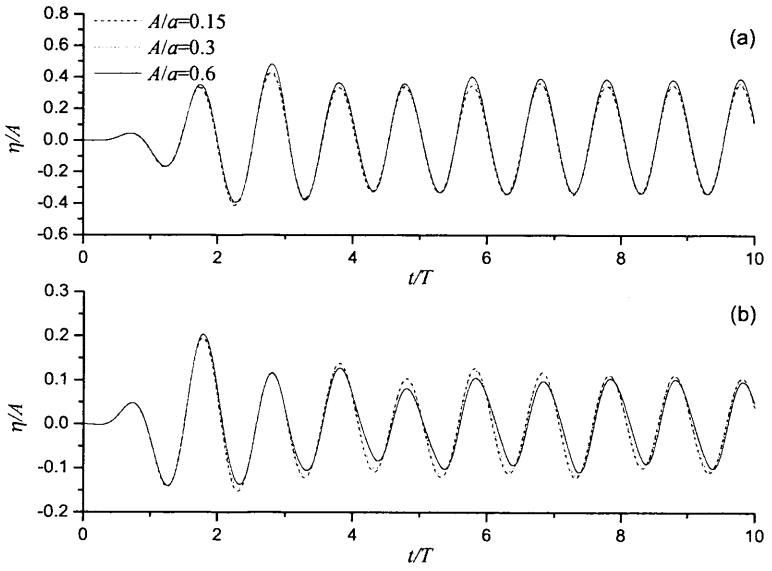

Figure 8.4.6 Wave histories at the centre of the configuration
(a) $k_0a=1.0$; (b) $k_0a=2.5$

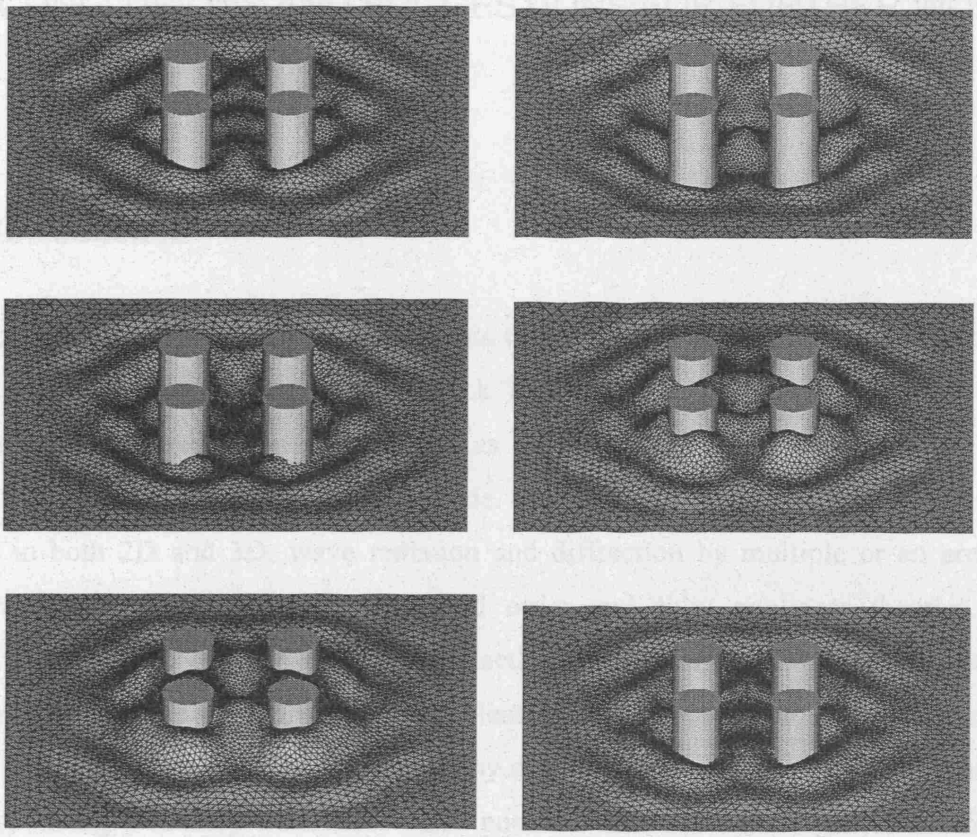

Figure 8.4.7 Wave profiles at t=8T, 8.2T, 8.4T, 8.6T, 8.8T, 9T

9. CONCLUSIONS AND SUGGESTIONS FOR FURTHER WORK

9.1 Introduction

The numerical method presented in this thesis is a substantial development of the work by Ma (1998) and Ma, Wu & Eatock Taylor (2001a, b). A major new feature is that the unstructured mesh is used and as a result many numerical procedures are modified. A much wider simulation is made. This includes flare structures in numerical tanks in both 2D and 3D, wave radiation and diffraction by multiple or an array of bodies, and analysis through the second order and fully nonlinear theories. The simulation is based on the finite element method. The fluid domain is first discretised with prism elements in 3D and triangular elements in 2D with linear shape functions. A finite element equation is then formulated by discretising the governing equation and its corresponding boundary conditions. The nonzero elements in the global coefficient matrix are stored in linear linked lists, whose length can dynamically increase or decrease, and we then convert the matrix in the lists to that in the compressed sparse row (CSR) format, which is more convenient for using the conjugate gradient (CG) method with a symmetric successive overelaxlation (SSOR) preconditioner. The computation of the global coefficient matrix is tested and is verified to be efficient, and the matrix equation is then solved using the CG method with the SSOR preconditioner to obtain the velocity potential in the whole domain. Finally, the velocity is calculated by the Galerkin method for flared structures and by a finite difference method for wall-sided structures.

Numerical results have been compared with analytical solutions, second order solutions and previous work in several cases with good agreement being achieved. The method is demonstrated to be flexible; it can deal with single and multiple cylinders, cylinders with and without flare, bottom mounted and truncated cylinders. All simulations are completed using the personal computer, which shows that the present numerical method is efficient.

In conclusion, the numerical method developed in this thesis is accurate, flexible and efficient thus it a good alternative for simulating wave-body interactions. All these have been demonstrated by various numerical examples.

9.2 Second order wave diffractions by a group or an array of vertical cylinders

The algorithm for the 3D second-order diffraction is based on a 2D unstructured mesh. The 3D mesh with prism elements is generated by extending the 2D mesh in the vertical direction. For an array of cylinders the advantage of the unstructured mesh becomes more obvious. The first- and second-order velocity potentials in the fluid domain are obtained by solving two linear systems at each time step. After the potential is obtained, the first- and second-order derivatives with respect to the vertical coordinate can be calculated through a cubic polynomial along a straight mesh line in the vertical direction, the derivatives along the mean free surface can then be obtained by a difference method, which is also adopted to calculate the derivatives of the potential and the wave elevation in the horizontal direction. The free surface is updated using the fourth order Adams-Bashforth scheme. The combination of the Sommerfeld-Orlanski radiation and the damping zone method is used to absorb reflected waves. A single-cylinder case is chosen to validate the present method to be effective by comparison of some results with those obtained from previous work. The simulation of the multi-cylinder case then shows that the influence of interference on the wave and the force is evident especially for the second order components. Further simulations are made for four-cylinder cases near the first- and second-order trapped modes with very large first- and second-order waves and forces being found respectively. Near the second order trapped mode, the nondimensionalised second order component is of significant magnitude and can be even larger than the first order one. The amplitude of the maximum second order wave has been compared with the frequency-domain result. Finally, some cases of 10 cylinder in a line and 2×4 cylinders in a double line have been simulated.

The algorithm can be used not only for the diffraction by structures without flare, but also for some special cases of radiation problems such as single cylinders in vertical

motion. For more general radiation problems, the algorithm needs to be extended to calculate second order derivatives such as $\partial^2\phi^{(1)}/\partial x\partial y$ accurately on the cylinder surface, which is part of the further development of this method.

9.3 2D fully nonlinear wave-body interactions

The algorithm here we used for calculating 2D wave-body interactions is based on the full 2D unstructured mesh and the Galerkin method is used to obtain the velocity in the fluid domain. The mesh gives far more flexibility and more rational distribution of elements for complex domains and complex flow fields. The adoption of the Runge-Kutta method for integration with respect to time can avoid extensive interpolation between results from different meshes. The introduction of the B-Spline to remeshing has maintained the quality of the mesh throughout the simulation. The use of the energy method for smoothing also removes the restriction of Longuet-Higgins & Cokelet's method to a uniform mesh. The method has been used to analyse fully nonlinear wave and fully nonlinear wave interactions with non-wall sided floating bodies. Some numerical results have been compared with analytic solutions and second order solutions to demonstrate the effectiveness of the method.

Further work should be considered to incorporate the adaptive mesh technique into the method and use it to simulate some problems with strong nonlinearity such as sloshing in large amplitude motions and overturning waves.

9.4 Interactions between fully nonlinear waves and vertical cylinders with flare

This is an extension of the 2D algorithm above. Similar to the second order wave diffraction, this algorithm employed the 3D mesh which is extended from the 2D unstructured mesh into the vertical direction but along a curve instead of a straight line. Correspondingly, the Galerkin method is used to calculate velocity in the whole fluid domain. The mesh is combined with a structured mesh near the wave maker to avoid the transverse instability. Smoothing is performed within the structured mesh. The

nonlinear features of waves and forces/moments for both the bottom-mounted and the truncated cylinders with flare have been captured. Comparisons of the waves and forces are made between the two types of cylinders with the same angle θ between the flare and the horizontal plane. The influence of flare on waves and forces has been studied for each type of cylinder. The result suggests that the flare with smaller value of θ is more effective to suppress the wave runup but may cause larger forces and moments on the cylinder. Some results for interactions between irregular waves and flare cylinders are also provided. This method is currently limited to a big angle θ between the flare and the horizontal plane. Further work is needed for a small angle in particular when a jet has been developed.

9.5 3D interactions between fully nonlinear waves and multiple cylinders without flare

In this algorithm, the calculation of velocity is the same as that in the second-order diffraction problem since we only consider wall-sided cylinders. The algorithm is used in two problems: multiple fixed and bottom-mounted cylinders in numerical wave tanks and radiation by multiple truncated cylinders in forced motions in open seas. The extensive simulations have provided a better understanding of the influence of mutual interference between cylinders on waves and forces, which has been overlooked by previous work based on the fully nonlinear theory. The future work is to consider a large array of cylinders, which is more relevant to bridges and floating airports. Work is also needed to consider the combined problem of wave diffraction and radiation, which is relevant to floating bodies in steep waves.

REFERENCES

Abul-Azm, A.G. and Williams, A.N., 1988, "Second order diffraction loads on truncated cylinders", *J. Waterway, Port, Coastal and Ocean Eng.*, ASCE, 114, 436-454.

Aitchison, J.M., 1980, "A finite element solution for critical flow over a weir", *Proc. Int. Conf. Finite Elements in Flow Problems*, Banff, Alberta, Canada, 2:52-59.

Allievi, A. and Calisal., S., 1993, "A semi-implicit semi-lagrangian finite element model for nonlinear free surface flow", *Proc. 6th Int. Conf. Numer. Ship Hydrodyn.*, Iowa.

Arai, M., Paul, U.K. and Inoue, Y., 1993, "Wave generation in 3D numerical wave tank", *J. Soc. Nav. Archi. Japan*, 173, 45-50.

Bai, K.J., 1975a, "A localized finite-element method for steady, two-dimensional free-surface flow problems", *Proc. 1st Int. Conf. Numer. Ship Hydrodyn.*, Gaithersburg, Md.

Bai, K.J., 1975b, "Diffraction of oblique waves by an infinite cylinder", *J. Fluid Mech.*, 68, 513-535.

Bai, K.J., 1977, "A localized finite-element method for steady, three-dimensional free-surface flow problems", *Proc. 2nd Int. Conf. Numer. Ship Hydrodyn.*, Berkeley, Calif.,78-87.

Bai, K.J., 1978, "A localized finite-element method for two-dimensional steady potential flows with a free surface", *J. Ship Res.*, 22, 216-230.

Bai, K.J., 1979, "Blockage correction with a free surface", *J. Fluid Mech.*, 94, 433-452.

Bai, K. J. and Han, J.H., 1994, "A local finite-element method for the nonlinear steady wave due to a two-dimensional hydrofoil", *J. Ship Res.*, 38, 42-51.

Bai, K.J. and Yeung, R.W., 1974, "Numerical solutions to free-surface flow problem", *10th Symp. Nav. Hydrodyn.*, Cambrige, Mass., 609-633, disc., 634-47.

Baker, G.R., Meriron, D.I. and Orszag, S.A., 1981, "Applications of generalized vortex method to nonlinear free surface flows", *Proc. 3rd Int. Conf. Numer. Ship Hydrodyn.*, Paris, 179-191.

Beck, R. F., 1994, "Time-domain computations for floating bodies", *Appl. Ocean Res.*, 16, 267-282.

Beck, R.F. and Liapis, S.J., 1987, "Transient motions of floating bodies at zero forward speed", *J. Ship Res.*, 31(3), 164-176.

Beck, R.F. and Magee, A.R., 1990, "Time domain analysis for predicting ship motions", *Proc. IUTAM Symp., Dynamics of Marine Vehicles and Structures in waves*, London.

Berkvens, P.J.F., 1998, "Floating bodies interacting with water waves", Ph.D. thesis, University of Twente, The Netherlands, 1-161.

Betts, P.L., 1979, "A variational princilpes in terms of stream function for free ssurface flowc and its application to the finite element method", *Comput. Fluids*, 7, 145-153.

Betts, P.L. and Assaat, M.I., 1980, "Finite element solutions of large amplitude water waves", *Proc. Int. Conf. Finite Element in Flow Problem*, Banff, Alberta, Canada, 2, 24-32.

Bingham, H.B., Korsmeyer, F.T. and Newman, J.N. 1994, "Prediction of the seakeeping characteristics of ships". *Proceedings of the 20th Symposium on Naval Hydrodynamics*, Santa Barbara, CA.

Boo, S.Y., 2002, "Linear and nonlinear irregular waves and forces in a numerical tank", *Ocean Engng*, 29, 475-493.

Boo, S.Y., and Kim, C.H., 1997, "Nonlinear irregular waves and forces on truncated cylinders in a numeical tank", *Proc. 11th Int. Offshore and Polar Eng. Conf.*, Honolulu, Hawaii, USA, 3, 76-84.

Bowyer, A., 1981, "Computing Dirichlet tessellations", *Comp. J.*, 24(2), 162-66.

Bratland, A.K., Korsm1eyer, F.T. and Newman, J.N., 1997, "Time domain calculations in finite water depth", *Proc. 12th Int. Workshop Water Waves Float. Bodies*, Marseille, France.

Buchmanna, B., Skourup, J. and Cheung, K.F., 1998, "Run-up on a structure due to second-order waves and a current in a numerical wave tank", *Appl. Ocean Res.*, 20, 297-308.

Bullock, G. N. and Murton, G. J., 1989, "Performance of a wedge-type absorbing wave maker", *J. Waterway, Port, Coastal and Ocean Eng.*, 115(1), 1-17.

Callan, M., Linton, C.M. and Evans, D.V., 1991, "Trapped modes in two-dimensional waveguides", *J. Fluid Mech.*, 229, 51-64.

Cao, Y., Beck, R. F. and Schultz, W. W., 1993, "An absorbing beach for numerical simulations of nonlinear waves in a wave tank", *Proc. 8th Int. Workshop Water Waves Float. Bodies*,, St. John's, Newfoundland, Canada, 17-20.

Cao, Y., Beck, R.F. and Schultz, W.W., 1994, "Nonlinear motions of floating bodies in incident waves", *Proc. 9th Int. Workshop Water Waves Float. Bodies*, Kuju, Oita, 33-37.

Celebi, M.S. and Beck, R.F., 1997, "Geometric modeling for fully nonlinear ship-wave interactions", *J. Ship Res.*, 41(1), 17-25.

Celebi, M. S., Kim, M. H. and Beck, R. F., 1998, "Fully nonlinear 3-D numerical wave tank simulation", *J. Ship Res.*, 42(1), 33-45.

Chakrabarti, S. K., 2001, "Application and Verification of Deepwater Green Function for Water Waves", *J. Ship Res.*, 45, 187-196.

Chan, R.K.C., 1977, "Finite difference simulation of the palnar motion of a ship", *Proc. 2nd Int. Conf. Numer. Ship Hydrodyn.*, Berkeley, Calif.

Chan, S.T.K. and Larock, B.E., 1973, "Free surface ideal fluid flows by finite elements", *ASCE J. Hydraul. Div.* 99: (HY6), 959-974.

Chang, M.S., 1977, "Computation of 3-D ship motions with forword speed", *Proc. 2nd Int. Conf. Numer. Ship Hydrodyn.*, U. California, Berkely.

Chaplin, J.R., Retzler C.H., Rainey, R.C.T., 1999, "Waves generated by a vertical cylinder moving in still waves", *Proc. 14th Int. Workshop Water Waves Float. Bodies*, Japan, March.

Chapman, R.B., 1975, "Numerical solutions for hydrodynamic forces on surface piercing plate oscillating in yaw and sway", *Proc. 1st Int. Symp. Numer. Hydrodyn.*, Gaithersburg, Md.

Chatry, G., Clement, A.H. and Sarmento, A.J.N.A, 1999, "Simulation of self-adaptively controlled OWC in a nonlinear numerical wave tank", *Proc. 9th ISOPE Conf.*, Brest, 3, 290-296.

Chau, F.P., 1989. The second order velocity potential for diffraction of waves by fixed offshore structures. PhD thesis, Department of Mechanical Engineering, University College London.

Chau, F.P. and Eatock Taylor, R., 1992, "Second-roder wave diffraction by a vertical cylinder", *J. Fluid Mech.*, 240, 571-599.

Chen, H.S. and Mei, C.C., 1974, "Oscillation and wave forces in a man-made harbor in the open sea", *10th Symp. Naval Hydrodyn.*, Cambridge, Mass, 573-596.

Chen X.B. and Wu, G.X., 2001, "On singular and highly oscillatory properties of the Green function for ship motions", *J. Fluid Mech.*, 445, 77-91.

Cheung, K.F., Isaacson, M. and Lee, J.W., 1996, "Wave diffraction around a three dimensional body in a current", *J. Offshore and Polar Engng.*, 118(4), 247-252.

Choi, Y.R., Hong, S.Y. and Choi, H.S., 2000, "An analysis of second-order wave forces on floating bodies by using a higher-order boundary element method", *Ocean Engng*, 28, 117-138.

Chung, T.J., 2002, "Computational Fluid Dynamics", Cambridge University Press.

Claerbout, J.F., 1976, "Fundamental Geophysical Data Process", McGraw-Hill, New York.

Clark, P.J., Bettess, P., Hearn, G.E. and Downie, M.J., 1991, "The application of finite element analysis to the solution of stokes wave diffraction problems", *Int. J. Numer. Methods Fluids*, 12, 343-367.

Clauss, G.F. and Steinhagen, U., 1999, "Numerical simulation of nonlinear transient waves and its validation by laboratory data", *Proc. 9th Int. Offshore and Polar Eng. Conf.*, Brest, France, 3, 368-375.

Clement, A. and Domgin, J. F., 1994, "Wave absorption in a 2D numerical wave basin by coupling two methods", In *modeling of Coastal and Estuarine Processes*, ed. F.J. Seabra Santos, A Temperville, 257-270.

Cohen, M. and Jennings, P.C., 1983, "Silent boundary methods for transient analysis", *Compuational Methods for Transient Analysis*, Edited by Belytschko, T. & Hughes, T.J.R., Elsevier Science Publishers B.V., Amsterdam.

Cointe, R. 1989, "Nonlinear simulation of transient free surface flow", *5th Int. Conf. Numer. Ship Hydrodyn.*, Hiroshima, Japan.

Cointe, R., Geyer, P., King, B., Molin, B. and Tramoni, M., 1990, "Nonlinear and linear motions of a rectangular barge in a perfect fluid", *Proc. of the 18th Symp. on Naval Hydro.*, Ann Arbor, Michigan, 85-98.

Cristescu, M. and Loubignac, G., 1978, "Gaussian quadrature formulas for functions with singularities in $1/R$ over triangles and quadrangles", *Recent Advances in Boundary Element Methods*, ed. C.A. Brebbia, Pentech Press, London, 375-390.

Cummins, W.E., 1962, "The impulsive response function and ship motions", Schiffstechnik, Band. 9.

Dale, N., 1998, "C++ plus data structures", Jones and Bartlett Publishers.

Dawson, C.W., 1977, "A practical computer method for solving ship-wave problems", *Proc. 2nd Int. Conf. Numer. Ship Hydrodyn.*, Berkelry, Calif..

Dean, R.G. and Sharmar, J.N., 1981, "Simulation of Wave Systems Due to Nonlinear Directional Spectra", *Proc. of the Intl. Symposium on Hydrodynamics in Ocean Engineering,* Norwegian Institute of Technology, 1211-1222.

Dingemans, M.W., 1997, "Water wave propagation over uneven bottoms", World Scientific Publ. Singapore.

Dommermuth, D.G. and Yue, D.K.P., 1987, "Numerical simulations of nonlinear axisymmetric flows with a free surface", *J. Fluid Mech.*, 178, 195-219.

Eatock Taylor, R. and Hung, S.M., 1987, "Second order diffraction forces on a vertical cylinder in regular waves", *Appl. Ocean Res.*, 9, 19-30.

Eatock Taylor, R., Hung, S.M. and Chau, F.P., 1989, "On the distribution of second order pressure on a vertical circular cylinder", *Appl. Ocean Res.*, 11, 183-193.

Emmons, H.W., 1972, "Gritique of numerical modeling of fluid-mechanics phenomena", *Ann. Rev. Fluid Mech.*, 2, 15-36.

Engeln-Müllges, G. and Uhlig, F., 1996, "Numerical Algorithms with C", Springer-Verlag, New York.

Euvrard, D., Jami, A., Lenoir, M. and Martin, D., 1981, "Recent progrss towords an optimal coupling between finite elements and singularity distribution procedures", *Proc. 3rd Int. Conf. Numer. Ship Hydrodyn.*, Berkeley, Calif..

Evans, D.V. and Linton, C.M., 1991, "Trapped modes in open channels", *J. Fluid Mech.*, 225, 153-175.

Evans, D.V. and Porter, R., 1997a, "Trapped modes about multiple cylinders in a channel", *J. Fluid Mech.*, 339, 331-356.

Evans, D.V. and Porter, R., 1997b. "Near-trapping of waves by circular arrays of vertical cylinders", *Appl. Ocean Res.*, 19, 83-99.

Evans, D.V. and Porter, R., 1999, "Trapping and near-trapping modes by arrays of cylinders in wave", *J. Engrg. Math.*, 35, 149-179.

Faltinsen, O.M., 1977, "Numerical solution of transient nonlinear free surface motion outside or inside moving bodies", *Proc. 2nd Int. Conf. Numer. Ship Hydrodyn.*, Berkeley, Calif.

Faltinsen, O.M., 1990, "Sea loads on ships and offshore structures", Cambridge University Press.

Faltinsen, O.M., 1993, "On seakeeping of conventional and high-speed vessels", *J. Ship Res.*, 37(2), 87-101.

Faltinsen, O.M., 1999, "Ringing loads on a slender vertical cylinder of general cross-section", *J. Engrg. Math.*, 35, 199-217.

Faltinsen, O.M. and Loken, A.E., 1978, "Drift forces and slowly varying forces ships and offshore structure", Norwegian Naritime Res., No 1.

Faltinsen, O.M. and Michelsen, F.C., 1974, "Motions of large structure in water at zero Froude number", *Int. Symp. Dynamics of Marine Vehicles and Structures in Waves*, 91-106, London.

Faltinsen, O.M., Newman, J.N. and Vinje, T., 1995, "Nonlinear wave loads on a slender vertical cylinder", *J. Fluid Mech.*, 289, 179-198.

Ferrant, P., 1993, "Three-dimensional unsteady wave-body interactions by a Rankine boundary element model", *Ship Technology Research*, 40(4), 165-175.

Ferrant, P., 1997, "Simulation of strongly nonlinear wave generation and wave-body interactions using 3D MEL model", *21st Symposium on Naval Hydrodynamics*, Washington.

Finkelstein, A., 1957, "The initial value problem for transient water waves", *Comm. Pure, Appl. Math.*, 10, 511-522.

Fonseca, N. and Guedes Soares, C., 1998, "Time-domain analysis of large-amplitude vertical motions and waves loads", *J. Ship Res.*, 42, 139-153.

Forristall, G.Z., 1985, "Irregular wave kinematics from a kinematic boundary condition fit (KBCF)", *Appl. Ocean Res.*, 7, 202–212.

Frank, W. 1967, "Oscillation of cylinders in or below the free surface of deep fluids", Report 2375, NSRDC.

Garrison, C.J., 1978, "Hydrodynamic loading of large offshore structure: three dimensional source distribution method", In: Zienkiewics, O.C. *et al.* (ed.) *Numerical Methods in Offshore Engineering*, Wiley., 87-140.

Gerritsma, J. and Beukelman, W., 1972, "Analysis of the resistance increase in waves of a fast cargo ship", *ISP*, 19, 217.

Goren, O., 1996, "On the second-order wave radiation of an oscillating vertical circular in finite-depth water", *J. Ship Res.*, 40(3), 224-234.

Greaves, D.M., 1995, "Numerical modelling of laminar separated flows and inviscid steep waves using adaptive hierarchical meshes", DPhil Thesis, Oxford University.

Greaves, D. M., 2004a, "A quadtree adaptive method for simulating fluid flows with moving interfaces", *J. Comp. Phys.*, 194 (1), 35-56.

Greaves, D. M., 2004b, "Simulation of interface and free surface flows in a viscous fluid using adapting quadtree grids", *Int. J. for Num. Methods in Fluids*, 44, 1093-1117.

Greaves, D.M., Borthwick, A.G.L., Wu, G.X. and Eatock Taylor, R., 1997, "A moving boundary finite element method for full nonlinear wave simulations", *J. Ship Res.*, 41(3), 181-194.

Grilli, S.T., Guyenne, P. and Dias, F., 2001, "A fully nonlinear model for three-dimensional overtMurning waves over arbitrary bottom", *Int. J. for Num. Methods in Fluids*, 35(7), 829-867.

Gu, X.K., Shen, J.W. and Moan, T., 2003, "Efficient and simplified time domain simulationof nonlinear responses of ships in waves", *J. Ship Res.*, 47, 262-273.

Guevel, P. and Bougis, J. 1982, "Ship motions with forword speed in infinite depth", *ISP*, 29, 10-117.

Haskind, M.D., 1946a, "The hydrodynamic theory of ship oscillations in rolling and pitching", (in Russian), Prikl. Mat. Mekh., 10, 33-36, (English Translation: SNAME Technical and Research Bulletin 1-12,3-43,1953).

Haskind, M.D., 1946b, "Oscillations of a ship on a calm sea", (in Russian), Izv, Akad. Nauk. SSSR. Otd. Tekh. Nauk 1, 23-34 (English Translation: SNAME Technical and Research Bulletin 1-12, 45-60, 1953).

Havelock, T.H., 1942, "The damping of the heaving and pitching motion of a ship", *Phil. Mag*, 33, 666-673.

Hearn, G.E., 1977, "Alternative methods of evaluating Green's function in three dimensional ship-wave problems", *J. Ship Res.*, 21(2), 89-93.

Hecht, F., 1998, "BAMG: Bidimensional anisotropic mesh generator", Website: http://www-rocq1.inria.fr/gamma/cdrom/www /bamg/eng.htm.

Hess, J.L. and Smith, A.M.O., 1964, "Calculation of nonlifting potential flow about arbitrary three dimensional bodies", *J. Ship Res.*, 8(2), 22–44.

Hu, P.X., Wu G.X. and Ma Q.W., 2002, "Numerical simulation of nonlinear wave radiation by a moving vertical cylinder", *Ocean Engng*, 29, 1733-1750.

Hu, Z. Z., Greaves, D. M. and Wu, G. X., 2002, "Numerical simulation of fluid flows using an unstructured finite volume method with adaptive tri-tree grids", *Int. J. for Num. Methods in Fluids*, 39, 403-440.

Hwang, J.H., Kim, Y.J. and Kim, S.Y., 1988, "Nonlinear hydrodynamics forces due to two-dimensinoal forced oscillations", *IUTAM, Symposium on Nonlinear Water Waves*.

Inglis, R.B. and Price, W.G., 1982, "A 3-D ship motion theory-computation between theoretical prediction and experimential data of the hydrodynamic coefficients with forword speed", *Trans. Roy. Inst. Nav. Arch.*, 124, 183-192.

Isaacson, M., 1982, "Nonlinear wave effects on fixed and floating bodies", *J. Fluid Mech.*, 120, 267-281.

Isaacson, M. and Cheung, K.F., 1990, "Time-domain solution for second-order wave diffraction", *J. Waterway, Port, Coastal and Ocean Eng.*, ASCE, 116(2), 191-210.

Isaacson, M. and Cheung, K.F., 1991, "Second order wave diffraction around two-dimensional bodies by time-domain method", *Appl. Ocean Res.*, 13(4), 175-186.

Isaacson, M. and Cheung, K.F., 1992, "Time-domain second-order wave diffraction in three dimensions", *J. Waterway, Port, Coastal and Ocean Eng.*, ASCE, 118(5), 496-516.

Isaacson, M. and Cheung, K.F., 1993, "Time domain solution for wave-current interactions with a two-dimensional body", *Appl. Ocean Res.*, 15, 39-52.

Isaacson, M., and Ng, J.Y.T., 1993, "Time-domain second-order wave radiation in two-dimension", *J. Ship Res.*, 37(1), 25-33.

Isaacson, M., Ng, J.Y.T. and Cheung, K.F., 1993. "Second-order wave radiation of three-Dimensional bodies by time-domain method", *J. Offshore and Polar Engng.*, 3(4), 264-272.

Israeli, M. and Orszag, S. A., 1981, "Approximation of radiation boundary conditions", *J. Comp. Phys.*, 41, 115-135.

Iwashita, H. and Ohkusu, M., 1989, "Hydrodynamic forces on a ship moving with forward speed in waves", *J. soc. Nav. Arch. Japan*, 166, 187-206.

Jagannathan, S., 1986, "Simulations of two-dimensional nonlinear free surface flows", OSDS'86.

Jagannathan, S., 1988, "Non-linear free surface flows and an application of the Orlanski boundary condition", *Int. J. Numer. Methods Fluids*, 8, 1051-1070.

Jami, A., 1981, "Numerical solving of transient linear hydrodynamics problems by coupling finite element and integral representation", *Proc. 3rd Int. Conf. Numer. Ship Hydrodyn.*, Berkeley, Calif.

Jensen, G., Bertram, V. and Soding, H., 1989, "Ship wave-resistance computations", *Proc. 5th Int. Conf. Numer. Ship Hydrodyn.*, Hiroshima, Japan.

Jensen, J. J. and Pedersen, P.T., 1979, "Wave induced bending moments in ships-a quadratic theory", *Transactions of Royal Institute of Naval Architects*, 121, 151-165.

Karami, G. and Derakhshan, D., 1999, "An efficient method to evaluate hypersingular and supersingular integrals in boundary integral equations analysis", *Engineering Analysis with Boundary Elements*, 23, 317-326.

Kashiwagi, M., 1995, "A new theory for oscillating and translating slender ships (in Japanese)", *J. Soc. Nav. Archi. Japan*, 178, 169-177.

Kashiwagi, M., 1996, "Full-nonlinear Simulations of hydrodynamic forces on a heaving two-dimensional body", *Journal of SNAJ*, 180, 373-381.

Kashiwagi, M., 1998, "Nonlinear simulations of wave-induced motions of a floating body by means of MEL method", *Proc. 3rd Int. Conf. on Hydrodynamics*, Seoul.

Kashiwagi, M. and Ohwatari, Y., 2002, "First- and second-order water waves around an array of floating vertical cylinders", *Proc. 17th Int. Workshop Water Waves Float. Bodies*, Cambridge, UK.

Kim, B. and Shin, Y.S., 2003, "A NURBS Panel Method for Three-Dimensional Radiation and Diffraction Problems", *J. Ship Res.*, 47, 177 -186.

Kim, D.J. and Kim, M.H., 1997, "Wave-Current interaction with a large three-dimensional body by THOBEM", *J. Ship Res.*, 41(4), 273-285.

Kim, M.H. and Yue, D.K.P., 1989, "The complete second-order diffraction solution for an axisymmetric body. Part 1. Monochromatic incident waves", *J. Fluid Mech.*, 200, 235-264.

Kim, W.D., 1965, "On the harmonic oscillating of rigid body on free surface", *J. Fluid Mech.*, 21, 241-255.

Kim, Y.W., Kring, D.C. and Sclavounos, P.D., 1997, "Linear and nonlinear interactions of surface waves with bodies by a three-dimensional Rankine panel method", *Appl. Ocean Res.*, 19, 235-249.

Koo, W. and Kim, M.H., 2004, "Freely floating-body simulation by a 2D fully nonlinear numerical wave tank", *Ocean Engng*, 31, 2011-2046.

Korvin-Kroukovsky, B.V., 1955, "Investigation of ship motions in regular waves", *Trans. SNAME*, 63, 386-433.

Korvin-Kroukovsky, B.V. and Jacobs, W.R., 1957, "Pitching and heaving motions of a ship in regular waves", *Trans. SNAME*, 65, 590-632.

Kotik, J. and Lurye, J., 1964, "Some topics in the theory of coupled ship motions", *Proc. 5th Symposium on Naval Hydrodynamics*, Bergen, Norway, 407–424, Office of Naval Research.

Lachat, J.C. and Watson, J.O., 1976, "Effective numerical treatment of boundary integral equations: A formulation for three dimensional elastostatics", *Int. J. Numer. Meth Eng.*, 10, 991-1005.

Lage, J. L. and Costa, J. A., 1987, "Potential problems solved by an analytical integration scheme", *Boundary Element Techniques: Applications in Fluid Flow and Computational Aspects*, eds. C. A. Brebbia and W. S. Venturini, Computational Mechanics Publications, Southampton, UK, 241-253.

Lamb, H., 1945, "Hydrodynamics", Dover, New York.

Larock, B.E. and Taylor, C., 1976, "Computing three-dimensional free-surface flow", *Int. J. Numer. Mech. Engrg*, 10, 1143-1152.

Lawson, C.L., 1977, "Software for Surface Interpolation", Mathematical Software III (John R. Rice, editor), pages 161–194. Academic Press, New York.

Lee, C.H., Maniar, H., Newman, J.N. and Zhu, X., 1997, "Computations of wave loads using a B-spline panel method", *Twenty-First Symposium on Naval Hydrodynamics*, Washington.

Lee, C.H. and Newman, J.N., 1991, "First and second order wave effects on a submerged spheroid", *J. Ship Res.*, 35(3), 183-190.

Lee, C.S and Kerwin, J.E., 2003, "A B-Spline Higher-Order Panel Method Applied to Two-Dimensional Lifting Problem", *J. Ship Res.*, 47, 290-298.

Lee, J.F. and Leonard, J.W., 1987, "A time-dependent radiation condition for transient wave-structure interactions", *Ocean Engng*, 14(6), 469-488.

Lenoir, M. and Jami, A., 1978, "A variational formulation for exterior problems in linear hydrodynamics", *Comput. Method Appl. Mech. Engrg.*, 16,341-359.

Li, Y., 1995, "Simulation of 3D nonlinear wave-structure interaction in a numerical wave basin", Ph.D. Thesis, Tech. Univ. of Nova Scotia Halifax.

Lin, W.C. and Read, A.M., 1976, "The second order steady force and moment of submerged bodies under waves", *11th Sym. on Naval Hydrodynamics.*, London.

Lin, W.M., Newman, J.N. and Yue, D.K, 1984, "Nonlinear forced motions of floating bodies", *Proc. 15th Symp. Naval Hydrodynamics*, Hamburg, Germany, 33-47.

Linton, C.M., 1991, "Radiation and diffraction of water waves by a submerged sphere in finite depth", *Ocean Engng*, 18, 61-74.

Lighthill, M. J., 1979, "Waves and hydrodynamic loading", *Proc. 2nd Int. Conf. Behavior Offshore Structures, BOSS*, London, 1-40.

Liu, Y.H., Kim, C.H., Lu, X.S., 1990, "Comparison of higher-order boundary element and constant panel methods for hydrodynamic loadings", *J. Offshore and Polar Engng.*, 1(1), 8–17.

Liu, Y. H., Kim, M. H. and Kim, C. H., 1995, "The computation of second-order mean and double-frequency wave loads on compliant TLP by HOBEM", *J. Offshore and Polar Engng.*, 5(2), 111-119.

Longuet-Higgins, M.S., 1963, "The effect of nonlinearities on the statistical distributions in the theory of sea waves", *J. Fluid Mech.*, 17, 459–480.

Longuet-Higgins, M. S. and Cokelet, E.D., 1976, "The deformation of steep surface waves on water, I. A numerical method of computions", *Proc. Roy. Soc. Series. A*, 350, 1-26.

Luke, J.C., 1967, "A variational principles for a fluid with a free surface", *J. Fluid Mech.*, 27, 395-397.

Lynch, D.R and Werner, F.E., 1987, "Three dimensional hydrodynamic on finite elements. Part I: Linearized harmonic model", *Int. J. Numer. Methods Fluids*, 7, 871-909.

Lynch, D.R. and Werner, F.E., 1991, "Three dimensional hydrodynamic on finite elements. Part Π : Non-linear time-stepping", *Int. J. Numer. Methods Fluids*, 12, 507-533.

Lysmer, J. and Kuhlemeyer, R.L., 1969, "Finite dynamic model for infinite media", *J. Engng Meth. Div.*, ASCE, 95, 859-877.

Ma, Q.W, 1998, "Numerical simulation of nonlinear interaction between structures and steep waves", Ph.D thesis, University College London.

Ma, Q.W., Wu G.X. and Eatock Taylor, R., 2001a, "Finite element simulation of fully nonlinear interaction between vertical cylinders and steep waves. Part 1: Methodology and numerical procedure", *Int. J. for Num. Methods in Fluids,* 36, 265-285.

Ma Q.W., Wu G.X. and Eatock Taylor, R., 2001b, "Finite element simulation of fully nonlinear interaction between vertical cylinders and steep waves. Part 2: Numerical results and validation", *Int. J. for Num. Methods in Fluids,* 36, 287-308.

MacCormack, R.W. and Lomax, H., 1979, "Numerical solution of uncompressible viscous flows", *Ann. Rev. Fluid Mech.*, 11, 289-316.

Maiti, S. and Sen, D., 2001, "Time-domain wave diffraction of two-dimensional single and twin hulls", *Ocean Engng*, 28, 639-665.

Malenca, S. and Molin, B., 1995, "Third harmonic wave diffraction by a vertical cylinder", *J. Fluid Mech.*, 302, 203-229.

Malenica, S., Eatock Taylor, R. and Huang, J.B., 1999, "Second order water wave diffraction by an array of vertical cylinders", *J. Fluid Mech.*, 390, 349-373.

Maniar, H.D. and Newman, J.N., 1997, "Wave diffraction by a long array of cylinders", *J. Fluid Mech.*, 339, 309-330.

Maruo, H., 1960, "The drift of body floating in waves", *J. Ship Res.*, 4, 1-10.

Maskell, S. J. and Ursell, F. 1970, "The transient motion of a floating body", *J. Fluid Mech.*, 44, 303-313.

McIver, M., 1994, "Second-order wave diffraction in two dimensions", *Appl. Ocean Res.*, 16, 19-25.

Mei, C.C., 1978, "Numerical methods in water-wave diffraction and radiation", *Ann. Rev. Fluid Mech.*, 10, 393-416.

Mei, C.C., 1983, "The applied dynamics of ocean surface waves", Wiley, New York.

Mei, C.C. and Chen, H.S., 1976, "A hybird element method for steady linearized free surface flows", Int. J. Numer. *Meth. Engrg.*, 10, 1153-1175.

Meyerhoff, W. K. and Schlachter, G., 1980, "An approach for the determination of hull grider loads in a seaway including hydrodynamic impacts", *Ocean Engng*, 7, 305-326.

Milgram, J. S., 1970, "Active water-wave absorbers", *J. Fluid Mech.*, 43(4), 845-859.

Miyata, H., Nishimura, S. and Masuko, A., 1985, "Finite difference simulation of nonlinear waves generated by ships of arbitrary three-dimensional configuration", *J. Comp. Phys.*, 60(3), 391-436.

Miyata, H., Sato, T. and Baba, N., 1987, "Difference solution of a viscous flow with free-surface wave about an advancing ship", *J. Comp. Phys.*, 72(2), 393-421.

Molin, B., 1979, "Second order diffraction loads upon three-dimension bodies", *Appl. Ocean Res.*, 1, 197-202.

Molin, B. and Marion, A., 1986, "Second order loads and motions for floating bodies in regular waves", *Proc. 5th Int. Offshore Mechanics and Arctic Engineering*, Tokyo, 353-360.

Nakayama, T. and Washizu, K., 1980, "Nonlinear analysis of liquid motion in a container subjected to a forced pitching oscillation", *Int. J. Num. Meth. Eng.*, 15, 1207-1220.

Nakos, D.E. and Sclavounos, P.D., 1990, "Ship motions by a three-dimensional Rankine panel method", *Proceedings of the 18th Symposium on Naval Hydrodynamics*, 21-40.

Nakos, D. E., Kring, D. C. and Sclavounos, P. D., 1993, "Rankine panel method for time-domain free surface flows", *Proc. 6th Int. Conf. Numer. Ship Hydrodyn.*, Iowa, USA, 614-634.

Newman, J.N., 1967, "The drift force and moment on ships in waves", *J. Ship Res.*, 11, 51-60.

Newman J.N., 1984, "Double-precision evaluation of the oscillatory source potential", *J. Ship Res.*, 28(3), 151-154.

Newman, J.N., 1985a, "Transient axisymmetric motions of a floating cylinder", *J. Fluid. Mech.*, 157, 17-33.

Newman, J.N., 1985b, "Algorithms for free-surface Green functions", *J. Engrg. Math.*, 19, 57-67.

Newman, J.N., 1990, "Second-harmonic wave diffraction at large depths", *J. Fluid Mech.*, 213, 59-70.

Newman, J.N. and Sclavounos, P., 1980, "The unified theory of ship motions", *13th Symposium on Naval Hydrodynamic*, Tokoyo, Japan.

Ng, J.Y.T. and Isaacson, M., 1993, "Second-order wave interaction with two-dimensional floating bodies by a time-domain method", *Appl. Ocean Res.*, 15, 95-105.

Noblesse, F., 1982, "The Green function in the theory of radiation and diffraction of regular water by a body", *J. Engrg. Math.*, 16, 137-169.

O'Carroll, M.J., 1976, "Variational technique for free-streamline problems", *Proc. 2nd Symp. Finite Element Methods in Flow Problem*, Ligure, Italy, 489-495.

Ogilvie, T.F., 1963, "First and second-order forces on a cylinder submerged under a free surface", *J. Fluid. Mech.*, 16, 451-472.

Ogilvie, T.F., 1964, "Recent progress toward the understanding and prediction of ship motions", *Proc. Fifth Symposium on Naval Hydrodynamics*, Bergen, Norway, 3-79, Office of Naval Research.

Ogilvie, T.F., 1983, "Second-order hydrodynamic effects on ocean platforms", *Proc. Int. workshop and platform motions*, Berkeley, California, 205-265.

Ogilvie, T.F. and Tuck, E.O., 1969, "A rational strip theory of ship motions", The Univ. of Michigan Report No. 013.

Ohkusu, M., 1969, "On the heaving motion of two circular cylinders on the surface of a fluid", Reports of Research Institute for Applied Mechanics, XVII, No.58, 167-185.

Ohl, C.O.G., Eatock Taylor, R., Taylor, P. H. and Borthwick, A.G.L., 2001, "Water wave diffraction by a cylinder array. Part 1. Regular waves", *J. Fluid Mech.*, 442, 1-32.

Ohyama, T. and Nadaoka, K., 1991, "Development of a numerical wave tank for analysis of nonlinear and irregular wave field", *Fluid Dynamics Research*, 8, 231-251.

Oomen, A., 1981, "Free surface potential flow compution using a finite element method", *Proc. 3nd Int. Conf. Numer. Ship Hydrodyn.*, Berkeley, Calif..

Orlanski, I., 1976, "A simple boundary condition for unbounded hyperbolic flows", *J. of Computational Phiysics*, 21, 251-269.

Orsag, S.A. and Israeli, M., 1974, "Numerical simulation of viscous incompressible flow", *Ann. Rev. Fluid Mech.*, 6, 281-318.

Pierson, W.J., 1993, "A third order oscillatory perturbation expansion for sums of interacting long crested Stokes waves", *J. Ship Res.*, 37, 345–383.

Pinkster, J.A. and Van Oortmerssen, G., 1977, "Computation of the first- and second-order wave forces on oscillating bodies in regular waves", In *Proc. 2nd Int. Conf. Numer. Ship Hydrodyn.*, ed. J.V. Wehausen and N. Salvesen, pp. 136-156, Berkeley:: University Extension Publications, University of California, Berkeley.

Prins, H.J. and Hermans, A.J., 1994, "Time-domain calculations of drift forces on floating two-dimensional object in current and waves", *J. Ship Res.*, 38(2), 97-103.

Raven, H.C., 1992, "A Practical Nonlinear Method for Calculating Ship Wavemaking and Wave Resistance", *19th Symp. Naval Hydrodynamics*, Seoul.

Retzler, C.H., Chaplin, J.R., Rainey, R.C.T., 2000, "Transient motion of a veridical cylinder: measurements and computations of the free surface", *Proc. 15th Int. Workshop Water Waves Float. Bodies*, Israel, March.

Rizzo, F. J. and Shippy, D. J., 1977, "An advanced boundary integral equation method for three-dimensional thermoelasticity", *Int. J. Numer. Meth Eng.*, 11, 1753-1768.

Robertson, I. and Sherwin, S., 1999, "Free-Surface Flow Simulation Using hp/Spectral Elements", *J. Comp. Phys.*, 155, 26–53.

Robertson, I., Sherwin, S.J. and Graham, J.M.R, 2004, "Comparison of wall boundary conditions for numerical viscous free surface flow simulation", *J. Fluids & Structures*, 19, 525-542.

Romate, J.E., 1992, "Absorbing boundary condiations for free surface waves", *J. Comp. Phys.*, 99, 135-145.

Saad, Y., 2003, "Iterative methods for sparse linear systems", 2nd edition, Society for Industrial and Applied Mathematics, Philadelphia, PA, USA

Salvesen, N., Tuck, E.O. and Fatinsen, O., 1970, "Ship motions and sea loads", *Trans. SNAME*, 78, 250-280.

Sarpkaya, T. and Isaacson, M., 1981, "Mechanics of wave forces on offshore structures", Van Nostrand Reinhold, New York.

Schneekluth, H. and Bertram V., 1998, "*Ship Design for Efficiency & Economy*", Butterworth-Heinemann, Oxford.

Schwartz, L.W. and Fenton, J.D., 1982, "Strongly nonlinear waves", *Annu. Rev. Fluid. Mech.*, 14, 39-60.

Scullen, D. and Tuck, E.O., 1995, "Nonlinear free-surface flow computations for submerged cylinders", *J. Ship Res.*, 39(3), 185-193.

Sen, D., 1993, "Numerical simulation of motions of two-dimensional floating bodies", *J. Ship Res.*, 37(4), 307-330.

Shen, S.F., 1977, "finite element methods in fluid mechanics", *Ann. Rev. Fluid Mech.*, 9, 421-445.

Skourup, J. and Schaffer, H. A., 1998, "Simulation with a 3D active absorption method in a numerical wave tank", *Proc. 8th Int. Offshore and Polar Eng. Conf.*, Montreal, Quebec, Canada, 3, 248-255.

Smith, D.A., 1974a, "Finite element analysis of the forced oscillation of ship hull forms", M.S. Thesis. Naval Postgraduate School, Monterey, CA.

Smith, D.A., 1974b, "A nonreflecting plane boundary for wave propagation problems", *J. Comp. Phys.*, 15, 492-503.

Smith, R.N.L, 2000, "Direct Gauss quadrature formulae for logarithmic singularities on isoparametric elements", *Engineering Analysis with Boundary Elements*, 24, 161-167.

Srivastava, R. and Contractor, D. N., 1992, "Efficient evaluation of integrals in three-dimensional boundary element method using linear shape functions over plane triangular elements", *Appl. Math. Modelling*, 16, 282-290.

Subramanya, R. and Grilli, S. T., 1994, "Kinematics and properties of fully nonlinear waves shoaling and breaking over a gentle slope", *Proceedings of the International Symposium: WAVES-Physical and Numerical Modeling*, University of British Columbia, Vancouver, Canada, 1106-1115.

Tanizawa, K., 1995, "A Nonlinear Simulation Method of 3-D body Motions in Waves (1st Report)", *J. Soc. Nav. Arch. Japan*, 178, 179-191.

Tanizawa, K., 1996, "Long time fully nonlinear simulation of floating body motions with artificial damping zone", *J. Soc. Nav. Archi. Japan*, 180, 311-319.

Tasai, F. and Takagi, M., 1969, "Theory and calculation of ship response in regular waves", *Proc. Symp. on Seaworthiness,* Soc. Naval Arch. Japan, Tokyo.

Tsai, W.T. and Yue, D. K.P., 1996, "Computation of nonlinear free-surface flows", *Annu. Rev. Fluid. Mech.*, 28, 249-278.

Telste, J.G., 1985, "Calculation of fluid motion resulting from large amplitude forced heave motion of two-dimensional cylinder in a free surface", *Proc. 4th Int. Conf. On Numerical Ship Hydro.*, 81-93, Washington, USA.

Teng, B. and Eatock Taylor, R., 1994, "Application of a higher order boundary element method in the calculation of wave run-up in a weak current", *Proc. 4th Int. Offshore and Polar Eng. Conf.*, Osaka, Japan, April.

Thompson, J.F., Soni, B.K. and Weatherill N.P., 1999, "Handbook of grid generation", CRC Press LIC.

Turnbull, M.S., A.G.L. Borthwick and Eatock Taylor, R., 2003, "Wave-structure intersection using coupled structured-unstructured finite element meshes", *Appl. Ocean Res.*, 25, 63-77.

Ursell, F., 1949, "On the heaving of circular cylinder on the surface of a fluid", *Quarterly J. of Mech. and Applied Math.*, 2, 218-231.

Ursell, F., 1951, "Trapping modes in the theory of surface waves". *Proc. Camb. Phil. Soc.*, 47, 347-358.

Vada, T., 1987, "A numerical solution of second-order wave-diffraction problem for submerged cylinder of arbitrary shape", *J. Fluid. Mech.*, 174, 23-37.

Van Daalen, E.F.G., 1993, "Numerical and Theoretical Studies of Water Waves and FloatingBo dies", Ph.D. thesis, University of Twente, The Netherlands, pp.1-285.

Van Oortmerssen, G., 1976, "The motion of a moored ship in waves", Netherlands Ship Model Basin (NSMB), Publication No. 510, Wageningen, the Netherlands.

Vantorre, M., 1986, "Third-order theory for determining the hydrodynamic forces on axisymmetric floating or submerged bodies in oscillatory heaving motion", *Ocean Engng*, 13, 339-371.

Varyani, K., 1993, "Added resistance on submersibles advancing in waves", *ISP*, 40(424), 311-331.

Vinje, T. and Brevig, P., 1981a, "Nonlinear Ship Motions", *Proc. of the 3rd Int. Conf. on Num. Ship Hydro.*, pp. IV3-1-IV3-10

Vinje, T., and Brevig, P., 1981b, "Nonlinear, two dimensional ship motions", Norwegian Hydrodynamic Laboratories, Report R-112.81, Trondheim, Norway, 1-97.

Wang, C.Z. and Khoo, B.C., 2005, "Finite element analysis of two-dimensional nonlinear sloshing problems in random excitations", *Ocean Engng*, 32, 107-133.

Wang, C.Z. and Wu, G.X., 2004, "Interaction between nonlinear water wave and structures with flare", *Proc. 19th Int. Workshop Water Waves Float. Bodies*, Cortona, Italy.

Wang, P., 1993, "Numerical research on (I) ship internal waves, and (II) breaking waves", Technical Report 93-93, Ocean Engineering Laboratory, University of California, Santa Barbara. Part II.

Wang, X.W. and Spaulding, M.L. 1988, "A two-dimensional potential flow model of the wave field generated by a semisubmerged body in heaving motion", *J. Ship Res.*, 32(2), 83-91.

Watson, D.F., 1981, "Computing the N-dimensional Delaunay tessellation with application to Voronoi polytopes", *Comp. J.*, 24(2), 167-172.

Wehausen, J.V., 1967, "Initial value problem for the motion in an undulating sea of a body with fixed equilibrium position", *J. Engrg. Math.*, 1(1), 1-17.

Westhuis, J.H., 2001, "The numerical simulation of nonlinear waves in a hydrodynamic model test basin", Ph.D thesis, University of Twente.

Wellford, C.L. and Ganaba, T., 1980, "Finite element procedures for fluid mechanics problems involving lagre free surface motion", *Proc. 3rd Int. Conf. Finite Element in Flow Problem.*

Whitham, G.B., 1967, "Nonlinear dispersion of water waves", *J. Fluid Mech.*, 27, 399-412.

Whitham, G.B., 1970, "Two-timing variational principles and waves", *J. Fluid Mech.*, 44, 373-395.

Whitham, G.B., 1974, "Linear and nonlinear waves", Wiley-Interscience, New York.

Williams, A.N. and Abul-Azm, A.G., 1989, "Hydrodynamic interactions in floating cylinder array-II. Wave radiation", *Ocean Engng*, 16, 217-263.

Wu, G.X., 1991a, "On the second order wave reflection and transmission by a horizontal cylinder", *Appl. Ocean Res.*, 13, 58-62.

Wu, G.X., 1991b, "Hydrodynamic forces on a submerged cylinder advancing in water waves of finite depth", *J. Fluid Mech.*, 224, 645-659.

Wu, G.X., 1993, "A relation between waves reflection and transmission by a submerged body at forward speed", *Appl. Ocean Res.*, 15, 311-331.

Wu, G.X., 1998, "Hydrodynamic force on a rigid body during impact with liquid", *J. Fluids & Structures*, 12, 549-559.

Wu, G.X., 2006, "Numerical simulation of water entry of twin wedges", *J. Fluids & Structures*, 22(1), 99-108.

Wu, G.X. and Eatock Taylor, R., 1987, "Hydrodynamic forces on submerged oscillating cylinders at forward speed", *Proc. Royal Soc. Lond.*, Series A, 414, 149-170.

Wu, G.X. and Eatock Taylor, R., 1989, "Second order diffraction forces on horizontal cylinders", *J. of Hydrodynamics*, 12, 55-65.

Wu, G.X. and Eatock Taylor, R., 1990a, "The hydrodynamic force on an oscillating ship with low forward speed", *J. Fluid Mech.*, 211, 333-353.

Wu, G.X. and Eatock Taylor, R., 1990b, "The second order diffraction forces on horizontal cylinders in finite water depth", *Appl. Ocean Res.*, 12, 106-111.

Wu G X and Eatock Taylor, R., 1990c, "The hydrodynamic forces on a submerged sphere moving in a circular path", *Proc. Royal Soc. Lond.*, Series A, 428, 215-227

Wu, G.X. and Eatock Taylor, R., 1994, "Finite element analysis of two-dimensional non-linear transient water waves", *Appl. Ocean Res.*, 16, 363-372.

Wu, G.X. and Eatock Taylor, R., 1995, "Time stepping solutions of the two dimensional nonlinear wave radiation problem", *Ocean Engng*, 22, 785-798.

Wu, G.X. and Eatock Taylor, R., 1996, "Transient motion of a floating body in steep water waves", *Proc. 11th Int. Workshop Water Waves Float. Bodies*, Hamburg.

Wu, G.X. and Eatock Taylor, R., 2003, "The coupled finite element and boundary element analysis of nonlinear interactions between waves and bodies", *Ocean Engng*, 30, 387-400.

Wu G.X. and Hu Z.Z., 2004, "Simulation of Nonlinear Interactions between Waves and Floating Bodies through a Finite Element Based Numerical Tank", *Proc. R. Soc. Lond.*, Series A, 460, 2797-2817.

Wu, G.X., Ma, Q.W. and Eatock Taylor, R., 1996, "Analysis of interactions between nonlinear waves and bodies by domain decomposition", *21st Symp. on Naval Hydrodynamics,* Trondheim, Norway

Wu, G.X., Ma, Q.W. and Eatock Taylor, R., 1998, "Numerical simulation of sloshing waves in a 3D tank based on a finite element method", *Appl. Ocean Res.*, 20, 337-355.

Wu, G.X., Sun, H. and He, Y.S., 2004, "Numerical simulation and experimental study of water entry of a wedge in free fall motion", *J. Fluids & Structures*, 9, 277-289.

Wu, M. K. and Moan, T., 1996, "Linear and nonlinear hydroelastic analysis of high-speed vessels", *J. Ship Res.*, 40, 149-163.

Xia, J. Z., Wang, Z. H. and Jensen, J. J., 1998, "Nonlinear wave loads and ship responses by a time domain strip theory", *Marine Structures*, Vol. 11, 101-123.

Xu, H. and Yue, D.K., 1992, "Computations of fully nonlinear three-dimensional water waves", *Proc. 19th Symp. On Naval Hydrodyn.*, Seoul, Korea, 177-201.

Yamamoto, Y., Fujino, M. and Fukasaw, T., 1978, 1979, "Motions and longitudinal strength of a ship in head sea and the effects of non-linearities", *J. Soc. Nav. Archi. Japan*, 143, 179-187, and 144, 205-213.

Yerry, M.A. and Shepherd, M.S., 1984, "Automatic 3D mesh generation by the modified-octree technique", *Int. J. Num. Meth. Eng.*, 20, 1965-90.

Yeung, R.W., 1973, "A singularity-distribution method for free-surface flow problems with an oscillating body", Report No. NA73-6, U. California, Berkely.

Yeung, R.W., 1982, "Numerical methods in free-surface flows", *Int. J. Numer. Methods Fluids*, 14, 395-442.

Yeung, R.W. and Wu, C.F., 1989, "Nonlinear wave-body motion in a closed domain", *Computers and Fluids*, 17, 351-370.

Yim, B., 1975, "A variational principle associated with a localized finite element technique for steady ship-wave and cavity problems", *Proc. 1st Int. Conf. Numer. Ship Hydrodyn.*, Gaithersburg, Md., 137-153.

Yue, D.K.P. and Bouger, Y.C., 1979, "A hybird integral-equation method for steady two-dimensional ship waves", *Int. J. Numer. Meth. Engrg*, 14, 17-36.

Yue, D.K.P, Chen, H.S. and Mei,.C.C., 1978, "A hybird element method for diffraction of water waves by three-dimensional bodies", *Int. J. Numer. Methods Fluids*, 12, 245-266.

Zhao, R., and Faltinsen, O.M., 1993, "Water entry of two dimensional bodies", *J. Fluid Mech.*, 246, 593-612.

Zhu, G., Borthwick, A.G.L. and Eatock Taylor, R., 2001, "A finite element model of interaction between viscous free surface waves and submerged cylinders", *Ocean Engng*, 28, 989-1008.

Zhu, X.X., 2000, "Modeling of free-formed curves and surfaces" (in Chinese). Science Press, Beijing.

Zienkiewicz, O.C., Kelly, D.W. and Bettess, P., 1977, "The coupling of the finite element method and boundary solution procedures", *Int. J. Numer. Methods Fluids*, 12, 343-367.

Zienkiewicz, O.C., Kelly, D.W. and Bettess, P., 1978, "The finite element method for determining fluid loadings on rigid structures", in LEWIS, R.W. (Ed.): *Numerical Methods in Offshore Engineering*, Wiley, Chap. 4.

APPENDIX A

Some abscissae and weights of Gauss and Hammer quadratures are given in tables A.1 and A.2, respectively.

n	i	ξ_i, η_i	w_i
2	1	$1/\sqrt{3}$	1
	2	$-1/\sqrt{3}$	1
3	1	0.0	8/9
	2	$\sqrt{3}/5$	5/9
	3	$-\sqrt{3}/5$	5/9
4	1	0.86113631	0.34785485
	2	-0.86113631	0.34785485
	3	0.33998104	0.65214515
	4	-0.33998104	0.65214515
7	1	0.0	0.41795918
	2	0.94910791	0.12948497
	3	-0.94910791	0.12948497
	4	0.74153119	0.27970539
	5	-0.74153119	0.27970539
	6	0.40584515	0.38183005
	7	-0.40584515	0.38183005

Table A.1 Abscissae and weights of Gauss quadrature

m	i	ξ_i	η_i	ζ_i	w_i'
1	1	1/3	1/3	1/3	1
3	1	1/2	1/2	0	1/3
	2	0	1/2	1/2	1/3
	3	1/2	0	1/2	1/3
4	1	1/3	1/3	1/3	-9/32
	2	3/5	3/5	1/5	25/96
	3	1/5	1/5	3/5	25/96
	4	1/5	1/5	1/5	25/96
7	1	0.33333333	0.33333333	0.33333333	0.11250000
	2	0.79742699	0.10128651	0.10128651	0.06296959
	3	0.10128651	0.79742699	0.10128651	0.06296959
	4	0.10128651	0.10128651	0.79742699	0.06296959
	5	0.05971587	0.47014206	0.47014206	0.06619708
	6	0.47014206	0.05971587	0.47014206	0.06619708
	7	0.47014206	0.47014206	0.05971587	0.06619708

Table A.2 Abscissae and weights of quadrature in a triangle

APPENDIX B

1. Shape functions of 3-node triangular elements

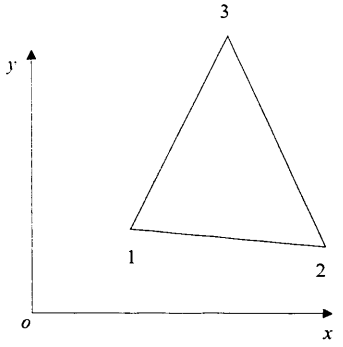

Figure B.1 3-node Triangular element

As shown in Figure B.1, the triangular element has three nodes numbered anticlockwise as 1,2,3 , and their corresponding coordinates are (x_i, y_i) $(i = 1,2,3)$. The three shape functions may be written as

$$N_i(x,y) = \frac{1}{2A}(a_i + b_i x + c_i y) \quad i = 1,2,3, \tag{B.1}$$

where A is the area of the triangle. a_i, b_i and c_i are given as follows

$$a_i = \frac{1}{2A}(x_j y_k - y_j x_k),$$

$$b_i = \frac{1}{2A}(y_j - y_k),$$

$$c_i = \frac{1}{2A}(x_k - y_i).$$

The values of j and k corresponding to $i = 1,2,3$ are $j = 2,3,1$ and $k = 3,1,2$ respectively.

In another way, we can obtain the shape functions by mapping a general triangle to a right-isosceles triangle (see Figure B.2). The coordinates (ξ, η) at nodes 1, 2 and 3 are (0,0), (1,0) and (0,1), respectively. The three shape functions are given as follows

$$\begin{aligned} N_1 &= 1 - \xi - \eta \\ N_2 &= \xi \\ N_3 &= \eta \end{aligned} \quad , \tag{B.2}$$

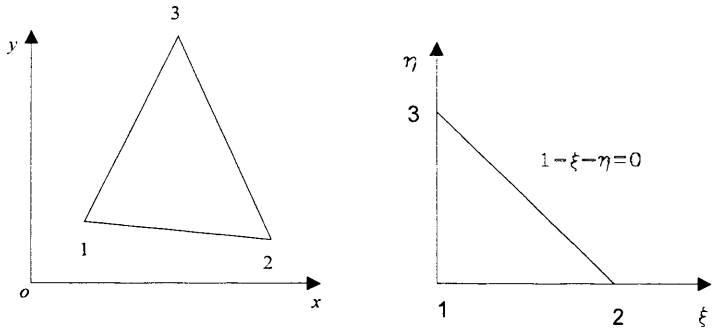

Figure B.2 Mapping from general triangle
to right-isosceles triangle

2. Shape functions of 4-node quadrilateral elements

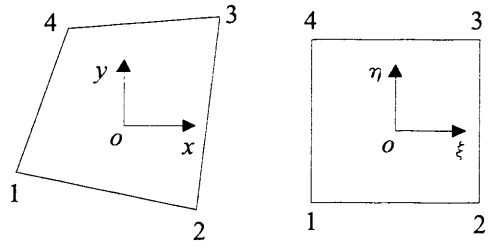

Figure B.3 Mapping from quadrilateral to square

Similar to the triangle as shown in Figure B.2, when mapping a quadrilateral to a square whose four nodes are at (-1,-1), (1,-1), (1,1) and (-1,1), respectively (see Figure B.3), the shape functions may be represented as

$$
\begin{aligned}
N_1(\xi,\eta) &= \frac{1}{4}(1-\xi)(1-\eta), \\
N_2(\xi,\eta) &= \frac{1}{4}(1+\xi)(1-\eta), \\
N_3(\xi,\eta) &= \frac{1}{4}(1+\xi)(1+\eta), \\
N_4(\xi,\eta) &= \frac{1}{4}(1-\xi)(1+\eta).
\end{aligned}
\tag{B.3}
$$